Environmental Hydraulics and Sustainable Water Management

Volume 1:
Environmental Hydraulics

Edited by J.H.W. Lee & K.M. Lam

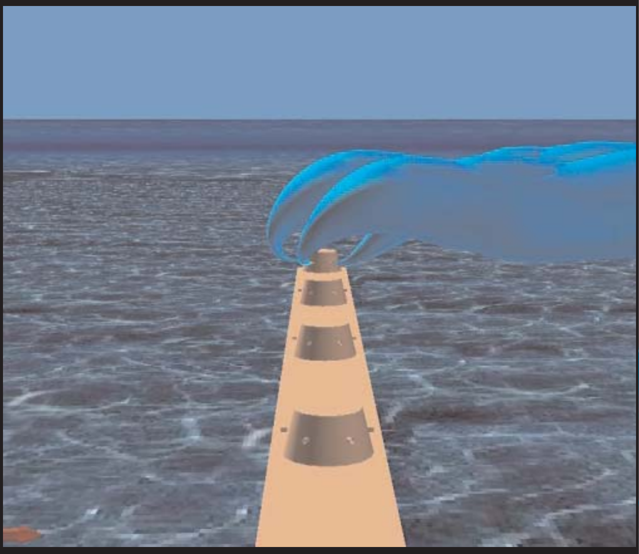

ENVIRONMENTAL HYDRAULICS AND
SUSTAINABLE WATER MANAGEMENT

This page intentionally left blank

PROCEEDINGS OF THE 4TH INTERNATIONAL SYMPOSIUM ON ENVIRONMENTAL HYDRAULICS AND THE 14TH CONGRESS OF ASIA AND PACIFIC DIVISION, INTERNATIONAL ASSOCIATION OF HYDRAULIC ENGINEERING AND RESEARCH, 15–18 DECEMBER 2004, HONG KONG

Environmental Hydraulics

Edited by

J.H.W. Lee
The University of Hong Kong, China

K.M. Lam
The University of Hong Kong, China

Volume 1

A.A. BALKEMA PUBLISHERS LEIDEN / LONDON / NEW YORK / PHILADELPHIA / SINGAPORE

Taylor & Francis
Taylor & Francis Group
6000 Broken Sound Parkway NW, Suite 300
Boca Raton, FL 33487-2742

Version Date: 20140416

International Standard Book Number-13: 978-1-4822-6286-5 (eBook - PDF)

Visit the Taylor & Francis Web site at
http://www.taylorandfrancis.com

and the CRC Press Web site at
http://www.crcpress.com

Environmental Hydraulics and Sustainable Water Management – Lee & Lam (eds)
© 2005 Taylor & Francis Group, London, ISBN 04 1536 546 5

Table of Contents

Editors' foreword XXV
Chairman's message XXVII
Organisation XXIX

Volume I

Keynote lectures

Artificial intelligence techniques in environmental hydrodynamics: The role of expert knowledge 3
A.E. Mynett, Q.N. Chen & V.M. Babovic

Hydraulic phenomena in urban atmospheric environments and their role in contaminant dispersion 15
H.J.S. Fernando

Invited lectures

Exchange flows and estuarine barriers 27
P.A. Davies & A.J.S. Cuthbertson

The interface smoothness criteria and its application for two layer flow from a circular weir 35
I.R. Wood

Water quality management of river and estuarine waters 45
R.A. Falconer & B. Lin

Fate and transport modeling vs. models: a management perspective 57
W.S. Lung

Internal waves in Monterey Bay: An application of SUNTANS 67
O.B. Fringer, M. Gerritsen & R.L. Street

Environmental and ecological impacts of the Three Gorges Project on the Yangtze River 77
Z.Y. Wang

Resolving environmental hydraulics complexity, linking theory, practice and conceptual ideas 87
K. Cederwall

1 Mixing and transport

1.1 Mixing and transport – I

Prediction of turbulent flow structure in compound channel with roughened floodplain using Large Eddy Simulation 99
M. Ifuku & K. Shiono

A field study of extremely rough, three-dimensional river flow 107
M.J. Franca & U. Lemmin

Influence of variable morphological conditions on the mass transport characteristics in rivers 113
V. Weitbrecht & G.H. Jirka

Longitudinal vortices in a water of finite depth in the absence of wind 121
Z. Huang & C.C. Mei

1.2 Mixing and transport – II

Field tests on transverse mixing in natural streams 129
I.W. Seo, K.O. Baek & T.M. Jeon

Effects of variable river geometry on longitudinal dispersion 137
M. Jamali & G.A. Lawrence

Vertical turbulent mixing in tidal estuary 143
Y. Du & J. Chu

Experimental scale effect of pollutant diffusion/dispersion in rivers 151
L. Luo, M.J. Wang & Y.L. Jiang

Trace experimental study on diffusion coefficients at heavy sediment-carrying reach of Yellow River 159
G.H. Hu & X.Q. Xiao

Advection and dispersion of substance discharged by intermittent point source in rivers 167
Z.H. Wu & H.T. Qiao

1.3 Gas transfer

Modeling wind-driven gas-transfer in a lake 177
C. Gualtieri

Experimental study on air-water interfacial turbulent hydrodynamics and gas transfer in wind-induced open channel flows 185
K. Yoshida & I. Nezu

Estimation of the transfer velocity of carbon dioxide at the surface of wind waves 193
H. Tsumori, Y. Sugihara & A. Masuda

Surface-renewal eddies at the air-water interface in oscillating-grid turbulence 199
Y. Sugihara & H. Tsumori

Numerical simulation of two-phase flow in aeration tank 207
J. Mao, Y. Chen & D. Wang

Study on numerical simulation for rupture of bubble at water surface by Level Set method 215
K. Asai & K. Tsubogo

2 Stratified flow

2.1 Stratified flow – I

The dynamic behavior of the benthic boundary layer in a thermally stratified lake 225
C.L. Marti & J. Imberger

Formation and expansion of a double-diffusive staircase in Lake Nyos, Cameroon 233
M. Schmid & A. Wüest

Turbidity currents in an Alpine pumped-storage reservoir 239
J. Bühler, C. Siegenthaler & A. Wüest

Interfacial waves in exchange flows over a sill 245
H. Fouli & D.Z. Zhu

Experiments on the stability analysis of thermally stratified shear flows in weakly curved open channel 251
K. Chu, Z. Hua & H. Wang

k-ε modeling of vertical mass transport in turbulent stratified open-channel flow 257
C. Reiher & Y. Niño

Q2D turbulence by Rayleigh-Taylor instabilities 263
X. Li & V.H. Chu

Numerical simulations and linear stability analysis of transient buoyancy-induced flow in a two-dimensional enclosure 269
C.F. Ihle, Y. Niño & R.L. Frederick

2.2 Stratified flow – II

A large, vertically distorted hydraulic model of outflow withdrawal from a thermally stratified reservoir 277
R. Ettema, M. Muste, A.J. Odgaard & O. Abaci

Use of physical model and 3D numerical models to design a selective withdrawal intake 283
P.J. Ryan, F.A. Locher & S. Tu

Application of sigma coordinate ocean model to strongly stratified estuary with steep bottom slopes 289
M. Irie, K. Nakatsuji & S. Nishida

Enhancement of mixing processes in semi-deep coastal channels by a bathymetry change 297
N. Ravlic

Numerical prediction of incompressible two-fluid system and its application to stratified flows with water and silicone-oil 303
K. Yoshida, S. Ushijima & I. Nezu

Numerical study of a turbulent oil slick 311
G.Q. Chen, L.Z. Zhang & J.H.W. Lee

3 Jets and plumes

3.1 Jets and plumes – I

Non-dimensional scaling of turbulent jets in confined spaces 319
P. Rinaldi & F. Valentin

Further investigations on jet spreading in oscillating grid turbulence 325
A.W.K. Law & D.W.F. Ho

Experimental study on tandem buoyant jets in crossflow 331
D. Yu, J.H.W. Lee & C.W. Li

Light attenuation data from weakly and strongly advected discharges 337
G. Kikkert, M.J. Davidson & R.I. Nokes

Integral model prediction and laser induced fluorescence measurement of round buoyant jet in counterflow 343
W.Y. Lee, K.M. Lam & C.H.C. Chan

Observation on the vertical upward discharge of dense liquid into the stagnant stratified ambient water 351
B.S. Shiau & B.J. Tsai

Spreading and mixing characteristics of a round jet in co-flow 357
H. Tang, Y. Xiao & M. Hua

3.2 Jets and plumes – II

LES of 2D and 3D vertical jets impinging on free surfaces 367
Y.P. Chen, C.W. Li & C.K. Zhang

Similarity analyses on flapping turbulent plane jets 375
J. Sun & C.T. Hsu

Study on the behavior of jets discharged vertically downward in flowing environment 381
W.X. Huai & Z.H. Yang

Laser Doppler velocimetry measurements on a duckbill valve jet in a co-flow 387
H.W. Tang, J.H.W. Lee, Zh. Gao & Y. Xiao

The characteristics of flow and concentration fields near bank outfall 393
X. Huang

3.3 Bubble plumes/jets

Entrainment and mixing properties of a simple bubble plume 403
C. Bergmann, D.G. Seol, T. Bhaumik & S.A. Socolofsky

Interaction between a bubble plume and the near field in a stratified lake 411
D.F. McGinnis, J.C. Little, A. Lorke, A. Wüest & A. Stöckli

3D PTV measurement of bubble jet in water 417
J. Funaki, Y. Yokoyama & K. Hirata

Upward flux of methane in the Black Sea: Does it reach the atmosphere? 423
D.F. McGinnis, A. Wüest, C.J. Schubert, L. Klauser, A. Lorke & R. Kipfer

The use of mechanical mixers to improve circulation and mixing of large bodies of water 431
K.H.M. Ali & L.S. Tong

Production of efficient bubble plumes for destratification: Theory and experiment 439
N.V.M. Odd, J.G. Rodger & C.B. Waters

3.4 Outfall discharge

Near- and far-field model coupling methodology for wastewater discharges 447
T. Bleninger & G.H. Jirka

Mixing and entrainment in tidal impoundments 455
K.H.M. Ali, M. Diamanti & G. Papapostolou

2-D numerical simulation of saline intrusion in marine sewage outfalls 461
W. Wu, J. Xia & Z.M. Yan

Probabilistic modeling of produced water outfall 467
H. Niu, T. Husain, B. Veitch & N. Bose

Formulas for dilution prediction of inclined buoyant jets in stagnant water 473
Z.R. Guo

4 Hydrodynamic modelling

4.1 Hydrodynamic models – I

3D LES on the formation mechanism of Langmuir circulations 481
K. Uzaki & N. Matsunaga

Semi-implicit sigma-coordinate hydrodynamic model 489
W.C. Pang & P. Tkalich

Effects of core-region vortices on near-wall vortices generated by steady incoming flows past a wall-mounted long circular cylinder 495
M.K. Kwan, C.T. Hsu & R.R. Hwang

Finite difference TVD scheme for modeling two-dimensional advection-dispersion 503
Y. Guan & D. Zhang

Study of island wakes in shallow waters 511
F.C. Chan & M.S. Ghidaoui

k-ε turbulent modeling of tidal bore in an idealized estuary 517
L.F. Lu, S.W. Li & Z. Shi

Numerical simulation of particle-laden gas wake flow by vortex method 525
H. Yagami & T. Uchiyama

4.2 Hydrodynamic models – II

Hydrodynamic characteristics of the new Athens 2004 Olympic Rowing Center 535
G. Christodoulou, I. Papakonstantis, A. Stamou, A. Andreadakis, K. Noutsopoulos & E. Romas

Stability of dumped sediment on sandbanks due to tidal currents off the East Anglia coast, UK 541
C.P. Kuang, P.K. Stansby, D.R. Laurence & B.E. Launder

Reservoir circulation modeling with analytical non-uniform wind boundary conditions 549
S. Rubbert, C. Reuter & J. Köngeter

Numerical analysis of flows in circular and square stones embedded fishways 557
S. Chhatkuli & M. Fujihara

On the time scale of sea water exchange in Ariake Sea 563
K. Asai & H. Sato

Numerical simulation on the research of cooling water engineering of fire plant considering the environmental protection under the impaction of coastal artificial land engineering 571
Z. Li, Q. Zhu, S. Zhang & R. Zhao

Numerical modelling approach in the sustainable development of a power plant 579
N.M.K. Nik Hassan, I.T.S. Tan & A.M. Hashim

Application of tidal flow mathematical model in the study on deepwater navigation channels in Xinghua Bay 587
M.G. Li

Development of coupled 1-D–2-D hydrodynamic models for tidal rivers 593
H. Yin & Z. Xu

Hydrodynamic and transport modeling study in a highly stratified estuary 599
F. Arega & E. Hayter

4.3 Hydrodynamic models – III

Modeling water quality for Mu-Dan Reservoir in southern Taiwan 607
C.C. Young, J.T. Kuo, W.C. Liu & W.S. Lung

A two-dimensional water quality approach in transient flow modeling 613
Gh. Naser, B.W. Karney & M.S. Ghidaoui

Hydrodynamic and water quality modeling approach for a dynamic lagoon system 621
A. Ekadal, M. Gurel, A. Erturk & A. Tanik

Analysis of water quality in Lake Ogawara using a coupled hydrodynamic and primitive ecosystem model 629
S. Suzuki, S. Nishida & K. Nakatsuji

The research of plane two-dimensional eutrophication ecological dynamics model in lake 637
Y. Wang & X. Zhou

The research of water environment capacities in lake – taking Bosten Lake as an example 643
J. Pan & Y. Wang

Grey relational assessment of water quality and space diversity analysis of pollution for coastal zone of Bohai Bay 651
G. Jiang, J. Tao & H. Wang

Application of 2-D vertical model in temperature forecast of Nuo Zha Du reservoir 657
X. Zhang, X. Zhou & L. Zhang

5 Water quality modelling

5.1 Water quality models

Calibrating steady-state river water quality models with field data 665
C.C.K. Liu

Design of a river water quality modeling software for Turkish rivers 671
A. Erturk, A. Ekdal, A. Tanik & A. Kucukballi

Simulation of water quality in networks of estuary 677
Z.Y. Mao, J.L. Wang & J.M. Ma

Establishing and applying water quality model of Suzhou Creek 683
Z. Xu & Z. Liao

Study on upstream water quality boundary and local pollution loads of Suzhou Creek based on mathematics model 689
Z.X. Xu, Z.L. Liao & J.P. Zhang

Linking watershed and receiving water models for water quality simulations of Tseng-Wen Reservoir, Taiwan 697
M.H. Hsieh, J.T. Kuo, H.C. Chen, W.C. Liu & W.S. Lung

Biodegradability evaluation and prediction of organic pollutants in natural river water 703
G.H. Lu & C. Wang

5.2 Non-point source pollution

Estimation of total nitrogen export in the East River (Dongjiang) Basin I. Export coefficient method 711
X.B. Ma, L. Fok, A. Koenig & Y. Xue

Estimation of total nitrogen export in the East River (Dongjiang) Basin II. Source apportionment and distribution using GIS approach 719
L. Fok, A. Koenig & P.J.-F. Yeh

Processes of nutrient load and transportation in a flooding river 727
H. Nagabayashi, Y. Ogawa, J. Yuda & A. Mano

5.3 Field studies

Field observation of salinity intrusion into Nagatsura-ura Lagoon 737
H. Tanaka, M. Takasaki, H.S. Lee & H. Yamaji

Measurements of ocean current in the vicinity of Yunlin Offshore Industrial Park 745
M.H. Hsu, J.L. Yu, T.-K. Liu, R.C. Kao & H.H. Hwung

An analysis of water circulation in the basin by stable isotopes 753
T. Kumekawa, M. Hasebe & H. Ii

Guangdong Dabaoshan Mine, China: impacts of acid mine drainage on downstream aquatic ecosystem 759
C. Lin & X. Tong

Impacts of land drainage on water quality in an Australian estuarine waterway: Chemical and biochemical processes 765
C. Lin & M. Wood

Fluctuation of nearshore water quality during a tidal cycle in Yunlin County 771
P. Chen, T.-K. Liu, J.L. Yu, R.C. Kao & H.H. Hwung

5.4 Impact assessment

Potential impact of northern flow diversion on Qiantang Estuary environment 781
A. You, Z. Han & Y. Shi

A prototype spatial expert system for evaluation and mitigation of groundwater contamination: The case of arsenic in Bangladesh 789
S. Shams, S. Langaas & P. Bhattacharya

Research on the water environment carrying capacity of river and reservoir – A case study of Wanjiazhai reservoir in Yellow River 795
K.Q. Chen, H. Qian, G.B. Li & P.Y. Xu

Analysis of effect of south-to-north water transfer project on aquatic ecosystems of Haihe River basin 801
Y. Pei, J. Wang & L. Luo

6 Ecohydraulics

6.1 Algal blooms/eutrophication

Predicting *Phaeocystis globosa* bloom in Dutch coastal waters 811
Q. Chen & A.E. Mynett

Methodologies to assess the effects of human interventions and pollution control measures in the Hong Kong coastal waters 819
F.J. Los, J.A.G. van Gils, A.N. Blauw, D.K. Vatvani, A.J. Nolte & L. Postma

Influence of sea currents to chlorophyll-*a* distribution of enclosed bay in Sanriku coastal area 825
H. Sato, K. Takahashi, M. Nomura & M. Sawamoto

A vertical stability theory and model for red tide forecasting 833
K.T.M. Wong & J.H.W. Lee

Phytoplankton-data assimilation in a coupled eco-hydrodynamic model of the Mediterranean Sea 839
E. Bournaski, G. Crispi & A. Crise

6.2 Ecohydraulics – I

Environmental aspects of the hydraulic design of the twin rivers diversion for Terminal 5, Heathrow Airport 847
P.B. Clark, D.K. Palmer, P. Joyce & R.V. Pether

Flow patterns in the wake of model mussel long-lines 853
D.R. Plew, R.I. Nokes & M.J. Davidson

Gradually varied flow through semi-rigid vegetation 859
B.Y.F. Tam & C.W. Li

Effects of vegetation and litter on flow 865
K.B.S.N. Jinadasa, N. Tanaka, K. Yutani & W. Seki

Recognition of wetlands hydraulics as a tool for their protection and restoration 873
T. Okruszko & S. Ignar

Hydrodynamic observations around a caged finfish aquaculture site 879
N.D. Hartstein, B. De Young & M.R. Anderson

Numerical analysis on the topographical change around artificial reefs 887
M. Minami & A. Mano

Bottom current characteristics near the openings of artificial reefs 893
K. Osanai, M. Minami & A. Mano

6.3 Ecohydraulics – II

Growth and interspecific competition of filamentous and non-filamentous periphyton on flat channel bed 901
Y. Toda, Y. Akamatsu & S. Ikeda

Oncomelania's environmental property and its control 907
D.M. Li & X.L. Fu

The distribution of *Chironomids* by flow mechanisms 913
S.H. Lee, K.S. Lee, T.W. Kim, J.P. Park & T.S. Chon

Japanese firefly habitat assessment based on hydrological simulation 919
S. Matsumoto, S. Kazama & M. Sawamoto

Study on the method of determining down stream minimal ecological flow in the river 927
L. Liu & H. Tan

Freshwater invertebrate community structure in a small urban river 933
M. Tamai, T. Fujisawa & N. Uenoyama

A study on physical feature of river channel which supporting the diversity of species of fishes 939
K. Kawamura & K. Sunada

Evaluation of weight of parameter for spawning of Ayu, *Plecoglossus altivelis*, and prediction of spawn density per unit area 947
T. Nagaya, K. Onitsuka, M. Higashino, T. Takami, N. Otsuka, J. Akiyama & K. Matsumoto

Estimation of the inhabiting possible ground of Raptorial birds in Saitama Prefecture 955
S. Tanaka, T. Hatta & G. Uehara

The proposed assessment criteria with habitat evaluation applied to ecotechnological works for upland river regulation in Taiwan 961
Y.C. Chen & C.H. Ho

Comprehensive assessment index system of ecological riparian zone 969
J. Xia, W. Wu & Z. Yan

7 Shallow water flow

Turbulence in shallow re-circulating flows 975
R.A. Delatolla, S. Babartutsi & V.H. Chu

Computations of 2D shallow mixing layers in open channel flows using a modified depth-averaged model 981
I. Kimura & T. Hosoda

Weakly nonlinear spatial stability analysis of shallow water flows 989
M.S. Ghidaoui & A.A. Kolyshkin

Shallow re-circulating flow in a cavity 995
W. Altai, C. Pinilla & V.H. Chu

8 Waves and coastal processes

8.1 Waves/coastal processes – I

Wave induced pressures and forces on parallel submarine pipelines at low KC numbers 1003
P.L. Vijayakumari, V. Sundar & K. Murali

Multi-layer modeling of nonlinear short waves 1009
S.C. Hsiao, Y.H. Chang & H.H. Hwung

Control of substance transport due to plural submerged asymmetrical roughness in wave fields 1017
H. Oshikawa, T. Komatsu & M. Hashida

Experiments on evolution of surface gravity waves from deep to shallow waters 1023
C.T. Hsu & Y.K. Law

Hydrodynamic characteristics of chambered breakwaters in regular waves 1029
R. Balaji & V. Sundar

Numerical wave modeling based on curvilinear element meshes 1035
V. Berkhahn & S. Mai

Water surface fluctuations inside the perforated circular caisson of a seawater intake well 1041
K. Vijayalakshmi, S. Neelamani, R. Sundaravadivelu & K. Murali

8.2 Waves/coastal processes – II

Energy partitioning in breaking internal waves on slopes 1051
S.K. Venayagamoorthy & O.B. Fringer

Effect of porosity of brushwood fences on wave transmission 1057
S.M. Sayah, J.-L. Boillat & A. Schleiss

Experimental study of damage caused by prolonged irregular wave impact on gently sloping sea dikes 1063
T. Takahashi, T. Abe, H. Konno & S. Arai

Studies on the evolution of bichromatic wave trains 1071
H.H. Hwung, W.S. Chiang, C.H. Lin & K.C. Hu

Transformation of ship waves on a sloping coast 1079
K.T. Dam, K. Tanimoto, N.B. Thuy & Y. Akagawa

8.3 Case studies/modelling

Improved air–sea interaction formulas for the modeling of environmental hydraulics 1089
S.A. Hsu

Shoreline change due to highly oblique waves in Lake Inawashiro 1095
Y. Fujita & H. Tanaka

Monitoring of long-term shoreline evolution on Sendai Coast 1101
H.W. Kang & H. Tanaka

Shoreline change in Yuriage Fishing Port due to breakwater extension 1109
S. Pornpinatepong, H. Tanaka, K. Watanabe & P. Srivihok

Modelling headland equilibrium bays with rotating DLA clusters 1115
A. Bhagatwala & K. Murali

Beach deformation and erosion measures in Misawa Coast, Japan 1121
M. Sasaki, T. Takeuchi, Y. Fujita & K. Ogasawara

Use of old maps for studying historical shoreline change in Japan 1129
H. Tanaka, H. Matsutomi & N. Izumi

Study on morphological variations and seawater exchange in a mangrove-fringed river mouth 1135
Y. Nihei & T. Nakamura

Estimation of water depth at a river mouth using water level variations – Application to Lake Jusan 1141
K. Watanabe, H. Tanaka & M. Sasaki

9 Impact of Reclamation

Impact of reclamation in Isahaya Bay on water environment in Ariake Sea, Japan 1149
S. Yano, T. Saita, H. Nishinokubi & T. Komatsu

Impact of large-scale reclamation on environmental hydrodynamics in Sansha Bay 1155
J.H. Zheng & Y.G. Wang

Impact of reclamation and HATS Stage I on Victoria Harbour, Hong Kong 1163
C.P. Kuang & J.H.W. Lee

Impact on the silt coast environment of tidal flat reclamation in Jiangsu – Take the coastal salt marsh as an example 1169
J. Chen

Subsurface injection of RO-treated waste water at a reclaimed land site 1175
L.H.C. Chua, K.C. Wong, N. Mzila, S.K. Tan, T.T. Lim, J.H. Tay, L.C.C. Koe & J.O. Leckie

The dispersion characteristics of sand under water 1183
T. Yamamoto, M. Takezawa & Y. Maeno

Author index 1191

Volume II

Keynote lectures

Water in a changing climate 1199
J. Imberger

Sustainable utilization of water resources and hydropower resources in China 1219
C.K. Zhang

Invited lectures

Ecosystem management for sustainability in the Changjiang (Yangtze) river catchment 1229
M. Watanabe

Connecting human and system health in the assessment, design and operation of water distribution systems 1239
B.W. Karney

Sewer sediments and processes 1247
J.-L. Bertrand-Krajewski

1 Water resource management

A new paradigm of river basin management – A case history study of Saigawa, Ishikawa Prefecture, Japan 1261
N. Tamai, M. Yamamoto & T. Fukumoto

Effects of alternative irrigation management models on the water delivery performance in Vietnam 1267
T.C. Trung, A.D. Gupta, R. Clemente & M.S. Babel

Control of Three Gorges Project and the sustainable development 1273
H. Dai & R. Wang

Mitigation of stream temperature change with reservoir management 1279
K. Yoshida, H. Tanji, H. Somura, K. Higuchi & O. Toda

Integrated watershed modeling using Finite Element Method and GIS approach 1285
A. Jha, T.I. Eldho, R. Jana & A.K. Singh

Sustainable development of the source area for the Eastern Route Project of South-to-North water diversion in China 1293
Y. Qian, Y. Zhang, X. Jiang, R. Wang, X. Zhu & G.F. Lu

Case studies on management measures of urban water environment 1299
Z.Y. Dong & P.L. Su

Water resources system simulation based on object-oriented technology 1305
H. Gan, J.J. You, L. Wang & S. Huang

Using WATERGEM for Taiwan water policy decision making 1311
Y.-F. Wang & J.-C. Hsu

2 Water distribution and management

Multiobjective design of water networks with random loads 1319
Y.R. Filion, B.W. Karney & B.J. Adams

Chance-constrained stochastic optimization applied to reservoir operation 1325
A.B. Celeste, K. Suzuki & A. Kadota

A study on the application of pressure management and continuous monitoring for controlling and reducing water mains leakage in a pilot area in the Hong Kong Special Administrative Region 1333
J.W.M. Lai, K.C. Luk, S. O'Brien, M. Tomkins, R. Spittle, S.K.S. Lai & P.W.H. Au

Available water model based on sustainable use of water resources in Beijing 1339
X. Zhang, Z. Liu, Z. Yang & X. Xu

Multiobjective optimization for water supply system management 1345
L.J. Cui

A multi-objective dynamic model for water resources management 1351
J.Z. Qian, J.Q. Wang, R.Z. Li & W.P. Wang

A new macroscopic model of multi-source water distribution network 1357
Z. Liao & G. Yu

3 Hydraulic transients

Investigation of transient leak detection using a 2D transient flow model 1365
W. Nixon & M.S. Ghidaoui

Simulation of transient flow in building drainage networks 1373
Z.Y. Mao, J.L. Wang & X. Zhao

Case study: Computed and measured transient pressures at Çatalan power plant 1379
B. Selek, M.S. Kirkgöz & Z. Selek

Study on propagation of pressure surge in steel pipe network 1387
Y. Kono, T. Moriya, Y. Sugai, M. Watanabe & M. Shimada

4 Urban stormwater management; urban drainage modelling

4.1 Urban stormwater management – I

Analytical probabilistic models for urban stormwater erosion potential 1397
J.A. Harris & B.J. Adams

Hydraulic model test of inundation water intrusion in underground space 1403
K. Toda, K. Inoue, T. Nakai & R. Oyagi

Hydraulic model test and calculation of flood in urban area with underground space 1411
T. Ishigaki, H. Nakagawa & Y. Baba

Coupled numerical model of flood inundation-groundwater flows 1417
K. Kawasaki, N. Piamsa-nga & K. Nakatsuji

Stormwater modelling for the South East Kowloon Development – A case study 1425
K.C. Luk, D.D. McLearie, R.J. Armstrong & B.R. Poole

4.2 Urban stormwater management – II

Implications for site drainage systems of reduced water use in buildings 1435
M. Escarameia & C.S. Lauchlan

The development of a comprehensive flood prevention strategy for Hong Kong 1441
S.K. Chui, J.K.Y. Leung & H.C.K. Chu

Rehabilitation priority of urban sewer systems considering storm water management
and inflow/infiltration 1449
J.H. Lee, D.J. Jo, J.H. Kim & M.J. Park

Inundation analysis of urban areas by using GIS – Application to the Tokai
Heavy Rain Flood 1457
H. Kiyomiya, A. Mano & T. Katada

Variability of combined sewer overflow emissions measured by means of online techniques 1463
M. Hochedlinger, G. Gruber & H. Kainz

Numerical analysis model of inundation due to river water and interior runoff 1471
M. Takeda, N. Matsuo & H. Kogiso

Field investigation of urban rainfall–runoff pollution 1479
Z.Y. Dong & M.E. Wang

Numerical analysis of inundation process in urban area with an underground space 1485
M. Sekine & N. Kawakami

Inundation flow analysis due to heavy rainfall applied to the Isahaya low-lying area 1493
K. Kawaike, H. Maruyama, M. Noguchi & S. Yoshimoto

4.3 Urban stormwater management – III

Energy losses at surcharged combining junction manholes 1503
C.H. Zhao, D.Z. Zhu & N. Rajaratnam

Prediction of storm tank performance using Computational Fluid Dynamics 1509
S. Lau, V. Stovin, I. Guymer & A. Saul

Outlet depth of sewerage pipe 1515
D.H. Yoo & J.T. Lee

Toilets and their impacts on water environment in Jiangsu Province, China – Sample survey in Xiaguan district of Nanjing city and Dapu town of Yixing city 1521
L.L. Liu, X. Qian, G.F. Lu, L.M. Gao, W.Y. Liu, G. Gu & H.H. Yin

5 Flood forecasting and prevention

A study of the effects of tidal variations on the return period of floods 1529
H.F. Cheong & G.T. Lim

Real-time simulation of flooding in the lower Illinois River with UNET model 1535
Y. Lian & M. Demissie

Impacts of Tongguan's elevation on the flood defense in the lower Weihe River 1541
C. Li, Z.Y. Wang & B. Wu

Application of appropriate modeling to assess flood risk 1549
Y. Huang, J.L. de Kok & A.E. Mynett

Effect of stem-breaking caused by flood on the transition of wetland vegetation in old river trace 1555
N. Tanaka, Y. Kitakami, T. Ogawa & T. Asaeda

Flood simulation coupled with remotely sensed data of land use and land cover 1563
L.L. Ren, R. An, H.M. Jiang, F. Yuan & M.R. Wang

Impact of land use change on watershed flood in Jingluowei River basin 1571
G. Huang, X. Rui & Shipeng

Simple method for flood inundation area predicting 1577
Y.R. Chung & K.T. Lee

Hydraulic modelling study for evaluation of the bridge induced hydro-morphological changes of the Dhaleswari River: A case study for a Bangladeshi River 1583
M. Mahboob-ul-Kabir, S. Jahan, J.Md. Abdul Hye & A. Abdullah Noor

6 Open channel flow

6.1 Open channel flow – I

3-D velocity measurements in transition region from straight to meandering open-channel flow with floodplains 1593
I. Nezu, M. Sanjou, H. Wakamoto & T. Doi

LES numerical calculation of a groin in open-channel flow 1601
M. Yano & I. Nezu

Investigation of generation mechanism of secondary flows in the open-channel flow using DNS data 1609
S.-U. Choi & Y. Joung

Hydrodynamic and concentration properties in permeable side-cavity open-channel flow by digital visualization technique 1617
I. Nezu, M. Yano & Y. Mitsunari

Discrete vortex simulation of horizontal vortices and effect on environment in compound straight open-channel flow 1625
M. Sanjou, I. Nezu & A. Kamiya

6.2 Open channel flow – II

An investigation on the flow resistance of a mountain river 1635
M. Habibi & Y. Guo

The effects of bottom settlement, vegetation and macro-roughness on the erosion stability of the relocated river Inde 1643
P. Kamrath, S. Rubbert & J. Köngeter

Numerical simulation of unsteadiness effect in depth-varying and time-dependent open-channel flow 1651
M. Sanjou & I. Nezu

Velocity distribution and discharge intensity of lateral overflow on mobile bed 1659
B. Rosier, J.-L. Boillat & A. Schleiss

Flow resistance in vegetated channels: Characteristics of natural woody vegetation 1667
J. Järvelä

A study on grain size distribution of bed material using fractal theory and analysis 1673
X. Wang, S. Cao, T. Liu & W. Lu

6.3 Open channel flow – III

Discharge formula of side-weir with zero height in subcritical open-channel flows 1681
K. Onitsuka, J. Akiyama, T. Tsunematsu & M. Takeda

Computation of free overfall 1689
Y. Guo & Y. Shen

Numerical study of submerged hydraulic jump 1697
H. Dai & L. Wang

Length of hydraulic jump on horizontal bed with abrupt rise 1703
K. Onitsuka, J. Akiyama, H. Isechi & D. Kiuchi

Manning's roughness coefficient for different types of open channel flows 1711
J.-J. He

7 Hydraulic structures

7.1 Hydraulic structures – I

High velocity two-phase flows over stepped chutes: Focus on air concentration 1719
S. André, J.-L. Boillat & A.J. Schleiss

Computational fluid dynamics analysis of three major dam spillway structures in Australia 1727
D.K.H. Ho, K.M. Riddette & S.M. Donohoo

Hydraulic experiment of arc-shaped gate on the Qinhuai River 1733
D.Y. Liu, Q.F. Zhang & H.M. Xu

Computational analysis of flow in bottom outlet conduits 1741
M.R. Kavianpour & A. Aghakouchak

Three-dimensional turbulence numerical simulation on the configuration optimization of aeration device of the free flow spillway tunnel 1747
H.-Y. Wang, G.-Q. Dai, Q. Yang & C. Liu

Design and construction of 1/100 scaled model of Cine Dam stepped spillway 1755
M.S. Guney, A. Ozgenc, C. Ozcelik & G. Bombar

Optimizing the hydraulic performance of a stilling basin for cooling-water discharge: An experimental study 1761
H. Yun & J. Ping

Determination of jet length in jet spillways 1769
E. Üzücek & G. Yildiz

Stabilization of the bottom plate of still basin under the action of jet flow from a flaring gate pier 1775
G. Yan, Q. Hu & F. Chen

Characteristics of wake flow in long bluff bodies 1781
W. Chen, J. Zhao, J. Guo & C. Li

Influence of gas nucleus on scale effect of cavitation 1787
Q. Yang, G.-Q. Dai, J.-M. Zhang, H.-Y. Wang & J.-Q. Wu

7.2 Hydraulic structures – II

Large eddy simulation of free surface over broad-crested weir 1795
X.J. Cheng, L. Luo & W.Q. Zhao

Study on flow structure and discharge over a permeable rubble mound weir 1801
K. Michioku & S. Maeno

Numerical simulation of the flow around a rubble mound weir 1809
S. Maeno & K. Michioku

8 Scour in hydraulic structures

3D numerical analysis of local flow and scouring around cylindrical piles 1819
H. Jin

The use of riprap protection as a countermeasure against scour downstream of two compound piers 1827
A. Kadota, R. Aragão, K. Suzuki & V.S. Srinivasan

Effect of seepage on scour caused by circular wall jets 1835
S.B. Dugad & B.S. Pani

Influence of the spur dike permeability on local velocities and scouring 1843
T. Mioduszewski, S. Maeno & Y. Uema

Numerical simulation of local scouring process by solid–liquid two-phase flow model 1851
E. Harada, T. Hoaoda, H. Gotoh & K. Obayashi

Study on local scour around circular pier with riblet 1859
K. Asai, N. Kawamoto & Y. Mimura

Research on downstream scouring of flip bucket with tongue-type 1867
F. Zhang, Y. Zhu & W. Xu

9 Treatment plant hydraulics

Helicoidal flow jet flocculator 1875
L.G. Patil & B.S. Pani

Interaction of sludge bed height and scraper operation in horizontal flow final settling tanks 1883
R. Hollenstein, P. Volkart & H.-E. Minor

Hydraulic evaluation of an active landfill 1889
E. Durmusoglu, A. Karademir, M. Bakoglu & S. Ayberk

On intermittence of air entrainment in a suction sump and three-dimensional PTV analysis 1895
K. Hirata, K. Saito & J. Funaki

10 Hydrological modelling

Sensitivity and uncertainty analyses of coupled surface – subsurface flow model on steep slopes 1903
Z. Lu, Y.-K. Tung, C.W.W. Ng & W.H. Tang

An evaluation of statistical downscaling methods for simulating daily precipitation and extreme temperature series at a local site 1911
V.-T.-V. Nguyen, T.-D. Nguyen & P. Gachon

Stochastic generation of GIUH-based flow hydrograph 1917
Y. Wang & Y.-K. Tung

Reliability of the Gama I Synthetic Unit Hydrograph after 15 years of its development as applied in South Sulawesi 1925
M. Farouk & Br. Sri Harto

Statistical characteristics of annual maximum 24-hour rainfall and 48-hour rainfall 1931
N. Suzuki & A. Mano

Study of hydrological simulation on the basis of digitized basin 1937
X. Zhang, L. Jing, D. Xia & H. Kuang

Hydrological simulation of the East River basin (Dongjiang) in China 1945
P.J.-F. Yeh, L. Fok & J.H.W. Lee

Methodology of a grid-based hydrological model and its application 1951
F. Yuan & L.L. Ren

Folding concept in rainfall excess transformation into runoff in natural watersheds 1959
M.R. Najafi

Rainfall–runoff modeling of a sandy soil catchment 1967
Y. Guan & D. Zhang

Some observations on the estimation of solute load in a small headwater catchment in Hong Kong 1975
M.R. Peart & L. Fok

Irrigated water estimation model to paddy fields using pump sets in Cambodia 1981
H. Somura, H. Tanji, K. Yoshida, K. Higuchi & O. Toda

11 Data driven methods in hydrology

Input correction in rainfall runoff models using the Ensemble Kalman filter 1991
T. Koster, G.E. Serafy, H.F.P. van den Boogaard, A.W. Heemink & A.E. Mynett

Hydrological time series forecasting SVM operated in feature space 1997
X. Yu & S.-Y. Liong

Evaluation of river velocity and discharge with a new assimilated method 2005
Y. Nihei, A. Kimizu, Y. Yamasaki & K. Sato

Application of artificial neural network for reference crop evapotranspiration estimation 2011
V. Jothiprakash & M.G. Devamane

Tidal level and current prediction using Adaptive Neural Fuzzy Inference System (ANFIS) 2017
A. Oveisy, M. Teshnehlab & M. Nassiri

12 Groundwater

Salinity intrusion – Its characteristics and impact – Cases in the Asia Pacific region 2027
G.S. De Costa, T. Kojiri & M. Porter

Study on the interaction between surface water and groundwater in Qin River basin using a distributed hydrologic model 2033
L. Wang, G. Ni & H. Hu

Subsurface water between adjacent rivers – Subsurface water from Nagara River to Kiso River 2039
K. Onitsuka, M. Yano, J. Akiyama & I. Nezu

Preliminary numerical study on groundwater system at the Hong Kong International Airport 2047
F. Wang & J.J. Jiao

Using adaptive finite element model to study groundwater flow and contaminant transport in the Yucca Mountain Repository 2053
Y. Chen, D.W. Pepper & L. Li

Flow movement and contaminant transport of groundwater in southern Bangladesh 2059
T. Umeki, A. Mano, Y. Ishibashi & Wahiduzzaman

Application of Modflow to the simulation of land subsidence due to the exploitation of groundwater 2067
M. Sun, Z. Lou & C. Pan

Application of groundwater flow measuring techniques: The use of colloidal borescope system (CBS) 2075
Y.-S. Wu, J.L. Yu, C.-C. Tseng, T.-K. Liu & H.-H. Hwung

13 Sediment transport

13.1 Sediment in rivers

CRS-1 river model verification and its field studies 2085
S. Cao, X. Liu & H. Er

Field studies of Late Cenozoic Minjiang River incision rate and its constraint on morphology of the eastern margin of the Tibetan plateau 2091
Y. Li, S. Cao, R. Zhou, A.L. Densmore & M.A. Ellis

Measuring system of suspended sediment concentration at a river entrance 2099
H. Tanaka, R. Sugawara, H. Yamaji & Suntoyo

Modeling river bed evolution in natural alluvial streams 2107
L. Schippa & S. Pavan

13.2 Sediments in reservoirs and estuaries

Deposition of sand–gravel mixture in a steep slope reservoir with hydraulic jump 2115
K. Suzuki, A. Kadota, B.B. Parajuli

Distribution of suspended sediment in a mesotidal estuary, Taiwan 2123
W.C. Liu, M.-H. Hsu, C.-R. Wu, A.Y. Kuo & S.-T. Chang

Field measurements and numerical simulation on sediment transport in an urban river estuary 2129
Y. Nihei, M. Oozeki, Y. Yamasaki & T. Nishimura

A field study on near-bottom turbulence and resuspension of fine sediment in the Tone River Estuary 2137
K. Shimizu, T. Ishikawa & M. Irie

Numerical simulation on entrainment of fluid mud in Lake Kasumigaura 2145
X. Qian, T. Ishikawa, M. Umeda & F. Gao

Numerical estimation of countermeasures against sedimentation in Masaki Dam Reservoir, Japan 2153
T. Okabe & H. Takebayashi

Large Eddy Simulation Sediment Transport Model for Deep Bay, Hong Kong 2161
P.C.B. Kwok & O.W.H. Wai

13.3 Sediment dynamics

Turbulence modulation and particle–fluid interaction in sediment-laden open-channel flows 2171
I. Nezu & R. Azuma

Effects of flow characteristic and boundary shear stress on sediment transport processes in two-stage meandering channel 2179
T.L. Chan & K. Shiono

Nonlinear theory study on incipient motion of sediment 2189
W. He, S. Cao, X. Feng & J. Yuan

Hydrodynamic and sediment transport properties in a Lid-driven Elongated Annular Flume (LEAF) 2195
W.Y. Chan & O.W.H. Wai

Modified vertically-integrated 2D suspended sediment transport equation by considering secondary flows in channel bends 2201
S.L. Huang, Y. Jia & S.S.Y. Wang

A PDA study of sediment transport in a sediment-laden flow for the estimation of pollutant fluxes at water/sediment interface 2207
Yuqi An & Daoyi Chen

Velocity profiles and von Karman constant in open-channel flows with suspended sediment 2213
R. Azuma & I. Nezu

Experimental investigation of velocity and density profile in highly concentrated sand–water mixture flows 2221
B. Pirouz, M.R. Kavianpour & P. Williams

Flow of water with hyper concentrated sediment and its numerical solution 2229
D. Legono

13.4 Other sediment problems

Numerical analysis of surface erosion and sediment yield from bare hillside 2237
M. Sekine & S. Hishinuma

Study on the measures to prevent severe sedimentation in the large inverted siphons for a sewage system 2243
C. Liu, Y. He, Z.Y. Wang & H. Wei

Some experiments of sand-draining funnel 2251
X.-Q. Zhou, S.Y. Cao & X. Liu

14 Sediment–water interaction

Mobility of estuarine sediments and its effect on nutrient distribution 2261
M.S. Chen, S. Wartel, L. Goeyens, L. Lavkulich & W. Baeyens

The mud suspension due to strong tidal motion and the oxygen consumption 2269
T. Tokunaga, N. Matsunaga, M. Kodama & H. Yasuda

Sorption equilibrium of phthalate esters on sediment particulates low in organic carbon using solid phase extraction disks 2277
N. Xu, J.R. Ni & W.L. Sun

Study on heavy metals and nutrient salts of bottom sediments in mountain lakes 2283
Y. Ogawa & H. Nagabayashi

A mathematical model of phosphorus release from the bed sediment of lake 2293
Y. Wang, Y. Xie & S. Guo

Relationships between ionic concentration and water and sediment in the lower Weihe River 2301
D. Cheng, Z.Y. Wang, J. Xu & C. Liu

Some characteristics of copper sorption by sediments in the middle Yellow River 2307
R. Zhao & J.R. Ni

Author index 2315

Editors' foreword

The 4th International Symposium on Environmental Hydraulics (ISEH) – 14th Congress of the Asia and Pacific Division of the International Association of Hydraulic Engineering and Research (IAHR-APD) was organised by the Department of Civil Engineering, The University of Hong Kong. The Symposium and Congress were jointly held in parallel at the Sheraton Hotel, Hong Kong during December 15–18, 2004.

The objective of the joint conference (ISEH&IAHR-APD2004) is to bring together scientists, engineers and researchers with a common interest in water environment and hydraulic problems. The conference aims to provide a forum for the exchange of ideas and experiences on recent developments in environmental hydraulics and water management issues. The main theme of the conference is "Sustainable Water Management in the Asia-Pacific Region".

The International Association of Hydraulic Engineering and Research (IAHR) was founded in 1935 as a world-wide independent organisation to promote basic and applied research in hydraulics. The Asia and Pacific Regional Division (APD) of the IAHR was formed in 1973 to promote the development of hydraulics and the competence of hydraulic professionals in solving the water problems in the region. As a major activity of APD, the biennial Congresses have a long history and provide a forum for discussion among APD members on current hydraulic research and engineering issues. It is our honour to host the 14th Congress, the first after the IAHR-APD Secretariat moved to Beijing in 2003.

Environmental hydraulic problems feature prominently in many of the infrastructure developments in Hong Kong in the past two decades. The University of Hong Kong hosted the 1st and 2nd International Symposium on Environmental Hydraulics, in 1991 and 1998 respectively. We are very pleased to host the 4th Symposium again after the success of the 3rd International Symposium held in Tempe, Arizona, USA in 2001.

The initial call for papers received an enthusiastic response with submission of over 400 abstracts. After review and selection, about 300 full papers are accepted for oral presentation and inclusion in the conference proceedings. Due to time constraints, we have not been able to include some worthwhile contributions and late papers that are presented orally at the conference.

This Proceedings was prepared in two volumes with the theme of Volume I as "Environmental Hydraulics" and Volume II as "Sustainable Water Management in the Asia-Pacific Region". The papers have been grouped into relevant topics under these two themes but of course many papers inevitably touch on and cut across both themes.

Volume I of the Proceedings contains 2 keynote lectures, 7 invited lectures and 153 contributing papers. The papers cover a broad spectrum of topics, ranging from basic science of environmental hydraulics including mixing and transport, stratified flow, jets and plumes, waves and coastal processes, to hydrodynamic and water quality models as tools of water management and impact assessment, and to field studies. In particular, there is a notable collection of papers on eco-hydraulics discussing the interaction of environmental hydraulics with ecology – e.g. vegetation and algal dynamics.

Volume II of the Proceedings covers topics in sustainable water resources management: water distribution, urban storm water drainage, flooding problems, groundwater, and hydrological modelling, as well as topics in open channel flow and hydraulic structures. The volume also contains a collection of papers on sediment transport and sediment-water interaction. There are 2 keynote lectures, 3 invited lectures and 143 contributing papers in the Volume.

We would like to express our sincere gratitude to the keynote and invited speakers and authors of all papers. Without their contribution, we could not have produced this valuable and latest state-of-the-art Proceedings. Thanks are due to the members of the Advisory Committee, the International Scientific Committee, and the IAHR-APD Executive Committee for their advice and support. The assistance of the Local Organising Committee, in particular the fund-raising and technical review sub-committees, are gratefully acknowledged. We thank the financial sponsors for their generous support, and A.A. Balkema for the professional production of the Proceedings.

J.H.W. Lee
K.M. Lam
December 2004

Environmental Hydraulics and Sustainable Water Management – Lee & Lam (eds)
© 2005 Taylor & Francis Group, London, ISBN 04 1536 546 5

Chairman's message

It is our great pleasure to host the 4th International Symposium on Environmental Hydraulics (ISEH) and the 14th Congress of the Asia and Pacific Division of the International Association of Hydraulic Engineering and Research (IAHR-APD) in Hong Kong. On behalf of the Local Organising Committee, I would like to express my gratitude to all participants of the Symposium and Congress for their kind participation, for the excellent papers they present, and for their contribution to idea exchange and discussion. The participants come from over 35 countries and regions.

In the macro-scale, the Asia-Pacific rim faces many water environment challenges in the new millennium. Examples include the assurance of an adequate and clean water supply, the prevention of urban and basin flooding, the search of a sensible sewage strategy, the achievement of sustainable water quality to enhance quality of life, the protection of aquatic and coastal fisheries. Water problems will be associated with increasing complexity and wider scope brought about by issues like global climate change, massive urbanisation, economic risks in infrastructure investments, cross-border pollution and government policies.

Since the 1st ISEH held in Hong Kong in 1991, environmental hydraulic problems have become issues of mounting importance in every country and region. Every government is targeted at sustainable water resources management. Water environment is crucial to the sustainability of Hong Kong and the Pearl River Delta region. We are indeed fortunate to have the opportunity to organise the 14th Congress of IAHR-APD jointly with the 4th ISEH in Hong Kong. The Symposium and Congress is a timely event following the Johannesburg Summit on Water Issues in 2002.

This Proceedings reflects the diversity and depth of the papers in covering the frontier research and practices in environmental hydraulics, hydraulic engineering and water resources management. I am sure that the Proceedings will remain a valuable reference to engineers, academics and researchers in the fields of hydraulics and water environment.

J.H.W. Lee
Redmond Chair of Civil Engineering
Chairman, Local Organising Committee

This page intentionally left blank

Environmental Hydraulics and Sustainable Water Management – Lee & Lam (eds)
© 2005 Taylor & Francis Group, London, ISBN 04 1536 546 5

Organisation

Organised by
Department of Civil Engineering
The University of Hong Kong

Sponsored by
American Society of Civil Engineers
Chinese Hydraulic Engineering Society
Japan Society of Civil Engineers
International Association of Hydraulic Engineering and Research
International Association of Hydrological Sciences
The Hong Kong Institution of Engineers
The Hong Kong Polytechnic University
The Hong Kong University of Science and Technology

Financially supported by
K.C. Wong Education Foundation
CLP Power Hong Kong Ltd.
William M.W. Mong Engineering Research Fund
Environmental Hydraulics Visiting Fellowship, The University of Hong Kong
Chun Wo Construction and Engineering Company Ltd.
WL|Delft Hydraulics, The Netherlands
SonTek/YSI Inc.
Marktec Technology Ltd.
Consulate General of Sweden
Consulate General of France
Macao Water Supply Company Ltd.
Leader Civil Engineering Corporation Ltd.
MWH Hong Kong Ltd.
Wo Hing Construction Company Ltd.
State Key Laboratory of Hydraulics, Sichuan University
Black & Veatch Hong Kong Ltd.

COMMITTEES

International Scientific Committee
J.P. Chabard, Electricite de France, France
H.F. Cheong, National University of Singapore, Singapore
V.H. Chu, McGill University, Canada
P.A. Davies, University of Dundee, UK
R.A. Falconer, Cardiff University, UK
C. Fenn, H.R. Wallingford Ltd., UK
H.J.S. Fernando, Arizona State University, USA
Z.R. Guo, South China Institute of Environmental Sciences, NEPA, China
W.X. Hui, Wuhan University, China

H.H. Hwung, National Cheng Kung University, Tainan, China
S. Ikeda, Tokyo Institute of Technology, Japan
J. Imberger, University of Western Australia, Australia
G.H. Jirka, University of Karlsruhe, Germany
P. Julien, Colorado State University, USA
B.W. Karney, University of Toronto, Canada
T. Komatsu, Kyushu University, Japan
A.W.K. Law, Nanyang Technological University, Singapore
G.F. Li, IWHR, Beijing, China
Z.H. Li, Guangdong Institute of Hydraulic Research, China
W.S. Lung, University of Virginia, USA
I. Nezu, Kyoto University, Japan
J.R. Ni, Peking University, China
P.E. O'Connell, University of Newcastle, UK
A.J. Odgaard, The University of Iowa, USA
B.S. Pani, Indian Institute of Technology, India
N. Rajaratnam, University of Alberta, Canada
W. Rodi, University of Karlsruhe, Germany
I.W. Seo, Seoul National University, Korea
G.S. Stelling, WL|Delft Hydraulics, The Netherlands
R.L. Street, Stanford Universty, USA
N. Tamai, Kanazawa University, Japan
J.H. Tao, Tianjin University, China
T. Tingsanchali, Asian Institute of Technology, Thailand
G.Q. Wang, Tsinghua University, China
H. Wang, IWHR, Beijing, China
S.S.Y. Wang, The University of Mississippi, USA
Z.Y. Wang, IRTCES, Beijing, China
S.J. Wright, University of Michigan, USA
F.D.L. Young, National Taiwan University, Taipei, China
W.Q. Zhao, Sichuan University, China
X.N. Zhang, Hohai University, China

Advisory Committee
Shucheng Wang (Honorary Chairman), Ministry of Water Resources, China
Y.K. Cheung (Chairman), The University of Hong Kong, Hong Kong, China
V.M. Bendre, Central Water & Power Research Station, India
D. Boyer, Arizona State University, USA
B.N. Lin, IWHR, Beijing, China
K. Yen, Hohai University, China
E.M. Zhu, China Hydraulic Engineering Society, China

Local Organising Committee
J.H.W. Lee (Chairman), The University of Hong Kong
A.W. Jayawardena (Vice-Chairman), The University of Hong Kong
C.W. Li (Vice-Chairman), The Hong Kong Polytechnic University
Y.K. Tung (Vice-Chairman), The Hong Kong University of Science and Technology
K.M. Lam (Secretary), The University of Hong Kong
E.W.K. Au, Environmental Protection Department, Hong Kong Government
E.W.S. Chiang, Drainage Services Department, Hong Kong Government
Y.L. Choi, The University of Hong Kong
A.K.C. Chow, Scott Wilson Ltd.
M.S. Ghidaoui, The Hong Kong University of Science and Technology

C.T. Hsu, The Hong Kong University of Science and Technology
J.J. Jiao, The University of Hong Kong
A. Koenig, The University of Hong Kong
G.Y. Li, Hyder Consulting Ltd.
X.Y. Li, The University of Hong Kong
V.K.Y. Lo, Water Supplies Department, Hong Kong Government
K.C. Luk, Montgomery Watson Harza
M.R. Peart, The University of Hong Kong
P. Purnell-Edwards, Consulting Environmental Engineer
O.W.H. Wai, The Hong Kong Polytechnic University
C.F. Wong, Environmental Protection Department, Hong Kong Government

This page intentionally left blank

Keynote lectures

This page intentionally left blank

Environmental Hydraulics and Sustainable Water Management – Lee & Lam (eds)
© 2005 Taylor & Francis Group, London, ISBN 04 1536 546 5

Artificial intelligence techniques in environmental hydrodynamics: The role of expert knowledge

A.E. Mynett
WL | Delft Hydraulics
UNESCO-IHE, Delft, The Netherlands

Q.N. Chen
UNESCO-IHE, Delft, The Netherlands

V.M. Babovic
WL | Delft Hydraulics, The Netherlands

ABSTRACT: Predicting algal blooms is an ambitious and difficult topic due to the complexity of aquatic ecosystem behaviour, insufficient knowledge of underlying processes, and shortage of high quality data. The same holds for the proper modelling of overland flows in wetlands and vegetated floodplains, which is of great practical importance in both flood early warning and in river restoration. Even though in both applications the purely hydrodynamic behaviour is conveniently formulated in terms of classical mathematical equations, some important physical, chemical or biological processes are often 'hidden' in the coefficients contained in these equations. It is demonstrated in this paper that Artificial Intelligence techniques can prove extremely valuable for establishing these coefficients or for providing complementary formulations of processes that can not (yet) be incorporated in these equations. Results are presented for the two cases of algal bloom prediction and vegetation flow resistance. It is shown that knowledge can be inferred from data directly, but that the techniques are applied most effectively when involving expert knowledge.

1 INTRODUCTION

Predicting algal blooms is an ambitious and difficult topic due to the complexity of the aquatic ecosystem behaviour. Quite often insufficient knowledge is available on the detailed processes and mechanisms involved, in particular when complicated interactions are involved. Also, high quality data are usually lacking. On the other hand, Artificial Intelligence (AI) techniques like Fuzzy Logic (FL) Rule Based Systems and Genetic Programming have the ability to deal with imprecise, uncertain or ambiguous data and can be used to explore relationships among data. Hence such techniques may prove useful for solving practical problems in environmental hydrodynamics, when dealing with water bodies in their natural environment, where physical, chemical and biological processes are often of relevance (Mynett, 2002).

In order to explore the occurrence of harmful algal blooms in coastal waters, a robust fuzzy logic approach has been developed that derives (inter)relationships directly from measurements, using expert knowledge as a reference. This allows the capability to combine partial knowledge on processes with partially available data from observations. In collaboration with the European Commission project Harmful Algal Bloom Expert System (EU-HABES), this approach was applied to the North Sea for modelling chlorophyll *a* (Chl-a) concentrations as an indicator for likely bloom events (Mynett, 2003).

A Fuzzy Logic approach is known to be a practical and successful technique when dealing with semi-qualitative knowledge and semi-qualitative data which is usually the case when trying to model algal biomass or algal blooms. However, the definition of appropriate membership functions and the induction of inference rules, common to any fuzzy logic modelling approach, remain difficult to achieve, since these very much depend on specific knowledge and expertise of specialist ecologists. Hence, the relatively new approach of inferring learning rules directly from measurement data is recently receiving considerable attention. In the next section, a methodology is presented that deduces membership functions and inference rules from measurement data directly, rather than from combined expert knowledge. This methodology is then verified by comparing results of modelling algal biomass (Chl-a) concentrations with observations obtained from station NW2 along the Dutch North Sea coast. Using total biomass as bloom indicator (model variable), the bloom dynamics are seen to be captured quite well.

Yet another example of applying AI-techniques to relevant environmental problems was chosen to be flow resistance in vegetated floodplains. Many research initiatives have been undertaken in order to improve on the description of the relationship between flow resistance and the presence and spatial distribution of vegetation. However, the approach presented here is based on Genetic Programming (GP). Just as natural evolution on earth is said to have started from a small initial population some 2 billion years ago, computer-based ('in silico') algorithms and artificial intelligence techniques also begin by creating an initial set of contending solutions for a particular problem. The set may be generated by *randomly* creating a population of initial solutions or by utilizing possibly available expert knowledge about the problem.

The 'parent' solutions then generate 'children' by means of sexual reproduction (crossover) or asexual alteration (mutation). Both of these operations are conceptually very simple. In mutation one replaces a *randomly* chosen piece of a formula with another *randomly* generated piece of formula. In crossover one swaps a *randomly* chosen piece from one formula with a *randomly* chosen piece from another formula. The resulting solutions (children) are evaluated for their effectiveness (their fitness) and undergo selection. Just as nature imposes the rule of 'survival of the fittest' those solutions that are least fit are removed from further consideration, and the process is repeated over successive generations. In the most general terms, evolution can be described as a two-step iterative process: *random* variation followed by selection. Genetic algorithms, evolution strategies, evolutionary programming as well as differential evolution represent a few examples of evolutionary algorithms.

In the hydrosciences, it is quite common and well established to account for dimensional correctness of expressions and problem solutions, viz. the results should be independent of measurement units. For this reason a dimensionally aware GP methodology was developed by Babovic & Keijzer (1999). An extra objective for selection, the *goodness-of-dimension*, is introduced that is used next to a *goodness-of-fit* objective. These two objectives are then used in a multi-objective optimization routine using the concepts of dominance and Pareto optimality. Goodness-of-dimension is measured by calculating how many constants with appropriate units should be introduced to render an equation dimensionally correct. In computer science terms: an incorrectly typed manipulation is resolved by casting one or all of the terms involved to appropriate types (Keijzer & Babovic, 1999).

The result of a single run of such unit typed genetic programming is a set of equations – a so-called Pareto front of non-dominated solutions – that balance dimensional correctness (goodness-of-dimension) with goodness-of-fit. The role of the user then is to choose the most suitable formulation for further analysis, exploiting his background knowledge or implementing some belief about the problem domain. The final step lies in examining the selected equation(s). When a reasonable explanation for the apparent goodness-of-fit of such an equation is produced, the user's belief in the correctness of the equation is enhanced. The equation then no longer functions as a black box for making accurate predictions but as a genuine empirical equation that can be used with more confidence than mere statistical security. Moreover, the resulting equation and corresponding interpretation is amenable to review by experts and peers. An example is presented below on inducing empirical equations for flow resistance.

2 FUZZY LOGIC MODELLING OF ALGAL BLOOMS

2.1 *Dominant processes and data availability*

Predicting algal blooms is an ambitious and difficult topic due to the complexity of the aquatic ecosystem behaviour, the insufficient knowledge available on the detailed processes and mechanisms involved, and the shortage of high quality data. However, Fuzzy Logic (FL) techniques have the ability to deal with imprecise, uncertain or ambiguous data or relationships among data, and hence can be a useful and practical method in algal bloom modelling.

In order to explore this, a robust fuzzy logic approach has been developed that derives (inter)relationships directly from measurements, using expert knowledge as a reference. This allows the capability to combine partial knowledge on processes with partially available data from observations. In collaboration with the European Commission project Harmful Algal Bloom Expert System (EU-HABES), this approach was applied to the North Sea for modelling chlorophyll *a* (Chl-a) concentrations.

The North Sea is a semi-enclosed shelf sea with a densely populated and very industrialised hinterland. It had been one of the most productive fishing areas in the world. In the last 20–50 years, the increase of nutrients discharged by the rivers has led to eutrophication of the coastal zones. Spring phytoplankton blooms dominated by *diatoms* and *Phaeocystis* occur regularly in the Dutch coastal waters.

These blooms (defined by chlorophyll $a \geq 30\ \mu g/l$) are usually non-toxic, but can still be annoying or even harmful since they are able to produce a thick foam (Fig. 1) under certain onland wind conditions, which gives rise to unpleasant looks and an evil smell. It is also speculated that the consequent mineralisation of settled *P. globosa* leads to anoxia and massive bivalve mortality.

2.2 *Fuzzy Logic model development*

A number of studies have been carried out to investigate the Dutch coastal ecosystems and to forecast possible *P. globosa* blooms through monitoring and modelling programs in order to minimize economic loss. Both expert knowledge on the underlying processes as well as data from in-situ measurements are available to construct a Fuzzy Logic model, involving a number of steps as decribed hereafter.

Figure 1. Dutch coast of the North Sea and monitoring stations (Left), foam after algal blooms (right).

Representing heuristic knowledge
A way to construct a reference for interpreting results from data analysis, is to set up a general rule base containing commonly accepted knowledge from expert ecologists; these rules need not be specified in great detail, but should provide an adequate benchmark for assessing the results (Chen, 2004).

Clustering input and output data
In order to characterise the measurement dataset, a self-organising feature map (SOFM) technique was applied to analyse the data for characteristic clusters or subsets, determining the mean values as well as 97.5% confidence interval bands of each cluster of model variables. If there is no statistically significant overlap between the clusters, the classification result is considered acceptable. The procedure of SOFM can be summarised as follows:

1. initialisation by choosing random values for the initial weight vectors $w_j(0)$, imposing that $w_j(0)$ are different for $j = 1, 2, \ldots, N$, where N is the number of neurones in the lattice;
2. sampling by drawing a sample X from the measurement dataset, using the probability distribution that is evolving through the process (initially random);
3. similarity matchinging by finding the best-matching (winning) neurone i at time t, using the minimum distance Euclidean criterium: $i(x) = \arg_j \min ||x(n) - w_j||,\ j = 1, 2 \ldots N$;
4. updating by adjusting the synoptic weight vectors of all neurones, using the update formula $\vec{w}_j(t+1) = \vec{w}_j(t) + \eta(t) \cdot \lambda(t, r) \cdot (\vec{\xi}_n - \vec{w}_j(t))$, where $\eta(t), \lambda(t, r)$ are the learning rate and neighbourhood function resp. and r the radius of neighbourhood;
5. continuation (step 2) until observed changes in the feature map are no longer relevant.

Defining membership functions
Now membership functions for each variable are defined by selecting proper function types and assigning the mean value of each cluster membership degree $\mu = 1.0$ (Fig. 2).

Inducing fuzzy rules
There are two common strategies for inference rules induction, viz. feature reasoning and case based reasoning. For feature reasoning, the clusters obtained from SOFM analysis are used; each feature (cluster) then provides at most one rule, which are added to the general (heuristic) rule base introduced above. An extend case based reasoning method involves 5 steps:

1. generating rules from each case by fuzzification expressed in linguistic terms;
2. checking whether this rule already exist in the general rule base;
3. checking if the newly generated rules conflict (same premise but different reasoning);
4. selecting relevant rules according to the Bernoulli test;
5. checking for any conflict among the remaining newly generated rules.

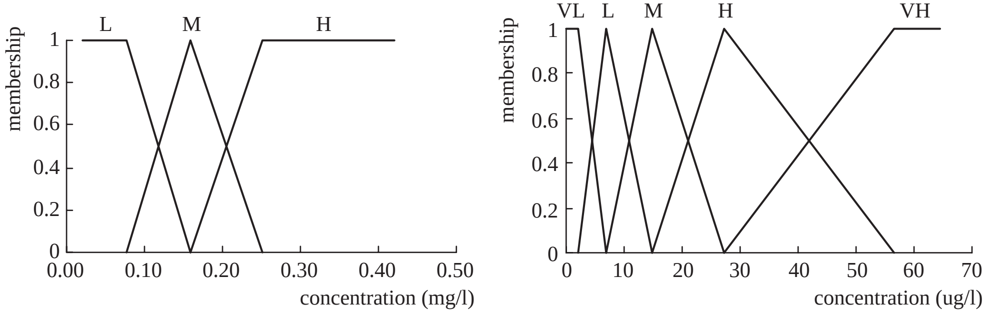

Figure 2. Membership functions of TIN (left) and Chl-a (right).

2.3 *Case study results for the Dutch coast*

Preliminary estimates of nutrient and light requirements for colonial blooms of *Phaeocystis* indicate values for inorganic phosphorus >0.2 μM (i.e. 0.0062 mg/l) and irradiance >100 Wh/m^{2}day^{-1}. A high nitrate-ammonia ratio is believed to promote the colonial life form as well. Relatively high growth rates (>0.5 day^{-1}) seem to occur at salinity levels of (20–35 psu) within a temperature range from (7–22°C) and a daily irradiance value of >100 Wh/m^{2}day^{-1}.

Biweekly data were collected at 17 stations (Fig. 1) during the period May 1975 to March 1983. The observations include temperature, pH, salinity, S_iO_2, total inorganic phosphorus, NO_2^-, NO_3^-, NH_4^+, chlorophyll α and others – 18 parameters in total. Since there is no observation of *Phaeocystis* concentration directly, it is assumed here that any Chl-a concentration above (30.0 μg/l) represents a *Phaeocystis* bloom. Since station Noordwijk2 (NW2) contained the least missing data, it was selected here. Salinity (S), temperature (T), total inorganic nitrogen (TIN) and total inorganic phosphorus (TIP) were used as input to predict the Chl-a concentration.

No data was available on wind or solar irradiance. The total dataset contained 171 records, of which 145 (May, 1975∼Dec, 1981) were selected for model construction and 26 (Jan, 1982∼Mar, 1983) were used for verification. Cluster analyses were preformed distinguishing between three pre-defined classes for TIN and TIP and five classes for Chl-a resp.; the constructed membership functions are presented in Figure 2.

The extended case reasoning strategy is applied for rule generation; after the membership functions of each variable are defined, the 145 learning data are fuzzified following the procedures described above. From these 145 records a limited set of 15 rules were obtained. In order to enable a quantitative comparison, the model outputs are defuzzified by the centre of gravity method in combination with a normalised weighted sum, according to

$$D = \frac{\sum_{i=1}^{I} w_i v_i M(B_i)}{\sum_{i=1}^{I} w_i v_i} \tag{2.1}$$

where D is numerical output, w_i is the weight associated with rule i, v_i is the fired degree of rule i, and $M(B_i)$ is the fuzzy mean of the corresponding output fuzzy set of rule i, given by

$$M(B) = \frac{\int_{-\infty}^{+\infty} x\mu_B(x)dx}{\int_{-\infty}^{+\infty} \mu_B(x)dx} \tag{2.2}$$

in which μ_B is the membership function of fuzzy set B on variable x. The defuzzified outputs are plotted against the observations for comparison (Fig. 3). The two series are seen to match reasonably well (having an R^2 of about 0.83 which can be considered quite acceptable) given the approximate

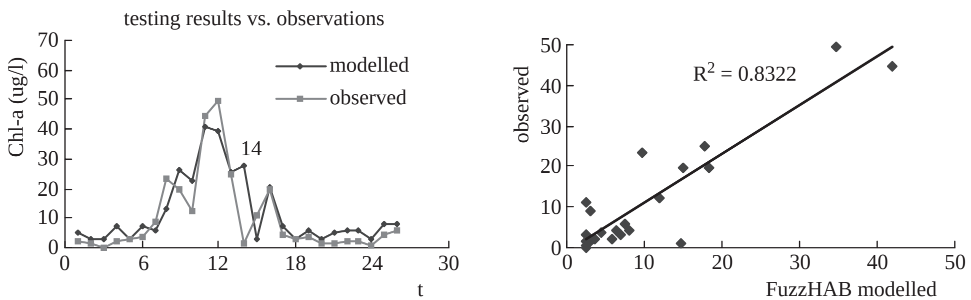

Figure 3. Chl-a concentration at NW2 with Δt ≈ 15 days (left), and scatter plot and R^2 (right).

nature of the procedure (Chen et al., 2004). It is seen that the model fails to numerically reproduce the very low or very high values. One reason is that the model variables are divided into three or five classes, which is too coarse to be very precise. Of course this can be improved by applying a finer division into (sub)classes if quantitative prediction is of interest and adequate data are available for membership function construction.

The overall conclusion is that a Fuzzy Logic rule-based model seems feasible for algal bloom alarm, provided irradiance data are available from meteorological observations and nutrient data from a hydrodynamic transport model, e.g. the Delft3D coastal hydrodynamic software system of WL | Delft Hydraulics (Chen & Mynett, 2004). Clearly, the role of expert knowledge is important in identifying the proper membership functions and establishing an appropriate rule-base.

3 GENETIC PROGRAMMING OF FLOW RESISTANCE DUE TO VEGETATION

3.1 *Modelling considerations*

Proper modelling of overland flows in wetlands and vegetated floodplains is of great practical importance both in flood early warning and in river restauration. Many research initiatives have been undertaken in order to improve on the description of the relationship between flow resistance and the temporal and spatial distribution of vegetation. Both analytical and experimental studies of vegetation-related resistance to flow and the equivalent resistance coefficients have shown that the resistance coefficients are very much waterdepth (and hence solution) dependent. Consequently, the traditional approach of using a single resistance coefficient fails to describe correctly the (nonlinear) physical behaviour of this phenomenon. One way of improving the description is updating the equivalent resistance coefficient based on the computed water depth. However, in order to do so, a relation between vegetation characteristics, bed resistance, water depth and equivalent resistance coefficient is needed. Genetic Programming is used here to derive such relation.

When refining a model of a physical process, a scientist focuses on the agreement of theoretically predicted and experimentally observed behaviour. If these agree in some accepted sense, then the model is considered ‘correct’ within that context. Here, the inverse problem to verification of theoretical models is considered: (how) can we obtain the governing equations directly from measurements? To do this, we will extend the notion of qualitative information contained in a sequence of observations to consider directly the underlying mechanisms. We will show that, using this information, one can deduce the effective governing equations. The latter represent up to an a priori specified level of correctness or accuracy, the deterministic portion of the observed behaviour.

3.2 *Equation building – the 1DV turbulence model*

One way of obtaining a detailed account of resistance description of flow through and above vegetation, is to perform detailed numerical simulations based on a one-dimensional turbulence model for the vertical (1DV) direction (Uittenbogaard, 2003). The 1DV model assumes that the flow is locally uniform in the horizontal directions, and calculates the orthogonal horizontal velocities $u(z)$ and $v(z)$ as a function of the vertical coordinate z. The 1DV model is a simplification of the full 3D Navier-Stokes equations by decoupling the vertical from the horizontal flow conditions. In order to include the effects of plants into the commonly used k-ε model for turbulence closure, the following modifications have been included:

1. the decrease of the available cross-section for the vertical exchange of momentum, turbulent kinetic energy and turbulent dissipation,
2. the drag force exerted by the plants in the horizontal direction,
3. an additional turbulence production term due to vegetation, and
4. an additional turbulence dissipation term due to vegetation.

After incorporation of these effects the equation of motion becomes:

$$\rho_0 \frac{\partial u}{\partial t} + \frac{\partial p}{\partial x} = \frac{\rho_0}{1-A_p} \frac{\partial}{\partial z}\left(\left(\nu + \nu_T\right) \frac{\partial u}{\partial z} \right) - F \tag{3.1}$$

where $(1 - A_p)$ denotes the specific area occupied by the fluid and F is the drag force exerted by the plants. The k-equation in the k-ε model is modified to account for the effect of plants:

$$\frac{\partial k}{\partial t} = \frac{1}{1-A_p} \frac{\partial}{\partial z}\left(\left(1 - A_p\right)\left(\nu + \nu_T/\sigma_k\right) \frac{\partial k}{\partial z} \right) + T + P_k - B_k - \varepsilon \tag{3.2}$$

For a more detailed description of this 1DV model the reader is referred to (Uittenbogaard, 2003). The purpose of running the 1DV k-ε model in this study was to obtain the detailed roughness description of resistance to the flow caused by vegetation and to obtain the commonly used roughness values like the Manning (n), Chézy (C) or Nikuradse (k_s) coefficients. Water-depth-dependent roughness relationship as well as the water-level slope are plotted in Figure 4 against ratio of plant height (k) and water depth (h). Two different conditions can be identified: (i) un-submerged vegetation, when the plants height exceeds the water depth, and (ii) submerged vegetation, when the water depth exceeds the plants height.

Clearly, for un-submerged flow conditions the water-level slope is much higher than for submerged conditions implying that the resistance of the vegetation is higher. Un-submerged flow conditions can be successfully treated analytically (Rodriguez, 2003). If the water level is high

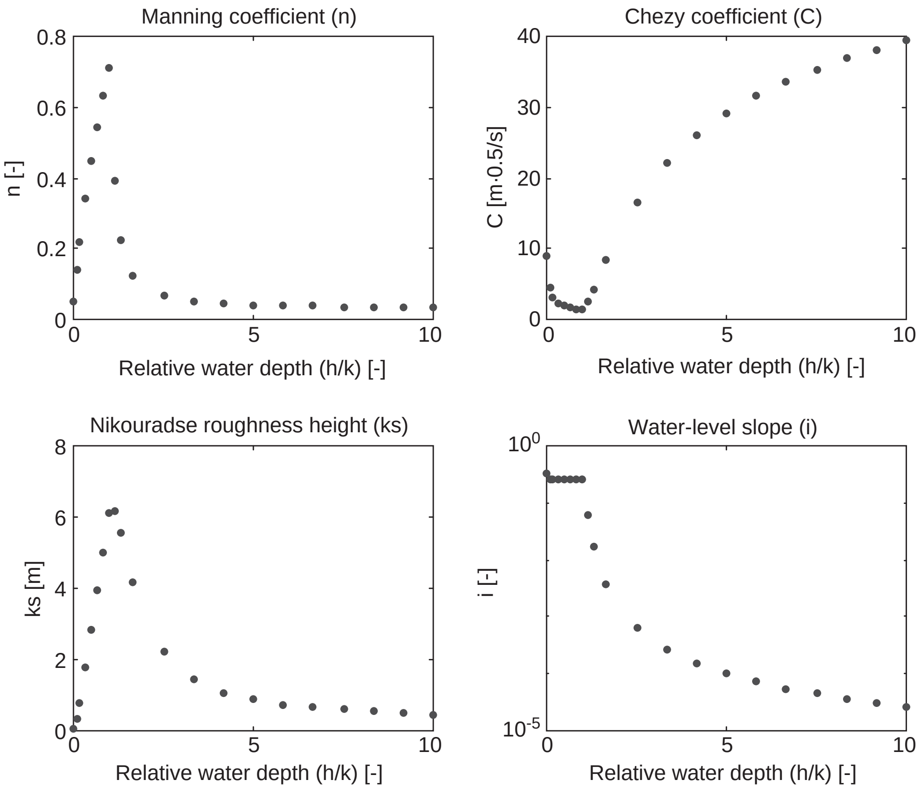

Figure 4. Vegetation-related resistance coefficients and water-level slope versus water depth.

Table 1. Inputs to the 1DV k-ε model.

Input	Dimension	Description
D	L	Diameter of the stems.
m	L^{-2}	Number of stems per square meter.
k	L	Plants height.
C_D	–	Drag coefficient of a single stem.
C_b	$L^{0.5}/T$	Bed Chézy resistance coefficient.
h	L	Water depth.

enough, flow through the vegetation is negligible compared to the flow above (Fig. 4); in the transition zone both the flow through vegetation and above it are relevant and consequently all resistance coefficients are depth-dependent.

3.3 *Genetic Programming – evolutionary development*

Genetic algorithms, evolution strategies, evolutionary programming as well as differential evolution represent a few examples of evolutionary algorithms that have been explored by a number of scientists during the past decades. However it was rather recently that John Koza (1992) of Stanford University proposed a special kind of evolutionary algorithm: Genetic Programming (GP) which involves symbolic expressions. Applications of genetic programming in hydrosciences were introduced by (Babovic & Abbott, 1997) and (Babovic & Keijzer, 2000).

Inspired by Koza's pioneering work and in order to improve the performance of his algorithm, the dimensionally aware GP algorithm was developed by (Keijzer & Babovic, 1999) which is considered extremely useful for knowledge discovery in engineering science. In that field it has been 'common scientific practice' to eliminate units of measurements through the introduction of dimensionless numbers (which can be derived systematically by applying Buckingham's Pi-theorem) in order to use knowledge-free induction tools such as regression analysis, neural networks or genetic programming. Moreover, as a consequence the original search space collapses, making it more effective for algorithms that fit models to the data.

The dimensionally aware genetic programming (Keijzer & Babovic, 1999) differs in that the raw observations are used together with their units of measurement. The system of units of measurement can be viewed as a typing scheme and as such can be used in some form of typed genetic programming. The dimensionally aware approach proposes what can be called a *weakly typed* or *implicit casting* approach – dimensional correctness is promoted, not enforced.

The role of the (expert) user is then to choose his most suitable formulation to further analyse the proposed relationships. The user can exploit background knowledge or implement some belief about the problem domain. The final step lies in examining the selected equation(s) in order to interpret them. When a reasonable explanation for the apparent goodness-of-fit of such an equation is produced, the user's belief in the correctness of the equation is enhanced. The equation then no longer functions as a black box for making accurate predictions but as a genuine empirical equation that can be used with more confidence than mere statistical accuracy. The equation and corresponding interpretation is amenable to review by experts and peers.

3.4 *Resistance formulae for submerged vegetation obtained from GP*

The dimensionally aware genetic programming approach was applied to a set of 990 calculations carried out with the 1DV numerical model for submerged vegetation, using the input variables as presented in the table above (Rodriguez, 2004).

For dimensional consistency a slightly adapted Chézy's coefficient was used:

$$C' = \frac{C}{\sqrt{g}} \tag{3.3}$$

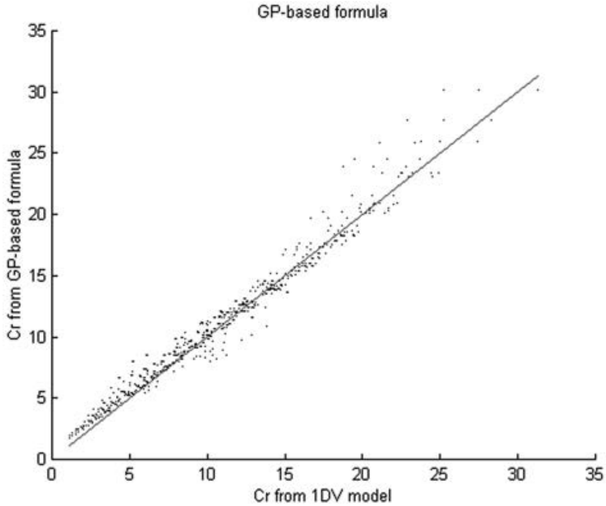

Figure 5. Scatter plot of C_r (GP based formula).

by virtue of which time-related units of measurements are avoided and the resistance coefficient becomes solely a function of the geometry of the system. GP was then employed in a multi-objective sense, simultaneously optimising the following three objectives: (i) root mean square error (RMSE): measure of overall the accuracy of the formula, (ii) coefficient of determination (CoD): measure of the goodness of the shape of the formula and (iii) dimensional error: measure of the dimensional consistency of the formulae. The following formula with smallest RMSE and highest CoD appeared:

$$\frac{C_r}{\sqrt{g}} = \sqrt{\frac{2}{c_D m D k}} + \ln\left\{\left(\frac{h}{k}\right)^2\right\} \tag{3.4}$$

which can be rearranged to give:

$$C_r = \sqrt{\frac{2g}{c_D m D k}} + 2\sqrt{g}\ln\left(\frac{h}{k}\right) \tag{3.5}$$

The RMSE of this formula was $0.98\,\mathrm{m}^{0.5}/\mathrm{s}$; its scatter plot is presented in Figure 5.

The relationship between the resistance coefficient C_r and the water depth h consists of an h-independent term and a logarithmic h-dependent term. For $h = k$ the log term reduces to 0, which will be denoted by C_k:

$$C_r(h = k) = C_k = \sqrt{\frac{2g}{c_D m D k}} \tag{3.6}$$

C_k is equivalent to the simplest expression of C_r for flow through un-submerged vegetation as derived by (Rodriguez, 2004):

$$C_r = \sqrt{\frac{2g}{c_D m D h}} \tag{3.7}$$

Substitution immediately gives:

$$C_r = C_k + 2\sqrt{g}\ln\left(\frac{h}{k}\right) \tag{3.8}$$

It can be seen that (3.8) may take the form of a differential equation with a boundary condition imposed at $h = k$; differentiating both sides with respect to h results in:

$$\frac{\partial C_r}{\partial h} = \frac{2\sqrt{g}}{h} \tag{3.9}$$

In turn, integration and applying the boundary condition $C = C_{ref}$ at $h = h_{ref}$ gives:

$$C - C_{ref} = 2\sqrt{g}\ln\left(\frac{h}{h_{ref}}\right) \tag{3.10}$$

In this case the logical boundary condition is $h_{ref} = k$ which is compatible with the simplest expression for C_r in case of un-submerged vegetation. However, in order to be compatible with the more accurate expression of (Rodriguez, 2004):

$$C_r = \left(1 - A_p\right)\sqrt{\frac{1}{\frac{1}{C_b^2} + \frac{1}{2g}C_D mDh}} \tag{3.11}$$

The corresponding expression for C_k becomes:

$$C_k = \left(1 - A_p\right)\sqrt{\frac{1}{\frac{1}{C_b^2} + \frac{1}{2g}C_D mDk}} \tag{3.12}$$

This expression provides more accurate results (RMSE $= 0.77\,\mathrm{m}^{0.5}$/s). Also, with this change in C_k, it was found that a better fit was possible using a slightly different coefficient in front of the

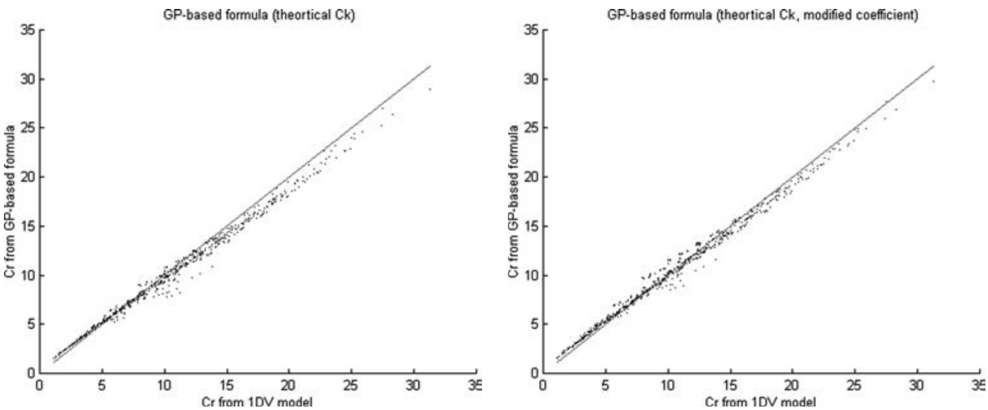

Figure 6. Scatter plots for C_r (GP based formula with theoretical C_k for different coefficients).

logarithmic term in (Eq. 3.8), corresponding to:

$$C_r = C_k + 2.22\sqrt{g}\ln\left(\frac{h}{k}\right) \tag{3.13}$$

which has a fit with an RMSE of 0.63 $m^{0.5}$/s, as indicated in Figure 6.

Using this modified coefficient, the differential equation (3.9) becomes:

$$\frac{\partial C_r}{\partial h} = \frac{2.22\sqrt{g}}{h} \tag{3.14}$$

4 CONCLUSIONS

The application of Artificial Intelligence (AI) techniques like Fuzzy Logic or Genetic Programming in essence concerns extracting useful information from data sources and combining available knowledge with new observations. However, *merely* applying AI-techniques is not the entire story, at least not in the field of scientific knowledge discovery. New scientific theories encourage the acquisition of new data and these data in turn lead to the generation of new theories. The authors strongly believe that the most appropriate way for scientific applications of data mining is to combine both *theory-driven* and *data-driven* approaches. By incorporating expert knowledge in the discovery process, one can take full advantage of knowledge discovery and advance the understanding of physical processes in the field of environmental hydrodynamics.

REFERENCES

Babovic, V. & Abbott, M.B. (1997). The evolution of equations from hydraulic data, Part I: Theory, and Part II: Application, *Journal of Hydraulic Research*, 35(3): 397–430.

Babovic, V. & Keijzer, M. (1999). Computer supported knowledge discovery – A case study in flow resistance induced by vegetation. In: *Proceedings of the XXVIII Congress of International Association for Hydraulic Research*, Graz, Austria.

Babovic, V. & Keijzer, M. (2000). Genetic programming as a model induction engine. *Journal of Hydroinformatics*, 2(1): 35–60.

Chen, Q. (2004). Cellular Automata and Artificial Intelligence in Ecohydraulics Modelling. PhD thesis, UNESCO-IHE, Taylor & Francis Group plc, London UK, ISBN: 90 5809 696 3.

Chen, Q. & Mynett, A.E. (2004). Predicting algal blooms along the Dutch coast by integrated numerical and fuzzy logic approaches. In: *Liong et al. (Eds.), Proc. 6th Hydroinformatics Conference*, Singapore.

Chen, Q., Mynett, A.E. & Teng, L. (2004). Integrated numerical and decision tree modelling of Phaeocystis globosa bloom along the Dutch coast", In: *Liong et al. (Eds.), Proc. 6th Hydroinformatics Conference*, Singapore., Vol. 1, pp 315–323.

Keijzer, M. & Babovic, V. (1999). Declarative and preferential bias in GP-based scientific discovery, *Genetic programming and evolvable machines*, 3: 41–79.

Koza, J.R. (1992) *Genetic Programming: On the Programming of the Computes by Means of Natural Selection*, MIT Press.

Mynett, A.E. (2002). Environmental Hydroinformatics: the way ahead. In *:Falconer et al. (Eds.), Proc. 5th Hydroinformatics Conference*, Cardiff, UK, Vol.1, pp 31–36.

Mynett, A.E. (2003). Hydroinformatics in ecosystem restauration and management. *Final Report, Science, Technology & Management Panel, 3rd World Water Forum*, Kyoto-Osaka-Shiga, Japan.

Mynett, A.E. (2004). Environmental Hydroinformatics tools for ecohydraulics modelling. In: *Liong et al. (Eds.), Proc. 6th Hydroinformatics Conference*, Singapore., Vol. 1, pp 13–23.

Rodriguez, J.R. (2004). Evaluation of Physically Based and Evolutionary Data Mining Approaches for Modelling Resistance due to Vegetation in SOBEK1D-2D. MSc thesis HH485, UNESCO-IHE.

Uittenbogaard, R. (2003). Modelling turbulence in vegetated aquatic flows. In: *Riparian forest vegetated channels workshop*, Trento, Italy.

This page intentionally left blank

Environmental Hydraulics and Sustainable Water Management – Lee & Lam (eds)
© 2005 Taylor & Francis Group, London, ISBN 04 1536 546 5

Hydraulic phenomena in urban atmospheric environments and their role in contaminant dispersion

H.J.S. Fernando
Environmental Fluid Dynamics Program, Department of Mechanical & Aerospace Engineering, Arizona State University, Tempe, AZ

ABSTRACT: Stable stratification associated with nocturnal thermal circulation in areas of complex terrain leads to interesting internal "hydraulic" phenomena. Given that most urban areas are in complex topography, understanding and prediction of such phenomena are of immediate practical importance. The results of some theoretical, laboratory and field experimental studies aimed at understanding stratified flow and turbulence phenomena in urban areas is summarized in this paper, with particular emphasis on internal hydraulic effects that arise during the topographic adjustment of stably stratified gravity-driven flows in complex topographies and turbulent diffusion in such flows.

1 INTRODUCTION

Although the subject of Hydraulics (hydōr + aulos = water + tube) has been historically used in conjunction with water motion in constrained engineering systems such as tubes, pipes, channels and elbows, the techniques used therein have also been used for air flows. A striking example in this context is the epoch-making work of Long (1953), wherein the techniques of free-surface hydraulics were applied to study the motion of layered (stratified) flow over obstacles, thus mimicking stratified air flow over mountains, which has been extended to oceanic and engineering flows. Natural flows are turbulent; layers of different densities mix significantly and thus the techniques of idealized internal hydraulic theory are barely applicable to such flows. The basic ideas and analyses, however, have been successfully used to study and predict many environmental flows. This paper attempts to identify and analyze internal hydraulic phenomena that have important bearing on air flow and dispersion in urban areas. World population is expanding at a rate of ~1.5% annually, and has a strong tendency to pool in ever larger and more complex urban settings in search of an enhanced quality of life (Fuchs et al. 1995). The population tends to settle along transportation corridors along waterways, which are typically associated with complex terrain (defined as areas replete with mountains, valleys and escarpments). Uneven topography not only causes perturbations to the background large (synoptic) scale (~1000 km) atmospheric flows, but also induces local flows within urban air basins (airsheds) known as *thermal circulation*; a combination of synoptic flow, thermal circulation and other local flows determines the local micrometeorology (Brazel et al. 2004). It is the internal hydraulic phenomena associated with urban meteorological flows that are of interest to this paper.

The thermal circulation, which is driven by local diurnal solar heating and cooling of the topography, is broadly classified into two classes, slope and valley flows, the former occurring on side slopes and the latter blowing along the valley. Up-slope (anabatic) and up-valley circulations occur during the day and down-slope (katabatic) and down-valley winds develop at night. These flows are exemplified in Figure 1 on a topographic map of the Salt Lake Valley, where an extensive measurement program – Vertical Transport and Mixing eXperiment (VTMX) – was conducted in October 2000 (Doran et al. 2002). VTMX concerned nocturnal thermal circulation under negligible (or weak) synoptic influence. Also of interest were the transition periods where winds shift their direction. In the evening, the winds switch from up slope/valley winds to down slope/valley winds (evening transition) and the opposite occurs during morning transition. At night, the air layer near

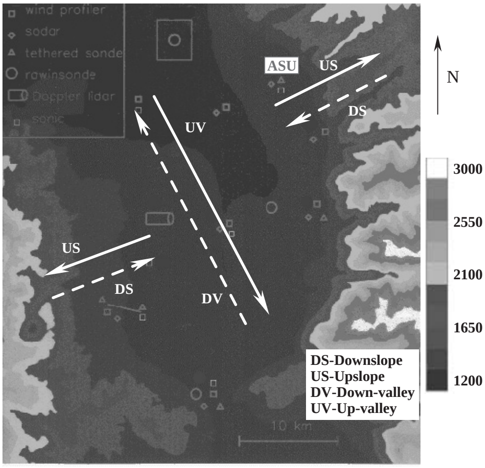

Figure 1. The thermal circulation in the complex terrain of Salt Lake Valley, Utah, where the VTMX campaign was conducted. The shading indicates the topography (in m).

the sloping ground become heavier and drains down as down-slope (DS) or katabatic flows. A part of this flow accumulates ("pool") in the valley bottom as a stably stratified layer (which acts as a "smog trap," given that vertical turbulent diffusion is inhibited by stable stratification), whereas the rest drains along the valley slope forming down-valley winds (DV). This circulation patterns reverses during the day, forming up-slope (US) and up-valley (UV) winds. Figure 1 also shows the suite of instruments deployed by various groups during the VTMX Program, and the measurements to be described here were taken at the ASU site located on a slope in the east valley. In addition, laboratory experiments and theoretical analyses were also conducted to elicit physical processes active in the thermally driven flows, some results of which are also summarized in this paper.

2 DOWN-SLOPE (KATABATIC) FLOWS AND HYDRAULIC ADJUSTMENTS

Katabatic flows are driven by radiative cooling of a thin fluid layer, and most of the previous studies have focused on quasi-steady state of such flows on simple slopes; see, for example, Figure 2 (Manins & Sawford 1979; Doran & Horst 1993). Here the mean flows are largely determined by local forces due to buoyancy, inertia and Reynolds stress gradients. In the thin-layer (shallow water) formulation, the equation of motion of two-dimensional katabatic flows over simple flows is written is the layer-averaged form (e.g. Manins & Sawford 1979),

$$\frac{\partial Uh}{\partial t}+\frac{\partial U^2 h}{\partial s}=\frac{\partial}{\partial s}\left(\frac{1}{2}\Delta b h^2\cos\alpha\right)-\Delta b h\sin\alpha - C_D U^2 - \left(\overline{u'w'}\right)_H \qquad (2.1)$$

$$\frac{\partial}{\partial t}(\Delta b h)+UhN^2(\sin\alpha - E\cos\alpha)+\frac{\partial}{\partial s}(U\Delta b h)=B_o-\left(\overline{b'w'}\right)_H, \qquad (2.2)$$

where the averages are defined in terms of a depth H at which katabatic velocity perturbations vanishes, i.e.

$$Uh=\int_0^H u\,dn;\quad U^2h=\int_0^H u^2\,dn;\quad U\Delta bh=\int_0^H Ub\,dn;\quad S_1\Delta bh^2=2\int_0^H bn\,dn$$

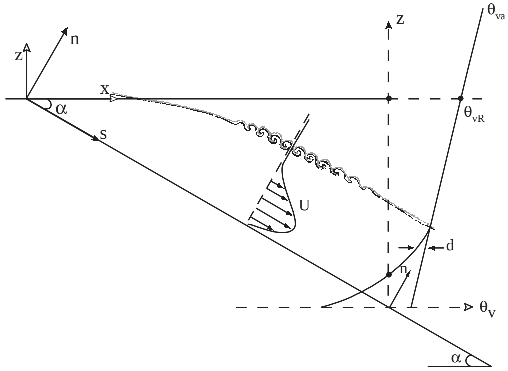

Figure 2. A schematic of a down-slope flow along a simple slope.

$$S_2 \Delta bh = \int_0^H b dn \text{ and } \int_0^H w dn = w_H \left(H - S_3 h\right), \tag{2.3, a-f}$$

where h is a characteristic thickness of the flow and the entrainment velocity w_H can be written in terms of the entrainment coefficient E as $w_H = -EU^2$. For top hat profiles, the profile factors S_1, S_2 and S_3 can be taken as unity, as in (2.1)–(2.2). Here a planar slope of inclination α (Figure 2), is assumed, the initial undisturbed (virtual) temperature stratification is $\theta_{va} = \theta_{vR} + \gamma z$, z is the vertical coordinate, s and n, respectively, are the along-slope and slope-normal coordinates, and γ is the ambient vertical temperature gradient. The nocturnal cooling of the surface causes a temperature deviation $-d(s,n,t)$ from the original θ_{va}, leading to an along-slope katabatic flow with temperature $\theta_v = \theta_{va} - d(s,n,t)$. With the usual definition of buoyancy based on a reference temperature θ_{vR} or reference density ρ_R (at z $= 0$), $b_{va} = g(\theta_{va} - \theta_{vR})/\theta_{vR}$ and $b_v = g(\theta_v - \theta_{vR})/\theta_{vR}$, it is possible to write

$$b_v = b_{va} + b\,,\; b = -gd/\theta_{vR} \text{ and } N^2 = g\gamma/\theta_{vR} = db_{va}/dz\,, \tag{2.4}$$

where N is the buoyancy frequency, $B_0 = Q_0 - (R_H - R_0)$, $Q_0 = (\overline{b'w'})_0$ is the surface buoyancy flux, $(R_H - R_0)$ is the buoyancy deficit caused by the differential net radiation between $n = 0$ and H and $(\overline{b'w'})_H$ is the turbulent buoyancy flux at the top of katabatic layer. The physical meaning of the terms of (2.1)–(2.4) has been discussed extensively and can be found in Manins & Sawford (1979) and Papadopoulos et al. (1997). Note that the second term in (2.1) can be expressed as

$$\frac{\partial U^2 h}{\partial s} = Uh\frac{\partial U}{\partial s} + U\frac{\partial Uh}{\partial s} = Uh\frac{\partial U}{\partial s} + \underbrace{EU^2}_{\tau_E}, \tag{2.5}$$

and the term $\tau_E = EU^2$ represents the shear stresses introduced by the entrainment flow into the katabatic current. Note that this shear stress differs from the Reynolds stresses at the edge of the katabatic flow. Both the surface stress $\tau_S = C_D U^2$ and τ_E contribute to the retardation of the gravity currents, but detailed measurements made during the VTMX campaign show that the τ_E/τ_S ratio can be as high as (10–20) when the Richardson number ($Ri = \Delta bh\cos\alpha/U^2$) is less than 0.8, whereupon the entrainment is dominant (Princevac et al. 2004). At larger $Ri(>1)$, the surface shear stress as well as the inertial term $Uh\partial U/\partial s$ become important.

In general, the scales of the first two terms in (2.1) become Uh/T and U^2h/L_H, respectively, and whenever their ratio L_H/UT, where T and L_H are the time and along-slope length scales, becomes small the unsteady terms can be neglected. For typical $L_H \sim 10$ km and $U \sim 3$ m/s, this requires consideration of time averages over about an hour. Under steady conditions, a balance of the along slope buoyancy and the inertia can be assumed for $Ri > 0.8$, since τ_E is assumed negligible or on

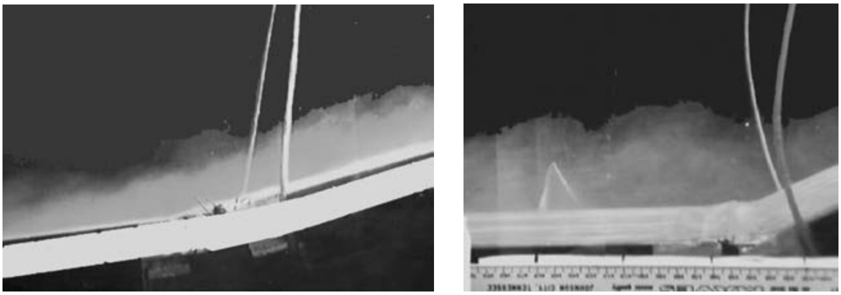

(a) (b)

Figure 3. The propagation of a gravity current with $Q_0 = 38\,\text{cm}^2/\text{s}$: (a) $\alpha = (10°, 20°)$ and (b) $\alpha = (0°, 26°)$ (the top of the concentration contour represents the 90% of the maximum concentration).

the same order as τ_S. The balance of forces, therefore, gives

$$\frac{U^2 h}{L_H} \sim \Delta bh \sin\alpha \quad \Rightarrow \quad U \approx \lambda_u (\Delta b L_H \sin\alpha)^{1/2}. \tag{2.6}$$

VTMX results show that $\lambda_u \approx 0.5 - 0.6$, although the data is somewhat scattered. If the entrainment stress is dominant for $Ri < 0.8$, then a major balance of the form

$$EU^2 \sim \Delta bh \sin\alpha \rightarrow U \sim (\Delta bh \sin\alpha / E)^{1/2} \tag{2.7a,b}$$

can be proposed, where at least for laboratory down-slope slows E can be expressed as (Turner 1986),

$$E = \frac{0.08 - 0.1Ri}{1 + 5Ri}. \tag{2.8}$$

Princevac et al. (2004) have argued that (2.8) underestimates the entrainment rate, given that the Ellison & Turner (1959) experiments were performed at lower Reynolds numbers. For very small Ri, E can be approximated as a constant and thus

$$U \approx \lambda_u^* (\Delta bh \sin\alpha)^{1/2}. \tag{2.9}$$

Figures 3a, b show a laboratory gravity current down a slope, and Figure 4 shows a comparison of results with (2.7b), the Richardson numbers at the measurement locations being small ($Ri < 1$). The directly measured entrainment coefficients were used in the calculations. In the experiments, the flow was introduced by releasing a 2-dimensional layer of dense water at the upper end of the slope. Measurements were made using the PTV technique at 10 cm upstream of the slope discontinuity under steady flow conditions for a range of slope angles ($0 < \alpha < 60°$) and source buoyancy fluxes $35 < Q_0 < 45\,\text{cm}^2/\text{s}$, where $Q_0 = V_0 \Delta b_0$, V_0 is the initial volume flux rate and Δb_0 is the buoyancy of the source fluid.

When considering time scales smaller than L_H/U, the unsteadiness in (2.1) plays a dominant role and, late into the night, the entrainment and buoyancy flux B_0 are negligibly small ($E << \tan\alpha$). Therefore, over small slopes, one may expect linear oscillations determined by

$$\frac{\partial Uh}{\partial t} \approx -\Delta bh \sin\alpha; \quad \frac{\partial}{\partial t}(\Delta bh) - N^2 (Uh) \sin\alpha \approx 0, \tag{2.10}$$

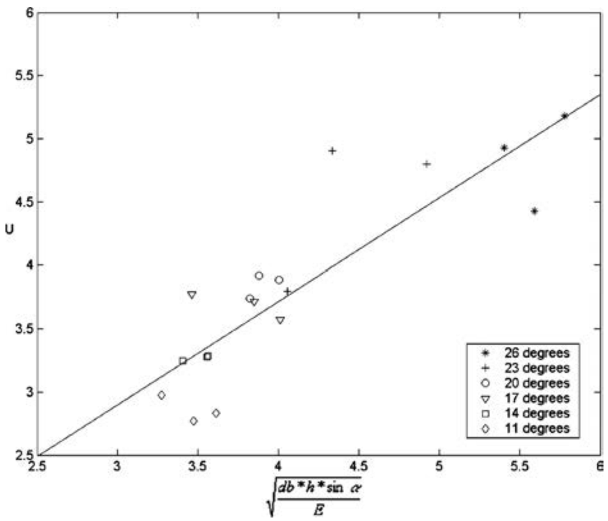

Figure 4. Comparison of steady state flow velocity with the predictions (2.7b).

with a frequency $N\sin\alpha$. Such oscillations in katabatic flows have been previously noted both observationally and on theoretical grounds (Fleagle 1950), but different mechanisms have been proposed with regard to their existence. Fleagle's (1950) model shows that, as the air accelerates down the slope, the development of an adverse pressure gradient due to adiabatic heating of air leading to flow retardation. If the friction can be written as $F = -kU$, then the friction reduces as air decelerates while radiational cooling continues to be the driving force. Porch et al. (1991) have argued that cross flows over the slopes also can cause oscillations. In this case, katabatic flow temporarily stops as drainage currents from tributaries intermittently enter the valleys. As cold air accumulates and buoyancy forcing increase in tributaries, there will be periodic releases of colder air onto the slope, causing oscillations. Oscillations described by (2.10), however, do not require such a mechanism nor do they rely on adiabatic heating of draining air. The major mechanism of oscillations here is a balance between unsteady inertia and buoyancy forces of fluid elements.

It is possible to obtain the characteristic layer thickness h and the buoyancy deficit scale Δb of katabatic flows by using the continuity equation in integrated form $\partial Uh/\partial s = EU$, an entrainment law of the form $E = A/Ri$ for larger Richardson numbers (Manins & Sawford 1979), (2.2), (2.6) and by employing a set of reasonable assumptions. After some simplifications, it is possible to obtain

$$E = B\left(\frac{s}{h}\right) tan\alpha \text{ , and } \frac{\partial Uh}{\partial s} = B\left(\frac{s}{h}\right) U \tan\alpha \text{ ,} \tag{2.11}$$

where $B = \lambda_u^2 A$. The buoyancy equation (2.2), with the assumptions of quasi-steadiness, $B_0 \approx 0$, $(\overline{b'w'})_H/(UhN^2) << E$ and $E <<\ \tan\alpha$ as well as by invoking the usual boundary layer approximation $h/s << 1$, becomes

$$\frac{\partial}{\partial s}(U\Delta bh) \approx -BUN^2 s\sin\alpha \text{ .} \tag{2.12}$$

Note that the gradual cooling of the entire slope over the night can be accounted in the analysis when Δb at the top of the slope is specified, $\Delta b = \Delta b_0$ at $s = 0$. Using (2.11) and (2.12), it is possible to obtain the invariant

$$\Delta b^{3/2} h = V_0 = \Delta b_0^{3/2} h_0^{3/2} , \tag{2.13}$$

where $h = h_0$ at $s = 0$, and

$$h^2 = h_0^{\,2} + \frac{3}{2} B s^2 \tan\alpha . \tag{2.14}$$

The layer thickness in (2.14) can be simplified to obtain $h \approx (3B/2)^{1/2} (\tan\alpha)^{1/2} s$ for the case of $s >> h_0/(3B \tan\alpha/2)^{1/2}$, but this condition is not typically satisfied in field situations.

Another interesting aspect is the hydraulic adjustment of flow near a slope break, for example, at the foot of a mountain. For the idealized case of laboratory flows described above, where the down-slope flow is given by (2.7), the internal Froude number can be written as

$$Fr = \frac{U}{\sqrt{\Delta b h}} = \lambda_u^* \sqrt{\frac{\sin\alpha}{E}} , \tag{2.15}$$

and for small Ri (<0.2), the above expression can be written as (with $\lambda_u^* \approx 0.9$ and $E \sim 0.1$) $Fr \approx 2.9\sqrt{\sin\alpha}$. Note that the flow becomes supercritical for $Fr > 1$ or $\alpha > 7°$, and thus any slope discontinuity connecting two slopes of sufficient length that satisfies $\alpha > 7°$ for both upper and lower slopes ought to realize a flow that remains supercritical on either side of the discontinuity. This phenomenon is exemplified in Figure 3a, where only a little change of the nature of the current is evident following the slope discontinuity. Here all disturbances caused by topography change are swept away by the flow, allowing little time for the flow to adjust at the discontinuity. Alternatively, if the lower (lesser) slope is less than 7° or so, with flow over the larger slope remaining supercritical, then it is possible to expect a sudden transition downstream of the slope break in the form of an internal hydraulic jump. This is evident in Figure 3b.

The flow will be different from the above laboratory case if the gravity-driven flow is to be highly stratified so that entrainment is negligibly small. The velocity in this case is given by (2.6), and thus the internal Froude number becomes

$$Fr_i = \frac{U}{\sqrt{\Delta b h}} = \lambda \sqrt{\frac{L_H \sin\alpha}{h}} = \lambda \sqrt{\frac{\sin\alpha}{\gamma}} \tag{2.16}$$

where $\gamma = h/L_H$. Using typical values of $\lambda \approx 0.5$ and $\gamma \approx 0.01$, we find that the flow is supercritical for about $\alpha > 2°$.

It will also be useful to consider the hydraulic adjustment process in light of the theory of Manins & Sawford (1979). They found that for the case of negligible ambient stratification the flow becomes supercritical when

$$S_1 \frac{\Delta b h \cos\alpha}{U^2} < 1 \text{ or, with simplifications, } \frac{S_1 c_3 c_1 (\sin\beta)^{-2/3}}{c_2^2} < 1 \tag{2.17}$$

where c_1, c_2 and c_3 are defined in terms of the solutions to the hydraulics equations with $N = 0$, viz.

$$h = c_1 (\sin\alpha)^{2/3} s \; ; \; U = c_2 (\sin\alpha)^{2/9} B_0^{1/3} s , \; \Delta b = c_3 (\sin\alpha)^{-8/9} B_0^{2/3} s^{-1/3} , \tag{2.18}$$

$c_1 \approx 0.073$, $c_2 \approx 2.5$ and $c_3 \approx 8.2$. Using the typical value $S_1 \approx 0.5$, the requirement for supercriticality becomes $\beta > 0.6°$. Accordingly, unless the terrain following a slope break is unwontedly flat, no hydraulic jumps can be expected.

3 DISPERSION IN NOCTURNAL FLOWS

One of the striking properties of nocturnal thermal circulation is its intrinsic stable stratification, which leads to drastic modifications in transport and dispersion properties. The dispersion is characterized by the eddy diffusivities of momentum and heat, respectively,

$$K_M = \frac{-\overline{u'w'}}{\left(\frac{\partial U}{\partial z}\right)} \text{ and } K_H = \frac{-\overline{w'\theta_v'}}{d\overline{\theta}_v/dz}. \tag{3.1a,b}$$

Figure 5 shows, respectively, the dimensional forms of K_M, K_H and their ratio K_H/K_M as a function of the averaged local gradient Richardson number $\overline{Ri_g}$ of the flow (Monti et al. 2002). Note that in the $\overline{Ri_g}$ range investigated both K_H and K_M are much larger than their molecular diffusive counterparts ($K_H = 2 \cdot 10^{-5}$ and $K_M = 1.5 \cdot 10^{-5}\ \mathrm{m^2\,s^{-1}}$, respectively), indicating the dominance of turbulent transport. As evident from Figure 5, K_H/K_M is approximately unity for $\overline{Ri_g} < 0.2$. In this range, the stratification effects are of lesser importance and the heat is carried by turbulent eddies at the same rate as momentum. When $\overline{Ri_g} > 0.2$, K_M becomes greater than K_H, which can be attributed to the increasing influence of buoyancy that facilitates internal gravity-wave activity. Internal waves transport momentum, but sustain only little (or in the ideal case of linear waves, no) buoyancy fluxes. In the range $1 < \overline{Ri_g} < 10$, the eddy diffusivities have only little dependence on $\overline{Ri_g}$. A commonplace assumption made in geophysical modeling is that K_H/K_M is a constant, but this does not hold true over the extended range of $\overline{Ri_g}$ investigated here. According to the stratified shear flow studies of Strang and Fernando (2001), K-H billowing is prominent when $\overline{Ri_g} < 1$, and at higher $\overline{Ri_g}$ the dominant mixing mechanism becomes sporadic breaking of Hölmböe and/or internal waves. The buoyancy flux associated with these latter mechanisms is smaller and hence a lower K_H/K_M can be expected. Due to the paucity of very high $\overline{Ri_g}$ events in the time series, data points for $\overline{Ri_g} > 20$ have not been subjected to extensive statistical averaging and hence need to be viewed with circumspection.

Suitable non-dimensional forms for the eddy diffusivities were sought during the VTMX data analysis, and the buoyancy scale $L_b = \sigma_w/N$, the shear scale $L_s = \sigma_w/|d\tilde{V}/dz|$, the nocturnal boundary layer height h and the integral length scale z of eddies at a distance z from the ground were considered as possible length scale candidates. Note that near the ground the approximation $|d\tilde{V}/dz| = \{(dU/dz)^2 + (dV/dz)^2\}^{1/2} \approx (dU/dz)$ applies and σ_w is the vertical *rms* velocity. It was found that the best scaling for both eddy coefficients is realized when $\sigma_w L_s$, or equivalently $\sigma_w^2/|d\tilde{V}/dz|$ is used. The normalization was found to arrange the data in Figure 5 to a more regular variation, with the following semi-empirical expressions for diffusivities:

$$\frac{K_M}{\sigma_w^2/\left|d\tilde{V}/dz\right|} \approx 0.34 \text{ and } \frac{K_H}{\sigma_w^2/\left|d\tilde{V}/dz\right|} \approx 0.08 \cdot \overline{Ri_g}^{-0.5} \tag{3.2a,b}$$

It is interesting that (3.2a, b) reduces to the expressions $K_M \approx 0.34 \cdot \sigma_w^2/|d\tilde{V}/dz|$ and $K_H \approx 0.08 \cdot \sigma_w^2/N$, one is dominated by shear and the other by buoyancy. The above expressions were implemented in the meso-scale meteorological models MM-5 and RAMS, which were then used to predict the basin-scale circulations in Salt Lake valley (Lee et al. 2004) and in Rome (Paolo Monti, personal communication), respectively. The new parameterizations (3.2a, b) were found to give significantly better predictions for the near-surface temperature, but only a marginal improvement was found with respect to velocity predictions. A number of possible causes could be identified for this anomalous behavior, one being the relatively straightforward dependence of temperature structure on eddy diffusivity of heat vis-à-vis the dependence of momentum distribution on both heat and momentum diffusivities in a convoluted fashion.

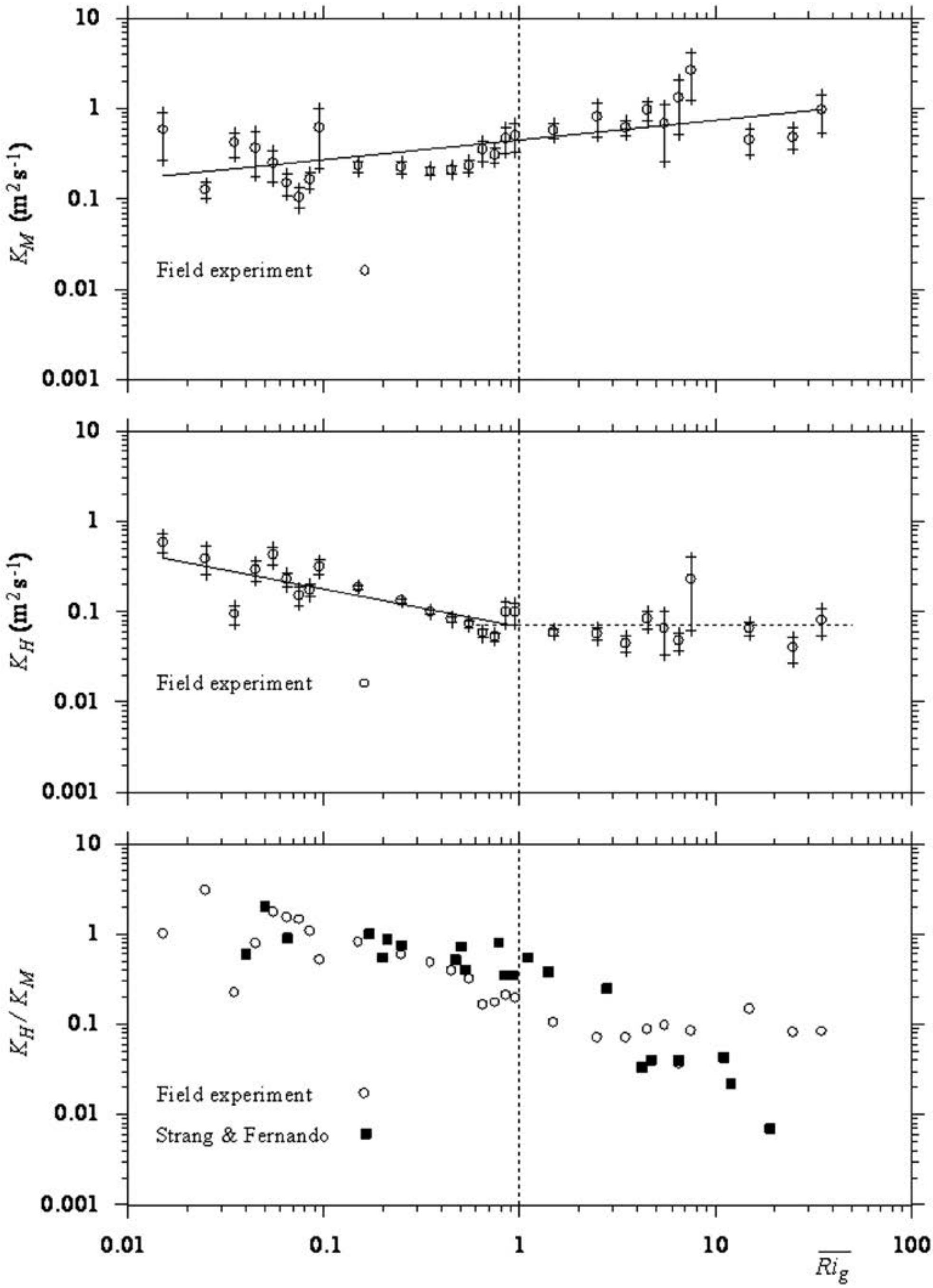

Figure 5. The variation of eddy diffusivities and their ratio with the local Richardson number, measured during the VTMX experiment. The lines show best fits for the entire K_M range and for the ranges $K_H > 1$ and $K_H < 1$. The K_H plots were separated into two regimes due to the striking change of behavior at $K_H = 1$ (Monti et al. 2002).

ACKNOWLEDGEMENTS

The contributions of the ASU VTMX team, especially Dr. Marko Princevac and Mr. Cristian Dumitrescu, are gratefully acknowledged. This work was supported by the DOE (EMP), NSF (CTS/ATM) and ARO (Geosciences).

REFERENCES

Brazel, A.J., Fernando, H.J.S., Hunt, J.C.R., Selover, N., Hedquist, B. and Pardyjak, E., 2004: The evening transition phenomena in Phoenix, Arizona. *Journal of Applied Meteorology*, In Press.

Businger, J.A. and Rao, K.R., 1965: The formation of drainage wind on a snow-dome. *J. Glaciol.*, 5, 833–841.

Doran, J.C. and Horst, T.W., 1993: Observations and models of simple nocturnal slope flows. *Boundary-Layer Meteor*., 18, 495–527.

Doran, J.C., Fast, J.D. and Horel, J., 2002: The VTMX 2000 campaign. *Bull. Amer. Meteor. Soc.*, 83, 537–551.

Fleagle, R.G., 1950: A theory of air drainage. *J. Meteor.*, 7 (3), 227–232.

Fuchs, R.J., Brennan, E., Chamie, J., Lo, F., Uitto, J.I., (Eds) 1995: Mega-city growth and the future, United Nations University Press, Tokyo.

Lee, S.M., Giori, W., Princevac, M. and Fernando, H.J.S., 2004: "A new turbulent parameterization for the nocturnal PBL over complex terrain," Submitted to *Boundary Layer Meteorology*.

Long, R.R., 1953: Some aspects of the flow of stratified fluids. I. A theoretical investigation. *Tellus*, 5, 42–57.

Mahrt, L., 1982: Momentum balance of gravity flows. *J. Atmos. Sci.*, 39, 2701–2711.

Manins, P.C. and Sawford, B.L., 1979: A model for katabatic winds, *J. Atmos. Sci.*, 36, 619–630.

Monti, P., Fernando, H.J.S., Princevac, M., Chan, W.C., Kowalewski, T.A. and Pardyjak, E.R., 2002: Observations of flow and turbulence in the nocturnal boundary layer over a slope. *J. Atmos. Sci.*, 59(17), 2513–2534.

Porch, W.M., Fritz, R.B. and Coulter, R., 1991: Tributory, valley and sidewall air flow interactions in a deep valley. *J. Appl. Meteor*., 28, 578–589.

Princevac, M., Fernando, H.J.S. and Whiteman, D.C., 2004: Entrainment into natural gravity driven flows, Submitted for publication.

Papadopoulos, K.H., Helmis, C.G., Soilemes, A.T., Kalogiros, J., Papageorgas, P.G. and Asimakopoulos, D.N., 1997: The structure of katabatic flows down a simple slope. *Quart. J. Roy. Meteor. Soc.*, 123, 1581–1601.

Strang, E.J. and Fernando, H.J.S., 2001: Turbulence and mixing in stratified shear flows, *Journal of Fluid Mechanics*, 428, 349–386.

This page intentionally left blank

Invited lectures

This page intentionally left blank

Environmental Hydraulics and Sustainable Water Management – Lee & Lam (eds)
© 2005 Taylor & Francis Group, London, ISBN 04 1536 546 5

Exchange flows and estuarine barriers

P.A. Davies & A.J.S. Cuthbertson
Department of Civil Engineering, University of Dundee, Dundee, UK

ABSTRACT: The hydrodynamic effects of incorporating or removing natural or constructed barriers (e.g. sand bars, tidal barrages) within estuaries are reviewed from the point of view of restricted tidal intrusion and flushing of saline waters and the suppression of associated density-driven exchange processes. Results from recent experimental studies investigating various aspects of these processes for fully- and partly-submerged barrier configurations are presented herein. In each case, attempts are made to describe these processes through appropriate scaling relationships of the controlling parameters. Applications to field scale observations are attempted.

1 INTRODUCTION

Recent interest in the commercial exploitation of port and dockland areas and management of urban estuaries has resulted in considerable capital investment for regeneration schemes aimed at enhancing the aesthetic, leisure and environmental value of the site in question. In some cases such as the Cardiff Bay scheme in the UK (Crompton, 2002), waterfront developments include the construction of barriers (Burt & Rees, 2001) across the estuary. Such structures restrict completely any tidal incursion and maintain the upstream water level at a controlled elevation allowing leisure and business activities to continue unhindered by low water for a substantial proportion of the day. In other developments such as the Wansbeck and Tawe barrages, submerged barriers are constructed in order to moderate rather than prevent the tidal exchange. Estuaries may also become fully or partially blocked by natural causes. For example, sediment deposition at the mouth of the estuary may be sufficiently strong as to cause a bar to form, thereby restricting exchange between the estuary proper and the coastal waters. Many shallow, micro-tidal estuaries exhibit this behaviour when prolonged low river flows persist during summer months (Coates *et al*. 2001) or where there is substantial abstraction of river water for agricultural or industrial use). Sea lochs and fjords have similar natural topographic constraints due to the presence of a submerged sill that provides an effective submerged barrier to full exchange.

The presence of such flow obstructions can have important implications for the overall estuarine ecology. The inhibition of natural tidal intrusion and flushing processes can result in stagnation and contaminant accumulation in the brackish water body trapped within the estuary. Such a situation is known to have deleterious effects on water quality and dissolved oxygen levels (Donnelly *et al*. 2000; Coates *et al*. 2001).

2 MODELLING APPROACHES

2.1 *Purging of a trapped brackish water pool*

The first and simplest case to be considered is that of a full barrier (such as a sediment bar) for which microtidal conditions obtain. The problem is then more of a purging problem than an exchange process *per se*. Figure 1 shows a schematic view of such a case. A trapped volume of salt water of prescribed initial density $\rho_0 + (\Delta\rho)_0$ initially fills an estuary of length L and uniform width b to the level H_s defined by the bottom slope α, (the estuary bed slopes with angle α over a distance of

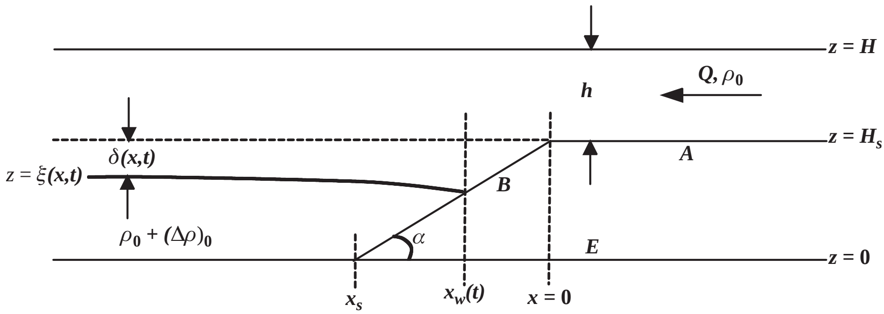

Figure 1. Defining sketch of physical system and laboratory channel.

x_s from the upstream height H_s). A surface flow of fresh water of density ρ_0, depth h, flow rate Q and discharge per unit width q $(= Q/b)$ is initiated upstream in the channel, causing the interface between the trapped salt water and the overlying fresh water flow to distort. By an elapsed time t after initiation of the fresh water surface flow, a salt wedge has formed with nose position $x = x_w(t)$ and nominal interface height $z = \xi(x,\ t)$ relative to the origin of a Cartesian coordinate system (x, y, z) defined by the undisturbed upstream location $(x = 0)$ of the trapped saline water and the base $(z = 0)$ of the channel respectively (see Figure 1). The behaviour of the saline water may be analysed in terms of the reduction $\delta(x, t)$ in interface level, where δ is defined as $\delta = (H_s - \xi)$. With such a system, the flow is described conveniently by the Froude number $Fr_0 = q/(g'h^3)^{1/2}$ and the additional parameters α, h/H_s, x_s/H_s and H_s/L, where $g' = g(\Delta\rho)_0/\rho_0$ and g is the gravitational acceleration.

For maintained steady discharges, Coates *et al.* (2001) showed that the response is characterised by an initial phase of intense shear-induced mixing at the nose of the wedge and a second phase where the mixing is significantly reduced and the wedge is forced relatively slowly down and along the bed slope. An energy balance analysis predicts that $k(t)$ $[(1/2)\ \rho_0 Q^3\, t/(hb)^2] \sim [(1/4)(2L - x_w)b\delta^2(\Delta\rho)g]$ where $k(t)$ is the proportion of the total kinetic energy "river" input allocated in time t to an increase in potential energy of the system due to flushing. The scaling prediction $\delta/h \sim k(t)^{1/2}$ $[(Q^3t/h^4b^3)/(2L - x_w)(g')_0]^{1/2}$ follows from the energy balance equation. Experimental results show good agreement with this scaling and indicate that the energy conversion factor k decreases with time to an asymptotic value k_a that scales well with Fr_0. For cases with multiple intermittent periodic flushing flows of duration t_s, experiments confirm the importance of the starting phase of each flushing event for the time-dependent behaviour of the saline wedge after reaching equilibrium in the intervals between such events. No significant differences are found in the position of the wedge between cases of sequential multiple flushing flows and steady single discharges of the same total duration.

2.2 *Transient exchange flow development over a descending barrier*

The second case to be studied (Cuthbertson *et al.* 2004) is that of a microtidal estuary in which the full blockage to the estuary is removed. For such cases, the reduction of the height of the barrier causes the development of a transient exchange flow between the initially-separated, quiescent fresh or brackish water of the estuary and the saline coastal waters. An important issue is the extent to which the developing exchange flow across the descending barrier may be analysed in terms of quasi-linear behaviour. Figure 2 illustrates the model flow configuration. A fresh water volume of homogeneous density ρ_0 fills a channel C with bottom slope α. This is separated from a large reservoir R of homogeneous saline water of uniform density $\rho_0 + (\Delta\rho)_0$ by an impermeable barrier I of initial height $(h_b)_{max}$. The barrier descends at a rate dh_b/dt, allowing the two water bodies (i) to connect above the submerged barrier crest at time $t = 0$ and (ii) to initiate a transient, buoyancy-driven exchange flow across the descending barrier. Details of this exchange process, and

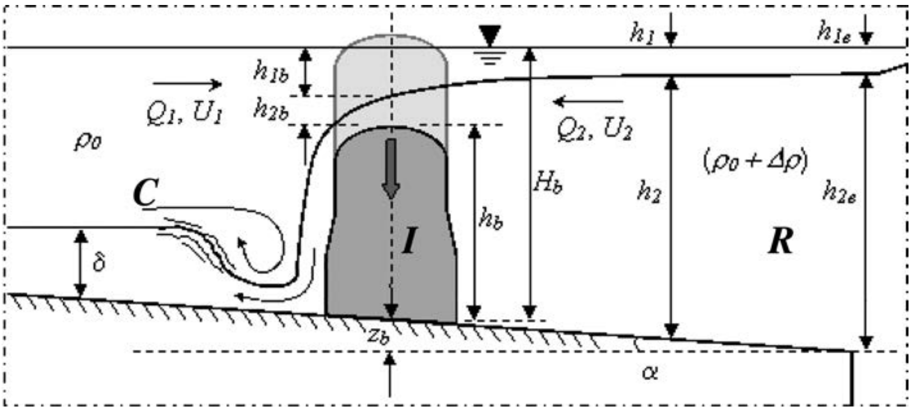

Figure 2. Schematic representation of experimental configuration.

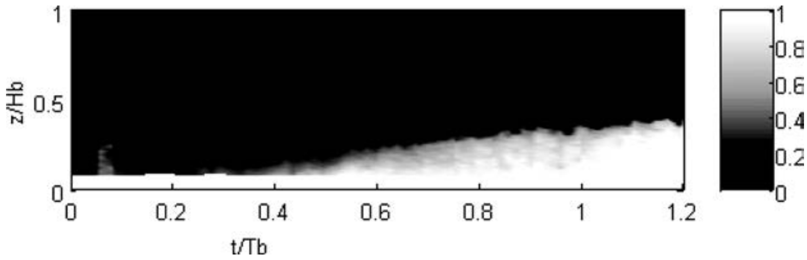

Figure 3. Integrated time series of vertical density profiles at $X/H_b = 1.75$, $g'H_b/(dh_b/dt)^2 = 3.31 \times 10^5$ and $(\Delta\rho)/(\Delta\rho)_0$ coded values shown.

associated formation of a near-bed brackish pool behind the descending barrier, may be analysed as a parametric function of barrier descent rate dh_b/dt, total fluid depth H_b at the barrier and the reduced gravitational acceleration g' associated with the proportional density difference $(\Delta\rho)_0/\rho_0$ driving the exchange flow.

Above the crest of the descending barrier, a well-defined density interface is established, separating an intruding dense saline water layer of thickness $h_{2b}(t)$ flowing over the barrier and descending into the initially-quiescent fresh water volume C, and a compensating outflow layer of fresh water at the free-surface with thickness $h_{1b}(t)$, flowing towards the saline reservoir R. The saline intrusion into the upper channel results in the formation of a near-bed layer of brackish water of nominal thickness $\delta(x,t)$ and mean density excess $(\Delta\rho)_m$, where $(\Delta\rho)_m < (\Delta\rho)_0$ due to turbulent mixing. The leading edge of this intrusion propagates away from the barrier as a gravity current as the intruded volume of brackish water increases. Figure 3 shows an integrated time series plot of the growth in thickness of this brackish layer in terms of normalised density contours $(\Delta\rho)/(\Delta\rho)_0 = 0 - 1.0$ for the growing layer. The brackish layer thickness δ can be defined arbitrarily by the elevation $\delta_{0.2}$ of the normalised contour $(\Delta\rho)/(\Delta\rho)_0 = 0.2$ within the interface between the brackish layer and the overlying fluid. The dependence of the temporal increase in $\delta_{0.2}$ upon the external forcing parameters g' and H_b is shown in Figure 4. These dimensional plots show that (for otherwise constant conditions) an increase in H_b is associated with an increased brackish layer thickness $\delta_{0.2}$, while larger g' values result in an accelerated brackish layer development.

To reflect the variation in detection time $(t_{det})_j$ of the brackish water layer at the different measurement stations X_j located successively upstream from the barrier and to integrate all experimental data, it is convenient to utilise a modified time scale $(t - t_{det})$ and express the model

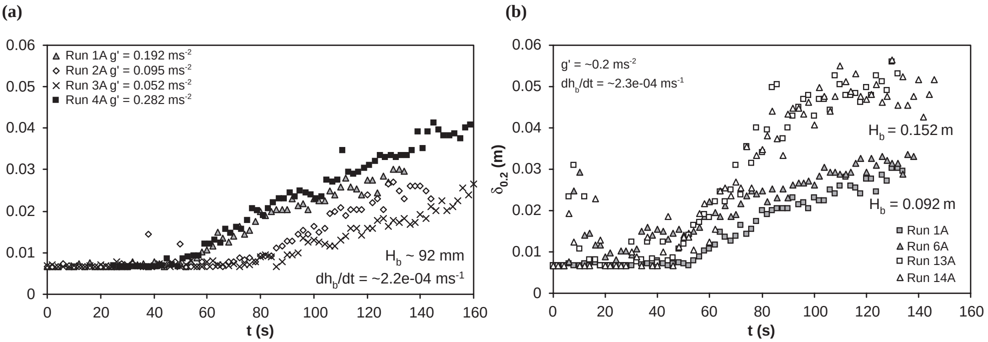

Figure 4. Plots of $\delta_{0.2}$ versus t for $X_j/H_b = 1.75$ illustrating effects of (a) H_b and (b) g'.

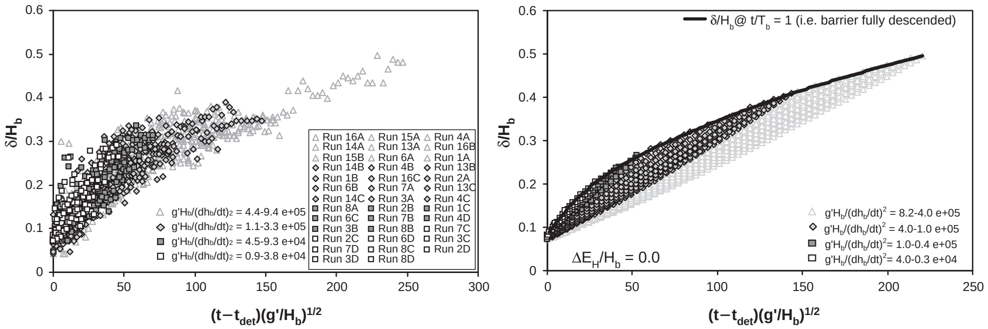

Figure 5. Non-dimensional plots of $\delta_{0.2}/H_b$ versus $(t-t_{det})(g'/H_b)^{1/2}$ for $g'H_b/(dh_b/dt)^2$ ranges shown for (a) experimental data obtained at $X/H_b = 2.65$, 1.75, 1.05 and (b) model-derived predictions.

results in dimensionless form. Dimensional analysis provides a functional relationship $\delta_{0.2}/H_b = \Phi[(t-t_{det})/(g'H_b)^{1/2},\ (g'H_b)/(dh_b/dt)^2,\ X_j/H_b]$, from which the complete data set of measured brackish water thicknesses $\delta_{0.2}/H_b$ can be plotted versus $(t-t_{det})/(g'H_b)^{1/2}$ for different values of $(g'H_b)/(dh_b/dt)^2$ and X_j/H_b (Figure 5(a)).

Predictions are also obtained from the maximal exchange flow model through computation of the saline fluid volume flowing over the descending barrier crest as a function of elapsed time t. By continuity, this volume of intruded saline fluid is used to calculate the resulting brackish layer thickness behind the barrier δ/H_b. Comparisons between the measured experimental data and model predictions (Figures 5(a) and 5(b), respectively) are encouraging: in particular, they reveal similar qualitative tendencies in the observed reduction in the rate of increase in $\delta_{0.2}/H_b$ values with $(t-t_{det})(g'/H_b)^{1/2}$ for larger values of $g'H_b/(dh_b/dt)^2$.

2.3 *Tidal overtopping of a fixed barrier*

Partially- or fully-submerged control structures (i.e. tidal weirs) within estuaries will generally allow a certain degree of exchange and mixing between the semi-enclosed fresh water body and coastal saline waters. For such cases the flow is determined by the relative influence of tidal and fluvial forcing, as well as density-driven processes. A laboratory model (see Figure 6) has been built to show the temporal variation in density stratification within the semi-enclosed channel resulting from cyclic tidal intrusions of saline water over a fixed barrier.

A barrier of fixed height h_b and submergence depth h_s separates a homogeneous salt water reservoir of density $\rho_0 + (\Delta\rho)_0$ from a channel of width B and slope α carrying a steady fresh

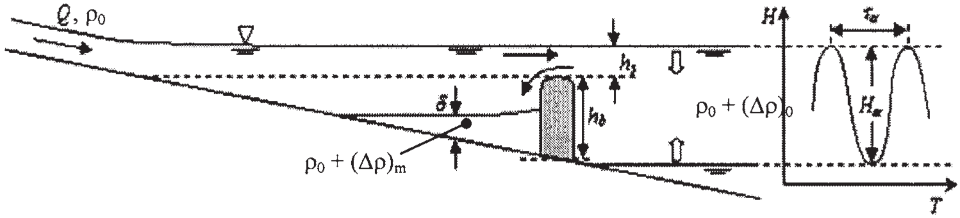

Figure 6. Schematic representation of physical system.

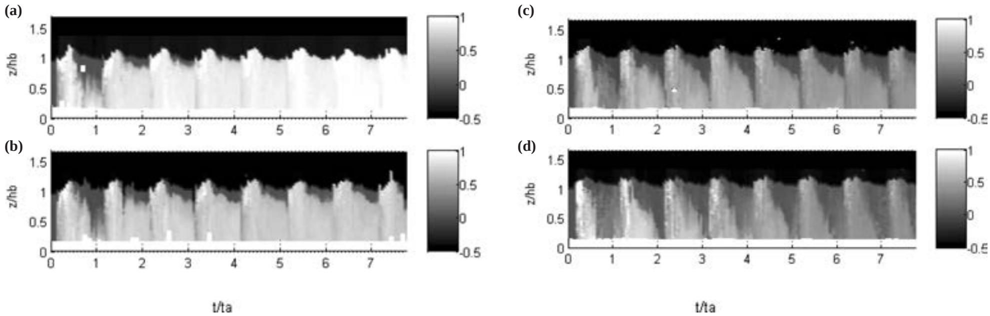

Figure 7. Time series of vertical density profiles at $X_j/h_b = 1.6$, $q/(g'h_b^3)^{1/2} =$ (a) 0.0, (b) 0.063, (c) 0.126 and (d) 0.189, with $h_s/h_b : H_\alpha/h_b : g'\tau^2/h_b = 0.25 : 1.3 : 5390$.

water "river" inflow at a discharge Q (i.e. discharge per unit width q $(= Q/B)$) and uniform density ρ_0. The free surface level of the salt water reservoir varies sinusoidally, with amplitude H_α and period τ_α.

If the temporal characteristics of the brackish water pool can be described adequately in terms of its thickness $\delta(X_j, t)$, the functional relationship $\delta/H_b = \Phi[q/(g'H_b^3)^{1/2}, h_s/h_b, H_\alpha/h_b, g'\tau_\alpha^2/h_b, t/\tau_\alpha]$ can be applied to describe the problem. Figure 7 shows typical integrated time sequences of density profiles obtained at high frequency over a series of tidal cycles at a fixed location X_j behind the barrier. These illustrate the cyclic nature of the intrusion and flushing process for different external conditions and indicate well the influence of the inflow discharge q for otherwise-identical conditions. Cases with no freshwater inflow (i.e. $q = 0$, Figure 7(a)), are characterised by a rapid filling of the pool over the first few tidal cycles. The brackish layer increases in thickness δ to fill the full flow depth, resulting in a near-homogeneous water column of density excess $(\Delta\rho)_m$ close to that of the undiluted saline water (i.e. $\rho\prime = (\Delta\rho)_m/(\Delta\rho)_0 \sim 1$). By contrast, cases with high freshwater inflow q (i.e. Figure 7(c) and (d)) show weaker intrusion resulting from increased mixing, which in turn inhibits the formation of a clearly-defined near-bed brackish pool. During the ebb phase of the tidal cycle, this high magnitude freshwater inflow typically flushes out a large proportion of the well-mixed brackish fluid from behind the barrier. Indeed, experimental findings suggest that the non-dimensional inflow parameter $q/(g'H_b^3)^{1/2}$ is dominant in determining the temporal development of the brackish layer behind the barrier, while parameters associated with the downstream tidal conditions (i.e. h_s/h_b, H_α/h_b and $g'\tau_\alpha^2/h_b$) are of secondary importance, at least for the range of parameters considered here.

The brackish water pool thickness $\delta(X_j, t)$ is again defined arbitrarily in terms of the elevation of a specific density excess contour representing the upper edge of the intruded layer at a given measurement station X_j (e.g. $\rho' = (\rho - \rho_0)/(\Delta\rho)_0 = 0.4 \rightarrow \delta_{0.4}(X_j, t)$). Composite dimensional time-series plots of the tidally-averaged brackish layer thickness $\delta_{0.4,ave}$ (which is spatially-averaged over four measurement locations X_j) are plotted in Figure 8 for different values of q, g' and h_b. These reveal the systematic reduction in $\delta_{0.4,ave}$ values for increasing values of q. This plot also indicates that

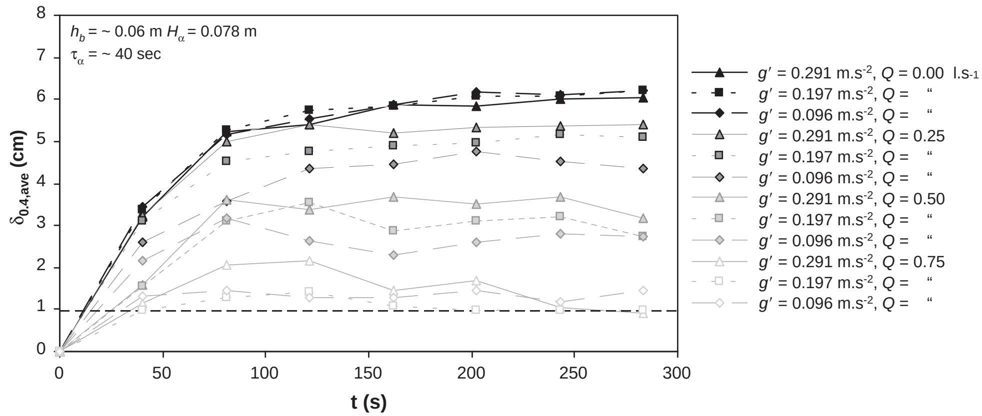

Figure 8. Tidally-averaged plots of $\delta_{0.4}$ versus t for h_b, H_α, g' and Q values shown.

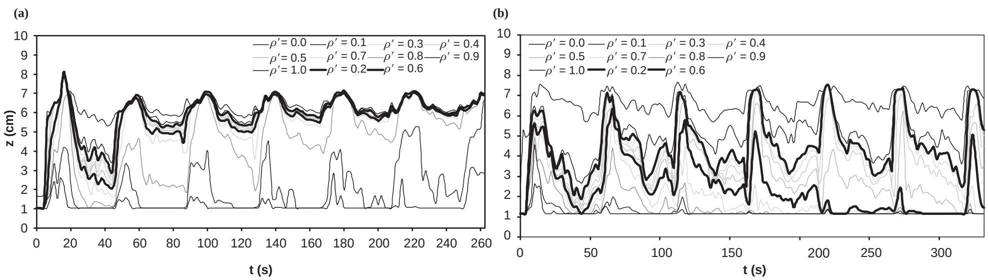

Figure 9. Time series of density contours ρ' for $q/(g'h_b^3)^{1/2} : g'\tau_\alpha^2/h_b =$ (a) $0 : 8230$ and (b) $0.123 : 13000$.

larger values of g' (for otherwise identical conditions) are generally associated with increased values of $\delta_{0.4,ave}$.

Two mixing mechanisms are postulated to operate within the flow, on different time scales. Firstly, significant mixing occurs as a result of turbulent entrainment of fresh and brackish water into the descending plume of denser saline water as it intrudes over the barrier at high tide. This process dominates when the freshwater outflow q is weak and the thickness δ of the intruded pool is small (i.e. the descent distance for the intruding plume is a maximum). This process would therefore be expected to weaken with time t as the pool fills and the descent distance diminishes. The second mechanism for mixing is the shear-induced entrainment between the upper layers of the brackish water pool and the overlying fresh water outflow. In contrast to the first mechanism, this process is expected to dominate when q is high and when the thickness δ of the brackish water pool is sufficiently large (i.e. after a number of tidal cycles) for the brackish water to be "eroded" and expelled by the freshwater discharge.

Time series plots of density contours for weak and strong freshwater outflows (Figure 9(a) and (b), respectively) appear to validate this conceptual mixing model. In the former case ($q = 0$; Figure 9(a)) the thickness of the interface between the brackish and freshwater layers (defined here by the difference in elevation between the $\rho' = 0.2$ and 0.6 contours, i.e. $\delta_{0.2} - \delta_{0.6}$) is largest after the initial tidal intrusion and decreases significantly with time t as the brackish layer thickness increases with time t. This provides clear evidence for the enhanced mixing between the intruding saline plume and receiving waters in the early stage of the exchange. By contrast, time series plots for a high magnitude inflow q (Figure 9(b)) reveal that the thickness of the brackish water pool and

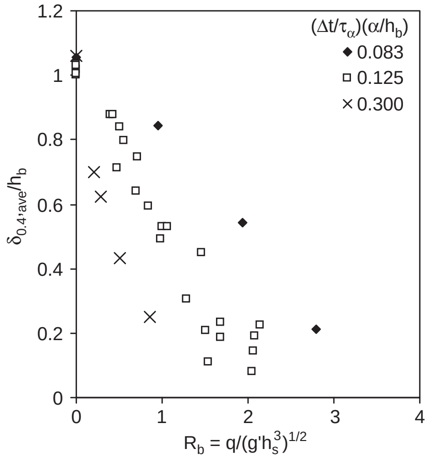

Figure 10. Non-dimensional plot of $\delta_{0.4,ave}/h_b$ versus the modified estuarine Richardson number R_b for values of $(\Delta t/\tau_\alpha)(H_\alpha/h_b)$ shown.

the interface thickness $(\delta_{0.2} - \delta_{0.6})$ increase significantly with time t. This is clearly indicative of upper surface mixing by shear-induced entrainment into the high fresh water flow q.

Within unblocked estuaries the *estuarine Richardson number R* is commonly used to measure the degree of turbulent mixing between the outflowing fresh water layer and the underlying saline water intrusion or *wedge*. This is generally defined as the ratio of buoyancy input from the fresh water inflow Q to the kinetic energy input from the tide (Fischer, 1979) such that $R = g'Q/(BU_t^3)$, where B is the channel width and U_t is the r.m.s. tidal velocity. In the presence of a tidal barrier, it may be hypothesised that U_t across the barrier crest may be represented by $k(g'h_s)^{1/2}$ (k being a numerical coefficient) and a modified *blocked* estuarine Reynolds number R_b given by $q/(g'h_s^3)^{1/2}$. This modified estuarine Reynolds number takes account of the contribution both from fluvial and tidal forcing. Figure 10 shows the tidally-averaged brackish layer thickness $\delta_{0.4,ave}/h_b$ plotted versus R_b for three groups of a dimensionless parameter $(\Delta t/\tau_\alpha)(H_\alpha/h_b)$, where $(\Delta t/\tau_\alpha)$ represents the relative time per tidal cycle over which the saline intrusion occurs and (H_α/h_b) is the relative tidal amplitude. This plot suggests that for a given brackish layer thickness $\delta_{0.4,ave}/h_b$, downstream tidal forcing becomes more significant (i.e. lower $q/(g'h_s^3)^{1/2}$ values) when the parameter $(\Delta t/\tau_\alpha)(H_\alpha/h_b)$ increases (i.e. larger relative intrusion times or tidal amplitudes).

3 SUMMARY AND CONCLUSIONS

The model studies reveal a range of different processes that can affect the hydrodynamic exchanges associated with natural or man-made barriers that restrict the flushing of open estuary environments. Turbulent mixing is seen to be influential throughout the transient adjustment of the flow, with turbulent entrainment and shear-induced overturning processes being dominant respectively during different phases of the flow development. Simple dimensional analysis is seen to produce useful functional relationships for these exchange processes.

ACKNOWLEDGEMENTS

The authors acknowledge the support provided for this work by the UK Engineering & Physical Sciences Research Council (EPSRC). As the reference list below indicates, much of the work reviewed in this paper was done in collaboration with Dr Mike Coates (Deakin University, Australia)

and Dr Yakun Guo (now University of Aberdeen, UK). Both individuals played important roles in the development of our understanding of exchange flows.

REFERENCES

Burt, N & Rees, A (eds), 2001. *Guidelines for the Assessment and Planning of Estuarine Barrages*, Thomas Telford Publishing, London, UK.

Coates, M J, Guo, Y & Davies, P A, 2001. Laboratory model studies of flushing of trapped salt water from a blocked tidal estuary. *J. Hydraulic Res*., 39, 6, 601–609.

Crompton, J, 2002. Cardiff Bay barrage. *Proc. Instn Civil Engrs, Water & Maritime*, 154, 81–88.

Cuthbertson, A J S, Davies, P A, Coates, M J & Guo, Y, 2004. A modelling study of transient buoyancy-driven exchange flow over a descending barrier. *Environm. Fluid Mech*., 4, 127–155.

Donnelly, B, Hamill, G A, Robinson, D J, MacKinnon, P & Johnston, H T, 2000. Interfacial layer development due to turbulent mixing at a density interface. *Proc. 5th Int'l. Sympos. Stratified Flows* (eds G A Lawrence, R Pieters & N Yonemitsu), University of British Columbia, Vancouver, 2000, Vol. II, 853–858.

Environmental Hydraulics and Sustainable Water Management – Lee & Lam (eds)

The interface smoothness criteria and its application for two layer flow from a circular weir

Ian R. Wood
Civil Engineering, University of Canterbury, Christchurch, New Zealand

ABSTRACT: The general equation for the energy difference between two flowing layers is derived. For a circular weir the gradually varied velocity near the free surface is matched with the spherical velocity distribution. For a single layer this implies the velocity in the layer flowing is self-similar and using the energy difference equation and the condition of interface smoothness give the critical flow. This discharge is then matched with the weir discharge. When two layers are flowing we use the critical flow for a single layer and assuming the density differences are small when the both layers are flowing this discharge is constant. When the interface is above the critical interface we require the interfaces to be smooth. We then use both the differential of both the energy difference equation and the equation at the free surface to determine the ratio of the discharge in the lower to the total discharge.

1 INTRODUCTION

For a circular weir and for a particular two layer stratification we wish to know the discharge from each layer. In this case there are two controls. The discharge control is complicated with curvature of the streamlines and the rating curve is normally determined by model studies. Away from the discharge control where the curved streamlines are important there is zero velocity in the lower layer we can use the spherical distribution matched with the uniform distribution of the gradually varied flow assumption and then use the steady state Bernoulli equation. We can either maximize the discharge or determine the conditions when the interface becomes tangent to the upstream face of the weir to determine the critical layer depth.

When two layers are flowing the second control (sometimes called the virtual control) is also in the region away from the curved streamlines and in this region we can make reasonable velocity assumptions and then using the two steady Bernoulli equations and differentiating them with respect to distance and obtain the expression for the surface slope. The smoothness condition leads to the calculation for control surface and matching the flow with weir discharge determines the discharge from the lower layer. We assume that this must be maximized. It is important to note that the theory considers steady flow only and these would be difficult to obtain in any practical situation. However the theory should be satisfactory provided the reservoir is sufficiently large that the time for a particle to travel between the controls is short compared to the time for changes in levels of the interface.

2 THE ENERGY DIFFERENCE EQUATION

Before looking at the specific flows it is appropriate to look at the equations at an interface which has a sharp density change. The case considered is illustrated in Figure 1. Above this velocity, density, potential energy and pressure are A_1, v_1, ρ_1, PE_1 and p_1 and below this interface variable are sub-scripted 2. Applying the Bernoulli equation for a steady flow between the flow and the infinite

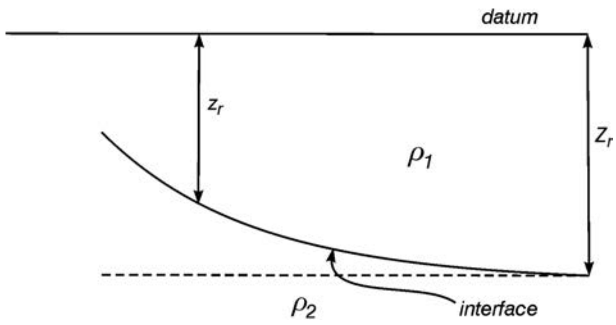

Figure 1. The nomenclature for energy difference equation.

reservoir we get on the upper side of the interface and the lower side of the interface we get

$$\begin{aligned}\frac{1}{2}\rho_1 v_1^2 + PE_{1r} + p_{nr} = PE_{1,r=\infty} + p_{r=\infty}\\ \frac{1}{2}\rho_2 v_2^2 + PE_{2,r} + p_{nr} = PE_{2,r=} + p_{r=\infty}\end{aligned} \tag{1}$$

We define I_t as ρ_1/ρ_2 and z_r and Z_r as the level of the interface at r and at infinity and assuming the velocity is constant at any r within each layer we can remove the pressure by subtracting the equation for the upper and the lower layer and scaling with Z_r we get

$$\frac{1}{2}\frac{q_2^2}{gA_2Z_r} - \frac{1}{2}I_t\frac{q_1^2}{gA_1Z_r} = (1-I_t)(-1+z_r') \tag{2}$$

where q_1 and A_1 and q_2 and A_2 are the discharges and area in the upper and lower layer. It is notable that this equation is not dependant on the hydrostatic assumption. The form of equation (3) is the same as used by Dalziel (1991) Armi(1986) and Lane-Serff (2000) and is sometime called the internal energy equation. (It is however the energy difference between the two layers). The smoothness criteria requires the differential of the equations

$$-\frac{q_2^2}{gA_2Z_r}\frac{1}{A_2}\frac{dA_2}{dr} + I_t\frac{q_1^2}{gA_1^2Z_r}\frac{1}{A_1}\frac{dA_1}{dr} = (1-I_t)\frac{dz_r'}{dr} \tag{3}$$

Defining

$$\omega' = \frac{q_q^2}{gA_1^2Z_r}, \quad \frac{v_2}{v_1} = v_{21}, \quad \frac{q_2^2}{gA_2^2Z_r} = v_{21}^2\omega' \tag{4}$$

And the energy difference becomes and differential energy equation become

$$\frac{1}{2}v_{21}^2\omega' - \frac{1}{2}I_t\omega' = (1-I_t)(-1+z_r') \tag{5}$$

And differential energy equation becomes

$$-v_{21}^2\omega'\frac{1}{2}\frac{dA_2}{dr} + I_t\omega'\frac{1}{A_1}\frac{dA_1}{dr} = (1-I_t)\frac{dz_r'}{dr} \tag{6}$$

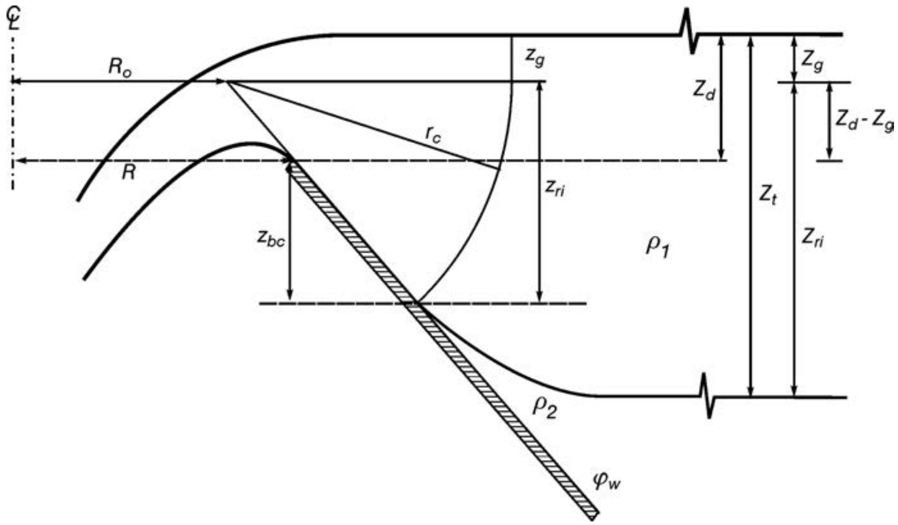

Figure 2. The nomenclature for the case of the critical flow for a single layer flowing over a circular weir with a sloping upstream face.

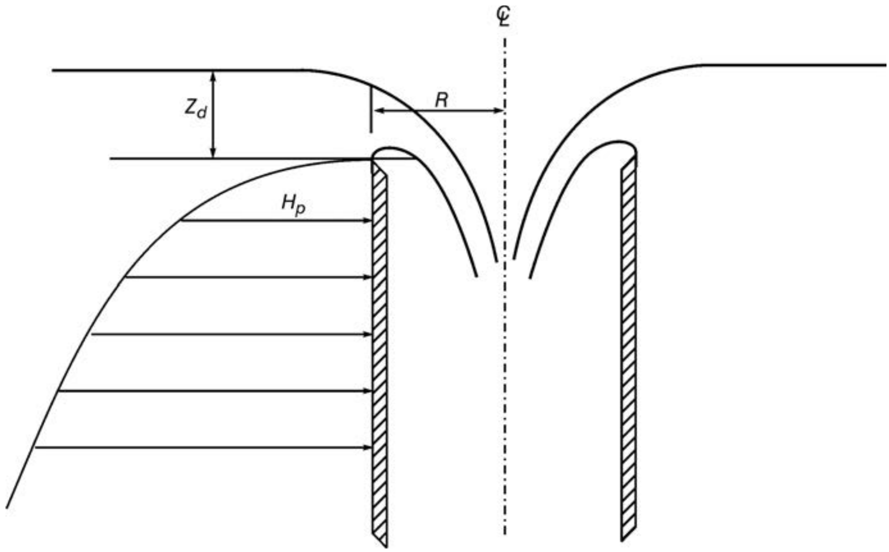

Figure 3. The flow over weir and the pressure distribution on the upstream face.

3 THE SINGLE LAYER FLOW WITH A SPHERICAL VELOCITY DISTRIBUTION

For any particular radius (R) and weir angle (φ_w) the critical discharge will depend on the depth of the interface below the crest. This is illustrated in Figure 2. For any flow, the outlet characteristics of weir is the first control and determines the discharge. For the case of two dimensional weir when the upstream face of the two dimensional weir is vertical. Figure 3 illustrates the pressure distribution on the vertical face (Reid and Rouse 1935). Close to the crest there is a region were the flow feels the zero pressure at the crest and the curvature of the streamlines at the weir and this will pull the interface over the crest. We assume that when R is finite this pattern of pressure does not change. When the flow is from layer above a stationary layer then for the critical flow there is a second control and we assume that is beyond the influence of the pressure at the crest. This control is where the interface intersects the upstream face of this weir. We assume that there is an origin on the extension of the upstream face of the circular weir, but the position of this origin will be determined later. At the origin, we consider a horizontal plane and define this level as a datum. Below this datum we define a radius, r, and the angle from the horizontal to the downstream face of the weir, φ_w and upstream of the contact with the interface the angle is φ_i. At the control point the interface becomes tangent to the wall and hence φ_i equals φ_w and r equals r_c. Upstream of the point of contact we assume that portion of the flow next to the surface is gradually varied and below this the velocity vectors are radial. We further assume that the division level between the gradually varied region and the radial velocity region is at the datum. (The horizontal datum enables the matching of the velocity and the gradient of the velocities at the junction of the two regions). We assume there is no mixing and hence the density along any streamline is constant and thus the ratio of the discharge in the gradually varied region to the discharge in the radial velocity region does not change with r. This assumption is an extension of the classic assumption used by Craya (1949).

The gradually flow region is z_g above the datum and below the datum the vector is radial. z_{ri} is the vertical distance from a point on the curve ob in the region where the flow is radial to the datum. z_s is the vertical distance from the free surface at any point along the curve ab and z_t is the sum of z_g and z_{ri}. When r equals infinity then the value of the gradually varied region, radial region and the total depth are Z_g, Z_{ri} and Z_t. For the single layers at the level of the interface at infinity the pressure are hydrostatic thus

$$I_t z'_g + z'_{ri}\left(I_t - 1\right) = I_t Z'_g + \left(I_t - 1\right) \tag{7}$$

This can be satisfied if

$$z'_g = z'_{ri}\,\frac{\left(1 - I_t\right)}{I_t} \qquad Z'_g = \frac{\left(1 - I_t\right)}{I_t} \tag{8}$$

And

$$A'_1 = 2\pi\int_0^{\varphi_i}\left(R'_0 + r'\cos\varphi\right)r'd\varphi + 2\pi\left(R'_o + r'\right)z'_g \tag{9}$$

Using equation (8) we get

$$A'_1 = 2\pi\left[r'R'_o\left(\varphi_i + \sin\varphi_i\right)\frac{\left(1 - I_t\right)}{I_t} + \frac{r'^2}{I_t}\sin\varphi_i\right] \tag{10}$$

substituting into the area into equation 6 with v_{21} as zero we get

$$+2\left(1 - I_t\right)\left(1 - r\sin\varphi_i\right)\left[\frac{\partial A'_1}{\partial r'} + \frac{\partial A'_1}{\partial\varphi_i}\frac{d\varphi_i}{dr'}\right] = A'_1\left(1 - I_t\right)\sin\varphi_i + A'_1\left(1 - I_t\right)r'\cos\varphi_i\,\frac{d\varphi_i}{dr'} \tag{11}$$

when φ_i is φ_w and $d\varphi_w/dr$ equals zero then equation 11 gives the expression for the control radius r'_c and noting that z'_c is $r'_c \sin\varphi_w$ we get

$$5z_c'^2 + z'_c\left[3R'_o\,\frac{\left[\left(1 - I_t\right)\sin\varphi_w - \varphi_w\right]}{\left(2 - I_t\right)} - 4\right] - 2\left[R'_o\,\frac{\left(1 - I_t\right)\sin\varphi_w - \varphi_w}{\left(2 - I_t\right)}\right] = 0 \tag{12}$$

This is a quadratic equation and using its solution we calculate the discharge as a function of z'_c and this with the normal weir equation for the main control.

$$q_{tc} = 2\pi(2g)^{\frac{1}{2}} \frac{2}{3} C R'_o \left(Z'_d\right)^{\frac{3}{2}}$$
$$= 2\pi(2g)^{\frac{1}{2}} \left[r'_c R'_o \left(\varphi_w + \sin\varphi_w \frac{(1-I_t)}{I_t} \right) + \frac{r_c'^{2}}{I_t} \sin\varphi_w \right] \left(\frac{(1-I_t)}{I_t} \right)^{\frac{1}{2}} (1-z'_c)^{\frac{1}{2}} \tag{13}$$

This give us the for Z'_{dc} .The value of C for a two-dimensional vertical weir is approximately 0.611. Senturk (1994) showed that the difference between a circular weir and the two dimensional weir is small. The USBR model experiments show that for a two dimensional weir the difference between the C for a vertical upstream face and a 45 degrees face is very small (Chanson 1999) and we will assume that differences are small for φ_w of $\pi/2$ and $3\pi/8$. This equation allows us to calculate Z_{dc}/Z_r for a range of angles.

When φ_w is $\pi/2$ the origin is vertically above the upstream face of the weir crest (Figure 2). Taking a new datum as the free surface at r equals infinity (Z'_{dc}) the origin for r is Z'_g below this. The crest is $Z'_{dc} - Z'_g$ below the r′ origin. When φ_w is less than $\pi/2$ the origin is obtained extending a distance r_c along the upstream face of the weir (Figure 2b). We then use an iterative process to determine the real R_o. We initially assume that R_o equal R. Calculating the value of r_c and Z_{dc}, and taking an origin Z'_{dc} (the origin for r is Z'_g) and the vertical position of the crest of the weir below the r datum we have the values of $Z'_{dc} - Z'_g$. Thus the new estimate of R'_o is $(Z'_{dc} - Z'_g)\cot \varphi_w$. If this is less zero there is no solution, otherwise we repeat until the value of R'_o converges. It remains to check whether the distance from the crest interface to the lower layer intersection with the upstream face (Figure 2 z_{bc}) for the assumed velocity to be reasonable.

4 THE TWO LAYER FLOW

For the case when the density difference is constant above the interface and a defined depth below the interface ($Z_{ri} + Z_g$) have determined the depth above the weir crest (Z_{dc}) and the critical discharge (q_{tc}) such that there was no flow below the interface. We now consider the case density difference between the layers is small and thus when the depth of the interface is decreased the discharge is then unchanged. For this critical discharge (q_{tc}) and we want to determine the ratio of flow from the lower layer to the total discharge as the depth of the interface below the free surface at infinity decreases. We assume that the upper flow may be divided into a region of gradually varied flow and radial flow as Figure 4 and it is noted that at infinity the depth of the upper layer tends to a finite value where as the depth of the lower layer tend to infinity. This implies that at infinity a finite velocity in the upper layer and zero in the lower layer and thus at infinity interface Z'_g is $(1 - I_t)/I_t$.

In the second layer there is a step change in the velocity magnitude. The flow is still radial and at the upstream face of the weir the flow direction is φ_w. In this case we need to use the free surface and the interface equations and consider only the virtual control (the second control) far upstream from the region where the streamline curvature affects the control. We scale with the new value of Z_r and the area of the flows are

$$\begin{aligned} A'_1 &= A'_{1r} + A'_{1g} = 2\pi\left(r' R'_o \varphi_i + r'^{2} \sin\varphi_i\right) + 2\pi\left(R'_o + r'\right)\varphi_i z'_g = F_1\left(r', \varphi_i, z'_g\right) \\ A'_2 &= 2\pi r'^{2}\left(\sin\varphi_w - \sin\varphi_i\right) = F_2\left(r', \varphi_i\right) \end{aligned} \tag{14}$$

Now it is worth noting that an infinity the depth of the upper layer tends to a finite value where as

$$\frac{1}{2}\frac{q_1^2}{gA_1^2} + z_g = Z_g \quad \frac{1}{2}\omega' + z'_g = \frac{I - I_t}{I_t} \tag{15}$$

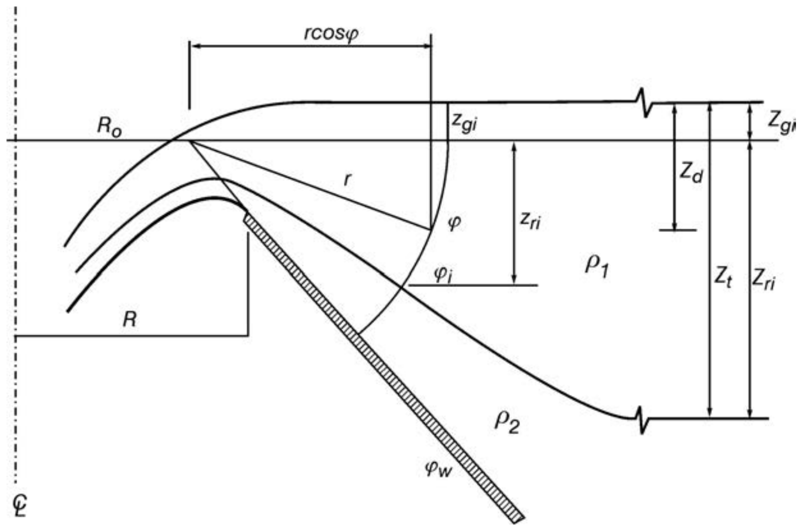

Figure 4. The nomenclature for the case of two layers flowing over a circular weir with a sloping upstream face.

Differentiating equation (15) we get the equation

$$+\left[-\omega'\frac{\partial A_1'}{\partial z_g'}+A_1'\right]\frac{dz_g'}{dr'}-\omega'\frac{\partial A_1'}{\partial \varphi_i}\frac{d\varphi_i}{dr'}=\omega'\frac{\partial A_1'}{\partial r'} \tag{16}$$

using equation 7 for the lower layer and noting that z'_{ri} is $r'\sin\varphi$ and inserting this into equation 6 we get

$$+I_t A_2'\frac{dz_g'}{dr'}+\left[-\nu_{21}^2\omega'\frac{\partial A_2'}{\partial \varphi_i}-(1-I_t)A_2' r'\cos\varphi_i\right]\frac{d\varphi_i}{dr'}=A_2\,(1-I_t)\sin\varphi+\nu_{21}^2\omega'\frac{\partial A_2'}{\partial r} \tag{17}$$

The coefficient of equations 16 and 17 are written as A_1, B_1 and C_1 and A_2, B_2 and C_2 and thus the slope of the interfaces are

$$\frac{d\varphi_i}{dr'}=\frac{A_2C_1-A_1C_2}{A_2B_1-B_2A_1}=\frac{D_1}{D_0}\qquad \frac{dz_g'}{dr'}=\frac{B_1C_2-B_2C_1}{A_2B_1-B_2A_1}=\frac{D_2}{D_0} \tag{18}$$

Now for all cases when r tends to infinity, D_0 tends to $1 - I_t$ and it is reasonable to assume that the form of the value of D_0 as in Figure 5. Thus, for these interfaces to be finite, when D_0 equals zero then both D_1 and D_2 also equal zero. When D_0 equals zero we get

$$+\nu_{21}^2\omega'\frac{\partial A_2'}{\partial \varphi_i}\left[-\omega'\frac{\partial A_1'}{\partial z_g'}+A_1'\right]=\left[+I_tA_2'\right]\left[\omega'\frac{\partial A_1'}{\partial \varphi_i}\right]-(1-I_t)\,A_2' r'\cos\varphi_i\left[-\omega'\frac{\partial A_1'}{\partial z_g'}+A_1'\right] \tag{19}$$

And when for D_1 equals zero we get

$$\nu_{21}^2\omega'\left[-\omega'\frac{\partial A_1'}{\partial z_g'}+A_1'\right]\frac{\partial A_2'}{\partial r'}=+I_tA_2'\omega'\frac{\partial A_1'}{\partial r'}-\left[-\omega'\frac{\partial A_1'}{\partial z_g'}+A_1'\right]\left[A_2(1-I_t)\sin\varphi_i\right] \tag{20}$$

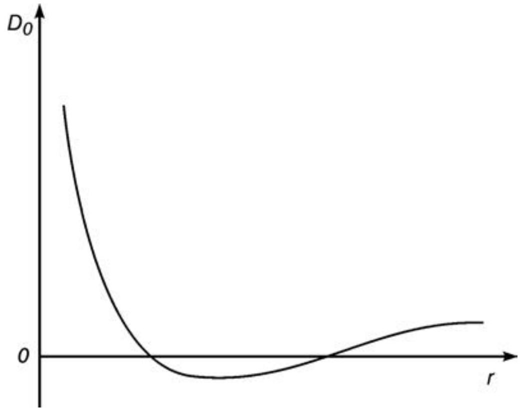

Figure 5. The variation of D_0 with r.

Equating we get

$$+I_t\omega'\left[\frac{\partial A_1'}{\partial\varphi_i}\frac{\partial A_2'}{\partial r'}-\frac{\partial A_1'}{\partial r'}\frac{\partial A_2'}{\partial\varphi_i}\right]$$
$$+(I-I_t)\left(-\omega'\frac{\partial A_1'}{\partial z_g'}+A_1'\right)\left[-r'\cos\varphi_i\frac{\partial A_2'}{\partial r'}+\sin\varphi_i\frac{\partial A_2'}{\partial\varphi_i}\right]=0 \qquad (21)$$

Now A_2' and its partial differentials are function of r' and φ_i. Similarly the partial differential of A_1' with z_g' are functions of r' and φ_i. However A_1' and the rest of its partial differentials are functions of z_g'. Equation 15 is used to obtain z_g' as a function ω' and we get after some algebra a quadratic equation in ω', and for any given ϕ_i this determines the smoothness criteria when D_0 and D_1 equal zero. For any R' and ϕ_w, we choose φ_i and can then obtain a solution for ω' as a function of r'. We then return to the either expression for v_{21} and obtain the equation for

$$\frac{q_w^2}{gZ_r^5}=A_2^2 v_{21}\omega_v' \qquad (22)$$

So far we have used the condition of smoothness and determined the virtual control and the ratio of the discharge above the interface and below it and with the Boussinesq approximation to calculate value of q_2/q_t. Hence for a given φ_w, I_t and R, we get ω' as a function of r_v' and ϕ_i. For each φ_i equation 22 with some algebra gives a plot of q_2'/q_t' as function of r_v'.

For the case when φ_w is $\pi/2$, R is 1.0 m, the depth below the free surface is 1.0 m and I_t is 0.98 the calculations in equation (13) gives the free surface height above the weir crest as 0.4483 m (Z_{dc}). We define a constant values of C_t ($Z_t/Z_{tc}=Z_r/Z_{rc}$) and using the smoothness equation (21) and (22) and assumption of constant discharge we get q_2'/q_t' as function of r_v' (Figure 6a) for a range of these constant values of C_t. This Figure shows that when φ_w is $\pi/2$ for each constant value of C_t there is a maximum of $q_2'/q_{t,}'$ and this maximum value determines the solution. Figure 7 shows the function of q_2'/q_t' at this maximum as a function of C_t (Z_t/Z_{tc}). For the same geometry when I_t is 0.93 the calculations in gives the free surface height above the weir crest as 0.6676(Z_d) and solutions which are negligibly different from Figures 6 and 7. This is not surprising as it infers that the major effect of the density differences ($1-I_t$) is accounted for by the determination of the critical discharge.

The most interesting portion of Figure (6a) is the step jump from the case when there is no flow in the lower layer to the solution q_2'/q_t' when C_t is 0.98. This is not surprising as the streamlines for

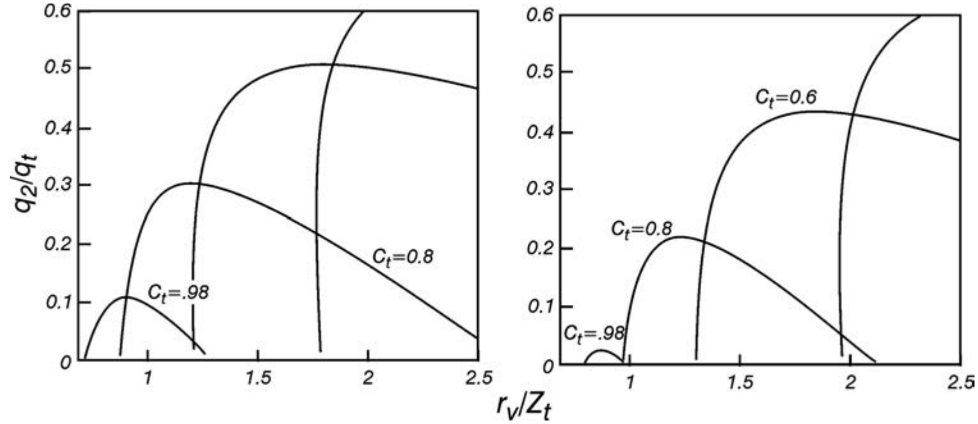

Figure 6. When R and the interface depth are 1.0 metre and I_t is 0.98 the smoothness criteria yields q_2'/q_t' as function of r_v' for a range of values C_t (Z_t/Z_c). Figure 6a is the case with ϕ is $\pi/2$ and the critical calculations give the free surface height above the weir crest as 0.4483 metres and Figure 6b is the case when ϕ_w is $3\pi/8$ and the critical calculations give the free surface height above the weir crest as 0.3905 metres.

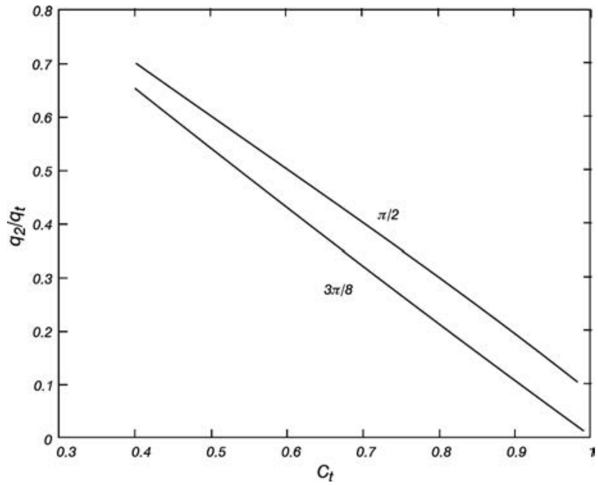

Figure 7. The final values of q_2'/q_t' as a function of C_t (Z_t/Z_{tc}) for the case when R is 1 m and ϕ_w is $\pi/2$ and $3\pi/8$. It is notable but not surprising that the small variation in the density ratio (I_t) is negligible.

the critical flow and the start of the flow from the lower layer are distinctly different. Figure (6a) also shows that the value r_v' at the maximum of q_2'/q_t' increases as the value of C_t decreases. Thus the distance between the discharge control and the virtual control increases and this may be important as the time for a particle to travel between the virtual control and the crest increases the steady solution may become invalid.

For the case when φ_w is $3\pi/8$, R is 1.0 m, the depth below the free surface 1.0 m and I_t is 0.98 the calculations from equation (13) gives the free surface height above the weir crest as 0.3905 m (Z_d). For smoothness condition we get for a range of value the graphs of C_t as function of r_v' in Figure 5b. Figure 6b for φ_w equal to $3\pi/8$ then gives the maximum of q_2'/q_t' as a function of C_t. The difference between the Figures 6a and Figure 6b is remarkable in that with the smaller slope of the upstream face of the weir there is no longer a major step change between the critical flow and the small flow coming from the lower layer. In this case the total discharge is the same as the critical discharge (q_c) and the equation in Figure 7 can be written as

$$\frac{q_2'}{q_c'} = 1 - C_t = 1 - \frac{Z_t}{Z_{tc}} \tag{23}$$

This implies that if we know the depth at infinity for the critical discharge (Z_{tc}) then for any lesser depth (Z_t) then we can obtain the proportion from the lower layer. This is not surprising as the density differences between the layers are small and flow behaves as if was of a uniform density.

5 CONCLUSIONS

The selective withdrawal of a surface layer of small density difference from a circular weir the most important variable is the critical discharge .When the upstream face of the weir is vertical there is a sharp change between the critical discharge and when there is flow from the lower layer and this must cause instabilities and may be avoided with a weir with a sloping upstream face.

ACKNOWLEDGEMENTS

The author would like to thank Mr. Choo of Lincoln University, Christchurch who drew my attention to this area of research and Dr Law of Nanyang Technology University, Singapore for encouragement me to continue with this work.

REFERENCES

Armi, l. 1986. The hydraulics of two flowing layers with different densities. *J. Fluid Mech.*, v163, 27–58.

Chanson, H. 1999. The hydraulics of open channel flow. Arnold Press.

Dalziel, S.B. 1991. Two Layer Hydraulics: a function approach. *J. Fluid Mech.*, v223, 135–163.

Lane-Serff, G.F, Smeed, D.A. and Postlethwaite, C.R. 2000. Multilayer exchange flows. *J. Fluid Mech.*, v416, 269–296.

Imberger, J. 1980. Selective withdrawal: a review. *Second International Symposium on Stratified Flows*, The Norwegian Institute of Technology, Trondheim, Norway, v1, 381–400.

Lawrence, G.A. and Imberger, J. 1979. Selective withdrawal through a point sink in a continuously stratified fluid with a pynocline. Report No ED-79-002 Environmental Dynamics, Department of Civil Engineering, University of Western Australia, Nedlands, Australia.

Ray, N.W. 1973. Some studies in stratified fluid flow. Water Research Laboratory, University of New South Wales, Manly Vale, NSW, Australia. No. 136.

Reid, L. and Rouse, H. 1935. Model research on spillway crests. *Civil Engineering*, v5(1).

Senturk, F. 1994. Hydraulics of dams and reservoirs. *Water Resources Publications*, Highland Ranch, Colorado, USA.

Wood, I.R. 1968. Selective withdrawal from a stably stratified fluid. *J. Fluid Mech.*, v32, 209–223.

Wood, I.R. 1978. Selective withdrawal from a two-layer fluid. *J. Hyd. Div*. ASCE, v104, HY12, 1647–1659.

This page intentionally left blank

Environmental Hydraulics and Sustainable Water Management – Lee & Lam (eds)
© 2005 Taylor & Francis Group, London, ISBN 04 1536 546 5

Water quality management of river and estuarine waters

R.A. Falconer & B. Lin
School of Engineering, Cardiff University, Cardiff, Wales, UK

ABSTRACT: Details are given herein of the limitations of physical and numerical models in predicting water quality indicator levels in river and estuarine waters and with particular emphasis being focused on faecal coliform levels. On-going research studies to improve on the predictive capabilities of such models for coliform and nutrient loadings are outlined, incorporating field, experimental, and computational hydraulics and hydroinformatics modeling techniques. Three case studies are cited, including: (i) Cardiff Bay, a freshwater body where dynamic decay rates were found to be significant, (ii) the Ribble Estuary, where diffuse source pollution was found to be significant during storm conditions, and (iii) the Severn Estuary, where bacterial-sediment interactions were found to have a key impact on compliance of bathing waters with the European Union Bathing Water Directive.

1 INTRODUCTION

In recent years there has been a growing global effort to address issues relating to water quality in river and estuarine waters. For example, in the U.K. much effort and expenditure has been focused on treating domestic and industrial effluent waste, with a view to reducing to a minimum the discharge of storm water overflows into riverine waters. As a result the water quality of many major rivers, e.g. the Thames, has improved considerably in recent years and aquatic life is once again thriving in numerous river and estuarine waters. In most cases the challenge to clean up river and estuarine waters has been driven by legislation, e.g. in Europe by EU Directives, such as the Bathing Water Directive, the Habitats Directive and, more recently, the Water Framework Directive. In connection with such water quality concerns and legislative requirements engineers and scientists have now been involved for some time in a range of hydroenvironmental impact assessment studies for water quality management. Typical causes of concern to engineers and scientists involved in improving river and estuarine water quality include, for example: (i) sewage discharges of untreated effluent, either directly or from storm water overflows, (ii) industrial and chemical waste from factories alongside rivers and estuaries, (iii) animal waste, either in the form of point sources from intensive husbandry or aquaculture, or diffuse source inputs from land or rivers, (iv) fertilizers from crop farming, and (v) other less obvious forms of impediment to good water quality. Such other forms of water quality impediment might include: increased temperatures from cooling water discharges, increased saline levels (or brine) discharged from desalination plants, high turbidity levels due to storms, and changes in the flow regime due to natural or human intervention with the geometric or bathymetric boundary conditions.

Over the past two or three decades there has been an increasing emphasis placed on using computational hydraulics and hydroinformatics tools, rather than physical modelling facilities, for predicting flow, water quality, sediment and contaminant transport and morphological processes in river and estuarine waters. This increased enthusiasm for using numerical and hydroinformatics models has occurred for a number of reasons; primarily due to problems associated with physical models such as: scaling, expense, transportability and adaptability. For further details see Falconer & Lin (2003). However, although computational hydraulicians have placed considerable emphasis on predicting the hydrodynamic processes with increasing levels of sophistication in river and estuarine waters, many of the bio- and geo-chemical processes are still often treated in a somewhat simplistic manner. In modelling numerically the flow and water quality indicator processes in river and estuarine waters, there are still a large number of uncertainties included in computational hydraulics models, and particularly with regard to the kinetic transformation rates and partitioning interactions between solutes and the bed sediments. The studies reported herein therefore focus on representing more accurately some of these complex kinetic and bio-geochemical processes.

In addition to the provision of brief details about the model, particular emphasis is focused herein on describing the refinements with regard to the kinetic transformation processes and the application of these developments to three site specific studies. The first two studies relate to refinements to the decay rate for faecal coliforms in Cardiff Bay, Wales, and the Ribble River Basin and Estuary along the North East coast of England. The third study, outlined briefly, relates to the partitioning and interaction between faecal coliform and heavy metals with the bed sediments in the Severn Estuary, with the basin again being sited in the U.K. The resulting field data acquired and the numerical model simulations have shown that the receiving water concentration predictions for coliforms, nutrients and heavy metals are all highly dependent upon the choice of constants and the formulation of complex kinetic and bio-geochemical processes.

2 HYDROENVIRONMENTAL MODEL DETAILS

2.1 *Hydrodynamic model*

The numerical models herein developed to predict the hydrodynamic features reported in the studies cited herein were set up to solve the 3-D Reynolds averaged Navier-Stokes (RANS) equations. Two 2-D/3-D models were used in these studies; the first being the Hydroenvironmental Research Centre's (HRC) own model, named TRIVAST (ThRee-dimensional layer Integrated Velocities And Solute Transport), which solves the layer averaged 3-D RANS equations (i.e. including the hydrostatic pressure assumption). Likewise, for the 2-D simulations the model DIVAST was used. These model are based on a regular finite difference grid solution in the horizontal plane and an irregular boundary fitting grid in the vertical plane. The models have been used extensively for coastal and estuarine studies, with further details of the 3-D model being given in Wu & Falconer (2000) and Lin & Falconer (2001). In extending either of these models well up any riverine basin, and where conditions could be adequately represented by a 1-D model, then the Centre's 1-D solver of the area integrated RANS equations – giving the St. Venant equations – was used, namely the FASTER (Flow And Solute Transport in Estuaries and Rivers) model. This model is again finite difference in form and further details are given in Falconer et al. (2001).

More recently the studies have been extended to use the HEMAT (Hydro-Environmental Model and Analysis Tool) model. This model has been primarily developed by the Water Research Centre in Iran, in collaboration with the HRC at Cardiff University. The model is ideally suited to predicting complex free-surface flows in estuarine and coastal basins, since it solves the 2-D RANS equations (including 3 types of turbulence models) and uses the finite volume method. Both second- and third-order accurate and oscillation free explicit numerical schemes are included in the model to solve the shallow water equations, together with an algorithm to predict for flooding and drying of inter-tidal regions. The model deploys an unstructured triangular mesh and incorporates two types of mesh layouts, namely the 'cell centred' and 'mesh vertex' layouts. A powerful mesh generator is also provided, which enables the user to adjust the mesh-size distribution interactively to create a desirable mesh. The quality of the mesh has been shown to have a major impact on the overall performance of the numerical model. Further details of this model are given in Namin et al. (in press).

2.2 *Water quality and sediment transport model*

In modeling numerically the flux of water quality indicator organisms, sediments or heavy metals etc. within river and estuarine basins, the conservation equation of a solute mass can first be derived in the general form for a 3-D flow field and then time averaged to give the following form of the equation for solution:

$$\frac{\partial \phi}{\partial t}+\frac{\partial \phi u}{\partial x}+\frac{\partial \phi v}{\partial y}+\frac{\partial \phi w}{\partial z}+\frac{\partial}{\partial x}\overline{u'\phi'}+\frac{\partial}{\partial y}\overline{v'\phi'}+\frac{\partial}{\partial z}\overline{v'\phi'}=\phi_s+\phi_d+\phi_k \tag{1}$$

where ϕ = time averaged solute (including suspended sediment and heavy metal) concentration; ϕ_s = source or sink solute input (e.g. an outfall); ϕ_d = solute decay or growth term; and ϕ_k = kinetic transformation rate for the solute.

The cross-produced terms $\overline{u'\phi'}$ etc. represent the mass flux of solute due to the turbulent fluctuations and are then layer (or depth or area) averaged to give a combined turbulent diffusion and longitudinal dispersion term. By analogy with Fick's law of diffusion, these terms are generally assumed to be proportional to the mean concentration gradient and with a positive flux being in the direction of decreasing concentration. For transport in the various directions the combined longitudinal dispersion and turbulent diffusion coefficient is often associated with the eddy viscosity (ε_t) through the Schmidt number, with typical values of the coefficient found to vary significantly depending upon the flow field and basin characteristics, see Fischer (1973).

In modelling faecal coliform (or similar) the decay in Equation (1) is generally expressed as a first order decay function in the form of the following formulation:

$$\phi_d = -k\phi \tag{2}$$

where k = coliform decay rate (day^{-1}), and with values of k being typically assumed to be a constant or a function of temperature. For hydroenvironmental management studies the decay rate is often expressed in terms of a T_{90} value, i.e. the time taken for 90% of the bacteria to die-off. The relationship between T_{90} and k is given as:

$$T_{90} = 24\log_e\left[\frac{10}{k}\right] \tag{3}$$

where T_{90} is the decay rate (hr), with values often varying from 0.5 hr to several days.

In modelling enteric bacteria in river and estuarine waters, as for heavy metals, faecal coliform can also be locked up in the sediments and in the studies reported herein the advective-diffusion equation (1) was first used to predict the depth averaged cohesive and non-cohesive sediment fluxes and concentrations. For the cohesive sediment transport flux the source term ϕ_s was equated to the net erosion-deposition, with resuspension and deposition rates being given by Sanford & Halka (1993). For the non-cohesive sediment transport flux the van Rijn (1984a,b) formulations were used to determine the bed load and suspended load concentrations. The corresponding source term in equation (1) was expressed in terms of the product of the particle settling velocity and the difference between the sediment concentration at a reference level 'a' above the bed and the equilibrium sediment concentration at the reference level 'a'. The reference level 'a' was assumed to be equal to the equivalent roughness height k_s, with a minimum value being given by: a = 0.01H – where H is the depth of the water column.

A new conceptual model has been developed for the interaction between enteric bacteria and the suspended and bed sediments (see Lei et al. 2004), with this model being further refined through current on-going studies. In developing new formulations of the link between enteric bacteria levels and suspended sediment concentrations in natural waters the following assumptions were first adopted: (i) that the adsorption of bacterial organisms to suspended solids takes place immediately; (ii) that there are enough suspended solids surfaces in the water column to provide living places for the bacterial organisms; and (iii) that within the water column the distribution of the suspended solids concentrations and bacterial populations are uniform along the water depth, therefore the bacterial populations absorbed onto the sediment surfaces are the same as that for

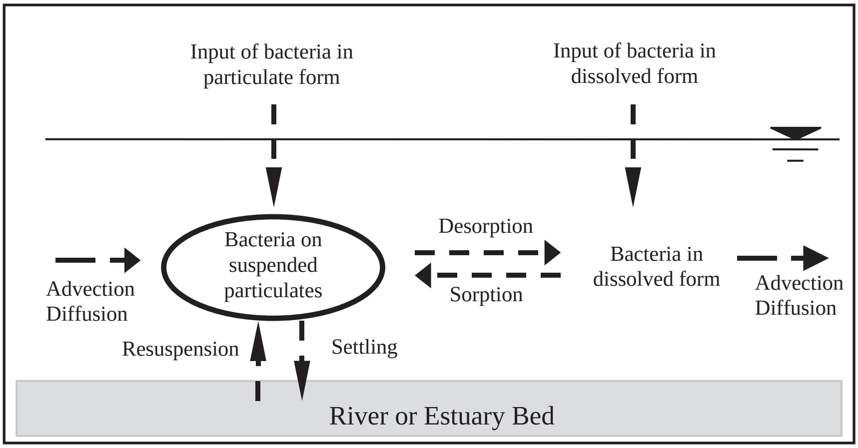

Figure 1. Schematic illustration of bacterial–sediment interaction in estuarine waters.

each unit of sediment concentration. In applying these assumptions and based on extensive field surveys the formulation for the source term in the advective-diffusion equation, expressed in a form enabling the enteric bacterial levels in the water column to be calculated, can be written as:

$$\Sigma \phi_s = -kC - \frac{dC_d}{dt} + \frac{dC_r}{dt} + \sum_{n=1}^{N} \frac{Q_o C_o}{A_o H} \tag{4}$$

where $\Sigma\phi_s$ source or sink term, including bacterial decay, deposition disappearance, entrainment from the bed and wastewater treatment outfalls etc; $C =$ depth averaged bacteria concentration (cfu/100 ml); $dC_d =$ loss of bacteria population due to deposition of the suspended solids during a time interval dt; $dC_r =$ bacterial population increase due to sediment resuspension in a time interval dt; $Q_o =$ outfall discharge (m^3/s); $C_o =$ outfall discharge concentration (cfu/100 ml); $A_o =$ horizontal discharge area (m^2); $H =$ water column depth (m); and $N =$ total number of outfalls. An example illustration of the bacterial–sediment interaction is illustrated in Figure 1.

3 HYDROENVIRONMENTAL MODEL DETAILS

3.1 *Cardiff Bay study*

The port of Cardiff was once one of Britain's largest international trading ports and has been through a period of decline since its heyday in the 1920s. Whole scale urban regeneration of the docks area was seen as the most appropriate means of regenerating the southerly part of Cardiff and a plan to construct a 1.4 km long tidal exclusion barrage across the mouth of Cardiff Bay was given Royal Assent in 1993. The barrage was designed to create a freshwater lake of 200 hectares, incorporating the rivers Taff and Ely, with 13 km of waterfront, enhancing opportunities for recreational water use and commercial and domestic development (see Figure 2).

In constructing the barrage and lock gate structures etc, across the mouth of the estuary, the impoundment of the two rivers and the change of the Bay from an estuary, with extensive flooding and drying, to a freshwater lake would have major changes on the hydroenvironmental management and water quality issues upstream of the impoundment. In particular, following impoundment the main water quality issues needing to be addressed can be summarized as follows:

- The Bay would now experience long retention times, whereas previously the estuary was well flushed with substantial tidal variations – up to 14 m during spring tides;

Figure 2. Photographic illustration of Cardiff Bay and Barrage and the rivers Taff and Ely.

- Several combined sewer overflows (CSOs) discharge directly into the watercourses under wet weather flow conditions, thereby leading to effluent discharges reaching the Bay;
- Nutrient and pathogenic inputs were expected in the form of diffuse source discharges from agricultural runoff etc, which in turn would flow via the rivers into the Bay; and
- Low dissolved oxygen levels were expected in summer, particularly in the lower layers of the water column, leading to stratification and interaction with contaminated sediments.

As a result of some of these concerns the Hydroenvironmental Research Centre at Cardiff University undertook a substantial on-going research study to refine and apply an integrated modelling tool for hydroenvironmental management of the Bay. The project strategy consisted of integrating a CSO model (namely SWMM), with the Centre's 1-D river model FASTER and 3-D model TRIVAST. The latter two models have been developed by staff within the Research Centre, whereas the model SWMM is a stormwater rainfall-runoff model developed by the U.S. Environmental Protection Agency. The integrated modelling tool is being continuously refined to predict faecal coliform and dissolved oxygen levels in the Bay for various scenarios. The numerical modelling has been complemented with an extensive field monitoring programme to establish more precise values for the kinetic decay rate and thereby provide enhanced predictions of coliform levels in the Bay. A laboratory model study has also been undertaken to establish retention times and provide an indication of dispersion values within the basin.

To enable the inclusion of a dynamic representation for determining the survival rates of bacteria in the numerical model, two field measurement exercises were undertaken to determine the key environmental parameters affecting the faecal indicator organism levels in the bay and the rivers Taff and Ely. These surveys were conducted in March (characterising cold, overcast conditions) and July (characterising hot, sunny conditions). The surveys involved the deployment of two survey boats within the bay, as well as land based survey teams to sample the rivers and other inputs. The surveys were conducted over the period dawn to dusk, to provide information on the diurnal variability of the relevant parameters. The main parameters measured, at various depths, included bacterial concentrations, solar irradiance in air and water, water temperature, turbidity, pH, salinity, conductivity, suspended particulate matter and water depth. The hydro-environmental model was set up with field values of the vertical light extinction coefficient for the March and July surveys and the die-off rate directly related to the solar intensity, implying that the die-off rate in darkness would be zero. Gameson and Saxon (1967) reported that the effects of sunlight on coliform die-off

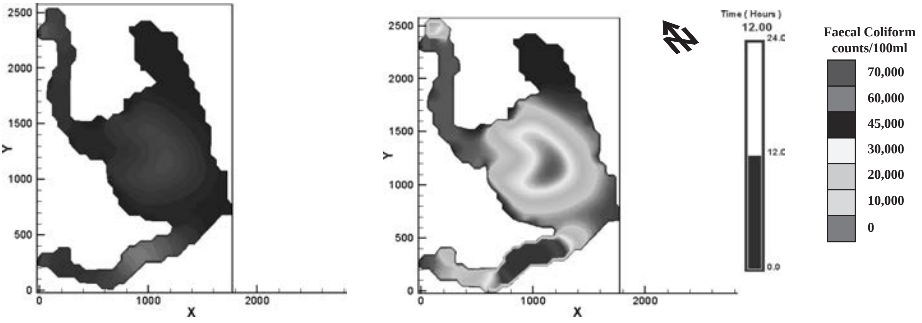

(a) 4 am release

(b) 4 pm release

Figure 3. Coliform levels for arbitrary release into rivers Taff and Ely at: (a) 4 am and (b) 4 pm.

were additive and independent of temperature, hence the die-off rate was expressed as the sum of the die-off rate for darkness, k_d, and the die-off rate due to sunlight, k_s. Assuming that the total faecal coliform mortality rate, k, can be defined by a simple relationship, taking into account darkness and sunlight mortality, then this relationship gives:

$$k = k_d + k_s \tag{5}$$

where typical values for k_d and k_s were 100 hr and 10 hr respectively. Extensive further research was undertaken by Kashefipour et al. (2002) and Lin et al. (2003) where extensive field data of faecal coliform levels were used, together with artificial neural networks, to develop new formulations for the faecal coliform decay rate k.

As part of this extensive research study, simulations were undertaken to investigate the impact of using the dynamically proposed varying decay rates for the faecal coliform levels of the receiving waters in the rivers and the Bay. In particular, comparisons were undertaken for a range of variables and the results showed that the receiving water faecal coliform levels were highly dependent upon the key variables cited above. The hydroenvironmental model was first run for hypothetical spillages into the rivers and for a constant decay rate (T_{90}) of 60 hr, both for day-time and night-time conditions. The model was then re-run for day-time and night-time decay rates cited above, i.e. ranging from 10 hr to 100 hr respectively and based on the representation given in Equation (5). The difference in the predictions was significant and indicated that, for this freshwater basin, night-time spillages during the autumn and winter months led to reduced faecal coliform levels in the rivers and Bay, in comparison with corresponding spillages occurring during the notional 12 hr day-time period (see Figure 3). Further field measurements and model predictions were undertaken, with the die-off related to sunlight intensity, temperature and irradiance.

The corresponding test case results showed a further significant variation in the coliform levels of the receiving waters, and highlighted the need for further studies into establishing more precisely the relationship between the decay rate and a range of meteorological, hydrodynamic and bio-chemical processes. Work is currently on-going within the Research Centre to relate the decay rate for faecal coliform to a range of other variables, including: pH, turbidity, air temperature and salinity.

More recently, the hydroenvironmental studies of Cardiff Bay have been extended to include genetic programming simulations, with these hydroinformatics tools offering new decision support software tools for predicting water quality levels in the Bay. The approach involves using extensive data to establish complex functional relationships, specifically for faecal coliform levels across Cardiff Bay in this instance. This approach enables real-time predictions to be made of the governing variables once the programme has been trained. Detailed measurements were taken across Cardiff Bay at 17 sites and typical comparisons of measured versus predicted coliform levels for one site are shown in Figure 4. Further details of this study are given in Harris (2003). This research

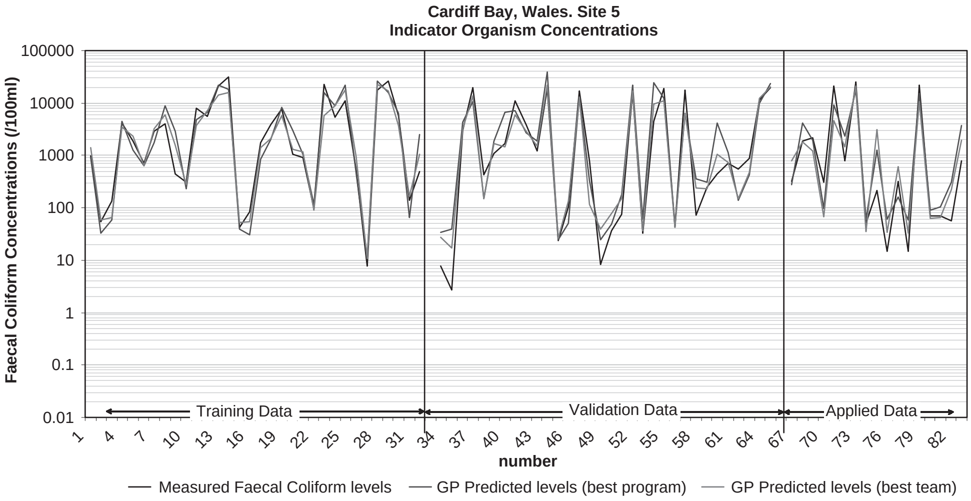

Figure 4. Comparison of measured and predicted faecal coliform levels using genetic programming.

relating to the application of genetic programming to predict faecal coliform levels in Cardiff Bay is also currently being integrated within the framework of 2-D and 3-D hydroenvironmental models with a view to using these tools together in a combined form. Major land use changes are currently on-going in the Cardiff Bay catchment area and the approach being developed is to use the deterministic model to predict the faecal coliform levels in the Bay for a range of input parameters and then to use the numerical model to provide the data to train and verify the genetic programme. Once trained for the new input conditions the genetic programme can then be used for on-line management of water quality within the Bay, with a 'predict and Protect' approach being used for signage when water quality standards become a potential health risk. The model has also been extended to produce gastro-enteritis disease burden risk levels, with the aim being to reduce hydroenvironmental health risk within the receiving waters and maximize the Bay for recreational water sports etc.

3.2 *Ribble estuary and river*

Another recent study undertaken by the authors relates to the refinement of the Centre's hydroenvironmental models for studying the Fylde Coast and Ribble River Basin in the U.K., where major concerns have arisen in recent years as a result of the coastal receiving waters failing to meet the European Union (EU) Bathing Water Directive mandatory standards, particularly during storm flow conditions. The Ribble river basin is situated along the North West coast of England, near the town of Blackpool – one of the U.K.'s largest seaside resorts and a key tourist centre. At the mouth of the estuary, there are two well-known seaside resorts, namely Lytham St. Anne's and Southport, and both designated EU bathing waters (see Figure 5). The area has three main centres of population, namely the towns of St. Anne's and Southport, located on the north and south coasts of the Ribble Estuary, and the town of Preston that straddles the Ribble near the tidal limit. In order to improve the receiving water quality, North West Water has invested over £500 m along the Fylde coast and in the Ribble river basin over the past 10 years. Examples include upgrading various wastewater treatment works from primary treatment to including UV disinfection and with storm discharges having been reduced by the construction of 260,000 m^3 of additional storage.

Although the decrease in the input of bacterial loads has resulted in a marked reduction in the concentration of bacterial indicators, elevated coliform counts are still encountered, particularly during flood conditions, and the bathing waters frequently continue to fail to comply with the EU Bathing Water Directive (1976) mandatory standards. The mandatory coliform standards given in the directive to assess compliance require that there be no more than 2,000 faecal coliform counts

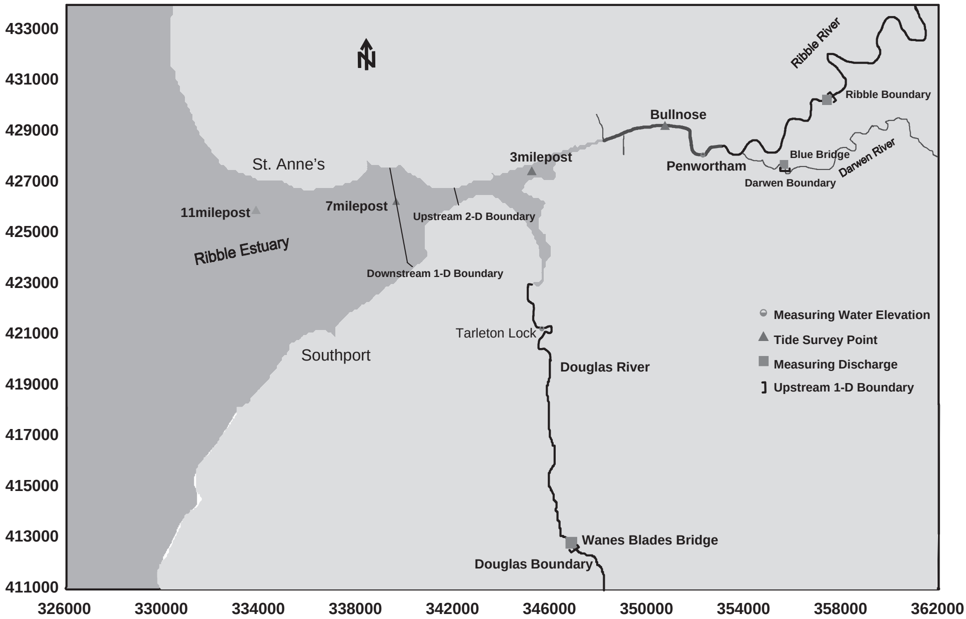

Figure 5. Schematic illustration of Ribble River Basin.

per 100 ml. For bathing waters to comply with this directive then 95% of the samples taken must meet these standards. The water quality failures have become a major threat to the local tourist industry. Considerable fieldwork has been undertaken by the Environment Agency and North West Water to investigate land use management issues and how these relate to the adverse water quality conditions. The main objective of the study was therefore to quantify the impact on various sewerage infrastructure inputs into the Ribble river basin and the receiving coastal waters.

In undertaking a comprehensive modelling study of the basin, the Centre's FASTER and HEMAT models were used for predicting water elevations, velocities, salinity, total and faecal coliform levels and suspended sediment loads in the river, the estuary and the coastal receiving waters. The main area of interest in this study was from the outer seaward boundary, of length 41.2 km, to the tidal limit of several rivers, each having a width at the limit of typically less than 10 m. Such a difference in the modelling scale made it almost impossible for either a 1-D or 2-D model to be used alone. Therefore a linked 1-D and 2-D modelling approach was used, with the domain being divided into two sub-domains and with diffuse source inputs included in the form of line sources from catchment land use model inputs provided by the Centre for Research in Environment and Health at the University of Wales, Aberystwyth.

In order to ensure that the integrated model could be used to predict accurately the impact of future improvement works and climate change on the river basin, the model was calibrated for water elevations, velocities, salinity, suspended solids, faecal and total coliforms and faecal streptococci against six datasets. Three of the datasets were used for initial calibration and the other three were used for model verification. The data were collected during winter and summer months, and for wet and dry weather conditions. Measurements were also taken for different tidal ranges, including neap and spring tides, and at the tidal limits of the rivers and the seaward boundary, to provide boundary conditions at the weirs for the model. Measurements were also taken within the basin at several sites, including: 11 milepost, 7 milepost, 3 milepost and Preston Bullnose (see Figure 5). Full details of the model study are given in Kashefipour et al. (2002).

For the calibration tests excellent agreement was obtained between the flow and faecal coliform predictions for the river basin. Model predictions of elevations and velocities were in close

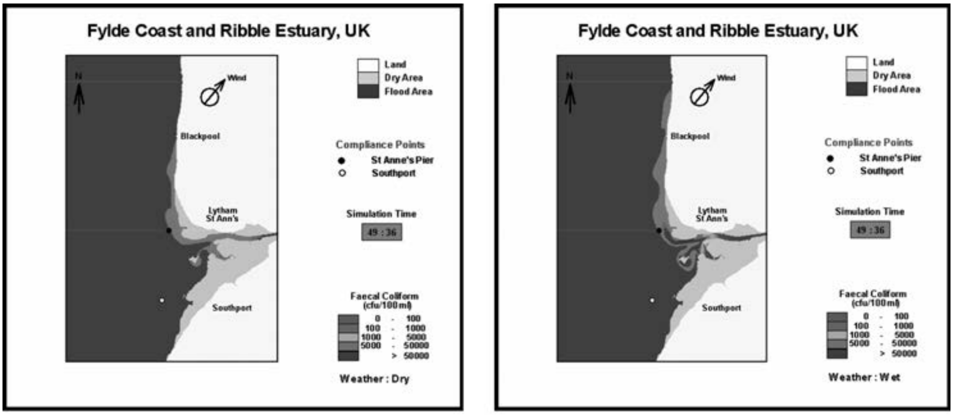

(a) Dry weather flow (b) Wet weather flow

Figure 6. Computed faecal coliform levels for: (a) dry and (b) wet weather river flows.

agreement with the measured data. Similarly, comparisons of the predicted and measured faecal coliform levels at all of the calibration points showed that the model was able to predict this water quality indicator satisfactorily. The calibrated wet weather event values of T_{90} for the 2-D and 1-D regions were 72 hr and 85 hr for day-time, and 106 hr and 142 hr for night-time conditions. Likewise, for dry weather conditions the corresponding calibrated T_{90} values were 37.3 hr and 50.1 hr for day-time and 80.8 hr and 132.2 hr for night-time conditions respectively. The measured and predicted coliform indicator levels at all of the calibration points were found to be much greater for wet weather events, in comparison with dry weather events. It was also interesting to note that for all wet weather events the coliform inputs from the catchments into the upstream reaches of the Ribble and Darwen rivers were significantly larger than for the corresponding dry weather loads.

Finally, a series of baseline simulations was undertaken for a range of river flows, tidal conditions and meteorological conditions. In addition to these baseline simulations, a number of scenario simulations were also undertaken to establish the impact on the coastal receiving waters of further investments in the wastewater treatment works (such as UV disinfection) at a number of sites along the rivers. The results showed that, whilst UV disinfection and storage tanks would undoubtedly reduce the effluent coliform inputs from the sewage works, the diffuse source inputs from the catchment were significant during flood (or wet weather) conditions and little could be done to reduce the adverse impact. Comparisons of the predicted faecal coliform levels for dry and wet weather conditions are shown in Figure 6, highlighting that non-compliance at the bathing water site was much influenced by diffuse source pollutants.

3.3 *Bristol Channel – Severn Estuary*

In the final study reported herein an extensive on-going 2-D modelling research project is being undertaken with the Centre for Research into Environment and Health, at the University of Wales, Aberystwyth, and the U.K. Environment Agency. The study involves an extensive programme of field monitoring and numerical modelling to predict faecal contamination and nutrient levels in the Bristol Channel and Severn Estuary where, despite extensive levels of wastewater treatment (including UV disinfection), high levels of enteric bacterial contamination are still found in some of the bathing waters along the estuary. In this study a new enteric bacterial–sediment transport interaction conceptual model has been developed and measured data used to estimate the sorption and desorption rates between the bacteria and the sediments. The data acquired through the field data monitoring studies have shown that the bacteria can remain trapped within the sediments for considerably long periods, only to be released and transported potentially to bathing waters during storm or spring tide conditions. When the bacteria are adsorbed onto the sediments and deposited to the bed then the decay rate is found to be very low and the bacteria can be regarded almost as a conservative substance. Relatively good agreement has been obtained between the measured and predicted levels of faecal coliform along the estuary, with the results highlighting considerable differences between the concentration levels measured and predicted when the interactions between the bacteria and the sediments are included in the model.

4 CONCLUSIONS

In recent years environmental hydraulicians have placed considerable emphasis on modelling accurately the hydrodynamic, mixing and sediment transport processes in river and estuarine waters. However, in many cases the level of contamination in the downstream receiving waters is often highly dependent upon the kinetic decay rates or the partitioning coefficients for coliform bacteria, nutrients and heavy metals etc. These coefficients are generally assumed to be constants in many model studies and insufficient emphasis is often placed on these coefficients in comparison with other hydrodynamic and mixing parameters and coefficients, such as the bed roughness and turbulence characteristics.

In the study reported herein brief details are given of the importance of the kinetic decay rate and the partitioning coefficient and the influence on these parameters of such variables as temperature, salinity, irradiance, turbidity etc. Three studies are highlighted to varying degrees, with the first study of Cardiff Bay highlighting the significance of irradiance on the decay rate for faecal coliform and the influence of this parameter on the receiving water coliform levels. This study is now being extended to investigate the influence of other master variables on the decay rate using artificial neural networks and other hydroinformatics tools. In the second study the significance of diffuse source pollutants has been illustrated, again using refined representations of the faecal coliform decay rate. Finally, in a study of enteric bacterial levels along the Bristol Channel and Severn Estuary an initial conceptual model – together with extensive field data – has highlighted the potential significance of the interaction of bacteria with the sediments and, like heavy metal fluxes, adsorption and desorption are predicted to be important processes in the transport of bacteria through and with the water column. This latter study is currently in its infancy and is now being extended to nutrient fluxes.

ACKNOWLEDGEMENTS

The research studies reported herein were mainly funded by the Natural Environment Research Council, the Engineering and Physical Sciences Research Council and the Environment Agency. The authors are also grateful to Cardiff Harbour Authority for the provision of data and their past research students involved these studies including: Dr Emma Harris, Dr Seyed Kashefipour and Ms. Lei Yang. The authors are also particularly grateful to Professor David Kay and Dr Carl Stapleton (CREH, University of Wales, Aberystwyth) for their collaboration with these studies.

REFERENCES

Falconer, R.A. & Lin, B. 2003. Hydro-environmental modeling of riverine basins using dynamic rate and partitioning coefficients. *Journal of River Basin Management* 1(1): 81–89.

Falconer, R.A., Lin, B. & Kashefipour, S.M. 2001. Modelling water quality processes in riverine systems. In M.G. Anderson, D. Walling & P.D. Bates (eds), Model Validation: Perspectives in Hydrological Science: 357–387. Chichester: John Wiley & Sons Ltd.

Fischer, H.B. 1979. Longitudinal dispersion and turbulent mixing in open-channel flow. *Annual Review of Fluid Mechanics*, 5: 59–78.

Gameson, A.L.H. & Saxon, J.R. 1967. Field studies on effect of daylight on mortality of coliform bacteria, *Water Research*, 1(1): 279–295.

Harris, E., Falconer, R.A., Kay, D. & Stapleton, C. 2002. Development of a modelling tool to quantify faecal indicator levels in Cardiff Bay, *Water and Maritime Engineering*, 154(2): 129–135.

Harris, E.L. 2003. Environmental hydroinformatics tools for recreational water quality modelling, *PhD thesis, University of Wales, Cardiff*, U.K.: 208.

Kashefipour, S.M., Lin, B., Harris, E.L. & Falconer, R.A. 2002. Hydro-environmental modelling for bathing water compliance of an estuarine basin, *Water Research*, 36(7): 1854–1868.

Lei, Y., Lin, B. & Falconer, R.A. 2004. Numerical modelling for bathing water enterococci estimation in the Severn Estuary. *Report for Environment Agency R & D Project Number 10208*: 1–51

Lin, B. & Falconer, R.A. 2001. Numerical modeling of 3-D tidal currents and water quality indicators in the Bristol Channel. *Water and Maritime Engineering, Proc. of Inst. of Civil Engrs.*, 48(3): 155–166.

Lin, B., Kashefipour, S.M. & Falconer, R.A. 2003. Predicting nearshore coliform bacteria using ANNs, *Water Science and Technology*, 48(10): 225–232.

Namin, M., Lin B. & Falconer, R.A. (in press). Modelling estuarine and coastal flows using an unstructured triangular finite volume algorithm. *Advances in Water Resources*.

Sanford, L.P. & Halka, J.P. 1993. Assessing the paradigm of mutually exclusive erosion and deposition of mud, with examples from upper Chesapeake Bay. *Marine Geology*, 97:37–57

van Rijn, L.C. 1984a. Sediment transport. Part 1: Bed load transport. *Journal of Hydraulic Engineering, ASCE*. 110: 1431–1456.

van Rijn, L.C. 1984b. Sediment transport. Part 2: Suspended load transport. *Journal of Hydraulic Engineering, ASCE*. 110: 1431–1456.

Wu, Y. & Falconer, R.A. 2000. A mass conservative 3-D model for predicting solute fluxes in estuarine waters. *Advances in Water Resources*, 23: 531–543.

This page intentionally left blank

Environmental Hydraulics and Sustainable Water Management – Lee & Lam (eds)
© 2005 Taylor & Francis Group, London, ISBN 04 1536 546 5

Fate and transport modeling vs. models: A management perspective

Wu-Seng Lung
Department of Civil Engineering, University of Virginia, Charlottesville, VA, USA

ABSTRACT: While fate and transport modeling of contaminants in natural waters has been a useful tool in managing water resources by the regulatory agencies, there is misconception about the use of models toward water quality management, particularly in the name of modeling vs. models. It should be pointed out that the skills of modeling are most crucial to the fate and transport modeling instead of applying models. More importantly, practical fate and transport modeling analyses require the support of water quality data. Modeling without data or simply applying models should not be encouraged for water quality management. This presentation demonstrates a number of practical fate and transport modeling studies in assisting regulatory agencies on water quality management.

1 INTRODUCTION

One of the purposes of fate and transport modeling is for management use. Managers must be convinced that the model is fully calibrated and verified prior to making projections and predictions for decisions that have a large sum of money at stake. Ranging from a modeling study of a small creek to clean up the point source discharges to the large scale study of the Chesapeake Bay, USA, managers keep asking questions such as: Are the model(s) calibrated, how good is the calibration, is the calibration/verification scientifically defensible, and how would the citizens buy in the study results?

Water quality managers at regulatory agencies must be convinced that the models are fully functional to produce credible results so they can submit them to the management for a full implementation of the modeling outcome. In addition, public citizens are well educated these days and they must also buy in to support the decisions related to the model results. They often ask intelligent questions on the modeling analysis at public meetings. Environmental groups are another watch dog that is closely monitoring the modeling analysis and scrutinizing the model results.

Based on the experience gained during the past two decades on fate and transport modeling of contaminants, it is clear that the most important question that managers ask is: How do you know your model results are right? That is the central theme of this paper: modeling vs. models. A number of technical issues relating to fate and transport modeling are presented to offer a perspective toward this question.

2 NATURE OF FATE AND TRANSPORT MODELS

Fate and transport models are mass balance based, i.e. the only equation that has a solid foundation in the model is the mass balance equation. Any thing else such as modeling algal growth, suspended solids settling and resuspension, or contaminant adsorption by sediments all have various degrees of empiricism. It is this empiricism that requires field data support in the modeling analysis. Essentially, it is the comparison of model results with data that demonstrates model calibration and verification.

The extent of field data to support the modeling analysis depends on the sophistication and complexity of the modeling framework configured for the analysis. Obviously, more complicated models require more data and simpler models use less data. A sound strategy is to use the simplest model possible to address the water quality problem(s) in practice.

3 FATE AND TRANSPORT MODELING IN WATER QUALITY MANAGEMENT

3.1 *Assigning and deriving key coefficient values*

Kinetic coefficients are highly dependent of the process formulation in most of the fate and transport models in practice today. For example, regulatory agencies issue discharge permits for point sources in terms of CBOD concentrations in the effluent, usually expressed as 5-day BOD or CBOD. To accommodate the permit writer's need, the modeler formulates the rate of consumption of dissolved oxygen in the receiving water using a first-order kinetics based on the remaining concentration of CBOD in the receiving water. Such a formulation is highly empirical and as such, assigning the in-stream deoxygenation rate becomes a formidable task without prior knowledge of the wastewater characteristics, particularly for the situations of upgrading the treatment level or constructing a new treatment plant (Lung, 2001). Failure to understand this key aspect would seriously compromise the modeling analysis, resulting in erroneous permit conditions.

A good example of such a practice is the modeling analysis of Walnut Creek in Alabama (AL), USA. The state regulatory agency had completed a modeling study of the wastewater treatment plant for the City of Troy, discharging into Walnut Creek. They used a very high CBOD deoxygenation rate in the order of 0.5 day^{-1} to 0.6 day^{-1} for the receiving water. Such a high rate would result in a very stringent permit (i.e. extremely low CBOD concentrations in the effluent). Yet, a close review of their long-term BOD data showed a low rate of 0.06 day^{-1}, suggesting a highly stabilized effluent. Figure 1 demonstrates the model calibration results matching the dissolved oxygen (DO) data, based on the much lower CBOD deoxygenation rate for the model.

Another example is the determination of stream reaeration rate in Shirtee Creek, AL. Initially, the state regulatory agency used a much lower reaeration rate, resulting in very stringent CBOD limits for the discharger. A critical review of their modeling analysis showed that they used the Langbien and Duram (1967) Equation for the receiving water, generating very low reaeration coefficients and thereby, extremely stringent effluent limits for CBOD. Because Shirtee Creek is a very small stream, the use of the Langbien and Duram Equation is not justified (Lung, 2001). Instead, the Tsivoglou Equation (Tsivoglou and Neal, 1976), designed for small streams, should be used. Table 1

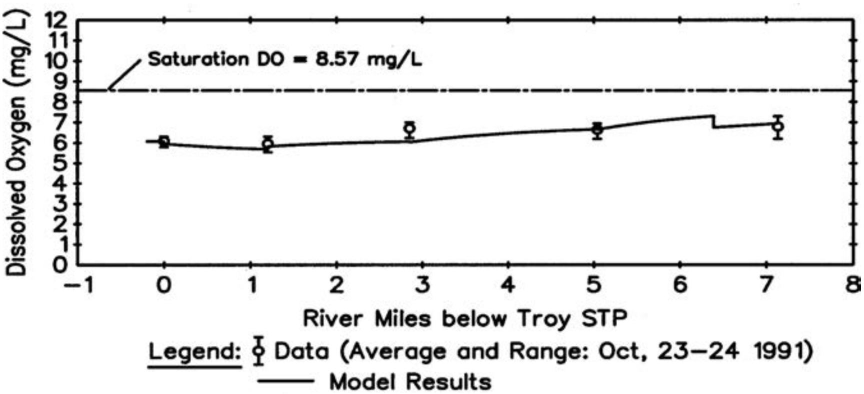

Figure 1. Model calculated vs. measured DO in Walnut Creek using October 1991 data.

shows the comparison of the reaeration coefficients for both equations to calibrate and verify the DO model of Shirtee Creek.

In both cases of Walnut Creek and Shirtee Creek, the saving of treatment cost was significant following the revised modeling analysis, further demonstrating the benefit of correct modeling analysis in the regulatory decision-making process. It is particularly important to note that these two modeling studies used a very simple BOD/DO model, which is exactly what was needed to address this water quality problem for the study sites. Was a more complex model needed? No. The model selected was the right tool for the job. What is most important, however, is how to use the model correctly – making a point for modeling vs. models.

3.2 *Selecting the right model to address the management question*

In a total maximum daily load (TMDL) modeling study for the Santa Fe River, NM, it was hypothesized that excess nutrients from the Santa Fe wastewater treatment plant result in attached algae in the river bed and might be causing the observed significant diurnal variations in DO and pH. The QUAL2E (see Chapra, 1997) model was originally selected and modified to accommodate attached algae coupled with DO and pH calculations. Further modeling analysis revealed that the QUAL2E code cannot support time-variable (i.e. diurnal in this case) calculations. A model capable of calculating DO levels in the water column on an hourly basis reflecting the transient impact of periphytons was needed. The WASP/EUTRO5 (Ambrose et al., 1993) code, capable of time-variable computations, was used instead. It was further modified from daily average time-variable algal growth dynamics to real time calculations to address the water quality problem (Lung, 2001). The mass transport component for attached algae would be bypassed in the code. Algal/nutrient dynamics between the attached algae and nutrient components in the water column was updated for the periphytons. Since the light level needed for the calculation would be the value reaching the bottom of the water column, no depth-averaged light effect was needed in the WASP code. The modified WASP/EUTRO5 model for the Santa Fe River performed well, producing real-time results of DO and pH, matching the measured values (Figure 2). The model was then used to develop the TMDL for the Santa Fe River, resulting in setting an instantaneous minimum DO of 4 mg/L for the receiving water (Lung, 2001), to meet the water quality standard.

3.3 *Uncover previously hidden interactions*

Super-saturation of DO in the surface layers of the water column has been observed in many reservoirs. In their modeling studies using the CE-QUAL-W2 model, Cole and Wells (1999) reported super-saturation in a number of reservoirs. Their model results consistently under-predict the DO levels in the surface layers. In a recent modeling study of the Loch Raven reservoir outside of the City of Baltimore, model results match the DO levels in the bottom water of the reservoir quite well but could not reproduce the supersaturation condition observed in the surface layers (Lung and Zou, 2004). The water quality model used for the Loch Raven reservoir was the EPA's WASP/EUTRO5

Table 1. Comparison of reaeration coefficients (day^{-1}) at 20°C in Shirtee Creek.

Mile point	August 1991[1]	March 1991[1]	August 1989[1]	August 1989[2]	October 1990[2]
0.0–0.53	5.074	6.266	5.392	9.77	1.82
0.53–0.75	9.886	11.79	14.62	0.76	0.10
0.75–2.02	14.94	17.05	17.45	0.76	2.25
2.02–3.95	8.427	9.222	9.181	0.76	1.44
3.95–6.07	4.897	3.598	3.072	0.76	1.44

[1] Tsivoglou Equation.
[2] Langbien and Duran Equation.

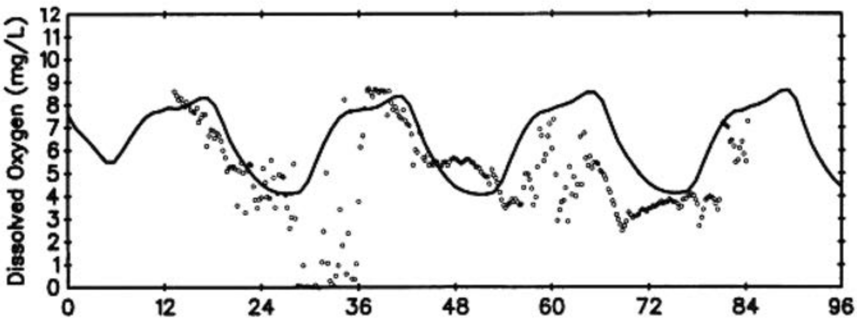

Figure 2. Comparison of model calculated vs. measured DO concentrations in the Santa Fe River, showing significant daily fluctuations over a 96-hour period in the water column.

model. Model calibration results of DO using the 1991 data consistently under-predict the measured DO levels in the surface layers (Lung and Zou, 2004).

Additional effort was launched to improve the DO prediction in the surface layers. Model sensitivity analyses indicated that increasing the algal growth rate in the water column would significantly raise the algal biomass (chlorophyll *a*) level and exhaust the inorganic nutrients. The high algal biomass level (significantly exceeding the observed chlorophyll *a* level); however, would not increase the DO level to achieve super-saturation in the surface layers due to depletion of inorganic nutrients.

The EUTRO5 module was then modified to provide rapid nutrient recycling rates. In addition, zooplankton was added into the model to serve as the predator of algae. Zooplankton death would complete the nutrient recycling process. An additional system, zooplankton was introduced to simulate zooplankton biomass in mg carbon L^{-1}. At high levels of phytoplankton biomass, zooplankton grazing levels off. The zooplankton gains biomass by assimilating phytoplankton and loses biomass by respiration, excretion, and death. These processes can be incorporated into a zooplankton balance (see Chapra, 1997).

Figure 3 presents model results vs. data at Station GUN0142 at the dam for 1992 simulations. The water quality constituents shown are DO, chlorophyll *a*, total phosphorus, and ammonia in the surface and bottom layers of the water column. Results from the original model (in dots) and the enhanced model (in solid lines) are displayed for comparison with the data (depth-averaged values and max/min values). Figure 3 shows that results from the enhanced model match the surface-layer DO levels much better than the results from the original model in 1992. The chlorophyll *a* match (particularly in the surface layer) also improves with the enhanced model and so do the total phosphorus results in both surface and bottom layers.

3.4 *Modeling with limited data*

While fate and transport modeling requires significant data support, there are modeling studies that must be made with very limited field data to support regulatory decisions. In that case, the modeler must rely on other information and try to establish as many check points as possible to guide the analysis. One approach would be to perform the modeling analysis using conservative assumptions in lieu of data support. If the model results, developed under conservative assumptions, yield the model results meeting water quality standards, they are much easier accepted by the regulatory agencies. The following example illustrates such a case study.

Mixing zone modeling is one of the important environmental hydraulic topics these days that must be addressed by the regulatory agencies under the current Clean Water Act in the US. The focus of the mixing zone modeling is now on many small wastewater discharges, either from municipal or industrial wastewater facilities. Unfortunately, field data to support a mixing zone analysis of small dischargers is usually lacking. One of the key elements is quantifying the mixing

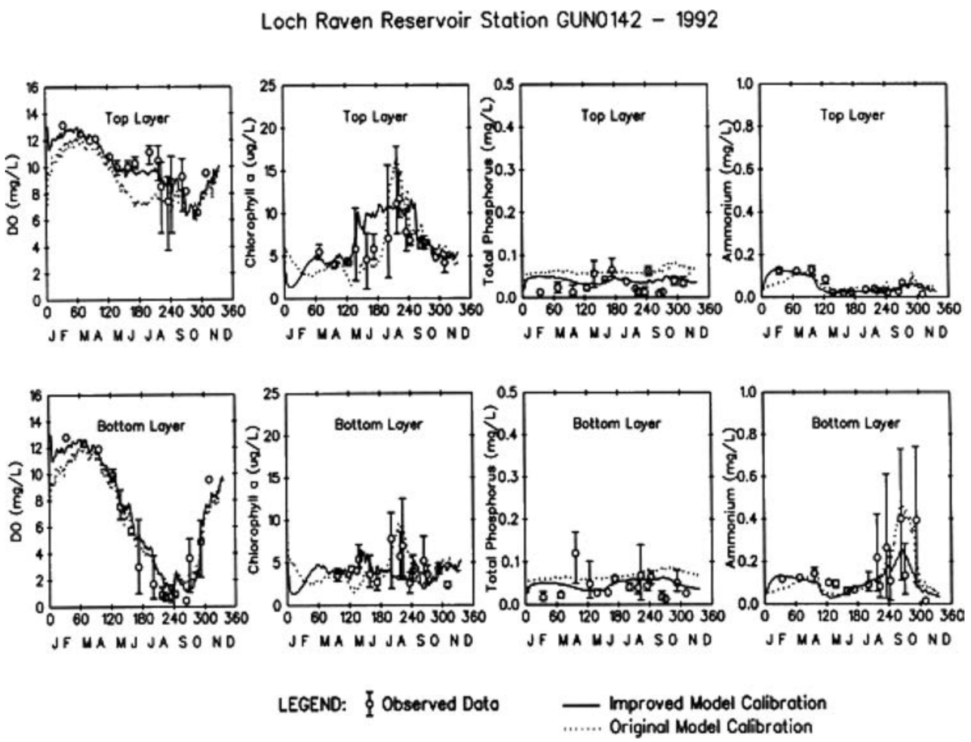

Figure 3. Original and improved model results vs. data of DO, chlorophyll *a*, total phosphorus, and ammonia nitrogen in a two-layer configuration for Loch Raven at station GUN0142 near the dam.

and dispersion coefficients in the receiving water. While regulatory agencies require field work to independently develop such data, carrying out a full scale dye dispersion study in the field is not only time consuming but also costly. In lieu of a field study, technical data from other sources could be used to support the modeling analysis as shown in the following case study.

With the completion of construction and commercial operation of Unit 6, a 550 megawatt combined cycle gas turbine unit, in 2003, several new wastewater streams entered the existing treatment pond system at the Possum Point power station in Dumfries, VA (Figure 4). This system is known as the low volume waste system and is regulated as outfall 004 by Virginia Department of the Environmental Quality (VDEQ). The discharge from this system enters Quantico Creek near its confluence with the Potomac River. One of these new wastewater streams, cooling-tower blowdown quench water, is thermally enriched. Because of this new thermal source, VDEQ expressed concern about the impact of the thermal loading from outfall 004 to the existing thermal mixing zone in Quantico Creek (see Figure 4).

The existing discharge permit stipulates that temperature rise over the ambient should not be greater than 3°C within the regulatory mixing zone. Temperature monitoring to record the thermal impact of outfall 004 has been conducted since 1985 on an annual basis and it has become a semi-annual event since 2001. Historical data from the monitoring indicate that temperature rises over the ambient has been consistently below 1°C. Thus, the key question to be addressed in this study is whether the new thermally enriched water from outfall 004 would significantly increase this temperature rise beyond that level. That is, would the combined temperature rise still be below 3°C?

A conservative modeling approach was adopted to determine if the temperature increase due to the effluent from outfall 004 would be below 1.8°C inside the regulatory mixing zone. A number

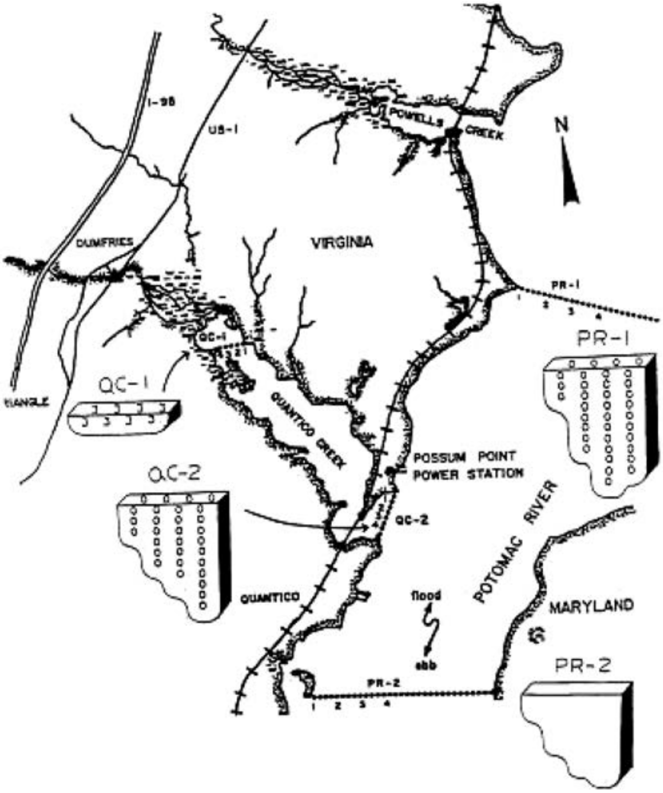

Figure 4. Possum Point Power Station, Quantico Creek, and the Potomac River, VA.

of assumptions for the modeling analysis are listed as follows:

1. Initial dilution of the effluent due to momentum impact is neglected. The flow rate of outfall 004 is very small that it carries little momentum on the receiving water.
2. Surface dissipation of heat from outfall 004 discharge is not included.
3. The temperature rise due to thermal sources other than outfall 004 could reach 1.2°C, thereby resulting in a balance of 1.8°C for outfall 004.

The above assumptions yield a very conservative approach to meet the water quality standard. A worse-case thermal load from the effluent at outfall 004 is associated with a flow rate of 3.5 MGD and temperature of 20°C above the ambient water (i.e. $\Delta T = 20$°C). The station operation records indicate that the ΔT at the outfall has been rarely over 10°C. The flow rate of 3.5 MGD is also a very extreme event. Therefore, such a thermal load scenario is on the conservative side.

Lung (1995, 2001) presented a simplified, analytical solution to track the fate and transport of pollutants in estuaries in a 2-D configuration with longitudinal and lateral dispersion:

$$C(x,y) = \frac{M}{\pi d (D_x D_y)^{1/2}} e^{\frac{ux}{2D_x}} K_0 [\frac{u}{2D_x^{1/2}} (\frac{x^2}{D_x} + \frac{y^2}{D_y})^{1/2}] \quad (1)$$

where

C = concentration at any given location downstream from the discharge
M = mass discharged/unit time

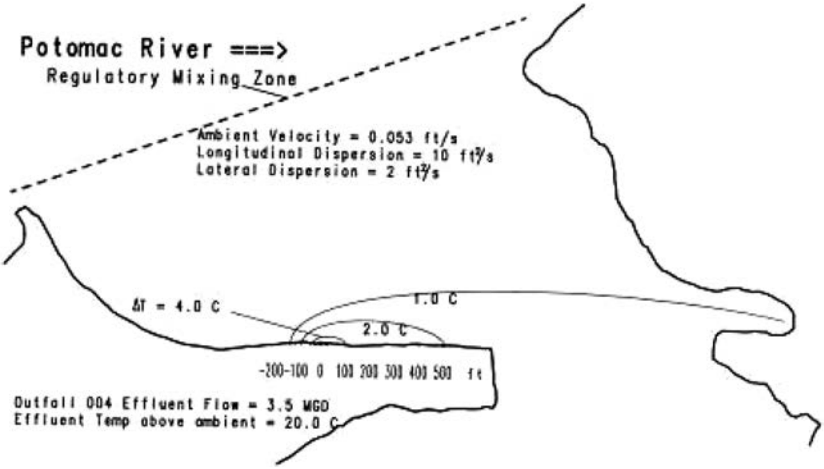

Figure 5. Model results showing ΔT contours in the Potomac River.

u = average velocity in the river
D_y = dispersion coefficient across the river
x = distance downstream from the discharge outfall
y = distance in lateral direction
d = average depth in the river
D_x = the longitudinal dispersion coefficient and
K_0 = the modified Bessel function of the second kind of order zero.

In this study, values of key model coefficients in Eq. 1 such as u, D_x and D_y were obtained from the EPA's Chesapeake Bay (including the Potomac River) hydrodynamic model instead of conducting a field study. Note that the Chesapeake Bay hydrodynamic model has been fully calibrated and verified with close match of long-term data; and rigorously scrutinized by peer reviews (Lung, 2001). The mixing pattern derived from that model was readily accepted by VDEQ. Figure 5 shows the model calculated temperature over the ambient, ΔT(°C) under the worst case scenario. The results clearly indicate that the 1.8°C contour of ΔT is well within the regulatory mixing zone.

3.5 *Tracking the fate and transport of nutrients in the receiving water*

In a study of analyzing the fate and transport of phosphorus from the Metropolitan Wastewater Treatment Plant (Metro Plant) in Minneapolis/St. Paul, MN, a numerical tagging technique was developed to identify the source of phosphorus in the algal biomass in the Upper Mississippi River. Such a technique is quite similar to the $^{32}PO_4$ technique that limnologists use in tracking phosphorus in natural water systems by measuring the amount of $^{32}PO_4$ in various phosphorus compartments in the water column. Instead of using a radioactive tracer, a numerical tracer was injected into one of the nutrient sources in the eutrophication model. A comprehensive presentation of this technique can be found in Lung (1996). Results of the numerical tagging analysis is presented in Figure 6, showing that despite the significant reduction of phosphorus loads from the Metro Plant, the phytoplankton biomass reduction in Lake Pepin amounts to only 10 μg/L. Such an outcome helped to convince the regulatory agency that spending a significant sum (i.e. over $400 M) on phosphorus removal at the Metro Plant would not be a wise strategy.

The model results are particularly useful in quantifying the contribution of an individual phosphorus source or a group of sources to the phytoplankton biomass in the receiving water. Applying the numerical tagging technique on a watershed basis would yield helpful information for developing a sound water quality management strategy, particularly in terms of the trade-off between

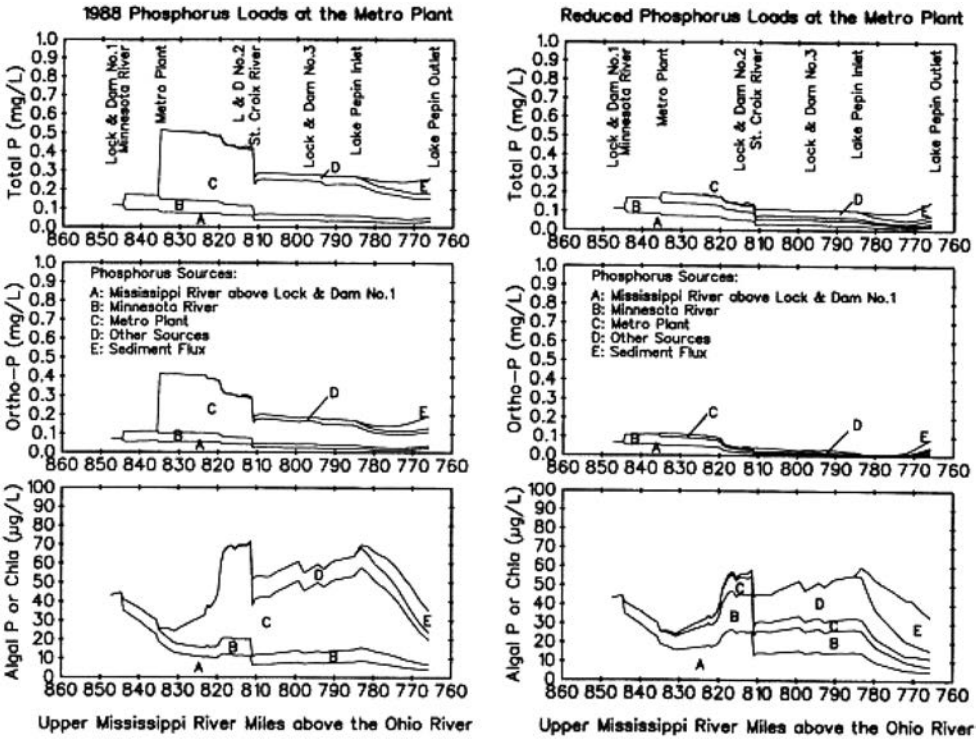

Figure 6. Model results showing the fate and transport of various phosphorus sources in the Upper Mississippi River and Lake Pepin under 1988 and reduced phosphorus loads at the Metro Plant.

point and nonpoint loads. This study has demonstrated the numerical tagging analysis that can be instrumental in improving the overall TMDL development of a particular watershed.

3.6 *Linking models*

Nonpoint sources in the watershed usually dominate the contaminant loads to the receiving waters these days. A complete fate and transport model package for water quality management must include a watershed model, a hydrodynamic model, and a receiving water quality model. Accurate predictions of watershed loads represent a key step in fate and transport modeling of the receiving water. Unfortunately, data to support the watershed modeling effort is far short of its need, thereby making watershed modeling one of the most inaccurate effort in the fate and transport modeling analysis and it is the weakest link of all the modules.

To strengthen this link, modelers rely on the receiving water modeling effort as a key check point for watershed modeling. Receiving water modelers should not take in everything that the watershed modelers provide. Instead, receiving water modelers are expected to offer feedbacks to the watershed modelers to calibrate the watershed model. Examples of such a practice have been reported in many nutrient TMDLs in US.

Another key step is linking the hydrodynamic and receiving water quality model. In the case of the Loch Raven Reservoir eutrophication modeling, the 2-D (longitudinal-vertical) CE-QUAL-W2 code (simply called W2 model) by Cole et al. (1998) was used to quantify the advective flows in the water column by running the hydrodynamic module. While the W2 code has the water quality module, the regulatory agency had chosen the WASP/EUTRO5 for water quality simulations (Lung, 2001). An important check point in linking the W2 and WASP/EUTRO5 models is to run the

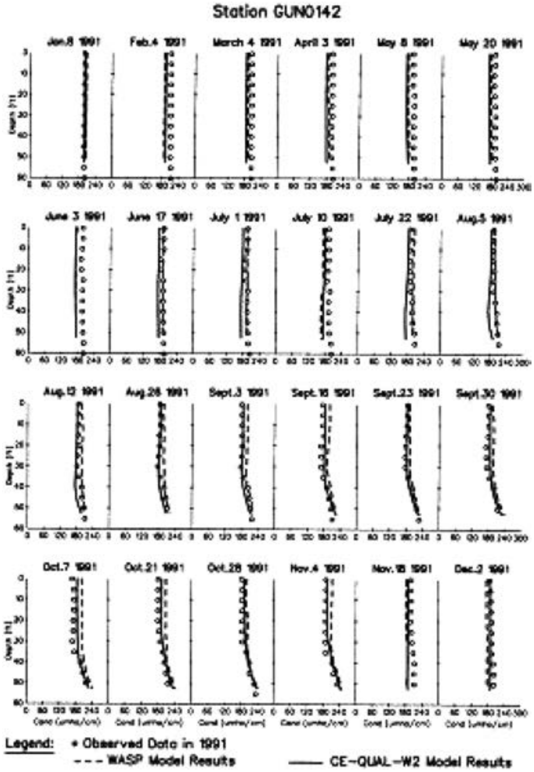

Figure 7. Linking a hydrodynamic model with a water quality model, matching results from both models with measured specific conductivity data in Loch Raven Reservoir, Maryland, 1991.

WASP model for a conservative substance (in this case, specific conductivity) using the flow field generated by the W2 model. Results from both models must match to insure a proper linkage. Figure 7 displays the model results for specific conductivity from both models of Loch Raven Reservoir using the 1991 data. Results from these two models match each other closely and also reproduce the same measured vertical profiles of specific conductivity levels in the reservoir. Note the slightly increased specific conductivity levels in the bottom waters during the summer months. The elevated specific conductivity levels are due to the release of iron and manganese ions from the sediment under anaerobic conditions (Lung, 2001). Results presented in Figure 7 further substantiate the validity of the mass transport calculations in the WASP model and indicate that the mass transport model is ready for water quality simulations.

4 PHYSICALLY BASED MODELS

The above case studies clearly demonstrate the necessity of field data support in fate and transport modeling analyses. An experience modeler would feel frustrated with any analysis lacking data support. Modeling does not generate data; it only interprets data to quantify the cause-and-effect relationship. Fate and transport models are most useful in quantifying such relationships between the pollutant loads and the receiving water response.

In recent years, the so-called “physically based models” have surfaced. Developers of these models claim that there is no need to calibrate the model at all, i.e. no model coefficients need to be adjusted for any applications. In light of the case studies presented, it is easy to see that such a claim is totally false and without a scientific base. One simple counter argument would be: Even the hydrodynamic models still need to adjust the Manning's *n* or its equivalent, how could a water quality model, which has significantly more coefficients than hydrodynamic models, be applied globally without any change of its values of parameters and coefficients?

Because of the current construct of the model, BOD/DO modeling of streams still requires a priori assignment of the deoxygenation coefficient values in the receiving water. It is almost impossible to quantify the deoxygenation coefficient in a stream without a full characterization of the wastewater input. An independent assignment of the deoxygenation coefficient values would be as difficult, if not impossible, as trying to quantify the bottom coefficients in a hydrodynamic model. It should be pointed out that turbulence closure modeling has been around for decades and still remains more an art than science today, let alone the independent quantification of the deoxygenation coefficients in stream BOD/DO modeling.

5 CONCLUSIONS AND SUGGESTIONS

Over the past two decades, fate and transport modeling has matured into a useful tool in water quality management for regulatory agencies, particularly for TMDLs in recent years. A scientifically defensible modeling study requires significant data support to configure, calibrate, and verify the model. A model should not be used for management use until it is properly validated with site specific data. The take home message of this paper is: conducting modeling analysis correctly instead of using models as a black box. Adequate training of modelers, not blindly applying models, is essential to the success of fate and transport modeling.

REFERENCES

Ambrose, R.B., T.A. Wool, and J.L. Martin, 1993. The water quality analysis simulation program, WASP5, part a: model documentation. U.S. EPA Center for Exposure Assessment Modeling, Athens, GA.

Chapra, S.C., 1997. Surface water-quality modeling. McGraw-Hill, New York, NY.

Langbien, W.B. and W.H. Durum, 1967. The aeration capacity of streams. U.S. Geological Survey Circular 542, Washington, DC.

Lung, W.S., 1995. Mixing zone modeling for toxic waste-load allocations. *J. Environ. Eng.*, 121(11): 839–842.

Lung, W.S., 1996. Fate and transport modeling using a numerical tracer. *Water Resources Res.*, 32(1): 171–178.

Lung, W.S., 2001. Water quality modeling for wasteload allocations and TMDLs. John Wiley & Sons, New York, NY.

Lung, W.S. and R. Zou, 2004. Modeling supersaturation of dissolved oxygen in reservoirs. Manuscript submitted for publication.

Tsivoglou, E.C. and L.A. Neal, 1976. Tracer measurements of reaeration: III. Predicting the reaeration capacity of inland streams. *J. Water Pollution Contr. Fed.*, 48(12): 2669–2689.

Environmental Hydraulics and Sustainable Water Management – Lee & Lam (eds)
© 2005 Taylor & Francis Group, London, ISBN 04 1536 546 5

Internal waves in Monterey Bay: An application of SUNTANS

O.B. Fringer, M. Gerritsen & R.L. Street
Stanford University, Stanford, CA, USA

ABSTRACT: Internal waves are ubiquitous in the oceans and their simulation is a necessary precursor to understanding ocean mixing and energy dissipation. Toward this end, we present an unstructured grid, nonhydrostatic, parallel Navier-Stokes simulator, SUNTANS, which employs unstructured grids in the planform and z-levels in the vertical. The grids for SUNTANS are partitioned with the ParMETIS parallel graph partitioning tool, and parallelization is accomplished with MPI, the message passing interface. We demonstrate the necessity of employing a nonhydrostatic solver to reproduce the physics of the lock-exchange problem, and find that, although the nonhydrostatic solver is five times as expensive per time step, the hydrostatic solver is less efficient because it requires 16 times as many time steps for the same simulation time. When applied to the Monterey Bay bathymetry, we show that SUNTANS correctly simulates the internal wave field by comparing the results to those from two field sites.

1 INTRODUCTION

Internal waves account for a significant portion of mixing and dissipation within the world's oceans. Based on a balance between mixing and deep-water upwelling, the average eddy diffusivity of the ocean is roughly $10^{-4}\,\mathrm{m^2\,s^{-1}}$. Despite this prediction, Munk and Wunsch (1998) report that profiler measurements in the ocean away from boundaries yield diffusivities on the order of $10^{-5}\,\mathrm{m^2\,s^{-1}}$. One possible explanation of this dichotomy is that the eddy diffusivity is very large in small, localized turbulent patches over a small percentage of the ocean. The most likely source for this elevated diffusivity is internal wave breaking.

In the continuously stratified ocean, internal wave energy propagates along beams at an angle θ with respect to the horizontal and slope dz/dx given by

$$\frac{dz}{dx} = \tan(\theta) = \pm\left(\frac{\omega^2 - f^2}{N^2 - \omega^2}\right)^{1/2}, \tag{1}$$

where ω is the internal wave frequency, f is the Coriolis parameter, and N is the buoyancy frequency. Unlike surface waves, internal waves retain their angle with the vertical after reflection from topography. For an internal wave beam propagating towards a topographic slope, supercritical topography implies that the topographic slope, γ, is steeper than θ, and results in internal wave reflection, whereas subcritical topography for which $\gamma < \theta$ results in transmission. When $\theta = \gamma$, critical topography results in focusing of internal wave energy that can lead to turbulence and mixing, as is shown by the numerical simulations of Slinn and Riley (1998).

Internal tides, or internal waves of tidal frequency, are generated at critical topography (Prinsenberg *et al.*, 1974). Steep ridges or breaks in topography transition rapidly from subcritical to supercritical slopes and serve as sources of generation of internal wave energy. Using field measurements and numerical simulations with the Princeton Ocean Model (POM) (Blumberg & Mellor, 1987), Petruncio *et al.* (1998; 2002) show that internal waves are generated at critical topography within Monterey Bay and this energy propagates into the Monterey Bay Submarine

Canyon. Their results show that submarine canyons along coastal margins act as conduits which focus internal wave energy which in turn leads to elevated levels of dissipation and mixing. Others (Kunze *et al.*, 2001; Lien & Gregg, 2001) have also measured elevated turbulence and mixing due to the internal tide in Monterey Bay.

Like Petruncio *et al.* (2002), Holloway (2001) and Holloway *et al.* (2001) used POM to study internal tides by simulating internal waves on the Australian Northwest Shelf. Although they used primitive equation models, these simulations yielded excellent results because internal tides are approximated well with the hydrostatic approximation, especially when the grid resolution is relatively coarse. Refining the grid is necessary if finer scale internal wave physics is to be captured, but at finer scales it becomes necessary to compute the nonhydrostatic pressure because in some regions evolution of the internal wave spectrum leads to shorter, nonhydrostatic and breaking waves. It is these processes that should define the energy dissipation and mixing.

The purpose of this paper is to present an overview of a nonhydrostatic parallel code, SUNTANS (Stanford Unstructured Nonhydrostatic Terrain-following Adaptive Navier-Stokes Simulator), which is capable of running at very high resolution on parallel computers. We present some results obtained with SUNTANS as applied to Monterey Bay.

2 THE SUNTANS CODE

SUNTANS is a nonhydrostatic, unstructured-grid, parallel, coastal ocean simulation tool that solves the Navier-Stokes equations under the Boussinesq approximation with a large-eddy simulation of the resolved motions (Fringer *et al.*, 2002; Fringer, 2003). The formulation is based on the method outlined by Casulli (1999), where the free-surface and vertical diffusion are discretized with the θ-method, which eliminates the Courant condition associated with fast free-surface waves and the friction term associated with small vertical grid spacings at the free-surface and bottom boundaries. The grid employs z-levels in the vertical and triangular cells in the planform. Advection of momentum is accomplished with the second-order accurate unstructured-grid scheme of Perot (2000), and scalar advection is accomplished semi-implicitly using the method of Gross *et al.* (1999), in which continuity of volume and mass are guaranteed when wetting and drying is employed. The wetting and drying capabilities of SUNTANS enable its use for coastal as well as estuarine domains. The θ-method for the free-surface yields a two-dimensional Poisson equation, and the nonhydrostatic pressure is governed by a three-dimensional Poisson equation. These are both solved with a preconditioned conjugate gradient algorithm that employs diagonal preconditioning. SUNTANS is written in the C programming language, and the message-passing interface (MPI) is employed for use in a distributed memory parallel computing environment.

Of critical importance to the study of parallel unstructured grid simulations is the method by which the grids are partitioned among the processors. Since the grids for SUNTANS are unstructured in the planform and z-leveled in the vertical, we partition in the horizontal to ensure that water columns remain contiguous on given processors. In addition to greatly simplifying the underlying parallel implementation, partitioning in this way allows contiguous allocation of water columns in memory which enhances performance. When partitioning a grid among processors, it is important to balance the workload so that each processor does not do more work than any of the others involved in the simulation.

While load-balancing ensures an equal workload distributed among the processors, the parallel performance of a particular unstructured grid code depends highly on the communication required between neighboring processors. Communication between processors is directly proportional to the surface area on interprocessor boundaries. A load-balanced partitioning that minimizes the interprocessor communication can be obtained with the ParMETIS software package (Karypis *et al.*, 1998) that partitions the unstructured two-dimensional planform grid using multilevel recursive bisection. As an example, Figure 1(a) depicts a typical unstructured grid of Monterey Bay. Using the depth as weights for the partitioning, a balanced partitioning among eight processors is depicted in

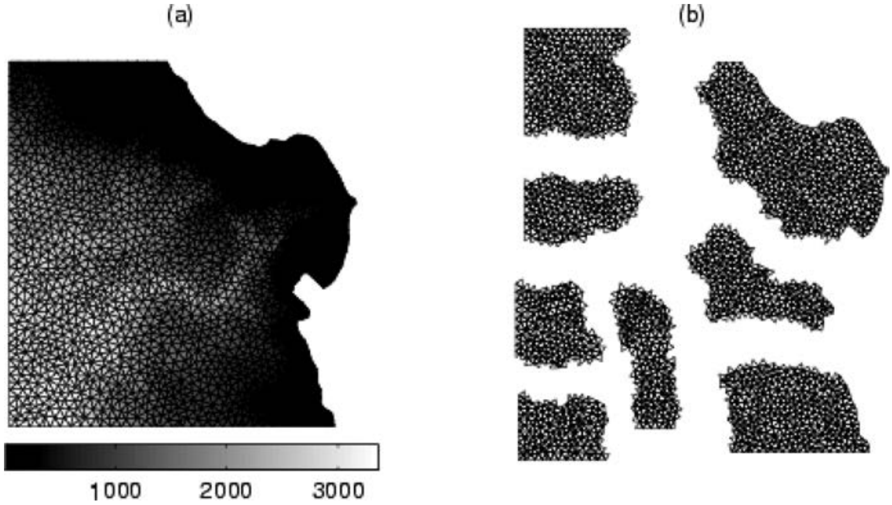

Figure 1. (a) Typical unstructured grid of the Monterey Bay region with 3026 grid cells, showing the depth in meters. The domain is 100 km × 100 km. (b) Load-balanced partitioning using eight processors.

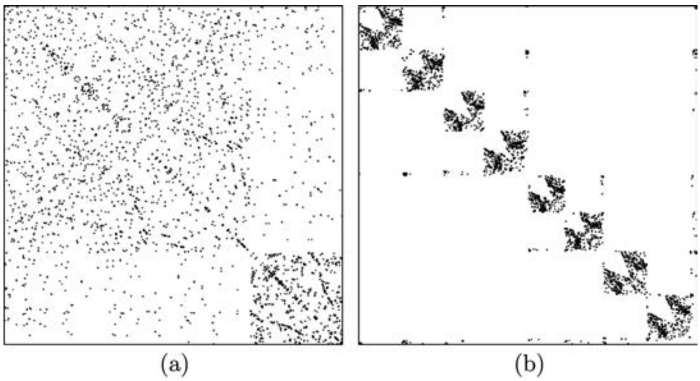

Figure 2. Connectivity matrices for the (a) original and (b) ordered cells.

Figure 1(b). Using ParMETIS, it is guaranteed that this partitioning results in a balanced workload and minimizes the communication time by minimizing the surface area between each processor. Because the deeper regions in Figure 1(a) have more cells in the water column, the planform area of the partitions containing these regions is smaller, as shown in Figure 1(b).

Performance can be further improved by ordering the cells such that the physical distance in memory between adjacent cells is minimized. The physical distance in main memory can be visualized with the boolean connectivity matrix. Specifically, row *i* of the connectivity matrix is populated by ones in the columns which correspond to neighbors of cell *i*, and zeros elsewhere. The connectivity matrix for a 1089-cell unstructured grid of Monterey Bay as output by the Triangle package of Shewchuck (1996) with no specific ordering is shown in Figure 2(a). The same connectivity matrix after using the grid cell ordering routines of ParMETIS is shown in Figure 2(b). Comparing the two shows how the reordered grid reduces the average distance in main memory between neighboring cells by a significant amount. Typical speedups due to reordering the cells result in a 20 to 30% reduction of the per-processor computation time.

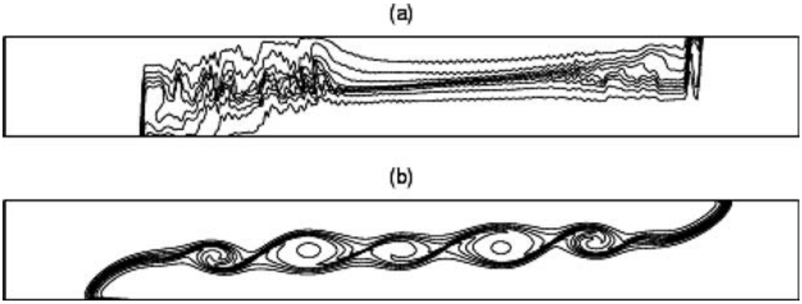

Figure 3. Comparison of the resulting density contours for the (a) hydrostatic simulation and (b) nonhydrostatic simulation after $t = 10T$ s. Contours are plotted every $0.1\Delta\rho/\rho_0$.

3 NONHYDROSTATIC EFFECTS

Kanarska and Maderich (2003) present a detailed set of numerical experiments which they use to verify the accuracy of a free-surface nonhydrostatic solver, including short surface wave experiments, run-up of a solitary wave on a vertical wall, a neutrally buoyant intrusion, and exchange flows. Following that work, we present the results of computing an exchange flow using the parameters of the direct numerical simulations of Hartel *et al.* (2000) and discuss the differences between the nonhydrostatic and hydrostatic results. The simulation is performed with SUNTANS in a two-dimensional domain of length $L = 0.8$ m and depth $D = 0.1$ m (one dimension of equilateral triangles in the planform) using 400×100 cells and employing a drag law on the lower boundary with a drag coefficient of $C_d = 0.01$. Figures 3(a) and (b) depict the density contours for the hydrostatic and nonhydrostatic simulations after $t = 10T$ s, where $T = \sqrt{D/2g'}$ and $g' = g\Delta\rho/\rho_0 = 0.01\,\mathrm{m\,s^{-2}}$ is the reduced gravity.

The hydrostatic simulation does not capture the generation of the Kelvin-Helmholtz billows, but does capture the speed of the front correctly. On average per time step, the nonhydrostatic simulation takes 5 times longer than the hydrostatic simulation. However, the maximum vertical velocity for the hydrostatic simulation is roughly 20 times larger than that for the nonhydrostatic simulation. This results from the assumption that vertical inertia does not play an important role in the hydrostatic simulation. Without vertical inertia, vertical accelerations result in excessively high vertical velocities. This disparity in the maximum vertical velocity between the hydrostatic and nonhydrostatic simulations is a direct result of the fact that this particular flow is highly nonhydrostatic. Thus, the hydrostatic simulation must be run with a time step 16 times smaller than the nonhydrostatic simulation to achieve roughly the same vertical Courant number, $C_w = w_{max}\Delta t/\Delta z$, where w_{max} is the maximum vertical velocity. For the hydrostatic simulation, $w_{max} = 0.20\,\mathrm{m\,s^{-1}}$ and $C_w = 0.57$, while for the nonhydrostatic simulation $w_{max} = 0.01\,\mathrm{m\,s^{-1}}$ and $C_w = 0.47$. Therefore, neglecting accuracy considerations, even though the nonhydrostatic simulation takes longer per time step, the hydrostatic simulation takes 3.2 times longer overall.

4 INTERNAL WAVES IN MONTEREY BAY

4.1 *Simulation setup*

As a demonstration, we simulate the internal wave field in Monterey Bay by employing SUNTANS on the $100\,\mathrm{km} \times 100\,\mathrm{km}$ domain shown in Figure 1(a) with a total of 24 963 cells in the planform and 100 cells in the vertical. Because SUNTANS does not store data associated with inactive cells that lie beneath the bathymetry, this yields substantial savings because only 41% of the 2.5 million cells are active. The total number of grid cells for this computation is then reduced to roughly 1 million. The planform cells are equilateral triangles with sides of length 840.33 m. The vertical

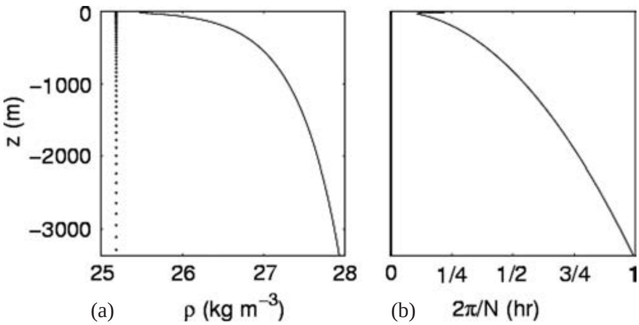

Figure 4. (a) Density field and (b) buoyancy period $2\pi/N$ taken from Petruncio *et al.* (2002). The dots in subplot (a) indicate the vertical position of every other z-level.

grid is stretched to refine the grid near the surface, where the density gradients are larger. The minimum vertical grid spacing at the surface where index $k=1$ can be expressed as

$$\Delta z_1 = D\frac{r-1}{r^{N_k}-1}\,, \tag{2}$$

where $D = 3\ 367.5$ m is the maximum depth, $r = 1.025$ is the algebraic stretching factor, and $N_k = 100$ is the number of vertical levels, yielding $\Delta z_1 = 7.8$ m. The vertical grid spacings beneath the surface are then given by $\Delta z_k = r\Delta z_{k-1}$, where $k = 2, \dots, N_k$, which yields a maximum vertical grid spacing of $\Delta z_{N_k} = 89.7$ m. The depth is interpolated from data with 1 km resolution obtained from the MBARI Multibeam Survey CD-ROM (Hatcher *et al.*, 1998).

The model is initialized with a stagnant velocity field and free-surface, and the initial density profile is taken from the work of Petruncio *et al.* (2002), which gives an average density profile obtained from 50 CTD casts in Monterey Bay. This density profile and associated buoyancy period are shown in Figure 4. The western boundary of the domain is forced with the most dominant semi-diurnal (M_2) and diurnal (K_1) components of the barotropic tide by imposing the horizontal velocity field in the form

$$u(y,z) = u_{M_2}\cos(\omega_{M_2}t) + u_{K_1}\cos(\omega_{K_1}t + \phi_{K_1-M_2})\,, \tag{3}$$

where $u_{M_2} = 2.445\,\mathrm{mm\,s^{-1}}$, $u_{K_1} = 1.82\,\mathrm{mm\,s^{-1}}$, $\omega_{M_2} = 1.41\times10^{-4}\,\mathrm{rad\,s^{-1}}$, $\omega_{K_1} = 7.27\times10^{-5}\,\mathrm{rad\,s^{-1}}$, and the phase difference beteen the arrival of the M_2 and K_1 tides is $\phi_{M_2-K_1} = 0.66$ rad. These parameters are obtained from the tidal component analysis of Petruncio (1996) using tidal gauge data near the Monterey Peninsula. The magnitudes of the barotropic velocity field at the western boundary are set to obtain sea-surface heights of 0.489 m for the M_2 tide and 0.362 m for the K_1 tide at the boundary. Since the Bay essentially co-oscillates, it is assumed that the sea-surface heights at the boundary are the same as those measured and computed by Petruncio near the Monterey Peninsula. Boundary conditions on the northern and southern boundaries are closed, while we employ a sponge layer at the western boundary in order to prevent reflections of the internal tides from that boundary. The sponge layer is implemented by adding a source term to the u-and v-momentum equations of the form

$$S_{u,v} = -\frac{u,v}{\tau_s}\exp\left(-\frac{x}{L_s}\right)\,, \tag{4}$$

where $\tau_s = 1000$ s and $L_s = 1$ km. We run the simulation for a total of four M_2 tides with a time step of $\Delta t = 29.808$ s. This simulation time is sufficient to generate internal tidal energy at the

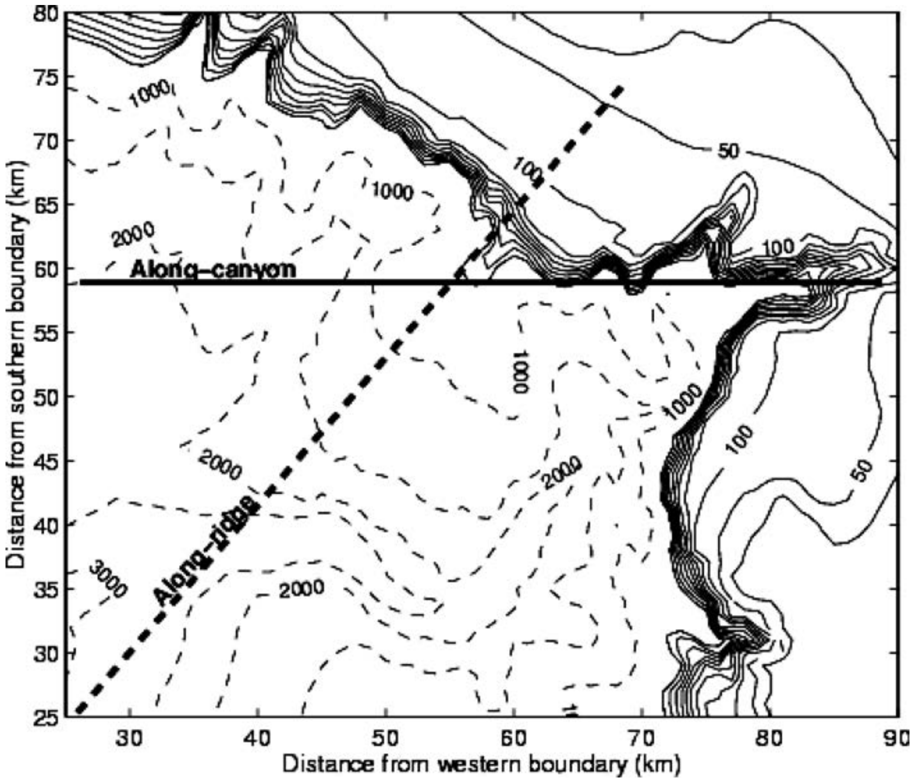

Figure 5. Transects used to compare the results of SUNTANS to the numerical and field studies of Petruncio *et al.* (1998; 2002) and Kunze *et al.* (2001) (along-canyon transect: –) and Lien and Gregg (2001) (along-ridge transect: – –).

semidiurnal and diurnal frequencies, but is short enough such that internal wave energy reflecting from the northern and southern boundaries does not drastically affect the results. We are currently implementing the Sommerfeld radiation condition to radiate internal wave energy from these boundaries in order to allow for longer simulation times.

When the simulation is run on a PC in nonhydrostatic mode with two processors, it takes roughly 1 minute of computation per time step. We have performed tests which show that speedup is linear with 16 processors using this grid size, indicating that we can run 8 times faster than real time using this time step if we use 16 processors. The vertical eddy-viscosity is constant and given by $\nu_V = 10^{-4}\,\mathrm{m}^2\,\mathrm{s}^{-1}$, the horizontal eddy viscosity is $\nu_H = 10\,\mathrm{m}^2\,\mathrm{s}^{-1}$, and there is no physical scalar diffusion. The normalized residual of the conjugate gradient solver for the free-surface is 10^{-10} and that for the nonhydrostatic pressure is 10^{-5}, and we use $\theta = 0.55$ for the theta-method.

4.2 *Internal wave generation sites*

Numerous works have documented the location of internal wave generation sites in Monterey Bay. The field and numerical studies of Petruncio *et al.* (1998; 2002) and the field observations of Kunze *et al.* (2001) show that internal wave energy is generated beyond the shelf break in Monterey Bay and that this energy propagates towards the shore and is focused within the Monterey Submarine Canyon. The transect we use to compare the results of our model with their findings is shown as the along-canyon transect in Figure 5. Lien and Gregg (2001) show that an internal wave beam that is generated at the shelf break just north of the along-canyon transect results in elevated dissipation

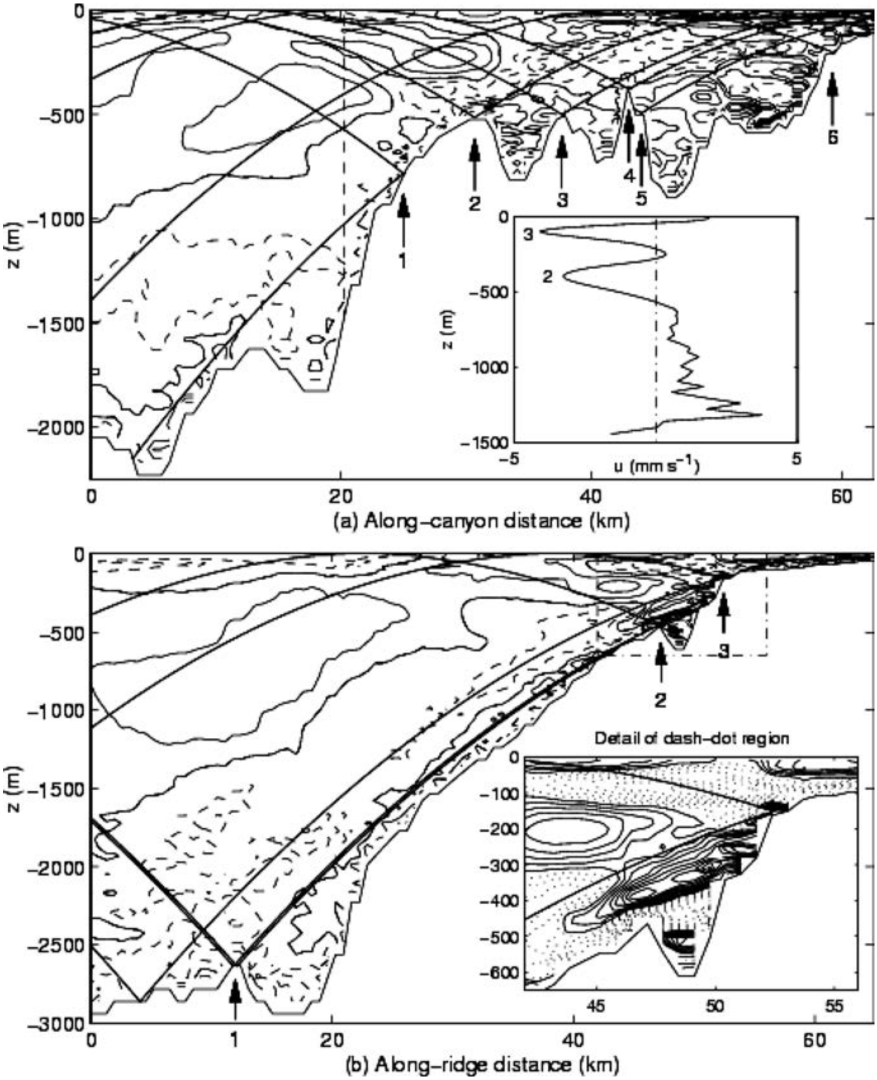

Figure 6. Baroclinic velocity contours in the (a) along-canyon and (b) along-ridge transects depicted in Figure 5 after 3.83 M_2 tides. Contours are plotted at intervals of 2 mm s^{-1} from -0.01 to 0.02 m s^{-1}. Positive contours are solid while negative contours are dashed. The numbers indicate possible generation sites for internal waves and indicate the origins of the ray paths predicted by linear theory. The inset in (a) depicts the horizontal velocity profile at the vertical transect depicted by the dashed line, with the numbers indicating the likely origin of the internal wave energy at that depth, while that in (b) is a detail of the dash-dot region surrounding generation sites 2 and 3.

and mixing. We compare the results of our model with their field results by studying the internal wave field in the along-ridge transect shown in Figure 5.

Contours of the east-west baroclinic velocity field after 3.83 M_2 tides are shown in Figure 6(a) for the along-canyon transect. From linear theory, internal waves are generated at regions where the internal wave ray path matches that of the local topography. Steep topographical ridges present effective regions of generation because the bottom slope passes through criticality in a narrow region where the vertical momentum is large. Linear theory predicts that the internal wave ray paths follow trajectories defined by the dispersion relation (1). Here we only consider internal M_2 tidal beams, because they dominate the internal wave field. The internal wave ray paths are depicted by the solid lines that emit from likely generation sites at locations 1–6 in Figure 6(a). As noted by Petruncio *et al.* (2002), most of the smooth ridge from which rays 1 and 2 are generated is critical, which is the likely source of the westward velocities in the upper 400 m of the water column between 0 and 20 km. Internal wave energy emitting from location 1 propagates downward into the deeper ocean where it encounters further critical topography. Generation sites 2–6 all generate internal wave energy that propagates out to the open ocean as well as onto the shallow shelf, and these intersect near the surface and generate large westward velocities. Generation sites 3, 4, and 5 also generate downward propagating energy but this is omitted for clarity. The inset plot in Figure 6(a) depicts the horizontal velocity field as a function of depth 20 km east of the start of the along-canyon transect. The profile indicates that the velocity is negative (westward) near the surface as a result of the internal wave beams that are generated at locations 2 and 3.

Figure 6(b) depicts the internal wave field in the along-ridge transect depicted in Figure 5. Internal wave energy is generated at the shelf break (location 3) that propagates on-and off-shore and generates the offshore beam (detailed in the inset plot) measured by Lien and Gregg (2001) which contains a region of enhanced turbulent mixing and dissipation. They measured eddy diffusivities in this region as large as $0.01\,\mathrm{m}^2\,\mathrm{s}^{-1}$, which are likely due to turbulence generated by a shear instability that results from the internal wave field. The present simulations show that internal wave energy is also generated along the bottom between generation sites 1 and 2, where the bottom slope is almost exclusively critical. This internal wave energy is also contributing to the elevated levels of shear which generates the turbulence in the tidal beam measured by Lien and Gregg.

5 CONCLUSIONS AND FUTURE PLANS

We have presented a parallel code, SUNTANS, which is capable of solving nonhydrostatic flows on unstructured grids using the message passing interface for parallelization. While computation of the nonhydrostatic pressure is expensive, for predominantly nonhydrostatic flows it can be more expensive to employ the hydrostatic approximation, since the vertical velocity can be an order of magnitude higher for the hydrostatic solver than it is for the nonhydrostatic solver. For field-scale simulations, the large-scale features of the flow are well approximated with a hydrostatic code, while smaller-scale features such as short internal waves or solitary waves can only be captured with a nonhydrostatic model.

We have employed SUNTANS to study the internal wave field in Monterey Bay and have found the results to agree well with the measurements obtained by two field studies. Both cases exhibit pronounced internal wave generation at critical topography. In particular, we have found that the turbulence generated in the beam that was measured by Lien and Gregg (2001) results from the intersection of upward and downward propagating internal wave energy from the critical deep slope as well as the shelf break.

Currently, we are employing SUNTANS on a highly-resolved grid to simulate the nonhydrostatic energy cascade as internal wave energy leads to breaking along critical topography and through highly nonlinear wave propagation on the shelf. This will yield an improved understanding of the mechanisms that lead to dissipation and mixing on coastal margins both by analyzing the results of the highly resolved simulations and employing SUNTANS as a tool to help design cruise tracks to better locate regions of elevated internal wave activity.

ACKNOWLEDGMENTS

The authors wish to acknowledge the support of NSF/ITR grant 0113111 (Program manager: Barbara Fossum) and ONR grant N00014-02-1-0204 (Scientific officer: Dr. C. Linwood Vincent).

REFERENCES

Blumberg, A. F., & Mellor, G. L. 1987. *A description of a three-dimensional coastal ocean circulation model, Three-Dimensional Coastal Ocean Models, Ed. N. Heaps.* American Geophysical Union. 1–16.

Casulli, V. 1999. A semi-implicit finite difference method for non-hydrostatic, free-surface flows. *Int. J. Numer. Methods Fluids*, **30**, 425–440.

Fringer, O. B. 2003. http://suntans.stanford.edu.

Fringer, O. B., Gerritsen, M., Jachec, S., & Street, R. L. 2002. A new nonhydrostatic parallel coastal ocean model. *Eos Transactions*, AGU, 83(47), Fall Meeting Suppl. Abstract OS11C-0238.

Gross, E. S., Koseff, J. R., & Monismith, S. G. 1999. Evaluation of advective schemes for estuarine salinity simulations. *J. Hydraul. Eng.*, **125**, 32–46.

Hartel, C., Meiburg, E., & Necker, F. 2000. Analysis and direct numerical simulation of the flow at a gravity-current head. Part 1. Flow topology and front speed for slip and no-slip boundaries. *J. Fluid Mech.*, **418**, 189–212.

Hatcher, G., Maher, N., & Greene, H. G. 1998. *MBARI Multibeam Survey CD-ROM.* http://www.mbari.org.

Holloway, P. E. 2001. A regional model of the semidiurnal internal tide on the Australian North West shelf. *J. Geophys. Res.*, **106**, 19,625–19,638.

Holloway, P. E., Chatwin, P. G., & Craig, P. 2001. Internal tide observations from the Australian North West shelf in Summer of 1995. *J. Phys. Oceanogr.*, **31**, 1182–1199.

Kanarska, Y., & Maderich, V. 2003. A non-hydrostatic numerical model for calculating free-surface stratified flows. *Ocean Dyn.*, **53**, 176–185.

Karypis, G., Schloegel, K., & Kumar, V. 1998. *Parmetis: Parallel graph partitioning and sparse matrix ordering library.*

Kunze, E., Rosenfeld, L. K., Carter, G. S., & Gregg, M. C. 2001. Internal waves in Monterey Submarine Canyon. *J. Phys. Oceanogr.*, **32**, 1890–1913.

Lien, R. C., & Gregg, M. 2001. Observations of turbulence in a tidal beam and across a coastal ridge. *J. Geophys. Res.*, **106**, 4575–4591.

Munk, W., & Wunsch, C. 1998. Abyssal recipes II: energetics of tidal and wind mixing. *Deep-Sea Res.*, **45**, 1977–2010.

Perot, B. 2000. Conservation properties of unstructured staggered mesh schemes. *J. Comput. Phys.*, **159**, 58–89.

Petruncio, E. 1996. *Observations and modeling of the internal tide in a submarine canyon.* Ph.D. thesis, Naval Postgraduate School.

Petruncio, E. T., Rosenfeld, L. K., & Paduan, J. D. 1998. Observations of the internal tide in Monterey Canyon. *J. Phys. Oceanogr.*, **28**, 1873–1903.

Petruncio, E. T., Paduan, J. D., & Rosenfeld, L. K. 2002. Numerical simulations of the internal tide in a submarine canyon. *Ocean Modelling*, **4**, 221–249.

Prinsenberg, S. J., Wilmot, S. L., & Rattray, J. M. 1974. Generation and dissipation of coastal internal tides. *Deep-Sea Res.*, **21**, 263–281.

Shewchuck, J. R. 1996. Triangle: *A Two-Dimensional Quality Mesh Generator and Delaunay Triangulator. Version 1.3.*

Slinn, D. N., & Riley, J. J. 1998. Turbulent dynamics of a critically reflecting internal gravity wave. *Theor. Comp. Fluid Dyn.*, **11**, 281–303.

This page intentionally left blank

Environmental Hydraulics and Sustainable Water Management – Lee & Lam (eds)
© 2005 Taylor & Francis Group, London, ISBN 04 1536 546 5

Environmental and ecological impacts of the Three Gorges Project on the Yangtze River

Zhao-Yin Wang
Professor, Department of Hydraulic Engineering, Tsinghua University, Beijing, China
Chairman of the Advisory Council, International Research and Training Center on Erosion and Sedimentation (IRTCES)

ABSTRACT: This paper reviews the studies on the Three Gorges Project (TGP) on the Yangtze River and its environmental and ecological impacts. Sedimentation in the reservoir will reach an equilibrium in 100 years with a total volume about 16 billion m^3. Experimental studies have showed that the impoundment will cause sediment deposition at the apron of the Chongqing harbor and even change the braided channel into a single thread one. The released water from the dam will scour 2.5 billion tons of sediment from the downstream channels in 40 years. The flood stage will then be reduced. The reservoir will not necessarily cause earthquakes, but will induce more landslides, which will threaten little the safety of the dam. It is reported that the impoundment of the reservoir so far has not obviously affected the water quality. The reservoir operation will change the hydrologic conditions, which may affect the life cycle and habitats of fishes and reduce the fishery harvest. The regulation of the flow for power generation and flood control may change the fluvial processes and some meandering and braided sections may become unstable, which will undermine the habitats of some endangered species. New resettlement policy has been implemented with overall arrangements for working and living conditions for the emigrants.

1 INTRODUCTION

The 6,300-km long Yangtze River is the largest and longest river in China, which has a watershed area of 1.80 million km^2. The Three Gorges Project (TGP) is constructed near Yichang in Hubei province (Fig. 1), where the Yangtze River's middle and upper reaches meet. Figure 1 also shows the main tributaries, riparian lakes and hydrological stations. The river poses high flood risk to the middle reaches, especially the Shashi-Wuhan reach. For instance the 1998 flood claimed 2,292 lives, caused serious flood damages and affected 8 million people. The recurrence period of the 1998 flood is only 7 years in terms of the crest flood discharge at Yichang, and is 100 year in terms of 30 days flood volume (Ministry of Water Resources, 1999). The flood stages in the middle reaches of the river were even higher than those in 1954 although the flood crest discharge and the total runoff were smaller (Zhou, 1999).

The Three Gorges Dam is at Sandouping, 38 km upstream from Yichang (Fig. 1). The main purposes of the project are flood control, power generation and navigation. The dam is 185 m high and the storage capacity of the reservoir is 39.3 billion m^3, in which 22.1 billion m^3 are for flood control. The dam controls 1 million km^2 of drainage area. The project started in 1993 and will be completed in 2009. The dam has stored water and generated electricity since 2002.

The flood defense system in the middle reaches consists of 3,570 km long grand levees along the Yangtze River, and more than 30,000 km long levees along the tributaries, riparian lakes and canals. Floodwater can be diverted into the Tongting Lake through three channels and flows back to the river at Chenglingji after the flood recedes, which can reduce peak flow of the river by about 10,000 m^3/s. The Tongting Lake, however, is shrinking quickly due to sedimentation and reclamation. The Three Gorges Reservoir, in co-ordination with the enhanced levees and utilization of temporary flood-diversion works, can raise flood control capacity to defend against 100-years

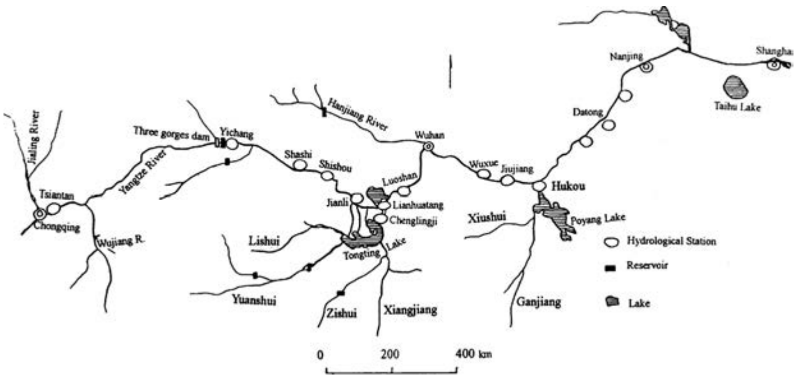

Figure 1. The Yangtze River and its tributaries, riparian lakes, hydrological stations and the dam site of the Three Gorges Project.

floods. It will reduce water and sand discharge into the Tongting Lake and reduce the rate of sedimentation of the lake.

The hydroelectric station of the TGP is the biggest in the world, with an installed capacity of 17,680 MW and an annual generation of 84 billion kwh. The project may replace several thermal power stations, thus reduce the consumption of coal by 50 million tons per year and cut carbon dioxide, sulphur-dioxide, carbon monoxide and nitrogen-oxide emissions by 100 million tons, 2 million tons and 10,000 tons and 370,000 tons, respectively.

The project will improve navigation conditions from Yichang to Chongqing, by eliminating shoals, deepening and widening the shipping lanes and reducing river currents, and thus enable 10,000-ton towboats to sail right up to Chongqing. The annual shipping capacity will increase to 50 million tons from the present 10 million tons and transport costs will be cut by 35–37%.

2 SEDIMENTATION IN THE RESERVOIR

The rate of sedimentation in the reservoir depends mainly on the pool levels and operation scheme. The normal pool level (NPL) is set at 175 m, and the flood control level (FCL), to which the pool will be drawn down at the beginning of the flood season generally in June, is set at 145 m. The reservoir is impounded to NPL after the flood season, usually from the mid of October and drawn down to FCL before and during flood. FCL is the major factor affecting the sediment deposition amount in the reservoir.

The long-term average annual runoff at Yichang Station is 450 billion m^3 and annual sediment load is 532 million tons, in which about 0.8 million tons are gravel bed load. The median diameter of suspended load is 0.033 mm and the median diameter of bed load is 24 mm.

The main strategy for sedimentation control is "storing the clear and releasing the turbid" (Sedimentation Panel, 1988). Sediment transportation in the Yangtze River occurs, of 80–90% of annual sediment load with 50–60% of annual runoff water, in 2–4 months of the flood season. The pool level is drawn down from 175 m to 145 m from June to September when the sediment concentration is high, allowing the turbid water through the dam. The reservoir stores water from October when the income water becomes clear. Fig. 2 shows the typical variation process of sediment concentration at Yichang and the operational pool level for sedimentation control. By employing the strategy of "storing the clear and releasing the turbid", much less sediment will deposit in the reservoir while the reservoir will be still able to store enough water for power generation in the low flow seasons.

Although the pool level is drawn down to FCL, the stage in a 400 km long reach within the reservoir is 10–70 m higher than those without the dam and the average velocity is much slower. For a discharge of 30,000 m^3/s, the average velocity would be 1.5–3.5 m/s if there were no dam,

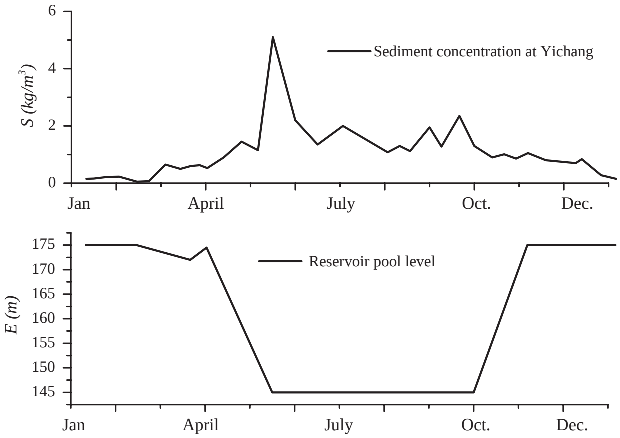

Figure 2. Typical processes of sediment concentration at Yichang and the operational pool level of the reservoir for sedimentation control.

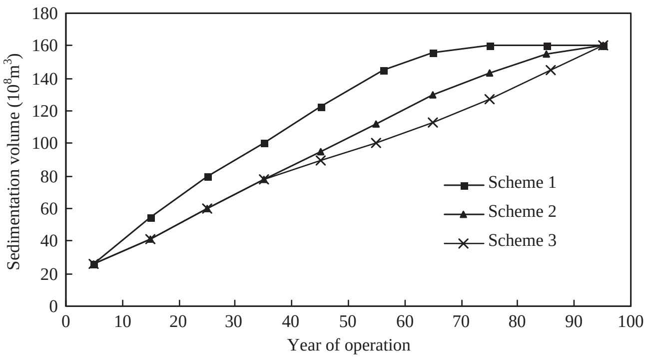

Figure 3. Calculated sedimentation volume in the TGP reservoir for the three scenarios: Scheme 1 = without upstream reservoirs; Scheme 2 = with the Xiangjiaba Reservoir; Scheme 3 = with the Xiluodu Reservoir (Sedimentation Panel of TGP, 2002).

and it is only 0.3–1.3 m/s with the dam. Therefore, sedimentation occurs and the riverbed is silted up. Calculation with numerical models shows that after 80 years operation, the accumulative sedimentation amount will approach equilibrium and will increase very slowly thenceforth. The total sedimentation in 100 years will be about 16 billion m^3 (Sedimentation Panel of TGP, 2002).

In order to reduce the rate of sedimentation and develop the hydropower of the river, two more reservoirs – the Xiangjiaba and Xiluodu reservoirs – will be constructed on the river. The Xiangjiaba dam will be located at 1,020 km upstream of the TGP dam, with a storing capacity of 5.06 billion m^3. The reservoir can be used to trap sediment for 60 years. The Xiluodu dam will be located at 1,180 km upstream of the TGP dam, with a total capacity of 11.57 billion m^3, which can be used to trap sediment for 90 years (YVPO, 2002). Bed load and coarse suspended load from upstream reaches can be trapped by the two reservoirs. Thus, the rate of sedimentation of the TGP reservoir will be reduced in the first 90 years. Fig. 3 shows the calculated sedimentation volume of the TGP reservoir for the three scenarios: Scheme 1 = without upstream reservoirs; Scheme 2 = with the Xiangjiaba Reservoir; Scheme 3 = with the Xiluodu Reservoir (Sedimentation Panel, 2002).

The industrial hub – Chongqing City – is in the fluctuating backwater region. The Jialing River flows into the Yangtze River at Chongqing. Chaotianmen harbor is a passenger ship terminal and Jiulongpo Harbor, which is about 610 km from the dam, is the most important freight ship terminal in southwest China (Fig. 4).

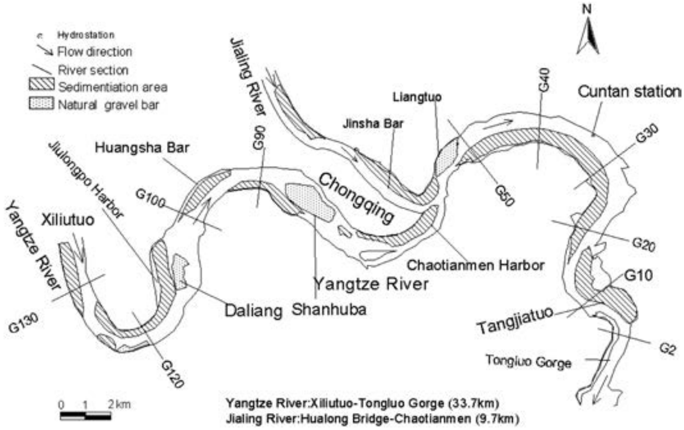

Figure 4. Sedimentation in the Chongqing reach after 80 years operation of the TGP reservoir (Physical model experimental results). The shadowed areas indicate the places where cumulative sedimentation would occur. G2–G130 represent the measurement cross sections (Wang et al., 1986).

Scale model experiments have been performed to study the sedimentation problems in a 33 km-long section around Chongqing. The experiments showed that impoundment of the reservoir will cause sediment deposition at the apron of the harbors, as shown in Fig. 4. The shadowed areas in the figure indicate the places where cumulative sedimentation would occur. There are two channels separated by the Daliang Bar. Water flows in the west channel during low flow season and the main stream flow shifted to the east channel during flood, but the west channel maintains around-the-year a depth over 3 meters, which is necessary for the harbor. After 80 years impoundment of the reservoir, however, cumulative sedimentation would occur in the west channel, which could result in blockage of the channel eventually. The harbor facilities would not be useful if dredging or other technical measures were not taken. The experiments showed that building spur dykes and groins to regulate the flow could solve the problem. The dykes and groins may narrow the channel and concentrate the flow, so that flow velocity in the west channel can be enhanced, which can prevent sediment from depositing (Wang et al., 1986).

3 DEGRADATION OF THE DOWNSTREAM REACHES

The discharge released from the dam will be higher from January to May but lower from October to November than that without the dam (Fig. 5a). It will remain unchanged during flood season from July to September. Fig. 5b shows the calculated annual sediment load released to the downstream reaches, compared with the annual sediment load at Yichang under natural conditions (recycle of the data in the period 1961–1970). The sediment load will be greatly reduced by the reservoir in the first 50 years. The load reduction must cause degradation of the downstream reaches (Tsinghua, 2002).

China Institute of Water Resources and Hydro-Power Research (IWHR, 2002) and Yangtze River Planning Office (YVPO) calculated the amount of sediment that will be scoured from the riverbed from Yichang to Wuhan with 1-D models. Fig. 6 shows the results of the two models, in which minus value means scoured volume. In the first 40 years the two models yield the same results, about −2.5 billion tons at the end of the 20th year and −4 billion tons at the end of the 40th year. Resiltation will occur from the 50th year (YVPO model) or from 70th year (IWHR model). The scour and reduction of riverbed will cause flood stage reduction, which will be 3 m at Shashi and 0.75 m at Wuhan for a flood of discharge 30,000 m^3/s. Fig. 7 shows the calculated bed profiles and stage profiles in the 120 km long reach. The scoured depth will be different at different places because the composition of bed materials and bedrock elevation are different (Sedimentation Panel, 2002).

The Tongting Lake regulates the flood flow. Water and sediment are diverted into the lake during high flood stage period through three channels and water flows back to the river from the

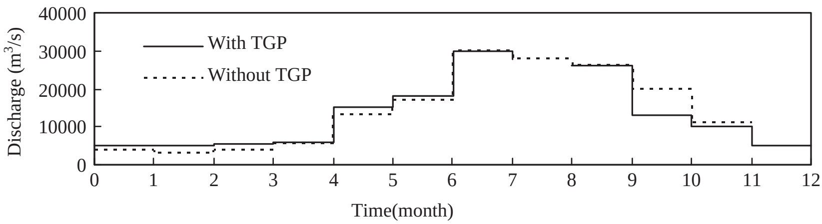

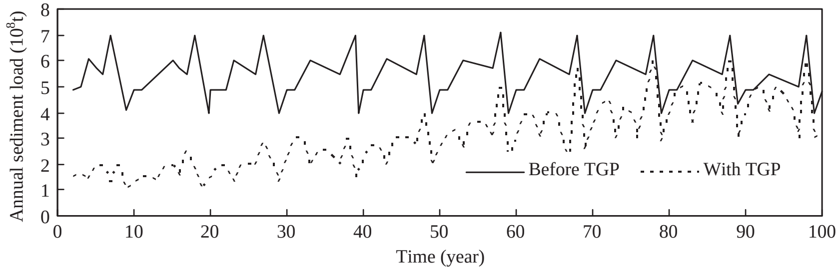

Figure 5. (a) Month-mean discharges under the natural conditions and with the regulation of the TGP reservoir. (b) Variation process of annual sediment load released to the downstream reaches from the reservoir compared with the annual sediment load at Yichang under natural conditions (recycle of the data in the period 1961–1970) (Sedimentation Panel, 2002).

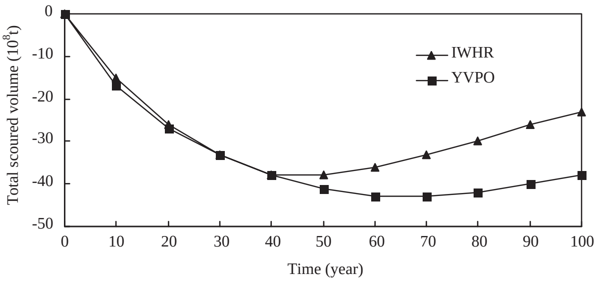

Figure 6. Calculated amount of sediment that will be scoured from the riverbed from Yichang to Wuhan by the China Institute of Water Resources and Hydro-Power Research (IWHR) model and Yangtze River Planning Office (YVPO) model (Sedimentation Panel, 2002).

lake during the falling limb of the flood through a downstream channel near Chenglingji. At the present, the lake shrinks at a rate of $-14\,km^2/a$ due to sedimentation. The reservoir will reduce the sedimentation rate of the lake and extend its useful life. According to model calculation, the ratio of flood water diverted into the lake will decrease from 11.5% to 8% after 10 years operation of the reservoir. Fig. 8 shows the reduction of floodwater volume and sediment volume diverted into the lake through the channels in the period 0–60 years. The floodwater diverted into the lake will be reduced by about 40% but sediment volume will be reduced by about 70% (Sedimentation Panel, 2002). The shrinkage of the lake will largely slow down but the function of the lake in flood regulation will also diminish.

Although the dam is about 1,900 km distant from the river mouth, the reservoir affects, more or less, the river mouth. Nowadays, 48% of the coast in the estuary are suffering from erosion, but 38% are extending toward the sea, and only 14% are stable. For instance the Nanhui beach is extending toward the sea due to sediment deposition. It is estimated that the impoundment of the TGP reservoir will increase the percentage of eroded coastline and cause the Nanhui beach retreating by 1,457 m in 40 years. Sand bars in the river mouth area will shrink as well.

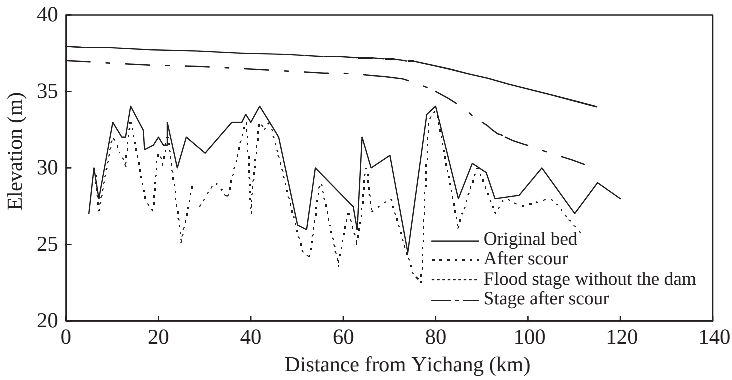

Figure 7. Calculated flood stage profiles and bed profiles before and after scouring of the riverbed (Sedimentation Panel, 2002).

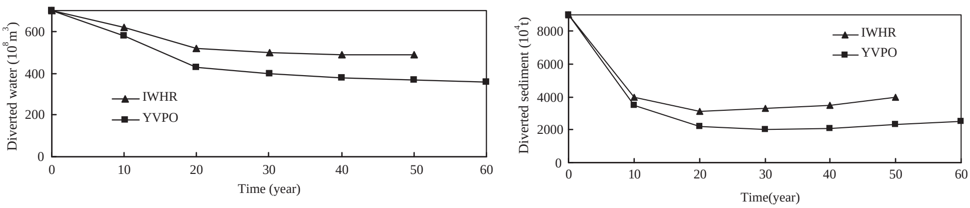

Figure 8. Reduction of floodwater volume and sediment volume diverted into the Tongting lake through the three channels in the period 0–60 years of reservoir operation (Sedimentation Panel, 2002).

4 ENVIRONMENTAL AND ECOLOGICAL IMPACTS

Earthquakes: The mechanism of reservoir-induced earthquakes has not been well understood yet so far. Since 1960 six reservoirs induced earthquakes of magnitudes over 6 on the Richter scale but caused no destruction of any dam. The quake induced by Xinfengjiang Reservoir in China has caused slight damage to the dam. Statistics shows that only 5% of reservoirs each with a storage capacity of more than 100 million m^3 have set off tremors in China. Although TGP reservoir has a huge capacity its impoundment will cause no great geological stress because the reservoir will extend over 660 km long and the increased stress is diverse. The dam is located in an area where the earth crust is relatively stable. Historical records covering the past 2,000 years indicate that no destructive earthquakes have ever occurred within a 300-km radius of the site of the dam. Seven seismic monitoring stations in the dam's vicinity have been monitoring tremors. A total of 2,910 shocks of a magnitude of 1 or higher have been recorded within a 300-km radius around the dam. Of these, only a few are of magnitude over 4. A new digital monitoring system has been put into use to monitor earthquakes since 2000 and 9 wells over 800 m deep have been used to sense the stress tension (Yang, 2003).

Landslides: The Yangtze River cut its bed deeply into the gorges and causes the slopes on the two banks unstable. For instance, the 1985 landslide at Xintan Town, Hubei Province, hurled 2.6 million m^3 of earth and stone into the river, forming a 55 m-high hillock. Investigations found that there are 263 landslides, rockfalls and deformed rock masses on the 1380 km long valley slopes from the dam site upstream to Jiangjin. The total volume of them is about 1.6 billion m^3 (Han et al., 1988). About 6% of the landslides are precarious and 10% may buckle after the reservoir is filled with water. Studies of the stability of the reservoir slopes have been going on for several decades and sufficient data have been acquired of the basic conditions of the reservoir banks. Fig. 9 shows the distribution of potential landslides in the reservoir.

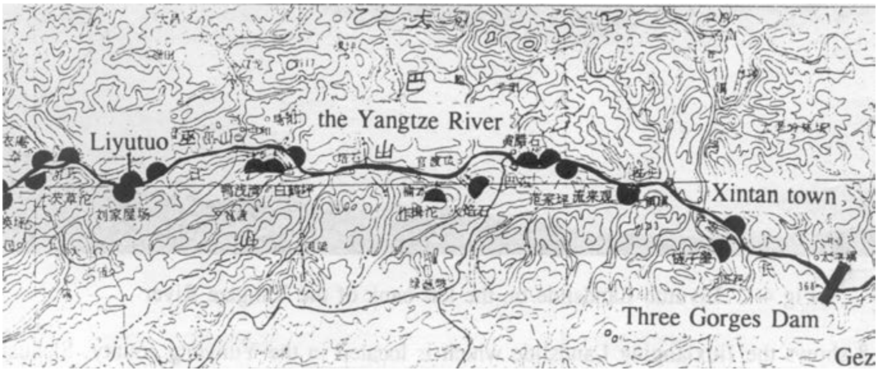

Figure 9. Distribution of potential landslides (black hemi-circles) in the TGP reservoir.

The pool level of the reservoir will vary in the range 145–175 m and the fluctuation of pool level will certainly induce instability of slopes and cause landslides. However, after the reservoir is filled with water, the river will broaden and the water will deepen. A landslide, which may hinder navigation under natural condition, will not do so in the reservoir. Studies indicate that any collapse of slopes will not clog the river nor form a blockage.

Water Quality: The annual runoff at the dam is over 400 billion m^3; and the total wastewater discharged into the reservoir is predicted to be about 1 billion tons. Now the water quality of the river, however, remains good, except for pollution belts along the banks near cities. Generally speaking, after impoundment the pollution in the reservoir will worsen due to lower flow velocity and lower concentration of dissolved oxygen. To a press conference on June 5, 2003, the director of State Environment Protection Bureau, Mr. Xie Zhenhua (2003), reported that the impoundment of the TGP reservoir has not obviously affected the water quality. In 2002, 144-million m^3 wastewater and 319-million m^3 sewage water were discharged into the reservoir. In the same period, 20 incidents of oil spills from boats occurred in the reservoir. The water quality in the reservoir is still in Grade III. Only in some places, the content of bacilli is higher. A pollution control project has been launched 2 years ago. All wastewater and sewage water will be treated after the completion of the project (Chinese Hydroweb, 2003). Studies indicate that the thermal stratification in the reservoir water will begin around April and end in May. The released water from the bottom outlets will be colder in this period, which may cause 20 days late for the temperature of downstream water to rise to the spawning temperature of 18°C.

Impacts on Fishery: There are 300 fishery species in the middle and lower Yangtze River, including catfish, bleak, carp, grass carp and so on. After the impoundment, the freshwater fishes that thrive in rapids would have to move upstream to find new habitats. The expanded water surface of the reservoir may create better conditions for aquatic farming. The existing eight spawning grounds located in the section between Chongqing and Zigui will be inundated in part or in whole. The breeding of farm fishes has to be moved to the uppermost end of the reservoir or even farther. In addition, the spawning and breeding period will occur later due to the changes in flow and water temperature.

Flood and stage rise are the main signals for fish to spawn (Yi and Liang, 1964). Fig. 10a shows the stage variations at Yichang and Jianli and the time of fish spawning, in which the solid circles represent spawning of fishes (Cao et al., 1987). Fig. 10b shows the relationship between the discharge increment in a few to ten days and the flux of fries, in which the flux of fries was about 4–6 days lag behind the discharge increase. The figures demonstrate that the spawning of fishes is excited by the stage and discharge increase. The higher the discharge increase is, the higher the flux of fries will be. The reservoir will moderate the stage rise and discharge increase in May, which will affect the spawning of fishes and reduce the flux of fries.

Impacts on Endangered Aquatic Species: There are several important species in the river, Chinese sturgeon, white-flag dolphin, Yangtze alligator, giant salamander and black finless porpoise are several among them. The reservoir will impact little on the living conditions of the Yangtze alligator,

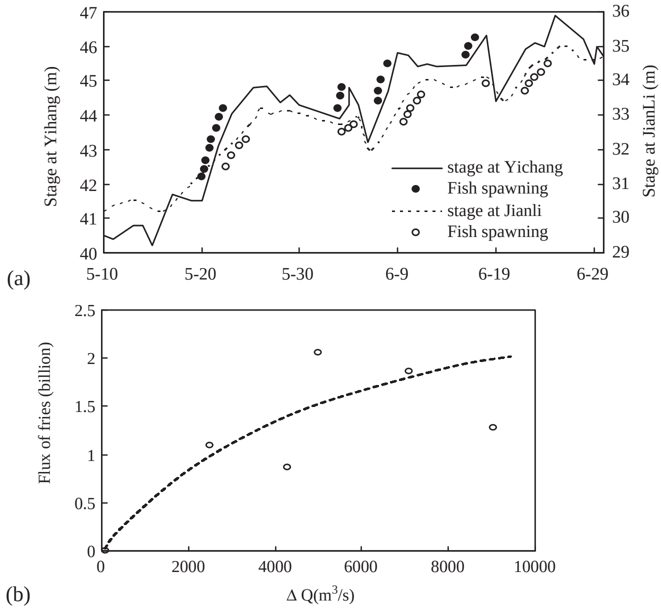

Figure 10. (a) Stage variation at Yichang and Jianli under natural conditions and the spawning time of fishery species; (b) Relationship between the discharge increment and flux of fries (Cao et al., 1987).

giant salamander and black finless porpoise. Chinese sturgeon usually swims upstream to spawn and then return to their home grounds. The Gezhouba Dam has made it impossible for the fish to swim upper and down the river during the spawning period. But the specie has spawned naturally in the waters below the dam. White-flag dolphin usually lives in meandering and braided sections below the TGP dam. Studies indicate that the species finds its best habitats in meandering and braided-meandering sections because it has been accustomed to the backwater zones created by the convex bank of meanders or the gravel and sand bars in the braided channels (Chen and Hua, 1987). The reservoir may change the fluvial processes and some meandering and braided sections of the river may become unstable, which will undermine the habitats of the species. More studies are needed for protection of the species.

5 EMIGRATION AND RESETTLEMENT

A total of 19 counties and cities, 13 county towns, 140 towns and 4,500 villages would be affected by the reservoir inundation. According to the data in 1985, the population to be dislocated will be 725,500, including urban population 285,200, towns' population 107,800 and villagers 332,500. New investigation in 1992 demonstrates that there are about 844,000 people in the submerged area. By taking the population growth into account, the total number of people to be emigrated from the reservoir will be 1.1318 million up to the year 2008 (Changjiang River Commission, 1997). The pilot resettlement projects began from 1984. Chinese government has invested 28.7 billion Yuan on emigration and 458,000 people have successfully resettled up to the end of 2003.

Production capita to be inundated includes 23,793 h of farmland (paddy field: 7,380 h, and dry farmland: 16,314 h), and 4,960 h of citrus orchards, 956 km long highways and 941 factories and mines; and over 200 million US dollars of fixed assets will be affected as well. The people in the submerged area will be emigrated from the area in 20 years (started from 1989). The basic policy is to resettle them in the surrounding area. The GDP per capita in the area is only 45% the national average and the income per capita is only 53% the national average. There is a big room to develop local industry and tourism industry. With help of the government, the urban resettled residents find jobs in the county towns and cities. Because the emigrants are leading a better life than before, 70% of the local people are willing to remove from their old homes.

The investment for the resettlement of the emigrants is about \$2,700 for each emigrant. Moreover the emigrants are paid back for their houses at a rate of \$35/m^2. The removed production facilities are also compensated according to the estimation of the market price. The resettlement programs are implementing at county and township level under the guidance of overall planning of local socio-economic development. Farmers in the submerged areas will lose their land, how can they continue farm production after resettled in the nearby areas? The number of people an area can accommodate depends on the natural conditions, resources, and economic developmental level. The water surface of the reservoir will be 1,084 km^2. The total area of land to be inundated will be 632 km^2, which equals 1% of the total area of the surrounding area (19 counties and cities). The total area of farmland to be inundated is 23,000 hectares but the largest proportion of it is low-yield hillside land. Experiments indicate that 2.7 million hectares of the barren slope-land in the surrounding area may be transformed into a terraced citrus orchard, and then it is able to turn out an output value equal to as much as three times farmland, thus the surrounding area will be able to support the resettled farmers (Chen and Zhou, 1987).

The emigrants are also encouraged to settle in other provinces at their willing. The State Council has made a decision that all provincial governments should provide assistance for emigration and resettlement. A number of economically developed provinces and municipalities have made agreements with the counties in the reservoir area to assist the resettlement. Many people have found their homes in lower reaches of the Yangtze River, the Chongming Island at the river mouth, the Xingjiang Urgle autonomous region, Hainan, Heilongjiang and other provinces.

6 CONCLUSIONS

The Three Gorges Project on the Yangtze River, with purposes of flood control, power generation and navigation, will impact the environment and ecology in both the upstream and downstream reaches. Cumulative sedimentation in the reservoir will reach an equilibrium in 100 years with a total volume about 16 billion m^3. The Xiangjiaba and Xiluodu reservoirs can be used to trap sediment and reduce the sedimentation rate of TGP reservoir in the first 90 years. The Jiulongpo harbor in Chongqing will be affected or even blocked by sedimentation after the reservoir is impounded for 80 years. Building spur dykes and groins to regulate the flow can solve the problem. The released water from the dam will scour 2.5 billion tons of sediment in 40 years and will cause the river channel degradation; and the flood stage will be reduced by about 3 m at Shashi and 0.75 m at Wuhan for a flood of discharge 30,000 m^3/s. The reservoir will not necessarily cause tremors, but will induce more landslides. Wastewater treatment projects are necessary to control pollution and maintain the water quality in the reservoir unchanged. The reservoir operation will affect the life cycles and habitats of fishes and reduce the fishery harvest. Some endangered species may be affected because some meandering and braided sections may become unstable. About 2.7 million hectares of barren slope-land in the 19 counties affected by the reservoir can be transformed into a terraced citrus orchard, which is able to turn out an output value equal to as much as those by the inundated land.

ACKNOWLEGEMENT

This work is supported by the 973 Program (No.2003CB415206).

REFERENCES

Cao Wenxuan et al., 1987, Impacts of the Three Gorges Project on Aquatic Ecosystems along the Changjiang River and Possible Countermeasures, in Environment and Ecology Panel of Chinese Academy of Sciences for the TGP Project (eds), Impacts of the Yangtze River Three Gorges Project on Environment and Ecology, Chinese Science Press (in Chinese).

Changjiang River Commission, 1997, Studies on the Emigration for the Three Gorges Project, Hubei Science and Technology Press.

Chen Hongzhao and Zhou Huizhen, 1987, Effects of the Three Gorges Project on land resources in the reservoir area and possible countermeasures, in Environment and Ecology Panel of Chinese Academy of Sciences for the TGP Project (eds), Impacts of the Yangtze River Three Gorges Project on Environment and Ecology, Chinese Science Press (in Chinese).

Chen Peixun and Hua Yuanyu, 1987, Prediction of Effects of the Three Gorge Project on Fish Resources in Lakes along the Middle Changjiang River and Study of Possible Countermeasure, in Environment and Ecology Panel of Chinese Academy of Sciences for the TGP Project (eds), Impacts of the Yangtze River Three Gorges Project on Environment and Ecology, Chinese Science Press.

Chinese Hydro-Web, 2003, http://www.Chinawater.com, on March 2, 2003.

Han Zongshan et al., 1988, Landslides and rockfalls of Yangtze Gorges, Geological Publishing House and Tai Dao Publishing Ltd.

IWHR (China Institute of Water Resources and Hydro-electric Power Research), 1989, Progress report on the physical model study on the channel regulation projects of the Chongqing section of the TGP reservoir (175 m scheme), Selection of Papers on the Sedimentation Studies for the Yangtze River Three Gorges Project, Chinese Science and Technology Press (in Chinese).

IWHR (China Institute of Water Resources and Hydro-Electric Power Research), 2002, Calculation of erosion and sedimentation of the Yangtze River from the TGP dam down to Datong with a 1D model, Sedimentation Studies for the Yangtze River Three Gorges Project, Vol.7, China Patent Press (in Chinese).

Ministry of Water Resources of China, 1999, 1998 floods in China, Water and Hydropower Press (in Chinese).

Sedimentation Panel for TGP Project, 1988, Suggestion for the pool level schemes for the Yangtze River Three Gorges Project, Proceedings of the Sedimentation Studies for the Yangtze River Three Gorges Project (160 m–180 m Schemes), Department of Science and Technology, the Ministry of Water Resources of China (in Chinese).

Sedimentation Panel for TGP, 2002, Comprehensive analysis on “9.5” sedimentation study results for the Three Gorges Project on the Yangtze River, Intellectual Copyright Press (in Chinese).

Tsinghua University, 2002, Comparison and assessment of the calculation results of erosion and sedimentation of the Yangtze River from the TGP dam down to Datong with a 1D models, Sedimentation Studies for the Yangtze River Three Gorges Project, Vol.7, China Patent Press (in Chinese).

Wang Zhaoyin, Lu Xiuzhen and Zeng Qinghua, 1990, Physical model experimental study on sedimentation in the Chongqing reach of the Yangtze River for the Three Gorges Project – a report for the 175 m scheme, in the Collection of Research Results on the Sedimentation in the Chongqing reach of the Yangtze River 195–1990, China Institute of Water Resources and Hydro-Power Research (in Chinese).

Xie Zhenhua, 2003, Press conference on June 5, Consulate-general of the People’s Republic of China in Milan, http://www.consolatocinami.it/.

Yang Shengjin, 2003, Will impoundment of TGP reservoir induce earthquake? WWW.Chinanews.Com, June 01, 2003.

YVPO, Yangtze River Research Institute, 2002, Calculation of erosion and sedimentation of the Yangtze River from the TGP dam down to Datong with a 1D model, Sedimentation Studies for the Yangtze River Three Gorges Project, Vol.7, China Patent Press (in Chinese).

YVPO, Yangtze River Research Institute, 2002, Calculation with 1-D numerical model for the sedimentation of TGP Reservoir in the scenarios of construction of the Xiluodu and Xiangjiaba Dam, Sedimentation Studies for the Yangtze River Three Gorges Project, Vol.5, China Patent Press (in Chinese).

Yangtze River Research Institute, YVPO, 2002, Physical model experiments on the regulation of the navigation channel in the Chongqing-Tongluo gorge reach, Sedimentation Studies for the Yangtze River Three Gorges Project, Vol.5, China Patent Press (in Chinese).

Yi B. and Liang Z., 1964, The natural conditions of the spawning ground and external factors affecting fish spawning in the Yangtze River, Journal of Hydrobiology, Vol.5, No.1, pp.1–15 (in Chinese).

Zhou Zhide, 1999, 1998 floods in the Yangtze River valley, International Research and Training Center on Erosion and Sedimentation, UNESCO Beijing Office.

Environmental Hydraulics and Sustainable Water Management – Lee & Lam (eds)
© 2005 Taylor & Francis Group, London, ISBN 04 1536 546 5

Resolving environmental hydraulics complexity, linking theory, practice and conceptual ideas

Klas Cederwall
Department of Land and Water Resources, Royal Institute of Technology, Stockholm, Sweden

ABSTRACT: Environmental systems studies often have a base in water transport and mixing focusing on the significance of preserving water quality. This presentation follows a learning process starting with point source and near field studies to the integration of larger parts of the natural environment and more diffuse patterns of pollution. The Stockholm archipelago is an example of a water system that has unique invaluable assets and at the same time is extremely sensitive to environmental disturbances. A combination of theoretical and empirical analysis provides means for developing effective environmental management principles.

1 INTRODUCTION

Engineering research is in a broader and deeper context concerned with the societal benefits and possible improvements of quality of life, which can be created by such efforts. This emphasizes a need for a mode of research that is more interdisciplinary and more socially accountable than the traditional disciplinary research. An example of the significance of developing comprehensive knowledge in environmental hydraulics and a qualified environmental management capacity, is the Stockholm archipelago.

The Stockholm archipelago and its Finnish counterparts Åland and Åboland archipelagoes form the world's largest continuous archipelago area. Thousands of islands provide a very complex water landscape with coastal basins and interconnecting straits. The water exchange and flushing of pollutants to the open sea is reduced and maintained by an estuarine circulation characterized by a brackish type and weakly stratified environment. The nature in this area is beautiful but vulnerable. There is great potential for conflicts between human activities and preservation interests in the future. To maintain good water quality is crucial and so is the capacity to monitor and control the environmental health status, since the water quality is threatened by a wide spectrum of point and more distributed sources of pollution.

The environmental situation of the archipelago is linked to Lake Mälaren, which outflows directly through Stockholm into the archipelago. For the analysis and modeling of water exchange, the archipelago forms a system of major water basins and their interconnecting straits, around 50 discrete basins and 100 straits – a few of these straits hydraulically control the estuarine circulation (Figure 1). Applying driving forces and environmental loadings on the system will provide the basis for prediction of water quality conditions as a dynamic process.

2 DEALING WITH COMPLEX DIFFUSION MECHANISMS

It takes some steps to establish physical insight into environmental mixing phenomenon. Two simple cases, i.e. a plume in a linearly stratified environment, and gravitational diffusion induced by an air-bubble plume, can be analysed with the powerful dimensional reasoning method. The following cases are elaborated briefly and further information is available in the references.

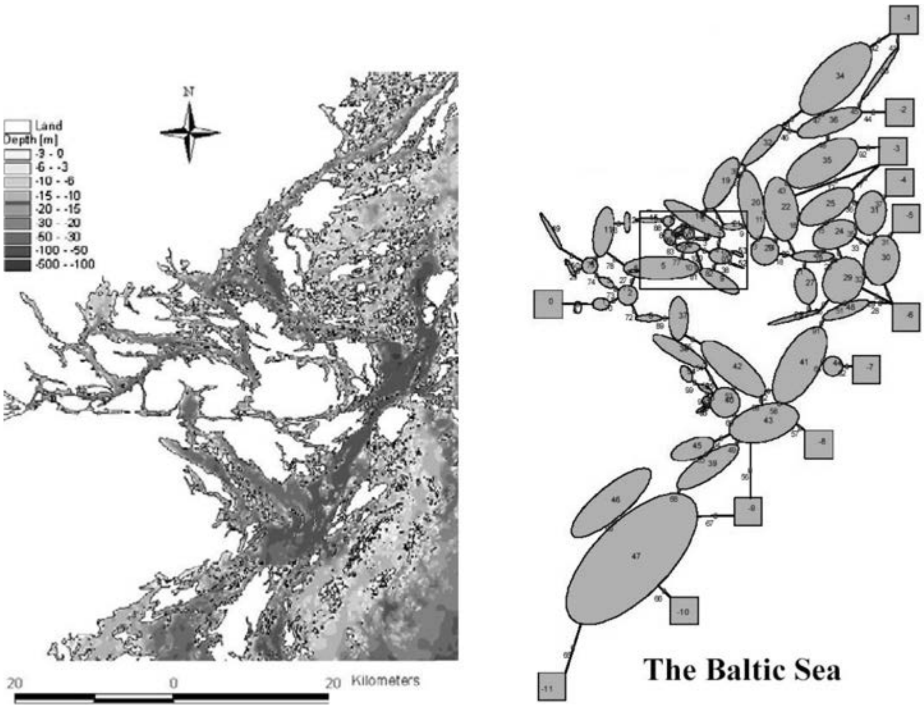

Figure 1. The Stockholm archipelago, bathymetry (left) and basin-decomposition (right) (Engqvist, A., and Andrejev, O., 2003, Stenström, P., 2003).

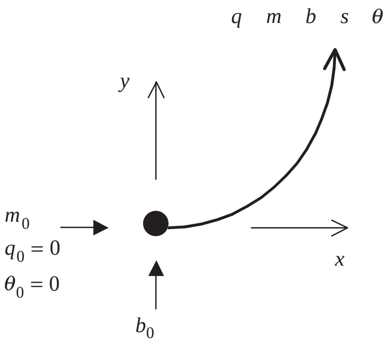

Figure 2. A three dimensional buoyant jet (Cederwall, 1975).

2.1 *Buoyant jet diffusion*

Let us assume an idealized source characterized by initial flux of momentum and buoyancy only having the same dynamic impact on the environment as a corresponding volume source with volume flux. To simplify, let the initial momentum flux be horizontal and the buoyant jet three-dimensional as illustrated in Figure 2.

The momentum, buoyancy and volume fluxes along the buoyant jet trajectory are all Eulerian quantities. However, *m* and *b* will be included in the following Lagrangian equations:

$$\frac{d}{dt}(m \cos\theta) = 0 \tag{1}$$

$$\frac{d}{dt}\left(m \cdot \sin\theta\right) = b \quad , \tag{2}$$

where t is a time variable defined by a Lagrangian velocity that moves a control volume along the jet trajectory so that there is no net momentum flux passing through the control volume. Consequently we have

$$\frac{ds}{dt} = u_L \tag{3}$$

$$\int_{A(l)} \rho\, u\, (u - u_L) \cdot dA(l) = 0 \quad , \tag{4}$$

where $A(l)$ is the lateral area of the moving control volume, a function of the typical jet width l only. This gives us the following equation defining the Lagrangian velocity.

$$\begin{cases} m - u_L \cdot q = 0 \\ u_L = \dfrac{m}{q} \end{cases} \tag{5}$$

The only change of momentum is then within the moving control volume and furthermore the buoyancy flux is conserved. Applying the principle of entrainment we get the following equation for conservation of volume flux where β is an empirical constant.

$$\frac{dq}{ds} = 2\pi\, l \cdot w = \beta \cdot s \cdot \frac{m}{q} \tag{6}$$

Hence, the following equations reduced to Eulerian form will characterize the diffusion process including also the equation for the jet trajectory

$$m\frac{dx}{ds} = m_0 \tag{7}$$

$$\frac{m}{q} \cdot \frac{d}{ds}\left[m\frac{dy}{ds}\right] = b_0 \tag{8}$$

$$\frac{dq}{ds} = \beta \cdot s \cdot \frac{m}{q} \tag{9}$$

$$\left(\frac{dy}{ds}\right)^2 + \left(\frac{dx}{ds}\right)^2 = 1 \tag{10}$$

Normalizing the equations and solving numerically for given starting conditions will give the result illustrated in Figure 3. The relation between mean dilution S from the present theory and the centerline dilution according to Abraham’s theory is found to be approximately in line with experimental findings.

2.2 *Air-bubble plumes*

Air-bubble plumes have been used for a variety of purposes such as pneumatic breakwaters, for prevention of ice formation, as barriers against salt water intrusion in rivers and locks, for stopping the spreading of oil spills on the water surface, for reduction of underwater explosion waves and for mixing and reaeration in density stratified reservoirs to improve water quality. The physical

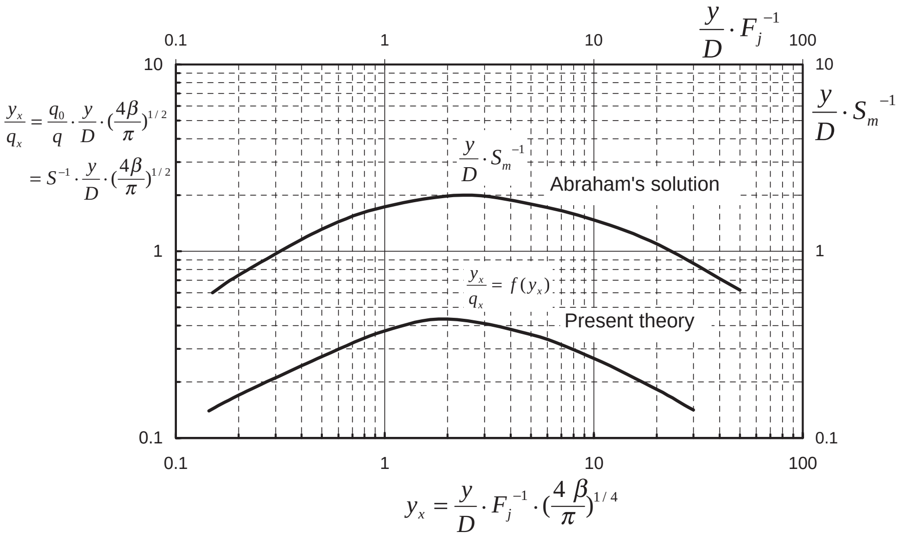

Figure 3. Horizontal buoyant jet dilutions according to present and existing theories (Abraham, 1963, Cederwall, 1975).

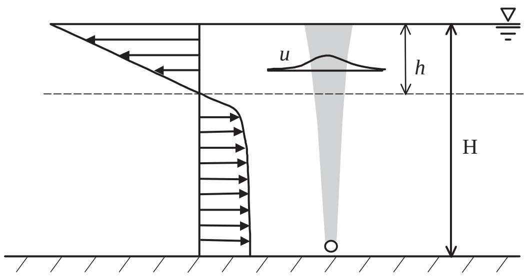

Figure 4. Velocity field close to the air-bubble plume (Cederwall, 1971).

structure of air-bubble systems is very complex making it difficult to provide a general theory. The gross behavior of the air-bubble plume can however be analyzed sufficiently well for design purposes. The velocity field close to the air-bubble plume is illustrated in Figure 4.

A flow model for the air-bubble plume can be based on the similarity to the basic buoyant plume phenomenon as previously discussed. The interaction between the rising bubbles and the ambient water is a complex function depending on several parameters.

An idealized model will be based on the following selection of significant variables:

q_0	The volume rate of air flow at atmospheric pressure
u_b	The differential velocity of the air bubbles relative to the water
$[(\rho_a - \rho_{air})/\rho_a]g$	Apparent gravity where ρ_a and ρ_{air} are the density of the ambient water and the air respectively and g the acceleration of gravity
H	The depth above the air flow source
H_0	Piezometric head equivalent to the atmospheric pressure (H_0 is regarded as a constant ≈ 10.4 m).

The terminal rise velocity of an air bubble in stagnant ambient water is assumed to be attained near the source and then remain essentially constant throughout the depth and to be equal for all bubbles. This has been found experimentally to be a good approximation. The expansion of the air bubbles as they rise through the water is neither adiabatic nor truly isothermal. The choice of gas law does not significantly affect the theoretical result. Assuming isothermal conditions gives the following volume rate of air flow.

$$q(x)\cdot(H_0+H-x)=q_0\cdot H_0 \tag{11}$$

Dimensional reasoning implies that we have two non-dimensional parameters, a design parameter and a scaling ratio, to characterize the flow phenomenon. The analysis is restricted to the zone where the horizontal flow near the surface does not affect the vertical flow, that is for x less than $H-h$.

$$\frac{u_b^3\cdot H}{q_0\dfrac{\rho_a-\rho_{air}}{\rho_a}g} \text{ or } \frac{u_b^3}{q_0\dfrac{\rho_a-\rho_{air}}{\rho_a}g} \text{ and } \frac{H}{H_0}\text{, for point or line source respectively.}$$

The first parameter is a "design parameter" and the second one a scaling parameter.

When the air-bubbles rise through the water the vertical flow resembles turbulent diffusion from a buoyancy source. To solve the problem an integral technique is used. The rate of entrainment at the edge of the plume is assumed proportional to the mean axial plume velocity. The similarity principle is used to describe velocity and density deficiency distributions. We then have for a point source of buoyancy only:

$$u=u_m\cdot e^{-r^2/b^2} \tag{12}$$

$$(\rho_a-\rho_m)=\Delta\rho_m\cdot e^{-r^2/(\lambda b)^2} \tag{13}$$

The volume flux and the rate of entrainment are given as follows where the coefficient of entrainment is assumed to be constant. Similarly relations for the buoyancy flux

$$Q=\int_0^\infty 2\pi\,u\,r\cdot dr=2\pi\,u_m\cdot\int_0^\infty e^{-r^2/b^2}\,r\cdot dr=\pi\cdot u_m\cdot b^2 \tag{14}$$

$$\frac{dQ}{dx}=2\pi\,b\,\alpha\,u_m \tag{15}$$

$$B=\int_0^\infty 2\pi(u+u_b)(\rho_a-\rho_m)\,r\cdot dr=\pi\,u_m\,\Delta\rho_m\frac{\lambda^2b^2}{1+\lambda^2}+\pi\,u_b\,\Delta\rho_m\lambda^2b^2$$

$$=q_0(\rho_a-\rho_{air})\frac{H_0}{H_0+H-x}$$

For

$$\rho_{air}<<\rho_a,\ B=q_0\,\rho_a\frac{H_0}{H_0+H-x}. \tag{16}$$

The momentum flux is given by

$$M=\int_0^\infty 2\pi\,u^2\,\rho_a\,r\cdot dr=\frac{\pi\,u_m^2\rho_a b^2}{2} \tag{17}$$

The driving force of the plume is the buoyancy and the momentum flux equation is then given by

$$\frac{dM}{dx} = \int_0^\infty 2\pi\ (\rho_a - \rho_m)\, g\, r \cdot dr = \pi\, g\, \Delta\rho_m\, \lambda^2\, b^2 \tag{18}$$

We then have the following equations for a point source to obtain the centerline values of the velocity and the half-width b of the plume:

$$\frac{d(u_m\ b^2)}{dx} = 2\alpha\ u_m\, b \tag{19}$$

$$\frac{d(u_m{}^2\ b^2)}{dx} = \frac{2g\, q_0\, H_0}{\pi(H_0 + H - x) \cdot (\frac{u_m}{1+\lambda^2} + u_b)} \tag{20}$$

The differential equations may be solved by numerical integration after a normalizing procedure as illustrated in the main reference.

2.3 *Tracer simulation of dispersion*

Field surveys by use of tracer technology are important measures in investigation of water circulation and exchange processes in receiving water bodies exposed to pollutants. The dispersion properties of the receiving water can be studied either by repeated instantaneous tracer injections or by a continuous adding of tracer material to for instance discharged sewage. An approach will be discussed with parallel and continuous injection of two tracers that makes possible simultaneous registration of distribution of concentration and residence time of effluent discharged into a water area (Cederwall, 1968, Cederwall and Hansen, 1968).

To be used for dual tracer injection, the two tracers have to fulfill the following conditions: The decay parameters must be well defined and differ significantly and the tracer substances must differ in at least one property, detectable in low concentration.

Consider a non-conservative tracer with decay factor k continuously injected at a constant rate into a receiving water area starting at time $t = 0$. At time $t = T$ the concentration $C(T)$ is recorded at a certain point in the receiving water as a sum of contributions from tracer elements released in succession from the injection point. Then $C(T)$ can be expressed by means of an age distribution $f(T - t)$ with reference to time of release.

$$C(T) = \int_0^T f(T-t) \cdot e^{-k(T-t)} \cdot dt = -\int_0^T f(s) \cdot e^{-ks} \cdot ds \tag{21}$$

A residence time for the tracer in the measuring point can also be defined.

$$C(T) = e^{-k\tau} \int_0^T f(T-t) \cdot dt = e^{-k\tau} \tag{22}$$

This time parameter τ depends on the dispersive properties of the receiving water and the decay factor of the tracer material. For practical purposes τ may be considered very close to the mean residence time. Assume that the two tracers 1 and 2 with decay parameters k_1 and k_2 are simultaneously and continuously released and the amount of tracer injected per unit time is constant. A time parameter τ is now defined through the following equations:

$$C_1 = C_1{}' \cdot e^{-k_1 \cdot \tau} \qquad C_2 = C_2{}' \cdot e^{-k_2 \cdot \tau} \tag{23}$$

where C_1 and C_2 are the tracer concentrations at the measuring site C_1' and C_2' are the corresponding concentrations of totally conservative tracers. Hence we have

$$\frac{C_1'}{c_1 \cdot q_1} = \frac{C_2'}{c_2 \cdot q_2} \tag{24}$$

where $c_1 \cdot q_1$ and $c_2 \cdot q_2$ are tracer injection rates. This gives us

$$\frac{C_1 \cdot e^{k_1 \cdot \tau}}{C_2 \cdot e^{k_2 \cdot \tau}} = \frac{c_1 \cdot q_1}{c_2 \cdot q_2} \tag{25}$$

$$\tau = \frac{\ln \dfrac{C_2 \cdot c_1\, q_1}{C_1 \cdot c_2\, q_2}}{k_1 - k_2} = \frac{\ln R \dfrac{C_2}{C_1}}{a} \tag{26}$$

where R and a have constant values. Consequently a τ value may be determined for each site in the receiving water area where tracers are found in measurable concentrations. Hence the method may provide us with both the spatial distribution of recorded physical dilution of the tracer in the receiving water, or discharged pollutant if the tracers have been used for tracking the pollutant, and the corresponding distribution of residence time.

2.4 *Float dispersion mechanisms*

The study that is referred to here was conducted in a laboratory flume using submerged floats of different sizes. Measured data on lateral diffusion revealed that the floats act as filters to certain frequencies of the turbulence spectrum. A similar effect was observed when studying the response of the floats to the vorticity field in the flume flow.

Dimensional considerations indicate a parameter of the principal form l/r and possibly also a form factor of the dispersed object to characterize the rate of diffusion in a homogeneous turbulence field. L is a typical geometrical dimension of the diffusing object and r is a typical length of the flow field also characterizing the scale of the turbulence spectrum. We assume that the turbulence field is not disturbed by the presence of the diffusing object and that only those eddies of the turbulence spectrum that are larger than a characteristic dimension of the object contribute to diffusion of the particle.

Laboratory experiments were carried out in a 40 m long and 110 cm wide flume. The floats used for the experiments were made of plexiglass and balanced to be almost neutrally buoyant. They varied in wing size from 4 to 16 cm. All the floats were submerged 6 cm below water surface and exposed to almost homogeneous turbulence. The lateral diffusion of the floats was determined by a simple two-scale method. The floats were released manually upstream from the first scale. In a separate series of experiments the response to vorticity in the flume flow was observed, see Figure 5.

The lateral diffusion was determined by a simple two-scale arrangement, see Figure 5. Let z be the reading of the position of the floats when passing the scales. A proper description of the frequency distribution of the diffence in position at the scales was accomplished by calculating the three characteristics of the distribution, namely the mean, the variance and the skewness. We define the mean as

$$\mu = \frac{1}{N} \sum \Delta z_i \tag{27}$$

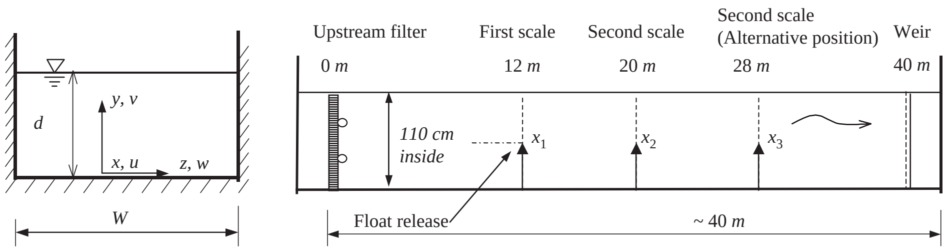

Lateral (left) and longitudinal (right) cross-sections

Figure 5. A 40-m flume and experimental setup for float experiments (Okoye, 1970, and Cederwall, 1971).

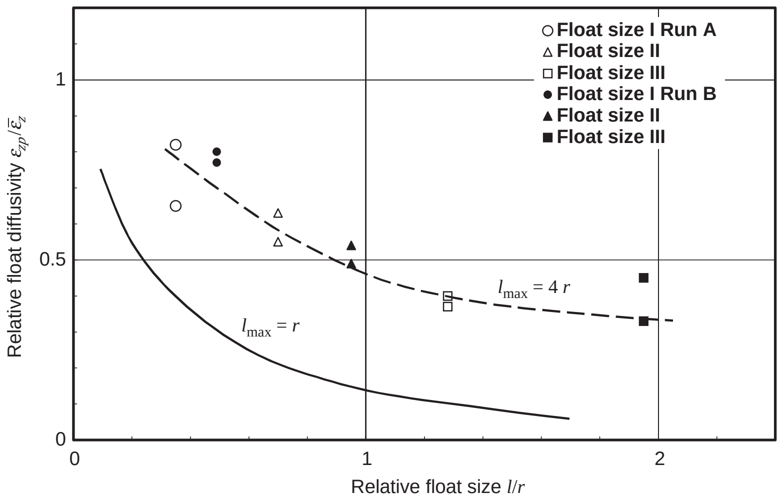

Figure 6. Relative float diffusivity $\varepsilon_{zp}/\bar{\varepsilon}_z$ as a function of relative float size l/r. Experimental data compared to predicted variation.

where N is the number of repetitive runs. The second and third moments are given as

$$\sigma^2 = \frac{1}{N}\sum(\Delta z_i - \mu)^2 = \frac{1}{N}\sum \Delta z_i^{\,2} - \mu^2 \tag{28}$$

$$\mu_3 = \frac{1}{N}\sum(\Delta z_i - \mu)^3 = \frac{1}{N}\sum \Delta z_i^{\,3} - 3\mu\sigma^2 - \mu^3 \tag{29}$$

To study how the floats picked up vorticity they were released at a distance from the left wall. The presence of eddies of both positive and negative rotation was found at all float positions in the flume. Large floats did not rotate very much but small floats picked up more vorticity. Floats respond more to eddies that are large relative to their own size.

The variance of the lateral diffusion of the floats can be compared with the depth-averaged lateral diffusion of dissolved substance. It is evident that there is a large reduction of lateral float diffusion. The lateral diffusivity of the floats are evaluated by

$$\varepsilon_{zp} = \frac{1}{2}u(y)\frac{\sigma_p^{\,2}}{x} \tag{30}$$

in analogy with lateral channel diffusivity. The relative float diffusivity are given in Figure 6 as a function of relative float size l/r where r is the hydraulic radius of the flume flow section. A comparison is made with a theoretical evaluation of particle diffusion, for further information see main reference.

3 CONCLUSIONS

Environmental hydraulics provides a part of the knowledge base for our understanding of environmental problems. Sustainable management of coastal and archipelago environments benefits from a continuous progress in our capacity to deal with point source pollution, more diffuse leaching of contaminants as well as water exchange mechanisms of marine environments. The learning process is often step-wise. We can identify fundamental needs for expanding knowledge in environmental engineering considering the complexity of environmental impacts we may have to handle. Strategic environmental impact assessments are required for controlling environmental threats for a wide range of activities from dredging to coastal erosion due to ship induced wave attacks. There are gaps to bridge between theory and practice, between empirical knowledge and advanced mathematical modeling, that still does not properly simulate man-made disturbances and all the background variability found in nature.

ACKNOWLEDGEMENTS

In the beginning of my post-graduate research I was lucky to meet Gerrit Abraham from Delft Hydraulics Laboratory, to share interests in environmental hydraulics. Later on I visited the research group at W M Keck Laboratory of Hydraulics and Water Resources at Caltech. Norman Brooks and Vito Vanoni and their graduate students provided a very friendly and efficient scientific atmosphere at the laboratory. The hydraulics departments in Scandinavia have close contact and for me that meant valuable and stimulating collaboration with particularly Torkild Carstens in Norway and Poul Harremoes and Jens Hansen in Denmark. I am very glad that I in all these years have had the possibility to work with Peter Larsen, during his many international academic assignments.

REFERENCES

Abraham, G. 1963. Jet Diffusion in Stagnant Ambient Fluid, *Report No. 29, Delft Hydraulics Laboratory*.

Brooks, N.H. and Vanoni, V.T. 1970. Post-graduate courses in "Environmental Hydraulics" (Hy. 106, Experimental Hydraulics and Similitude, Hy. 210, Hydrodynamics of Sediment Transportation). *W.M. Keck Laboratory of Hydraulics and Water Resources, California Institute of Technology*.

Cederwall, K. 1968. Hydraulics of Marine Waster Disposal. *Report No. 42 (PhD-thesis), Dept. of Hydraulic Engineering, Chalmers Institute of Technology*.

Cederwall, K. and Hansen, J. 1968. Tracer Studies on Dilution and Residence Time Distribution in Receiving Waters. *Water Research,* Vol. 2, pp. 297–310.

Cederwall, K. 1970. Dispersion Phenomena in Coastal Environments. Journal of Boston Society of Civil Engineers, January 1970.

Cederwall, K. 1970. The Oslo Fjord. A Model for Circulation and Diffusion of Discharged Sewage. *Vatten,* Vol. 3.

Cederwall, K. and Ditmars, F.D. 1970. Analysis of Air-bubble Plumes, W.M. Keck Laboratory of Hydraulics and Water Resources. *Report No. KH-R-24, California Institute of Technology*.

Cederwall, K. 1971. A Float Diffusion Study. *Water Research*. Vol. 5, pp. 889–907.

Cederwall, K. 1971. Buoyant Slot Jets Into Stagnant or Flowing Environments. *W.M. Keck Laboratory of Hydraulics and Water Resources. Report No. KH-R-25, California Institute of Technology*.

Cederwall, K. 1975. Gross Parameter Solutions of Jets and Plumes. *Journal of the Hydraulics Division, ASCE,* May 1975.

Cederwall, K. and Svensson, T. 1976. Sediment Flushing after Dredging in Tidal Bays. *Journal of the Hydraulics Division, ASCE*, July 1976.

Engqvist, A. and Anderjev, O. 2003. Water Exchange of the Stockholm Archipelago – A Cascade Framework Modeling Approach. *J. Sea Research*: 1–20.

Okoye, J. 1970. Characteristics of Transverse Mixing in Open-channel Flow. *W.M. Keck Laboratory if Hydraulics and Water Resources, Report No. KH-R-23, California Institute of Technology*.

Stenström, P. 2003. Exchange Flows in Estuaries and Archipelagos. *Hydraulic Engineering Division, Royal Institute of Technology*.

1 Mixing and transport

1.1 Mixing and transport – I

Environmental Hydraulics and Sustainable Water Management – Lee & Lam (eds)

Prediction of turbulent flow structure in compound channel with roughened floodplain using Large Eddy Simulation

M. Ifuku
Department of Civil and Environmental Engineering, Ehime University, Japan

K. Shiono
Department of Civil and Building Engineering, Loughborough University, UK

ABSTRACT: This paper presents quantitative analyses of large eddies, turbulence and secondary flow in compound channel with floodplain roughened by trees for overbank flow using simulation results of a 2-D depth averaged Large Eddy Simulation (LES). The results are compared with the experimental data obtained from Flood Channel Facility UK (FCF). The predicted longitudinal velocity and bed shear stress were compared with the experimental data and were a reasonably good agreement. The contributions of the Reynolds stress and secondary flow to flow resistance were found to be relatively significant in the shear layer.

1 INTRODUCTION

Floodplains are an integral part of a river system and flooding is a natural consequence of periodic increase in the hydrological flow regime. The benefits of flooding include the ability to replenish nutrient supplies on floodplains and to provide water to seedlings and trees requiring periodic inundation, all of which contribute to a unique environment for both flora and fauna. Overbank flow is natural and also desirable, of course, with no risk to human life. It is therefore a need to investigate roughness effect of floodplains due to vegetation with trees and bushes on mixing and transport processes in compound channels. In recent years, there have been many studies on flow structure in straight compound channels without roughened floodplains (e.g, Shiono & Knight, 1991). As a result, large horizontal eddies, secondary flow and high turbulence have been observed in the shear layer between the main channel and the floodplain. There are also a few experimental studies on flow structure in straight compound channels with trees on the floodplain carried out by Pasche and Rouve, (1985) and Thornton et. al. (2000). These studies have shown more complex flow structure in the shear layer caused by the interaction between a typical compound channel flow and the flow around trees on the floodplain. On the other hand, numerical modelling of compound channel flow has been undertaken using mostly Reynolds averaged Navier Stokes models with turbulence closure models e.g. Shiono and Lin (1992), and Naot et.al. (1994), however these models can not produce large horizontal eddies. Large Eddy Simulation (LES) can produce large eddies and has been also used by Thomas and William, (1995), who showed flow structure in a straight compound channel with smooth floodplain but did not show evolution of large eddies. This paper investigates large horizontal eddies, turbulence and secondary flow in a straight compound channel with the floodplain roughened by trees using simulation results of a 2-D depth averaged model of Large Eddy Simulation (LES) and the results are compared with the experimental data obtained from the Flood Channel Facility UK (FCF).

2 MODELLING

2.1 *Basic equations*

The 2-D depth averaged model with Large Eddy Simulation is adopted in this study. The governing 2-D depth averaged equations of motion are as follows:

$$\begin{aligned}&\frac{\partial U}{\partial t}+U\frac{\partial U}{\partial x}+V\frac{\partial U}{\partial y}=-g\frac{\partial \eta}{\partial x}-\frac{f}{\tilde{h}}U\sqrt{U^2+V^2}-\frac{1}{2}\frac{C_{Dx}}{\lambda}U\sqrt{U^2+V^2}\\&+\frac{1}{\rho}\left[\frac{\partial}{\partial x}\left(\tau_{xx}-\frac{2}{3}K_G\right)+\frac{\partial \tau_{yx}}{\partial y}\right]\end{aligned} \tag{1}$$

$$\begin{aligned}&\frac{\partial V}{\partial t}+U\frac{\partial V}{\partial x}+V\frac{\partial V}{\partial y}=-g\frac{\partial \eta}{\partial y}-\frac{f}{\tilde{h}}V\sqrt{U^2+V^2}-\frac{1}{2}\frac{C_{Dy}}{\lambda}V\sqrt{U^2+V^2}\\&+\frac{1}{\rho}\left[\frac{\partial \tau_{xy}}{\partial x}+\frac{\partial}{\partial y}\left(\tau_{yy}-\frac{2}{3}K_G\right)\right]\end{aligned} \tag{2}$$

where t is the time, U and V are the depth averaged velocities in the x and y directions respectively. g is the gravitational acceleration, η is the free surface elevation, ρ is the density of water, $\tilde{h}$ is the water depth, λ is the density of vegetation, C_{dx} and C_{dy} are the drag coefficients in the x and y directions respectively, τ_{xx}, τ_{yx}, τ_{xy} and τ_{yy} are the Reynolds stresses. K_G is turbulence kinetic energy of subgrid scale.

The Reynolds stresses can be expressed in the tensorial form:

$$\tau_{ji}=(\upsilon+\upsilon_t)\left(\frac{\partial U_j}{\partial x_i}+\frac{\partial U_i}{\partial x_j}\right)\quad \text{i = 1 and 2 } (x_1 = x \text{ and } x_2 = y). \tag{3}$$

Where υ is the kinematics viscosity. υ_t is the eddy viscosity of subgrid scale (SGS) given by

$$\upsilon_t=(C_s\Delta)^2\left[\left(\frac{\partial U_j}{\partial x_i}+\frac{\partial U_i}{\partial x_j}\right)\frac{\partial U_j}{\partial x_i}\right]^{1/2} \tag{4}$$

where C_s is a Smagorinsky constant, $\Delta=(\Delta x\Delta y)^{1/2}$, Δx and Δy are a computational mesh size in the x and y directions respectively.

The turbulence kinetic energy of SGS is given by $K_G=(\upsilon_t/C_e\Delta)$ where C_e is a model constant. The free surface elevation is determined by the continuity equation:

$$\frac{\partial \eta}{\partial t}+\frac{\partial}{\partial x}(\tilde{h}U)+\frac{\partial}{\partial y}(\tilde{h}V)=0 \tag{5}$$

2.2 *Boundary conditions*

The upstream boundary condition was given by discharge. The lateral component of velocity was set to zero. The downstream boundary condition was set to the fixed water depth as with the experimental data and with the following conditions

$$\frac{\partial(U\tilde{h})}{\partial x}=0 \text{ and } \frac{\partial(V\tilde{h})}{\partial y}=0 \tag{6}$$

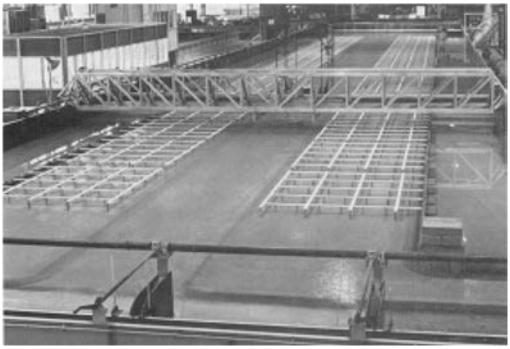

Figure 1. Experimental compound channel.

2.3 *Computation*

The mesh in the longitudinal direction was set to be 2.5 cm uniformly, but the mesh in the lateral direction was set to vary in the range of 1.25∼5 cm, of which a mesh of 1.25 cm was used in near walls and in the vicinity of the junction between the main channel and floodplain. The Smagorinsky constants, C_s and C_e in the subgrid scale model have been normally adopted between 0.1 and 0.2 in the literature, in this study the best values for this experimental case chosen through calibration were 0.1 and 0.094 respectively. The flow resistance due to the boundary was fixed to a Manning coefficient of 0.012 as with experimental smoothed bed. The density of rods on the floodplain was 12 rods/m^2 and the drag coefficient of the rod was assumed to be 1.0. The time step was set to 0.005 sec. The LES was solved by a second-order central difference scheme with a staggered grid.

3 EXPERIMENTAL DATA

The experimental data used in this study is from Series 07 of the UK-FCF experiments (see Fig. 1). The experimental flume was 60 m long and 10 m wide, with a maximum discharge of 1.1 m^3/s. The experiments were performed in a straight compound channel consisting of flat floodplains with rods (a diameter of 0.025 m). The density of rods was 12 rods/m^2. The top width of the main channel was 1.8 m and the floodplain width was 2.3 m. The side slopes were 45 degrees with a bankfull depth of 0.15 m. The longitudinal bed slope was 1.024×10^{-3}. The velocity and boundary shear stress were measured using an array of 10 miniature propeller meters and a Preston tube respectively. The water depth of the experiment varied from Dr = 0.1 to Dr = 0.5, where Dr = relative depth defined as floodplain water depth/main channel water depth.

4 RESULTS AND DISCUSSION

The 2-D depth averaged LES model was applied to the FCF experiment to predict turbulent flow structure in the shear layer. The results of turbulent fluctuations of two velocity components at 197.5 sec and 200 sec after the LES execution in the reach between 35 m and 45 m for very shallow flooding, Dr = 0.093 are shown in Fig. 2 as a horizontal eddy vector form. The vectors were generated by subtracting the instantaneous turbulent velocities from a stream-wise velocity of 0.5 m/s around the edge of the floodplain, thus the directions of flow in the main channel and floodplain far from the edge are opposite. It can be seen from the figure that there are three different horizontal eddies moving downstream over the 10 m reach. The pattern of eddy formation shows that relatively strong flow from the floodplain rapidly enters into the main channel and the main channel flow slowly moves onto the floodplain, which is similar to that observed by Fukuoka et al. (1989). When water depth increases, see Dr = 0.25, in Fig. 2, the start of evolution of large

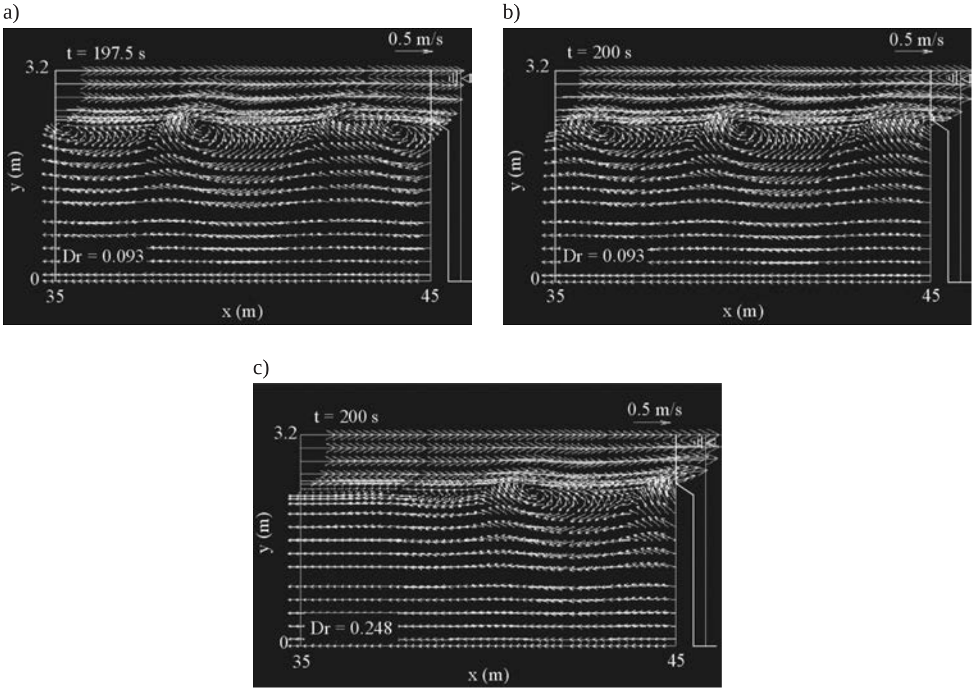

Figure 2. (a) Large horizontal eddies at t = 197.5 s, (b) Large horizontal eddies at t = 200 s, (c) Large horizontal eddies for Dr = 0.25.

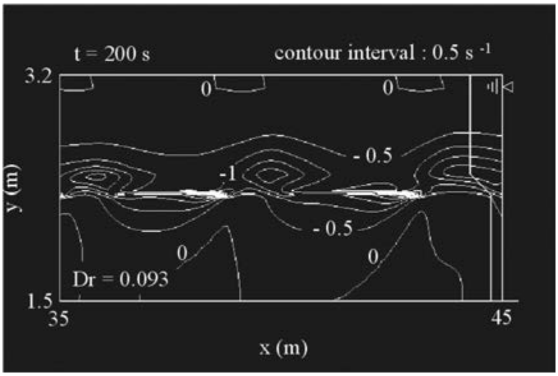

Figure 3. Vorticity for Dr = 0.093.

eddies is noticeably downstream compared with that of Dr = 0.093. Figure 3 shows the magnitude of vorticity for Dr = 0.093. The vorticity has a maximum value of −2. Pair of vorticity peaks are normally found in the either side of inflexion point of velocity distribution for simple shear instability flow, like a Kelvin-Helmholtz instability, but in this case, not quite pairing up. This may indicate that there are different perturbations of velocity due to difference levels of turbulence across the side slope section (i.e. cause of variation of water depth).

The depth averaged stream-wise velocity distributions for Dr = 0.093 and 0.25 are shown in Fig. 4 together with the measured data. Both cases of the LES results are a good agreement with the experimental data except around the edge of floodplain for Dr = 0.25. The predicted boundary

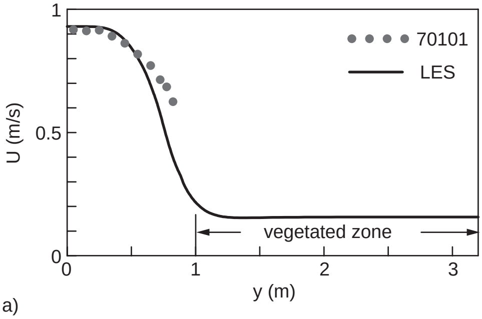

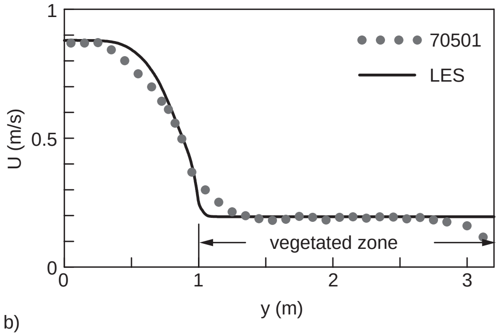

Figure 4. (a) Stream-wise velocity for Dr = 0.093, (b) Stream-wise velocity (Dr = 0.248).

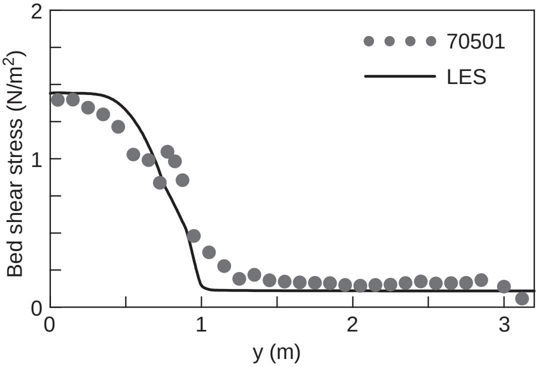

Figure 5. Boundary shear stress (Dr = 0.248).

shear stress was also compared with the experimental data and again both are a good agreement in the main channel, but LES slightly overestimates on the floodplain (see Fig. 5).

The secondary flow and Reynolds stress were not measured in this experiment, but the contribution of those to flow resistance can be estimated using the equation given by Shiono and Knight (1991) and compared with the results of LES. The equation is as follows

$$\underset{(I)}{\frac{\partial(\rho HUV)}{\partial y}} = \underset{(II)}{\rho g H S_o} - \underset{(III)}{\tau_b} + \underset{(IV)}{\frac{\partial(H\tau_{xy})}{\partial y}} - \underset{(V)}{\frac{1}{2}\rho C_d A U (U^2 + V^2)^{0.5}} \tag{7}$$

(I) = secondary flow contribution, (II) = weight component, (III) = bed shear stress, (IV) = Reynolds stress contribution and (V) = drag force.

Each term can be normalised by the weight component of $\rho gHSo$ to see each contribution. (II), (III) and (V) were worked out from both experimental data and LES, knowing velocity and boundary shear stress, which gives the combined (I) and (IV). Figure 6 shows both experimental and LES results for Dr = 0.25 as an example. For experimental data, the combined contribution is increasing from positive 30% to 50% towards the floodplain in the main channel, decreasing to negative 200% near at the floodplain junction and back to 0% at some distance on the floodplain. The LES result has a similar trend to that of experimental data in the main channel and most floodplain, but much shaper change occur in the main channel side slope wall region, and the peak magnitude is much larger.

LES gives U and V so that the contribution of secondary flow (I) can be worked out. (I) was first calculated, then the contribution of the Reynolds stress was estimated. Both contributions

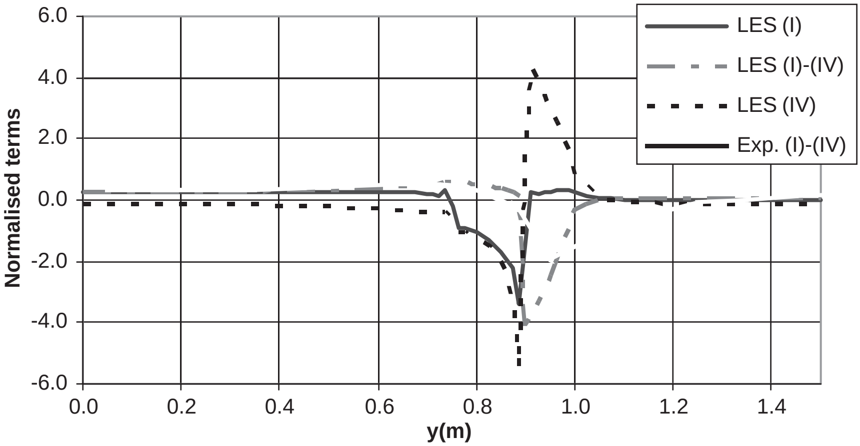

Figure 6. Contribution terms in equation (7) normalised by $\rho gHSo$.

normalised by $\rho gHSo$ are also shown in Fig. 6. It can be seen from the figure that both magnitudes are significantly larger than the weight component of 1.0 and boundary shear stress in the shear layer region. The Reynolds tress term (IV) shows first negative in the main channel, then becomes positive with a sharp gradient where the peak Reynolds stress occurs. The peak Reynolds stress occurs at the edge of the floodplain where is consistent with that occurs for smooth floodplain case shown by Knight and Shiono (1990). The magnitude of the secondary flow term in the main channel is larger than a value of 0.15 given by Shiono and Knight (1991) for the smooth floodplain case whereas, on the floodplain, it becomes positive and negative in the vicinity of the junction instead of a value of -0.25 given by Shiono and Knight. When the magnitude of the secondary flow term was estimated for various water depths, it was noticed, in the main channel, there was a certain trend in magnitude, which it increases as water depth increases. This might suggest that an influence of turbulence anisotropy to the mean flow would become larger owing to trees on the floodplain. This analysis indicates that the contributions of secondary flow and Reynolds stress to flow resistance in the hear layer are significantly high.

5 CONCLUSIONS

The LES predicted two components of instantaneous turbulent velocity along the 10 m reach in the straight compound channel, which clearly shows large horizontal eddies in the shear layer. The flow pattern from the eddy formation was found to be very much similar to those observed by experimental studies in the literature. The predicted velocity and boundary shear stress were a good agreement with the experimental data. The contributions of secondary flow and Reynolds stress to flow resistance are much higher than the weight component and boundary shear stress in the shear layer. The contribution of secondary flow to momentum equation becomes larger when water depth increases, which might suggest that the influence of anisotropic turbulence to the main flow would increase. Finally, the 2-D depth averaged LES can reasonably predict turbulent flow structure in the shear layer of compound channel with roughened floodplain.

REFERENCES

Fukuoka, S and Fujita, K (1989), Prediction of flow resistance in compound channels and its application to design of river courses, *Proc. JACE*, Vol. 411/11-12, pp.63–72.

Naot, D, Nezu, I and Nakagawa, H (1994), Towards the modelling of the hydrodynamic forces in compound open channel with vegetated flood plain. *Proc. Hyd. Eng.* 38 pp.437–442.

Knight, DW and Shiono, K, (1990), “Turbulent measurements in a shear layer region of a compound channel”, *J. Hydraulic Research*, IAHR, Vol. 28, 2, pp.175–196.

Pasche, E and Rouve, G (1985), Overbank flow vegetative roughened flood plains. *J. Hyd. Eng.* 111 (9) pp.1262–1278.

Shiono, K and Knight, DW (1991), Turbulent open channel flows with variable depth across the channel, *J F M* , 222, pp.617–646.

Shiono, K and Lin, B, (1992), “Three dimensional numerical model for two stage open channel flows”, *Hydrocomp ’92*, 25–29 May, Budapest, Hungary, pp.123–130.

Thomas, TG and Williams, JJR, (1995), Large eddy simulation of turbulent flow in an asymmetric compound open channel, *J. Hydraulics*, IAHR, No. 1, Vol. 33, pp.27–41.

Thornton, CI, Morris, CE and Fischenich, JC, 2000, Calculating shear stress at channel-overbank interfaces in straight channels with vegetated floodplains. *J. Hyd. Eng.* 126 (12) pp.929–936.

This page intentionally left blank

Environmental Hydraulics and Sustainable Water Management – Lee & Lam (eds)
 ISBN 04 1536 546 5

A field study of extremely rough, three-dimensional river flow

M.J. Franca & U. Lemmin
LHE – École Polytechnique Fédérale de Lausanne, Switzerland

ABSTRACT: Field measurements using a deployable 3-D Acoustic Doppler Velocity Profiler were made under stationary conditions, during a low water period in the Swiss lowland river Venoge. The riverbed is hydraulically rough; it is composed of coarse gravel and has randomly spaced protuberances as high as half the water depth. The measurements were made in one half of the cross section of the river. The present analysis focuses on the three-dimensional character of the mean river flow and its implication on mixing and transport. The mean velocity cross river distribution is affected by the riverbank effect and large bottom roughness. The three-dimensionality of the mean flow induces secondary motion due to large-scale bottom roughness. As a consequence, the turbulence distribution across the section and along the water depth is modified. It is concluded that 2-D concepts developed for open-channel flow are of limited value under these conditions.

1 INTRODUCTION

Field measurements of velocity including turbulence features are needed for the validation and calibration of engineering tools in river simulations with respect to sediment transport, morphology evolution, secondary flows and mixing and transport of heat and matter. Only a small number of field studies have been carried out in natural or canalized rivers, mainly due to the lack of suitable instrumentation. Some recent publications give a limited insight into turbulent flow aspects under natural conditions (González et al. (1996); Nikora and Smart (1997); Powell et al. (1999); Smart (1999); Nikora and Goring (2000); Babaeyan-Koopaei et al. (2002); Hurther et al. (2002); Tritico et al. (2002) and Roy et al. (2004)).

In this paper we present the results of a field measurement campaign made on a lowland stretch of the Swiss river Venoge, during the summer of 2003. A deployable three-dimensional Acoustic Doppler Velocity Profiler (ADVP) developed at the LHE was used. The instrument which permits three-dimensional, quasi-instantaneous profiling of the fluctuating velocity flow field along the whole water depth (Rolland and Lemmin, 1997), is positioned at several points across the river section. The flow conditions were stationary and the riverbed was extremely rough. Our results focus on the three-dimensionality of the mean river flow and on the turbulence distribution across the section and along the water depth.

2 FIELD STUDY

The field measurements were made during a low water period, across the Swiss lowland river Venoge (Table 1). They were carried out on a single day and under stationary flow conditions, as confirmed by discharge data provided by the Swiss Hydrological and Geological Services. The chosen cross section was situated along a straight river reach, about 120 m upstream of the Moulin de Lussery (Figure 1).

In Table 1, Re is the Reynolds number; $\overline{U}$, the vertical mean of the longitudinal velocity; ν, the cinematic viscosity; Fr, the Froude number; g, the gravity acceleration and D_{50}, the bottom grain

Table 1. Summary of the Venoge river flow characteristics.

Mean slope (%)	Discharge Q (m^3/s)	Av. water depth δ (m)	Width B (m)	$Re = \overline{U}\delta/\nu$ ($\times 10^4$)	$Fr = \overline{U}/\sqrt{sg\delta}$ (-)	D_{50} from the riverbed[(1)] (mm)
0.13	0.80	0.21	6.30	3.0–14.4	0.2–0.9	40

[(1)] D_{50} obtained from a sample of the bottom material using Wolman (1954) method.

Figure 1. View of the study reach and of the deployable support structure for the ADVP field measurements.

size diameter for which 50% of the grain diameters are smaller. Considering the average water depth, one obtains $B/\delta = 30$ which corresponds to shallow water conditions.

The riverbed is hydraulically rough, composed of coarse gravel and randomly spaced protuberances as high as half the water depth ($0.5\overline{\delta}$). The measurements were made in half the cross section of the river starting from the right riverbank (y/B = 0). The deployable 3-D ADVP was used for the measurements. ADVP spatial and time resolutions are sufficient to estimate the main turbulent parameters related to open-channel flows within the production and inertial subranges of the spectral space. In the present study, 25 profiles were measured for 5 min. each with horizontal spacing of 10 to 12.5 cm. A Pulse Repetition Frequency (PRF) of 2000 Hz and a Number of Pulse Pairs (NPP) equal to 32 was used for the estimation of the Doppler shift and subsequently the three-dimensional velocity components, resulting in a sampling frequency of 62.5 Hz. Though a low degree of aliasing was expected, a correcting algorithm developed by the authors was applied to the data. This algorithm rectifies directly the instantaneous values of the Doppler frequencies measured by the receivers through a procedure that follows the signal history and chooses the best correction to be made. A deployable support structure was constructed for the easy displacement of the ADVP along two directions (horizontal and vertical, see Fig. 1). The installation minimizes the disturbance of the flow field and instrumentation vibration. This structure is leveled and aligned and allows to carry out the measurements of the cross section over a short period of time.

3 RESULTS

3.1 *Mean velocity field*

Figure 2 shows the mean velocity field in the longitudinal, transversal and horizontal planes across the section. Each vertical line corresponds to one measured profile and each vector results from

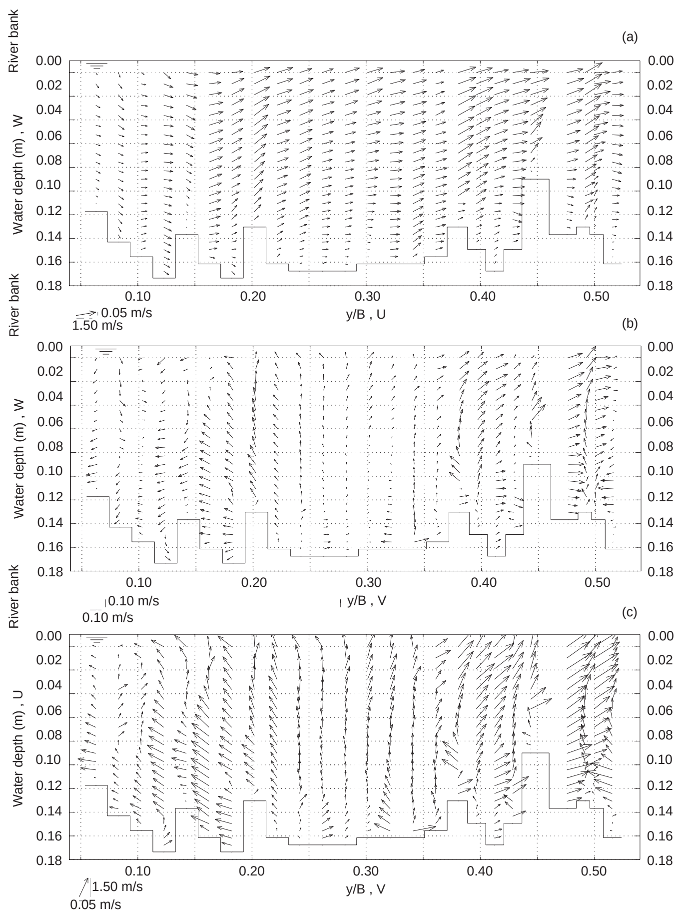

Figure 2. Mean vector fields (U: longitudinal; V: transversal; W: vertical component) in cross section of the river Venoge: (a) longitudinal plane (U-W); (b) transversal plane (V-W); (c) horizontal plane (U-V). Measurements cover half the river width.

one of the ADVP bins. The local water depth is determined from the backscattering echo intensity of the ADVP with a resolution of ± 5 mm.

The high three-dimensionality of the flow is evident from Figure 2, best seen in the near bank zone and around the higher riverbed protuberances. In fact, the large-scale bottom roughness locally produces important secondary mean motion in the flow, as seen from the transversal (V) and vertical (W) components of the mean velocity field (Figure 2b). This leads to a strongly 3-D flow field over most of the cross section (Fig. 2b and c). On a cross section average, the transversal and vertical velocities represent about 5.3% and 7.5% of the longitudinal component, whereas they become locally more important over the large-scale roughness. No structured secondary flow cells were detected. In agreement with observations by Studerus (1982), higher intensity cells in the (U) field are observed across the section where large-scale bottom roughness is found (Fig. 2a). The transversal decrease of the longitudinal velocity component (Fig. 2a) towards the riverbank is associated with a secondary recirculation flow (Fig. 2b and c) and indicates the drag effect of the riverbank occurring for $y/B < 0.15$.

The profiles of the longitudinal component of the mean velocity field measured in the river Venoge were compared to the classical log-law approach. Despite the three dimensional character of the flow, the mean longitudinal velocity distribution shows a logarithmic layer in the lower 40%

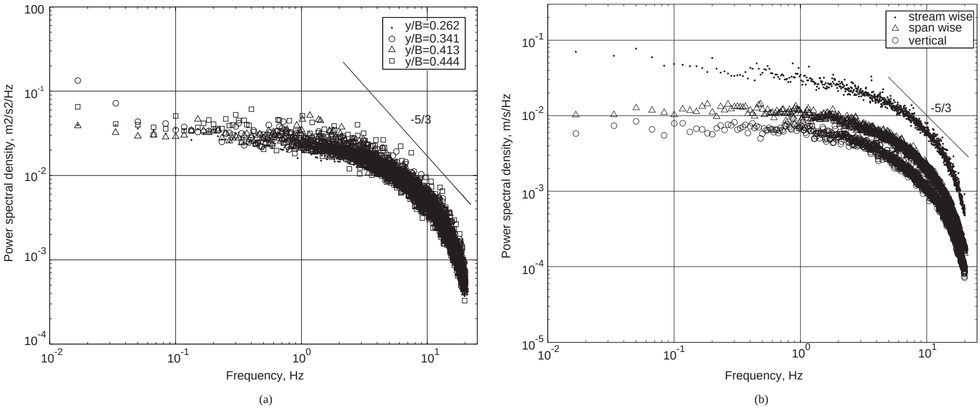

Figure 3. Power spectral density of the turbulent velocity fields: (a) vertically averaged power spectral density of the streamwise velocities for several profiles measured across the section; (b) vertically averaged power spectral density of the streamwise, spanwise and vertical velocity components, for $y/B = 0.282$.

of the water column along most of the section, and classical 2-D boundary layer profiles are found over most of the depth in sections where the bottom is relatively homogeneous ($0.25 > y/B < 0.35$). For all the 25 measured profiles only one did not correspond to hydraulically rough turbulent conditions. The average dimensionless roughness is $k^+ = 9500$; with the dimensionless roughness defined as $k^+ = k_s U^*/\nu$, where U^* is the friction velocity. The computed value of $k_{s,50}$, defined as the equivalent roughness for which 50% of the values are higher, is equivalent to the grain diameter D_{85} taken from the grain size distribution of the riverbed.

Obviously, a 2-D approach of a rough flow is impossible especially in the inner bank zone and near the large-scale bottom roughness. Therefore, concepts developed for open channel flow particularly concerning bottom friction velocities are of limited value in these flows. This is important because sediment transport is controlled by bottom friction and new concepts for the prediction of sediment transport in these flows may be needed. The three-dimensional mean field has its maximum value around the protuberance correspondent to $y/B = 0.45$. In this vertical the mean vertical velocity component assume the highest values, representing about 14% of the maximum longitudinal one. In the profile $y/B = 0.50$ the spanwise velocity acquires its maximum, representing about 10% of the maximum longitudinal one. Taking these two latter values as reference, it is obvious that the secondary mean velocity field introduces an additional advection of about 25% for any physical property present in the flow in its balance equation. The spanwise and the vertical terms should thus be included in this calculation.

The three dimensionality of the flow is confirmed by the inexistence of mass conservation within the cross section. In this flow, mass conservation can only be verified over a river stretch. The secondary mean motion induced by the large-scale bottom roughness is important in the spreading of matter, heat and momentum across the river section. Due to the strong shear zones this may locally be more efficient than background turbulence. Turbulence production is not restricted to the shear due to the bottom roughness. Instead, the shear zones observed in the mean velocity field provide for an additional turbulence production along the whole water column.

3.2 *Fluctuating velocity field*

Figure 3 presents estimates of the power spectral density of the fluctuating velocity fields. The data was split into blocks of one minute duration and the Welch method with 50% overlapping was used for the calculation of the power spectral density. The vertically averaged spectral density for several measured profiles, representing the bulk average streamwise turbulent energy distribution is shown in Fig. 3a.

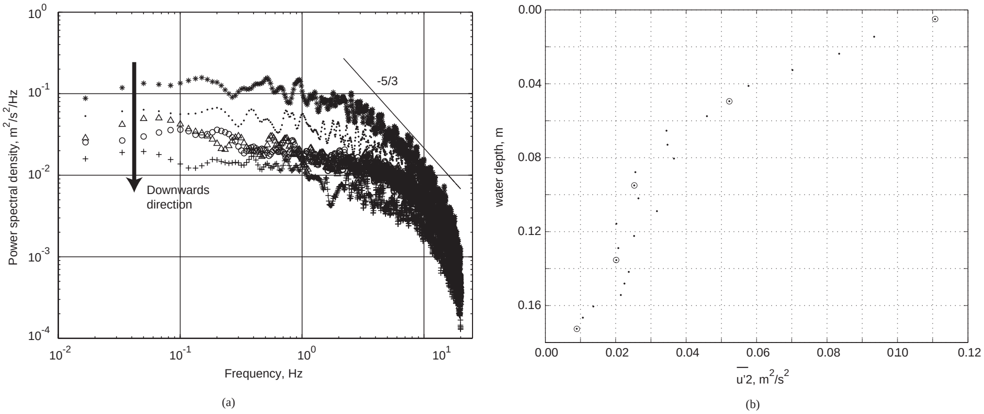

Figure 4. For the streamwise component at y/B = 0.282: (a) Power spectral density of the turbulent velocities for several points along the water depth; (b) vertical distribution of turbulence intensity. The points corresponding to the spectral density plots shown in Fig. 4a are represented by a dot surrounded by a circle in Fig. 4b.

No particular tendency of the total bulk energy distribution between y/B = 0.262 and y/B = 0.444 is detected, despite the difference in roughness and water depth between these two flow zones. The vertically averaged spectral density for the three velocity components for the profile y/B = 0.282 is given in Fig. 3b. It shows a strong anisotropy of the flow, with the streamwise velocity component dominating in the energy production, in agreement with the conclusions by Buffin-Bélanger *et al.* (2000). It was also verified that in the transversal plan (y-z), the anisotropy level decreases in the upward direction, towards nearly complete isotropy conditions.

Figure 4 shows the streamwise spectral density for several water depths and the vertical distribution of the streamwise turbulent intensity for y/B = 0.282.

High values of the turbulent intensity are found, particularly in the near surface area (Fig. 4). The turbulent energy distribution decreases downwards in the water column, confirmed by the spectral density distribution (Fig. 4a) and by the turbulence intensity profile (Fig. 4b). Thus, in the present flow the bottom production does not seem to be the main source of turbulence. In order to explain the turbulence distribution shown, several other production sources can be envisioned and will be investigated. The flow features here shown for the vertical y/B = 0.282 are generally valid for the rest of the cross section.

4 DISCUSSION

Macro roughness and high protuberances present on the riverbed promote mixing in the water mass (pollutants, heat or momentum), due to the existence of secondary mean flow and due to an increase of the turbulence levels within the flow. The effect of the secondary mean flow on the structure of the flow provides for a supplementary advection term in a balance equation, in both the spanwise and vertical directions. This is not considered in exclusively two-dimensional approaches. Furthermore, the high turbulence levels observed are of major importance for mixing.

The strong variation of the mean streamwise velocity field across the section (Fig. 2a) is responsible for additional shear zones that produce horizontal eddies, thus providing for a turbulent energy production all along the water depth. Due to the random distribution of the protuberances and macro-roughness along the studied river reach, the high turbulence levels are equally distributed across the river section. We concluded that in the present flow, sources other than bottom shear contribute to the turbulent energy production.

The presence of macro-roughness elements in the riverbed induces large flow structures with length scales of the water depth. These dominate the turbulence production and are present in the entire flow depth (Roy 2004). These large structures are conveyed upwards within the water column where the higher longitudinal velocities together with the constraint imposed by the water surface distort them in the streamwise direction. This process explains the high values of stream wise turbulence near the surface and can be considered to be similar to the rapid distortion for which a theory was first developed by Batchelor and Proudman (1954).

At the same time, a regular occurrence of alternating periods of faster and slower streamwise velocity with respect to the mean velocity is observed in the whole water column in the present data, though is not discussed here. This velocity variation induces an additional oscillating component with extremely high amplitude which affects the longitudinal turbulent intensity. This periodic oscillation occurs at a periodicity lower than 1 Hz and can be considered as a quasi-stationary feature of the flow. It will therefore not contribute to the small-scale turbulence. However, the existence of these alternating time cells, sugested by Yalin (1977) can be responsible for the strong anisotropy in the streamwise direction observed in the turbulence intensity analysis.

The authors acknowledge the financial support of the FCT (BD 6727/2001) and the Swiss National Science Foundation (2000-063818).

REFERENCES

Babaeyan-Koopaei K., Ervine D.A., Carling P.A. and Cao Z. (2002), Velocity and turbulence measurements for two overbank flow events in river, Severn, J. Hydr. Eng., 128(10), 891–900.

Batchelor G.K. and Proudman I. (1954), The effect of rapid distortion of a fluid in turbulent motion, Q. J. Mech. Appl. Maths, 7, 83.

Buffin-Bélanger T., Roy A.G. and Kirbride A.D. (2000), Vers l'intégration des structures turbulentes de l'écoulement dans la dynamique d'un cours d'eau à lit de graviers, Géogr. Phys. Quat., 24(1), 105–117.

González J.A., Melching C.S. and Oberg K.A. (1996), Analysis of open-channnel velocity measurements collected with an acoustic doppler current profiler, Proc. 1st Int. Conf. New/Emerging Conc. Rivers, Chicago (USA).

Hurther D., Lemmin U. and Blanckaert K. (2002), A field study of transport and mixing in a river using an acoustic Doppler velocity profiler, Proc. Riverflow 2002 – Int. Conf. Fluv. Hydr., Louvain-la-Neuve (Belgium).

Nikora V. and Goring D. (2000), Flow turbulence over fixed and weakly mobile gravel beds, J. Hydr. Eng., 126(9), 679–690.

Nikora V. and Smart G.M. (1997), Turbulence characteristics of New Zealand gravel-bed rivers, J. Hydr. Eng., 123(9), 764–773.

Powell D.M., Reid I. and Laronne J.B. (1999), Hydraulic interpretation of cross-stream variations in bed load transport, J. Hydr. Eng., 125(12), 1243–1252.

Rolland T. & Lemmin, U. (1997). A two-component acoustic velocity profiler for use in turbulent open-channel flow, J. Hydr. Res. 35(4): 545–561.

Roy A.G., Buffin-Belanger T., Lamarre H. and Kirkbride A.D. (2004), Size, shape and dynamics of large-scale turbulent flow structures in a gravel-bed river, J. Fluid Mech., 500, 1–27.

Smart G.M. (1999), Turbulent velocity profiles and boundary shear in gravel bed rivers, J. Hydr. Eng., 125(2), 106–116.

Studerus, X. (1982), Sekundärströmungen im offenen Gerinne übn rauhen Längsstreifen. Ph.D. thesis, Institut für Hydromechanik und Wasserwirtschaft – ETH, Zurich.

Tritico H.M., Stone M.C. and Hotchkiss R.H. (2002), Turbulence characterization in the wake of an obstruction in a gravel bed river, Proc. Hydr. Meas. Exp. Met., Estes Park (USA).

Wolman M.G. (1954), A method of sampling coarse river-bed material, Trans. Amer. Geoph. Un., 35(6), 951–956.

Yalin, M.S. (1977), *Mechanics of Sediment Transport*. Surrey: Pergamon Press.

Environmental Hydraulics and Sustainable Water Management – Lee & Lam (eds)
© 2005 Taylor & Francis Group, London, ISBN 04 1536 546 5

Influence of variable morphological conditions on the mass transport characteristics in rivers

Volker Weitbrecht & Gerhard H. Jirka
Institute for Hydromechanics, University of Karlsruhe

ABSTRACT: A 2-D Lagrangian-Particle-Tracking-Method (*LPTM*) has been developed to simulate dispersive mass transport in rivers under the influence of dead-water zones, such as groin fields. Results from laboratory experiments are used in the *LPTM* to include velocity and diffusivity distribution and the mean residence time. With the help of different *LPTM* simulations where the retention effect of the groin fields varies along the travel distance, the influence of morphological changes on the transport characteristics has been analyzed.

1 INTRODUCTION

The mass transport of dissolved pollutants in a river reach is difficult to predict, due to the limited knowledge of the relation between morphological conditions and transport characteristics. In rivers with strong morphological heterogeneities like dead-water-zones (see Fig. 1, i), channel meandering or varying channel width, the prediction of transport velocities, maximum concentration and skewness contains strong uncertainties. A far-field 1-D prediction tool called the River-Rhine-Alarm-Model (Spreafico, 1993) has been developed by the "International Commission for the Hydrology of the River Rhine" (*CHR*) and the "International Commission for the Protection of the Rhine" (*ICPR*) for cases of accidental pollutant releases. For this kind of predictive models, much effort and money is spent on calibration by means of extensive in-situ tracer measurements (van Mazijk, 2002). In the case of the River Rhine Alarm Model, which uses a one-dimensional analytical approximation for the travel time and concentration curve, a dispersion coefficient and a lag coefficient have to be calibrated. The model works well for cases of similar hydrological situations. However, variations in discharge, and thus, changes in water surface levels, lead to increased errors if the same calibrated parameters are used for different hydrological situations.

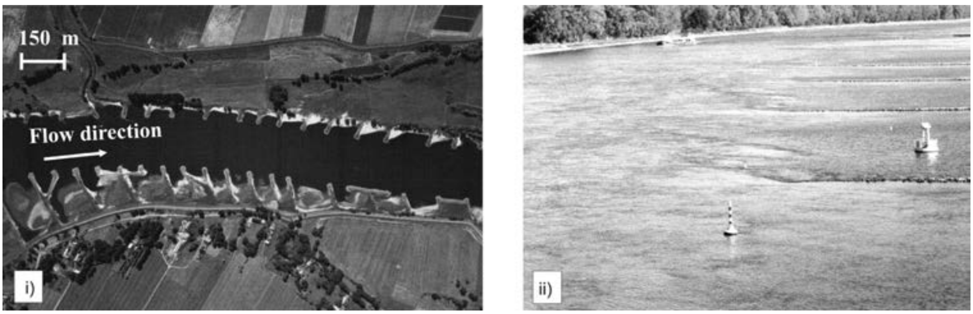

Figure 1. Morphological heterogeneities due to groin fields and related flow pattern; (i) Aerial photograph of the River Elbe taken at 490 km, with low discharge conditions, authorized by WSD Ost, Berlin; (ii) Flow structures in the mixing layer between dead-water zone and main stream, observed in the river Rhine near Karlsruhe.

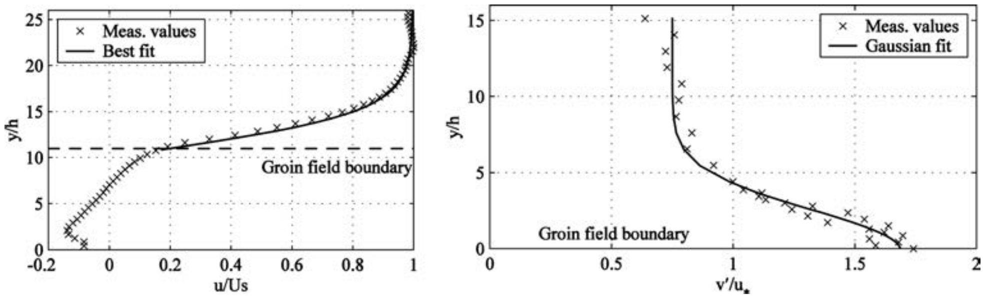

(i) normalized mean velocities (ii) normalized rms velocities

Figure 2. Results of velocity measurements for (i) mean velocities approximated with a *tanh* function and (ii) turbulent velocity fluctuations v' approximated with a Gaussian curve, measured in a cross section with groins fields of an aspect ration width/length = 0.4.

Hence, predictive methods that are appropriate for variable flows and changing morphological conditions are needed.

In the present research project, the influence of dead-water zones such as, groin fields, on the transport characteristics has been investigated (Weitbrecht, 2004). The influence of groin fields on the transport characteristics can be described by three different aspects that are caused by the dynamics of the mixing layer between the dead-water zone and the main stream, which is dominated by large coherent horizontal eddy motion due to the shallowness of the flow (see Fig. 1). Taylor (1954) showed that the two main processes with respect to longitudinal dispersion are longitudinal velocity shear and transverse diffusion. The mixing layer leads to enhanced transverse mixing and therefore, reduces longitudinal dispersion. The mean horizontal velocity distribution is also strongly affected by the mixing layer. Compared to a mixing layer along a smooth wall the velocity distribution is much less homogeneous which enhances longitudinal stretching. The third aspect is given by the mass exchange between the dead-water zone and the main stream, which is also driven by the mixing layer dynamics. Mass that travels in the main stream gets retained in the dead water zone and therefore, leads to additional stretching of a pollutant cloud.

With the help of detailed velocity and concentration measurements the flow and transport phenomena in the presence of groins has investigated systematically for varying geometrical conditions. The mean and turbulent flow properties have been measured with a Surface-Particle-Imaging-Velocimetry system (Weitbrecht et al. 2002). In Figure 2 typical results of the velocity measurements for the mean velocities and rms-velocities are illustrated. The measurements were performed in a tilting flume of 20 m length and 1.8 m width. The water depth h was 4.6 cm and the mean flow velocity U about 16 cm/s. The groins were placed on one side of the flume with a length of 50 cm and a varying spacing from 15 cm to 145 cm. The profiles in Figure 2 represent measurements with a spacing of 125 cm and are used later in the numerical transport simulation (*LPTM*) to determine the advective and diffusive step.

With the help of concentration measurements where dye is injected instantaneously into one single groin and by analyzing the concentration decay the mean residence times could be determined for the various groin field geometries (Jirka, 2004), which are used in the transport simulations to parameterize the influence of the particle retardation as described above. The transfer of the measured results locally at single groin fields into a system of many groin fields has been performed using a Lagrangian-Particle-Tracking-Method (*LPTM*) described in the next section.

In Jirka (2004), it was shown that the influence of groin fields on the dispersion process is strongly related to the current Peclet Number defined as $(UB)/D_y$ with U as the mean flow velocity B the channel width and D_y the transverse turbulent diffusion coefficient. The Peclet Number as it is defined here, is directly related to the time scale that describes the transverse mixing time. It was shown that with increasing Peclet Number the influence of the groin field retardation T_D as a second time scale gets much stronger. Furthermore, it has been shown, that the dimensionless mass exchange coefficient k (Valentine & Wood, 1979) that describes the strength of the mass exchange between dead-water zone and main stream, scales with a certain shape factor R_D, defined similar as a hydraulic radius of the groin field $WL/(W+L)/h_s$, where W is the width and L length of a groin field and h_s the water depth in the main channel. k lies in the range between 0.012 and 0.035 and increases with increasing R_D. Using this information in a *LPTM* simulation as boundary condition it could be shown (Jirka, 2004) that with increasing R_D, which corresponds to smaller residence times, the dispersion coefficient decreases and the transport velocity increases. In the present paper additional results of *LPTM* simulations are presented, where the influence of varying morphological conditions along the main flow direction can be analyzed.

2 LAGRANGIAN PARTICLE TRACKING METHOD

A transport model based on a 2-D Lagrangian-Particle-Tracking-Method (*LPTM*) has been developed to determine transport characteristics in the far-field of a pollutant transport scenario by analyzing the statistics of such a particle cloud at any position of the simulation. The method represents a random walk approach as has been used, for example, by Sullivan, 1971 to model turbulent shear flow based on statistical mechanical transport theories presented by Taylor (1921).

A random walk simulation can be understood as the tracking of discrete particles, under the influence of the governing flow processes. Typically, the particle displacement dX_i is described by a deterministic and a stochastic part, leading to the so called Langevin equation (Gardiner, 1985)

$$dX_i = f(X_{i,t})dt + Z(t)g(X_i,t)dt \tag{1}$$

where XS_i is the position x, y and z. *f(X_i,t)* represents the advective or drift component, which can be interpreted as the mean flow velocity field. The expression *g(x_i,t)* describes the diffusive or noise component of the particle movement that describes the strength of the turbulent diffusion in space. The stochastic part is represented by the Langevin force Z, which is a Gaussian distributed variate with a mean value of zero and a variance equal to one.

In the present case the governing processes are advection in longitudinal direction x and diffusion in transverse direction y, which implies that we can neglect the drift component in y-direction and the noise component in x-direction in eq. 1. An important part of such a model is the link between the diffusive step size and the length of the time step. Here the approach given by Taylor, 1921 is used, who stated that the spreading of a particle ensemble measured with the standard deviation under the influence of turbulent diffusion can be treated as a Fickian type of diffusion, where $\sigma \sim (2D_y t)^{0.5}$ with D_y as the turbulent diffusion in y-direction and the time t. The diffusive step size for a single particle at a certain time step in y-direction is therefore given with

$$v'\Delta t = \sqrt{2D_y \Delta t} \tag{2}$$

Using these assumptions, the position of the particles in every time step Δt can be described by a simplified 2-D version of eq. 1.

$$x_{new} = x_{old} + (\Delta t\, u(y)) \tag{3}$$

$$y_{new} = y_{old} + Z\sqrt{2D_y(y)\Delta t} + \frac{\partial D_y}{\partial y}\Delta t \tag{4}$$

where x_{old}, y_{old} and x_{new}, y_{new} are the spatial locations at times t and $t + \Delta t$ respectively. The function $u(y)$ denotes the mean flow velocity in relation to the position in transverse direction. $D_y(y)$ is the transverse component of the turbulent diffusion coefficient related to the position in y-direction. In order to satisfy continuity an extra advection term in y-direction has to be included, to achieve consistency with the governing Advection-Diffusion-Equation. This extra term in eq. 4 is called the noise-induced drift component (Dunsbergen, 1994). Consequently, in every time step, a particle moves convectively in x-direction depending on the velocity profile and does a positive or negative diffusive step in transverse y-direction.

Also the boundaries of the calculation domain and their effect on the particles are important. The inflow and outflow boundaries do not affect the particles as in our case the domain has an infinite length. In case of horizontal shear the boundaries representing the channel bank and channel centre line act as reflective walls. With the given equations and boundary conditions transport in open channel flow can be simulated with a depth-averaged velocity profile (Fig. 2, i) in transverse direction and a certain distribution of the diffusivity (Fig. 2, ii). The next step is to include the influence of dead-water zones into the LPTM, which can be achieved by introducing the mean residence time of tracer material in the dead-water zone. Weitbrecht, 2004 showed, that it is possible to model the influence of the mass transport by including this parameter into the boundary conditions as a transient-adhesion-boundary, such that this boundary simulates the behavior of mass trapping and mass release. A particle that reaches such a boundary is fixed to that x-position until the mean residence time T_D has elapsed.

The outcome of a LPTM simulation are x and y-positions of every single particle at every time step. By analyzing the statistics of the particle positions, information about the transport characteristics can be determined. The 1-D longitudinal dispersion coefficient D_L, as a measure of the spatially averaged spreading rate of a tracer cloud, can be determined by calculating the time change of the longitudinal variance σ^2 particle distribution.

A second result will be the skewness G_t of the particle cloud, which is defined as the relation between the quotient of the third moment about and the third power of the standard deviation.

The skewness of a certain distribution describes the degree of asymmetry of a distribution. The skewness can be used as an indicator for the length of the advective zone, in order to define when it is acceptable to apply the Taylor solution to a pollutant transport problem. Another parameter of interest is the transport velocity c of the tracer cloud, defined as the velocity of the center of mass of a particle ensemble. In the case of regular channel flow with ordinary reflective boundary conditions c is equal to the mean velocity if the particles are homogeneously distributed over the river cross-section. In case of point sources this can be reached after the tracer has passed the advective zone. The transport velocity is defined as the velocity of the center of mass of the particles.

3 SIMULATIONS WITH VARYING BOUNDARY CONDITIONS

In the present paper two different simulations are presented using the flow conditions from the experiment described in the introduction. The transverse mean velocity is represented by a *tanh* function (see Fig. 2, i), such that the velocity at the groin field boundary is not zero. The turbulent diffusivity in the main channel is taken to be constant with $D_L = 0.15\,u_* h$. Close to the groin fields the transverse diffusivity increases related to the Gaussian distribution given in Figure 2(ii). Simulation **A** (Fig. 3) starts without the influence of groin fields for the first 1000 times the channel width B. For x/B > 1000, the effect of the groin fields is turned of by setting the residence time T_D at the adhesive boundary to 92 seconds. In case **B** (Fig. 4) the simulation starts with a channel reach with groin fields for $0 < x/B < 1000$. For $x/B > 1000$ the residence time is set to zero. In both cases the number of particles is 10,000, they are homogeneously distributed over the inflow boundary at $x = 0$ and the length of a time step is 5 s.

In Figure 3(i–iv) the results for simulation **A** are visualized where the simulation starts without the influence of dead-water zones. In Figure 3(i) the results after the first time step is plotted where particle distribution in the upper part shows exactly the related velocity distribution. At this time step the particle distribution in longitudinal direction is strongly skewed because, most of the particles sit in the homogeneous part of the velocity distribution in the main channel. In Figure 3(ii) and (iii) the particle distribution is still strongly skewed but, the dispersion coefficient tends to a final value of about $0.04\,\mathrm{m^2/s}$, long before $x/B = 1000$ is reached. Part (iii) shows that exactly

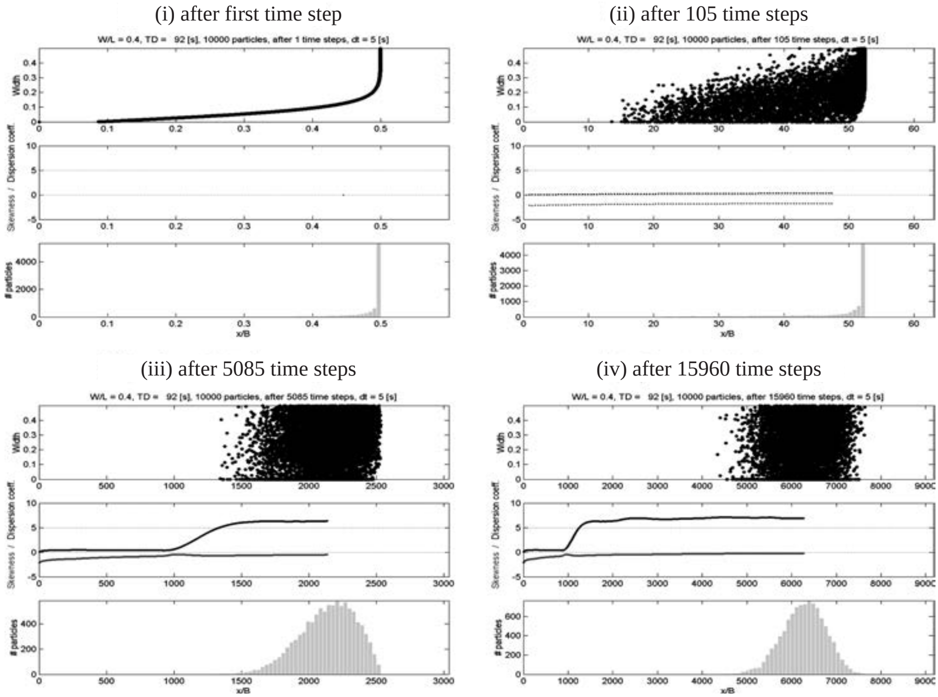

Figure 3. Results of simulation **A** where in the initial phase $x/B < 1000$ no groin fields are present, visualized at four different time steps. In the upper diagram of the four figures the particle position is plotted, in the mid part the dispersion coefficient [m^2/s] as well as the coefficient of skewness is shown, and in the lower part the particle distribution in longitudinal direction is visualized.

at $x/B = 1000$, where the channel section with transient-adhesion boundary starts the dispersion coefficient increases as expected to reach the final value of about $7\,m^2/s$, which is the same result as if the simulation starts from the beginning with the influence of groin fields.

Interesting in case **A** is the evolution of the coefficient of skewness plotted in red in the mid part of Figure 3. According to previous studies (Schmid, 2002) strong morphological changes, as the begin of a channel section with groin fields would lead to strong local increase of the skewness coefficient. In the present simulation (Fig. 3, iii and iv) the influence on the skewness is almost not visible. In contrary, at $x/B = 1000$ a local decrease of the skewness can be observed, which leads to the assumption that the process of particle retention in a dead-water zone leads to increased homogenization in longitudinal direction. In Figure 3(iv) the final stage of mixing is achieved with almost Gaussian particle distribution in longitudinal direction.

The results of simulation **B** where the groin fields stop at $x/B = 1000$ stop, in principle lead to the same conclusions as the results of simulation **A**. The initial mixing conditions do not influence the final results. In case **B** the final dispersion coefficient (Fig. 4, iv) is the same than without the groin field section in first phase. In Figure 4(ii) the influence of the transient-adhesion boundary is clearly visible. Five different particle clouds follow the main particle cloud where the mean residence time T_D is visible as the distance between these clouds divided by mean flow velocity. In case **B** an interesting phenomena occurs with respect to the dispersion coefficient at $x/B = 1000$. Here, the effect of the groin fields is virtually turned off by setting the mean residence time to zero. Against our first expectations the dispersion does not immediately decrease but increases over a travel distance that is of the order of the standard deviation of particle distribution in longitudinal direction. The dispersion coefficient increases about 30% in this region for this configuration. The stretching effect

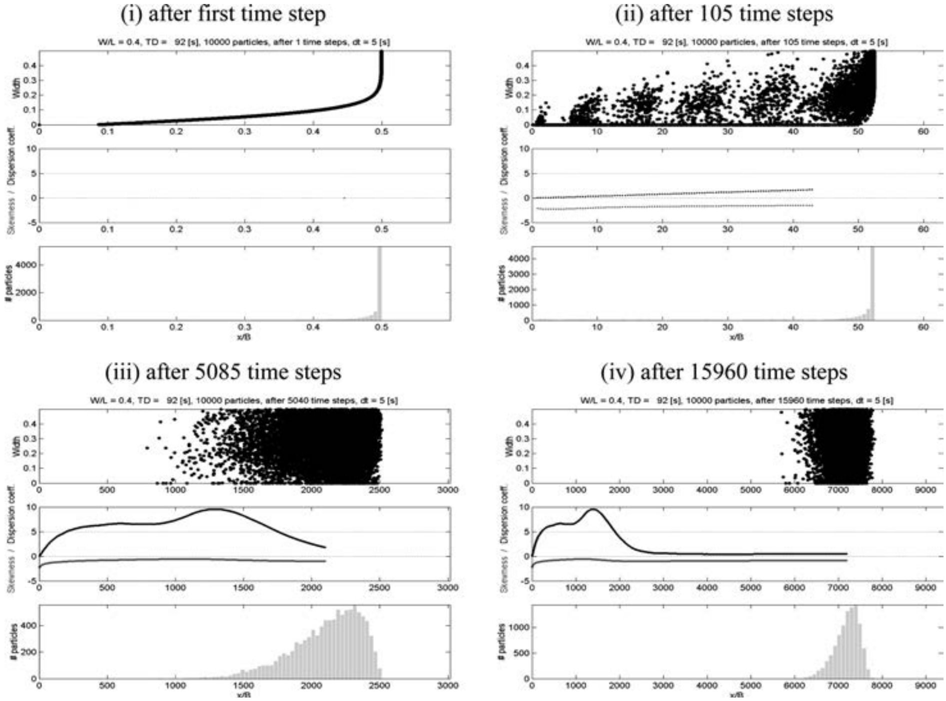

Figure 4. Results of simulation **B** where only in the initial phase $x/B < 1000$ groin fields are present, visualized at four different time steps.

is enhanced because the front of the cloud does move from $x/B = 1000$ with the mean velocity U, whereas the other part of the cloud still travels with transport velocity given by the ratio of particles that are sitting in the dead zone to the number of particles in the main stream. Also in case **B** the skewness (Fig. 4, iv) is almost not affected by the changing morphological conditions. Figure 4(iv) shows again, that the groin fields enhance the homogenization of the particle cloud in longitudinal direction and the particle distribution is still more skewed at the end of the simulation in case **B**.

4 CONCLUSIONS

In the present paper it has been shown that *LPTM* is a simple to use tool to simulate dispersive mass transport in rivers and to transfer results obtained locally at single dead-water zones in the laboratory into the far-field transport characteristics of a system with many groin fields. With two simulations where the effect of groin fields is virtually turned on, or turned off respectively, after a travel distance of 1000 times the channel width, it could be shown that the initial conditions do not affect the final result. In case **B** where the groin field effect is turned off after 1000 times the channel width the stretching rate and hence, the dispersion coefficient increases locally before it reduces to the final value. Both simulations showed that the skewness of the particle distribution in longitudinal direction is almost not influenced by this strong change of the boundary conditions that simulate a sudden change in the morphological conditions. The skewness of the particle distribution tends in the presence of dead-water zones faster towards zero than without groin fields, due to the fact that the particle retention in the groin field enhances homogenization in longitudinal direction.

REFERENCES

Aris, R. (1959), 'The longitudinal diffusion coefficient in flow through a tube with stagnant pockets', Chemical Engineering Science 11, 194–198

Dunsbergen, D.W. (1994), Particle Models for Transport in Three-Dimensional Shallow Water Flow, PhD thesis, TU-Delft, Faculty of Civil Engineering

Fischer, H.B., List, E.J., Koh, R.C.Y., Imberger, J. and Brooks, N.H. (1979), 'Mixing in Inland and Coastal Waters', Academic Press, New York

Jirka, G.H. (2004), 'Mixing and dispersion in rivers', Proc. 'River Flow 2004', Greco, Carravatta & Della Morte eds., IAHR, Naples

Schmid, B.H. (2002), 'Persistence of Skewness in Longitudinal Dispersion Data: Can the Dead Zone Model Explain It After All? J. Hydr. Engrg. 128, 848 (2002)

Spreafico, M. and van Mazijk, A. (1993), Alarmmodell Rhein. Ein Modell für die operationelle Vorhersage des Transportes von Schadstoffen im Rhein. Bericht Nr. I-12, Kommission für die Hydrologie des Rheins, Lelystad

Sullivan, P.J. (1971), 'Longitudinal dispersion within a two-dimensional turbulent shear flow', J. Fluid Mech. 49, 551–576

Taylor, G.I. (1921), 'Diffusion by continuous movements'. Proc. London Math Soc. 20, 196–211

Taylor, G.I. (1954), 'The Dispersion of matter in turbulent flow through a pipe', Proc. of the Royal Soc., London, England Vol. 233, pp. 446–468

van Mazijk, A. (2002), 'Modelling the effects of groyne fields on the transport of dissolved matter within the rhine alarme model', J. of Hydrology 264, 213–339

Weitbrecht, V., Kuhn, G., Jirka, G.H. (2002), 'Large scale PIV-measurements at the surface of shallow water flows', Flow Measurement and Instrumentation 13 (5–6) pp. 237–245

Weitbrecht, V. (2004), 'Influence of Dead-Water Zones on the Dispersive Mass Transport in Rivers', doctoral hesis, IfH-University of Karlsruhe

Weitbrecht, V., Uijttewaal, W.S.J. & Jirka, G.H. (2003), '2-D Particle Tracking to Determine Transport Characteristics in Rivers with Dead Zones', Int. Symp. for Shallow Flows, IAHR, Delft

This page intentionally left blank

Environmental Hydraulics and Sustainable Water Management – Lee & Lam (eds)
© 2005 Taylor & Francis Group, London, ISBN 04 1536 546 5

Longitudinal vortices in a water of finite depth in the absence of wind

Zhenhua Huang
Hong Kong University of Science and Technology, Hong Kong, P.R. China

Chiang C. Mei
Massachusetts Institute of Technology, Massachusetts, USA

ABSTRACT: It has been found from laboratory measurements that near-surface velocity of a turbulent current can be reduced by following-waves but increased by opposing-waves. For both wave-following and -opposing currents, longitudinal vortices have been observed in the experiments on wave-current interaction. By a depth-varying eddy viscosity, we show analytically that the change of the mean-velocity near the surface is the result of the wave-current interaction, in particular the second-order mean shear stress on the mean surface. Comparisons with existing experiments are discussed about the change of the near-surface velocity of a turbulent current. By analyzing the instability of the wave-current system to the span-wise perturbation, we show that a second-order mean shear stress exists on the mean water surface. This mean shear stress, together with the vortex force found by Craik and Leibovich (1976), causes the span-wise perturbation to grow in time, and leads to instability and the formation of longitudinal vortices. The side-wall effects which always exist in laboratory experiments will also be addressed.

1 INTRODUCTION

In a shallow lake or sea, fine sediments can be stirred up by waves and then transported by the current in the form of suspended particles. Understanding the transport of these suspended sediments is important to the study of the water quality as the fine sediment particles may be the carries of the contaminants or nutrients. Notable decrease/increase of the near-surface mean velocity has been found experimentally when long-crested waves are following/opposing a uniform turbulent shear current in a water of finite depth (see, Kemp and Simons (1983), etc.). This decrease/increase of the near-surface mean velocity may affect the transport processes that depend on the near-surface shear of the mean current. Also the unstable growth of the span-wise perturbation to this two-dimensional wave-current system can lead to the formation of longitudinal vortices similar to Langmuir cells, which have been observed in deep ocean, large lakes (Langmuir (1938)) and shallow lagoon (Szeri(1996)). These large-scale longitudinal vortices can affect the transport of the suspended sediments as well. We first present a two-dimensional theory to explain the wave-induced change of the near-surface mean velocity, and then study the instability of the two-dimensional wave-current system to the span-wise perturbation and the formation of longitudinal vortices. The longitudinal vortices produced by side walls will be discussed based on the linearized instability analysis and the concept of vortex force.

2 WAVE-INDUCED CHANGE OF NEAR – SURFACE MEAN VELOCITY

We study the wave-induced change of the mean current over a bottom characterized by a dimensionless roughness height z_b, normalized by the inverse of the wave number k. The mean current velocity is assumed to be comparable to the wave orbital velocity, which is appropriate for swells riding on a tidal current in a shallow water environment. The eddy viscosity near the surface will be affected by the presence of waves. In the core region (above the bottom oscillatory boundary layer), similar to the eddy viscosity used for wind over water waves (Townsend (1972)), we adopt the following eddy viscosity ν_e to account for the effect of the moving surface η and the water depth h on the eddy viscosity:

$$\nu_e = \nu - \frac{\kappa u_f}{k}(z-\eta)\left(1+\frac{z}{kh}\right), \tag{1}$$

where ν is the molecular viscosity, u_f the friction velocity and $\kappa = 0.4$. Both z and η in equation (1) have been normalized by the inverse of the wave number. In the core region, the friction velocity u_f is dominated by the turbulent current but slightly affected by the presence of waves, thus the friction velocity u_f will take a value different from that without waves. Inside the bottom oscillatory boundary layer where the effect of η can be omitted, we adopt the linear eddy viscosity mode of Grant and Madsen (1986), who showed that waves may greatly enhance the turbulence intensity in this thin layer and leads to friction velocity u_f larger than that in the core region.

The total velocity of the mean motion can be written as the sum of the unperturbed turbulent current and the wave-induced current u_c'. After a perturbation analysis, it was found that a second-order, non-zero mean shear stress exists on the mean surface even without wind (Huang and Mei (2003)), who also showed that in the core region the mean shear stress experienced by u_c' can be expressed by

$$\begin{aligned}\bar{S}_c\frac{\partial u_c'}{\partial z} &= -|A|^2\hat{S}_c\frac{\sinh(kh+z)}{\sinh(kh)} \pm \frac{\alpha_c-\alpha_0}{\kappa^2}\left(\frac{-z}{kh}\right) + \frac{\beta|A|^2}{\alpha_c}\frac{(z+kh)(2kh+\sinh(2kh))}{8kh\sinh^2(kh)} \\ &-\frac{\alpha_b}{\alpha_c}\frac{|A|^2(kh+z)}{2kh\sinh^2(kh)}\int_{Z_B}^{Z_\delta}\mathrm{Im}(K)dZ - |A|^2\frac{\partial^2\bar{S}_c}{\partial z^2}\frac{\sinh(2(kh+z))-2(kh+z)}{2\sinh^2(kh)}\end{aligned} \tag{2}$$

in which A is the dimensionless wave amplitude (normalized by the typical wave amplitude), The dimensionless friction velocity in the core region α_c is defined by

$$\alpha_c = \kappa u_f / C\varepsilon^2, \alpha_c = O(1) \tag{3}$$

with C being the wave speed and ε the wave slope. The dimensionless friction velocity inside the bottom wave boundary layer (α_b) and the dimensionless friction velocity without waves (α_0) are defined in a similar way. β is the dissipation rate of wave energy, which has been given in Huang and Mei (2003) for a spatially-decaying waves in a turbulent current. The shape of the unperturbed eddy viscosity and the shape of the surface distortion of the eddy viscosity are given, respectively, by

$$\bar{S}_c = z_\nu - z\left(1+\frac{z}{kh}\right), \quad \hat{S}_c = 1+\frac{z}{kh}, \text{ where } z_\nu = \frac{k\nu}{\kappa u_f}. \tag{4}$$

In (2), symbol Im $(\cdot)$ stands for the imaginary part of its argument. K (Z), a function describing the bottom Stokes boundary layer, is defined by

$$K = K_0\left(2\sqrt{Z}e^{-i\pi/4}\right)/K_0\left(2\sqrt{Z_B}e^{-i\pi/4}\right), \; Z = kh + z/\alpha_0\varepsilon^2, \; Z_B = z_b/\alpha_0\varepsilon^2 \tag{5}$$

with $K_0(Z)$ being the Kelvin function of the zero-*th* order. Z_δ is the thickness of the bottom wave boundary layer, determined by a matching procedure (Huang and Mei(2003)). It can be seen from (2) that the perturbed mean shear stress is controlled by the following factors: (1) the surface distortion of eddy viscosity; (2) wave-induced change of the friction velocity; (3) wave-damping; (4) wave-induced Reynolds stress due to the bottom Stokes layer, and (5) the curvature of the eddy viscosity. Predicted wave attenuation and mean velocity profile agree well with available

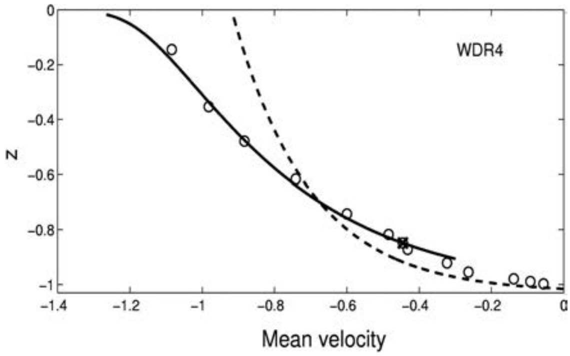

Figure 1. Comparison between the measured (circles) and the predicted (solid line) mean velocity for wave-opposing current. The dashed line is the mean velocity without waves. Data points are from the run WDR4 of Kemp and Simons (1983) for wave-opposing current, which shows the increase mean velocity near surface by opposing wave. Symbol cross (x) is the location where velocity patching was made. The water depth was 0.2 m, wavelength 1.23 m and the wave amplitude 2.5 cm.

experiments. Figure 1 shows the comparison of the measured and predicted mean velocity profiles for wave-opposing current. To certain extent, the change of the mean current profile due to waves will contribute to the generation of the longitudinal vorticity discussed in the next section.

3 LONGITUDINAL VORTICES DUE TO INSTABILITY

Longitudinal vortices in shallow water can produce large-scale cellular motions similar to Langmuir circulations in deep sea. These cellular motions can extend down to the bottom in a water of finite depth, thus are crucial to the mixing processes and the transport of suspended sediment in shallow water environments. We present a linear instability analysis to study the unstable growth of a span-wise perturbation to the two-dimensional wave-current system. Similar problems for wind-driven current comparable to the wave orbital velocity in deep seas have been studied by Craik (1982) and Phillips (1997). We study here the problem for tidal current in a shallow water environment. Following a standard perturbation analysis (Huang (2003)) , the linearized equations governing the longitudinal velocity u_0 and the longitudinal vorticity ξ_0 of the span-wise periodic motion are obtained

$$\frac{\partial u_0}{\partial \tau} + \left(w_0 \frac{\alpha_0}{\kappa(kh+z)} + w_0 \frac{\partial u_c'}{\partial z} \right) = \alpha_c \left(\overline{S}_c \frac{\partial^2 u_0}{\partial y^2} + \frac{\partial}{\partial z}\left(\overline{S} \frac{\partial u_0}{\partial z} \right) \right), \tag{6}$$

$$\begin{aligned} \frac{\partial \xi_0}{\partial \tau} + \frac{\partial u_0}{\partial y}\frac{\partial U_s}{\partial z} = \alpha_c \overline{S}_c \left[\frac{\partial^2 \xi_0}{\partial z^2} + \frac{\partial^2 \xi_0}{\partial y^2} \right] - 2\frac{\partial \overline{S}_c}{\partial z}\left[\frac{\partial^2 v_0}{\partial y^2} + \frac{\partial^2 v_0}{\partial z^2} \right] \\ - \frac{\partial^2 \overline{S}_2}{\partial z^2}\left[\frac{\partial w_0}{\partial y} + \frac{\partial v_0}{\partial z} \right], \end{aligned} \tag{7}$$

which are supplemented by, respectively, the definition of the longitudinal vorticity and continuity equation for the span-wise perturbation.

$$\xi_0 = \frac{\partial w_0}{\partial y} - \frac{\partial v_0}{\partial z}, \quad \frac{\partial v_0}{\partial y} + \frac{\partial w_0}{\partial z} = 0. \tag{8}$$

In equation (7), U_s is the Stokes drift computed by the linear waves. The second term on the left-hand side of equation (6) is due to the shear in the unperturbed current which is logarithmic with

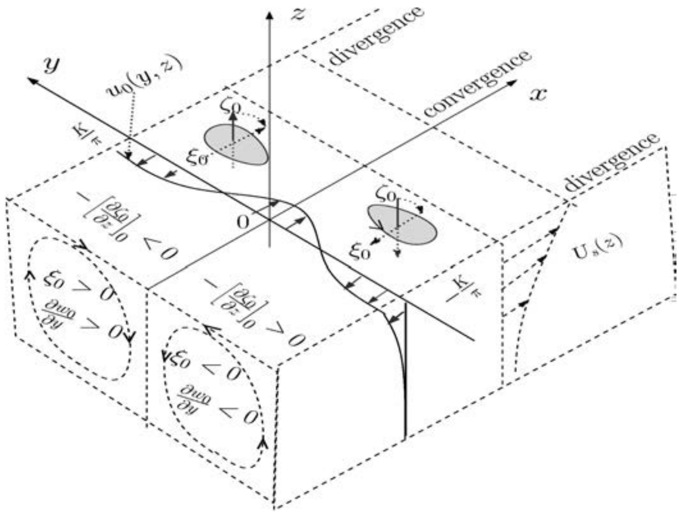

Figure 2. Illustration of the physical mechanism of instability caused by mean surface stress (equation (9)). The undisturbed current, absence from the mean stress on the surface, is not shown in the figure.

respect to the distance from the bottom; the third term on the left-hand side of (6) is due to the shear in the wave-induced current (u_c'), whose shear rate in the core is comparable with that of the unperturbed current (see Huang and Mei (2003)). The nonlinear interaction between the primary waves and the secondary waves (due to the interaction between primary waves and the span-wise perturbation) produces a non-zero mean shear stress on the mean surface which is the one of the surface boundary conditions of the spane-wise motion (Huang (2003), Huang and Mei (2004))

$$\frac{\partial u_0}{\partial z} = s|A|^2 \frac{\coth(kh)}{2} \frac{\partial w_0}{\partial z}, \text{ or } \frac{\partial}{\partial z}\frac{\partial u_0}{\partial y} \equiv -\frac{\partial}{\partial z}\zeta_0 = s|A|^2 \frac{\coth(kh)}{2} \frac{\partial}{\partial z}\frac{\partial w_0}{\partial y}. \quad (9)$$

where u_0 the longitudinal mean velocity, w_0 vertical mean velocity, and $\zeta_0 = -\partial u_0/\partial y$ the vertical vorticity. s is a known numerical parameter depending on the wave and current conditions (Huang (2003)). The other surface boundary conditions are $\partial v_0/\partial_z = 0$ and $w_0 = 0$ on the mean surface. No-slip and no-flux are required on the bottom.

The non-zero mean shear stress (9) couples the transverse motion (v_0, w_0) with the longitudinal motion (u_0) and causes a further growth of the span-wise perturbation, as illustrated in the Figure 2. Suppose that surface has the initial surface divergence/convergence due to small perturbation (see Leibovich (1983)), there must be upwelling and down-welling motion as sketched in Figure 2. Consider a half y-period where $\partial w_0/\partial y > 0$ in the core but $\partial w_0/\partial y = 0$ on the mean surface. It then follows that near the water surface the vertical gradient of $\partial w_0/\partial y$ is negative. Because of (9), there will be a downward influx of the vertical vorticity. This influx is diffused downward by eddy viscosity to increase the vertical vorticity in the core. In view of (7), the increment of vertical vorticity ζ_0 forces further increase of the longitudinal vorticity ξ_0 by the shear in the Stokes drift, which in turn forces further increase of the vertical vorticity on account of (6). Thus surface boundary condition (9) contributes to the unstable growth of span-wise perturbation. Within the half-y period where $\partial w_0/\partial y < 0$ in the core region, all signs reversed.

It is found by numerical examples that this non-zero mean shear stress is as important as the vortex force in the formation of the longitudinal vortices by an instability mechanism. There are two vertical modes which may grow in time. The first mode is due mainly to the surface stress (cf. (9)); while the second mode is driven by both the vortex force in the core and the mean shear stress on the surface. Effects of wave steepness (ε), wave number of span-wise perturbation (K), water depth (kh) and relative current strength u_f/C on the growth rate of the span-wise perturbation

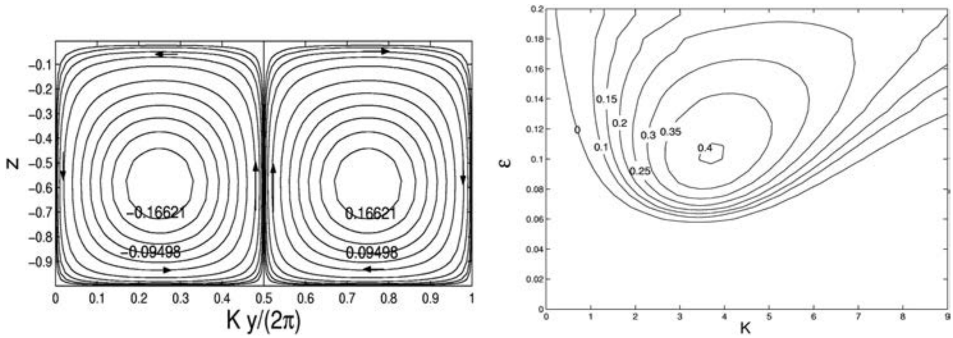

Figure 3. Left figure: Computed cell pattern of longitudinal vortex motion for $\varepsilon = 0.18$ in which the arrows indicate the flow direction and the numbers indicate the values of stream function; Right figure: Growth rates of the second mode as a function of the lateral wave-number K and wave slope ε in which the numbers indicate the growth rate σ_r. Conditions: $u_f/_C = 0.003$, $kh = 1.0$ and $z_b = 2 \times 10^{-6}$.

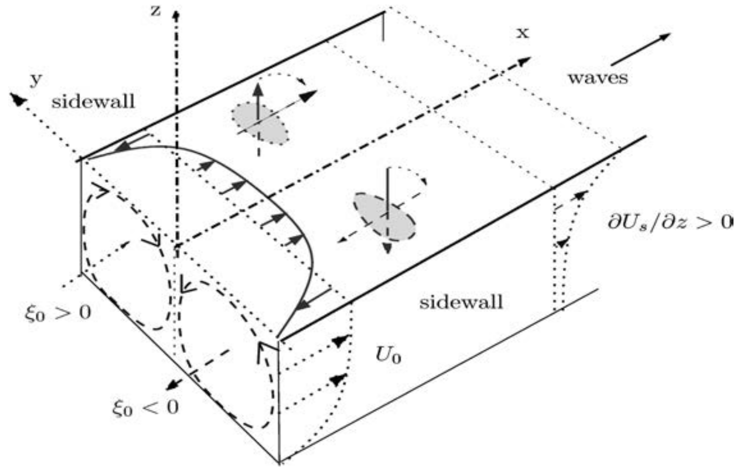

Figure 4. Longitudinal vortices due to sidewalls in current following waves. U_0 is the unperturbed open-channel flow which has boundary layer structures near the two sidewalls.

σ_r were studied by Huang (2003), who found that the second mode is more important to the transport processes. Figure 3 shows a typical cell pattern and contour of the growth rate σ_r in (σ_r, K) space for the second mode. The minimum wave slope needed for the instability is $\varepsilon = 0.06$ below which the wave-current system is stable to all span-wise perturbations. The maximum growth rate occurs at $\varepsilon = 0.1$ and $K = 3.8$. Further increasing wave slope will reduce the growth rate due to the wave-induced reduction of the mean velocity near the surface (i.e. negative shear rate $\partial u_c'/\partial z$ in (6)). Longitudinal vortices can also be formed in a wave-opposing current, but they are much weaker than those in a wave-following current and are of less practical importance.

4 LONGITUDINAL VORTICES DUE TO SIDEWALLS

In laboratory experiments on the formation of longitudinal vortices, effects of side walls cannot be neglected. As strong shears (due to sidewall current boundary layers) exist near the sidewalls, a pair of longitudinal vortices can be formed in both the wave-following and opposing currents.

Consider waves following a turbulent current in a tank as shown in Figure 4. The vertical vortices exist due to current boundary layers next to sidewalls and are finite in magnitude. The presence of the finite vertical vorticity will produce longitudinal vorticity because of the vortex force (cf. (7)). As a result, traces placed on water surface will eventually collect themselves in the centerline of the wave tank. For wave-opposing current, all signs of vertical and longitudinal vortices reversed, and tracers placed on the water surface will collect themselves next to the two sidewalls. In view of the analysis given above, the longitudinal vortices measured by Klopman (1997) were not the results of the instability of the wave-current system. Therefore it is not appropriate to use them to test the theory on the instability of the wave-current system to the span-wise perturbations.

5 DISCUSSION

Two important aspects of the wave-current interaction in shallow water have been discussed here: the change of the turbulent mean current by waves and the instability of the wave-current system to the span-wise perturbations which leads to the generation of longitudinal vortices. It is found that the surface distortion of the eddy viscosity contribute most to the change of the velocity profile of the turbulent current. The nonlinear interaction between waves and current gives rise to a mean shear stress at the mean surface, which has a span-wise variation and contributes a great deal to the growth of the span-wise perturbation in both wave-following and wave-opposing currents. The theory presented here can find its application in the study of the transport of fine sediment grains or nutrients in the coastal environment where the swells and tidal currents dominate. Even though Craik and leibovich instability theory provides us a mechanism to explain the presence of longitudinal vorticity in a wave-current system, but it is still subject to observational verification both in field and in laboratory conditions. It seems so far that this verification is not an easy task on account of the complex field conditions and the sidewall effects in the laboratory conditions.

The work was supported by US Office of Naval Research (Grant N00014-89J-3128, Dr. Thomas Swean) and US National Science Foundation (Grant CTS-0075713, Dr. C.F. Chen and Dr. M. Plesniak).

REFERENCES

Craik, A.D.D. 1982. Wave-induced longitudinal vortex instability in shear layer. *J. Fluid Mech.* 125: 37–52.

Craik, A.D.D. and Leibovich, S. 1976. A rational model for Langmuir circulation. *J. Fluid Mech.* 73: 401–426.

Grant, W.D. and Madsen, O.S. 1986. The continental shelf bottom boundary layer. *Ann. Rev. Fluid Mech.* 18: 265–305.

Huang, Z.H. 2003. Wave-current interaction in water of finite depth. PhD thesis, Massachusetts Institute of Technology.

Huang, Z.H. and Mei, C.C. 2004 Effects of surface waves on a turbulent current over a smooth or rough seabed. *J. Fluid Mech.*, 497, 253–287.

Huang, Z.H. and Mei, C.C. 2004. Wave induced longitudinal vortices in a shallow current. *Submitted to J. Fluid Mech.*

Kemp, P.H. and Simons, R.A. 1983. The interaction between waves and a turbulent current: wave propagating against the current. *J. Fluid Mech.* 130: 73–85.

Klopman, G. 1997. Secondary circulation of the flow due to waves and current: Laser-doppler flow measurements for waves following or opposing current. Tech. Rep. Z2249. Delft Hydraulics.

Langmuir, I. 1938. Surface motion of water induced by wind. *Science* 87: 119–123.

Leibovich, S. 1983. The form and dynamics of Langmuir circulation. *Ann. Rev. Fluid Mech.* 15: 391–427.

Longuet-Higgins, M.S. 1953. Mass transport in water waves. *Phil. Trans. Roy. Soc. Lond. (A)* 245: 535–581.

Phillips, W.R.C. 1998. Finite-amplitude rotational waves in viscous shear flows. *Stud. Appl. Math.* 101: 23–47.

Szeri, A.J. 1996. Langmuir circulations on Rodeo lagoon. *Monthly Weather Review*, 124(2): 341–342.

Townsend, A.A. 1972. Flow in a deep turbulent boundary layer over a surface distorted by water waves. *J. Fluid Mech.*, 55: 719–753.

1.2 Mixing and transport – II

This page intentionally left blank

Environmental Hydraulics and Sustainable Water Management – Lee & Lam (eds)
© 2005 Taylor & Francis Group, London, ISBN 04 1536 546 5

Field tests on transverse mixing in natural streams

I.W. Seo, K.O. Baek & T.M. Jeon
Seoul National University, Seoul, Korea

ABSTRACT: Tracer tests were conducted in natural streams to investigate the characteristics of the transverse mixing of pollutants. These field tests were carried out at six different sites in Han River system in Korea, three in Sum River, two in Hongcheon River, and one in Cheongmi Stream. At each field test, six transections were selected to obtain hydraulic and concentration data. Using the acquired concentration data and hydraulic data, the transverse dispersion coefficients were evaluated via three methods such as moment method, modified moment method, and routing procedure which is newly proposed in this study. Those results calculated by three methods are in good agreement with each other. It is also found that the transverse dispersion coefficient (TDC) is inversely proportional to the dimensionless radius of curvature of the meander (R_c/W), whereas TDC is increasing as the aspect ratio (W/H) increases. TDC also tends to increase with increasing ratio of average velocity to the shear velocity (U/U_*).

1 INTRODUCTION

There is lack of studies on the two-dimensional tracer test in natural streams compared with those in laboratory channels. The transverse dispersion coefficients have been observed in the laboratory channel and can be well predicted at such situations. However, predictions were not credible when trying to extend this information to natural stream flows. Thus, it is necessary to perform field tests in order to determine the transverse dispersion coefficient of a particular river at given stages. In this study, field tracer tests were conducted in three streams at six reaches which had various meandering patterns. And transverse mixing characteristics in natural streams were analyzed and determining method of the transverse dispersion coefficient was newly developed.

2 THEORETICAL BACKGROUND

The simple moment method was derived by several researchers (Sayre and Chang, 1968; Holley, 1971 and Holley et al., 1972). When both the velocity and depth are constant, and the transverse velocity are negligible small, the simple moment equation can be written as

$$D_T = \frac{U}{2}\frac{d\sigma_y{}^2}{dx} \tag{1}$$

where D_T is the transverse dispersion coefficient; U is mean velocity; and σ_y^2 is the variance about the transverse distribution of depth-averaged concentration.

Beltaos (1980) proposed another moment method which was derived through the stream-tube concept. The governing equation is

$$\frac{\partial C}{\partial x} = \frac{\partial}{\partial q}\left(E_T\frac{\partial^2 C}{\partial q^2}\right) \tag{2}$$

where q is the flow discharge between the left bank and any location at y. Also, the diffusion factor, E_T, can be written as

$$E_T = \Psi D_T U H^2 \tag{3}$$

where Ψ is a dimensionless shape-velocity factor found to lie in the range $\Psi = 1.0 \sim 3.6$ (Sayre, 1979; Beltaos, 1980) and defined by

$$\Psi = \frac{1}{Q}\int_0^Q h^2 u dq \tag{4}$$

where Q is total flow discharge. Normalizing C and q through the definitions, Equation (2) can be transformed as

$$\frac{\partial C'}{\partial x} = \frac{E_T}{Q^2}\frac{\partial^2 C'}{\partial \eta^2} \tag{5}$$

where $\eta \equiv q/Q$; $C' \equiv C/C_\infty$; and $C_\infty = \int_0^1 C d\eta$. Through Equation (5), the moment method combined with the stream-tube concept can be derived as (Baek, 2004)

$$\frac{d\sigma_\eta^2}{dx} = \frac{2E_T}{Q^2}[1-(1-\eta_0)C_1' - \eta_0 C_0'] \tag{6}$$

where σ_η^2, η_0 are the variance and centroid of the $C' - \eta$ distribution respectively; and C_0', C_1' are normalized concentration at left bank and right bank, respectively. Plotting σ_η^2 versus corresponding values should result in a straight line of slope $2E_T/Q^2$, which can be used to compute the corresponding value of D_T.

The preceding analysis, Equation (1) and Equation (6), apply only when concentration is independent of time, i.e., for steady-state concentration condition. However, Beltaos (1975) showed that moment methods also be applied to the results of transient tests without complex calculation, if C is replaced by the dosage which is defined by

$$\theta(x,q) \equiv \int_0^\infty C(x,q,t)dt \tag{7}$$

where θ is dosage of the solute mass.

The stream-tube routing procedure is developed in this study. The concept of the stream-tube routing procedure is to combine the stream-tube model and the routing procedure. Using the routing procedure (Fischer, 1968) one can obtain dispersion coefficient by matching a downstream observation of passage of a tracer cloud to the prediction based on an upstream observation. The conceptual diagram of an application of the stream-tube routing procedure at a stream is shown in Figure 1. The derivation of the stream-tube routing procedure can start with Equation (5). Recalling the suggestion of Beltaos (1975) under the transient concentration condition, the dimensionless dosage is defined as

$$S \equiv \frac{\theta}{\Theta} \tag{8}$$

where S is dimensionless dosage and Θ is total dosage. In Equation (5), C' is substituted into S, then Equation (5) becomes

$$\frac{\partial S}{\partial x} = B_C \frac{\partial^2 S}{\partial \eta^2} \tag{9}$$

where B_C is a bulk dispersion coefficient defined as

$$B_C = \frac{E_T}{Q^2} \tag{10}$$

The analytical solution to Equation (9) for a vertical line source being instantaneously injected at $x = 0$, $\eta = \omega$ can be obtained (Carslaw and Jaeger, 1959) as:

$$S(x,\eta) = \frac{\Theta}{\sqrt{4\pi B_C x}} \exp\left(-\frac{(\eta-\omega)^2}{4B_C x}\right) \tag{11}$$

Based on Fischer (1968), the stream-tube routing equation can be expressed as (Baek, 2004)

$$S(x_2,\eta) = \int_0^1 \frac{S(x_1,\omega)}{\sqrt{4\pi B_C (x_2 - x_1)}} \exp\left(\frac{-(\eta-\omega)^2}{4B_C (x_2 - x_1)}\right) d\omega \tag{12}$$

where $S(x_1, \omega)$ is the observed dosage as a function of dimensionless discharge at an upstream site, $S(x_2, \eta)$ is the predicted dosage as a function of dimensionless discharge at a downstream site, and ω is a normalized dummy transverse distance variable of integration. Through Equation (12), the dosage profile at a downstream can be calculated, and then by fitting between the calculated dosage and the observed dosage, the bulk coefficient can be evaluated. Using the acquired bulk coefficient, the transverse dispersion coefficient can be calculated as

$$D_T = \frac{B_C Q^2}{\Psi H^2 U} \tag{13}$$

3 FIELD TESTS

In order to conduct field tests, three mid-sized streams were selected considering the degree of a meander, hydraulic characteristics, and so on. The Sum River and the Cheongmi Stream which are

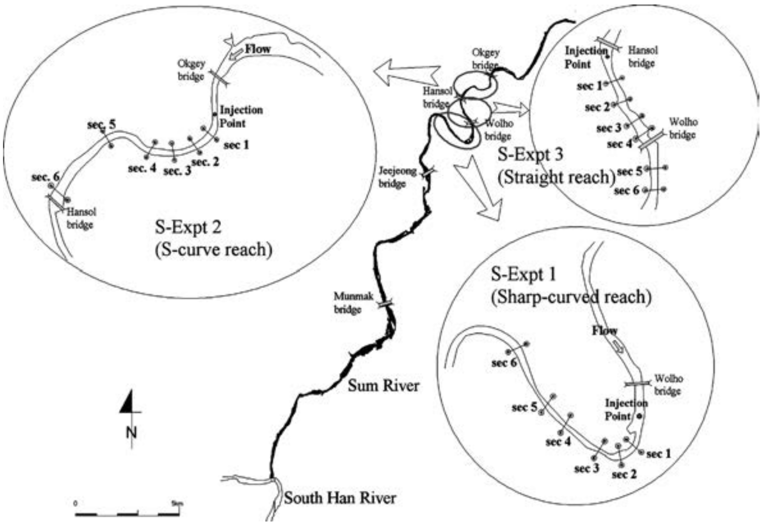

Figure 1. Sum River test reaches.

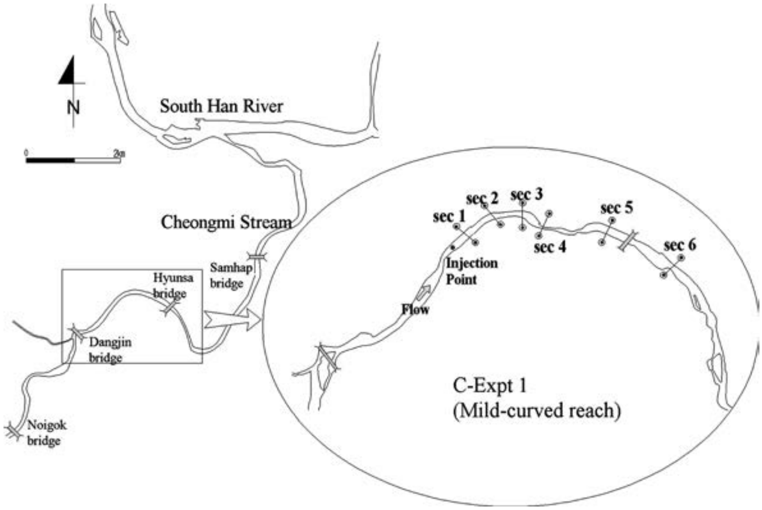

Figure 2. Cheongmi Stream test reach.

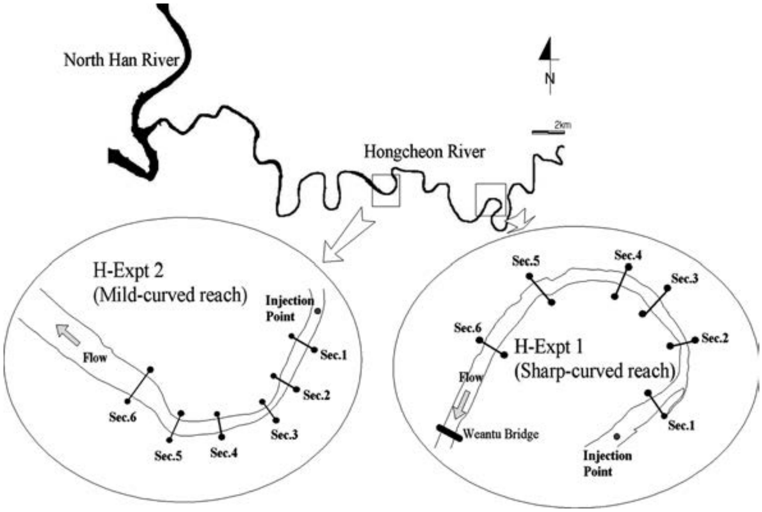

Figure 3. Hongcheon River test reaches.

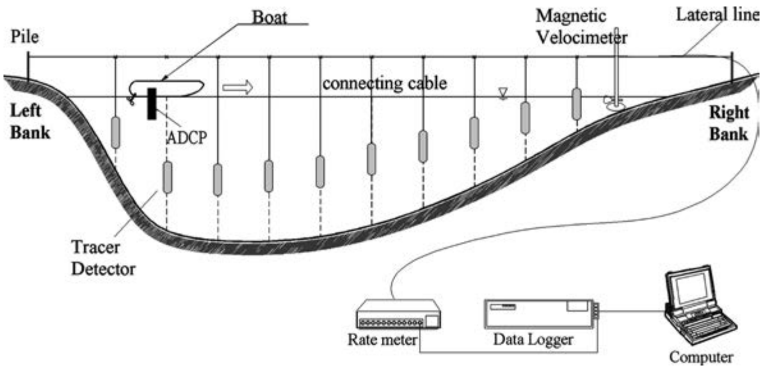

Figure 4. Installation of measuring equipments.

tributaries of the South Han River, and the Hongcheon River which is tributary of the North Han River were selected as the test sites. The layout of the test reaches are shown in Figures 1~3. The measuring systems of the tracer are depicted in Figure 4. Lateral lines which were fixed by piles located at both banks were set up perpendicular to a flow direction. The interval of each lateral line ranged 200~400 m, and six lateral lines were set up at each test reach (Figures 1~3). Using lateral lines, measurements of the hydraulic and concentration data were performed.

Before the tracer tests, both velocity and depth were measured at each transection using the Acoustic Doppler Current Profiler (ADCP) of which the principle of operation is based on the Doppler effects. After finishing measurement of velocity and depth, tracer tests were performed in the same locations. Among the radioisotopes, I-131 was used as a tracer. In order to conduct two-dimensional analysis, the tracer was injected instantaneously into the stream as a full-depth vertical line source at the centerline of the stream width. The concentration of a tracer was detected at ten points transversely at the mid-depth.

4 EXPERIMENTAL RESULTS

4.1 *Hydraulic data*

Through field experiments of six cases, the mean hydraulic data could be obtained. Natural streams at which experiments were conducted are about 30~100 m wide and 0.3~2 m deep. Distributions of the depth-averaged primary velocity and depth at each transection for the case of S-Expt 2 are plotted in Figure 5. The reach of S-Expt 2 consisted of alternative bends so that the thalweg was biased toward the left bank in the first bend, and skewed toward the right bank in the second bend. Also, the transverse distribution of the velocity arose according to the trace of thalweg.

4.2 *Concentration data*

After finishing measurement of velocity and depth, tracer tests were performed in the same transections. In general, high concentration was detected transversely according to the high flow discharge through the whole experiments. In order to visualize the behavior of the tracer cloud, the concentration spatial distributions which could be obtained through the concentration-time curve by the interpolation technique are plotted in Figure 6 for the case of H-Expt 1. As shown in Figure 6, it is obviously observed that the core of the tracer cloud is biased toward the outer bank by the

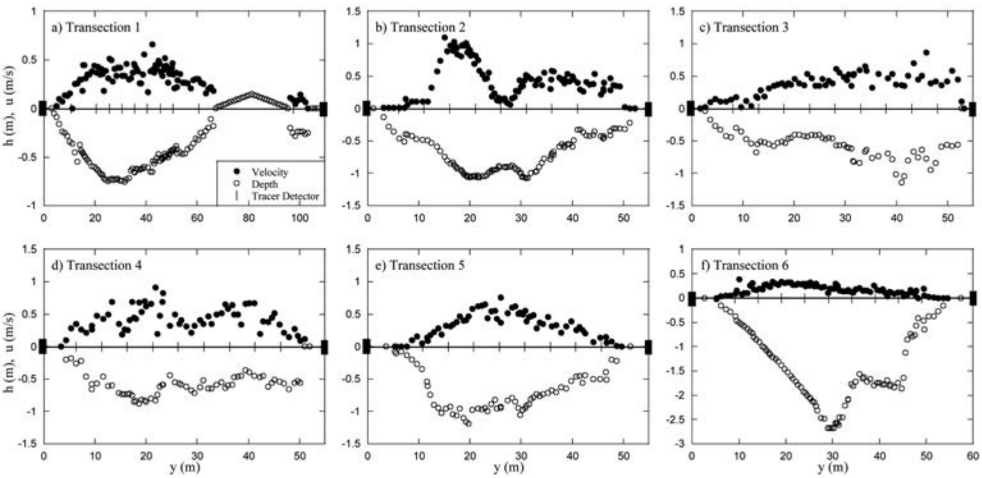

Figure 5. Distributions of velocity and depth on S-Expt 2.

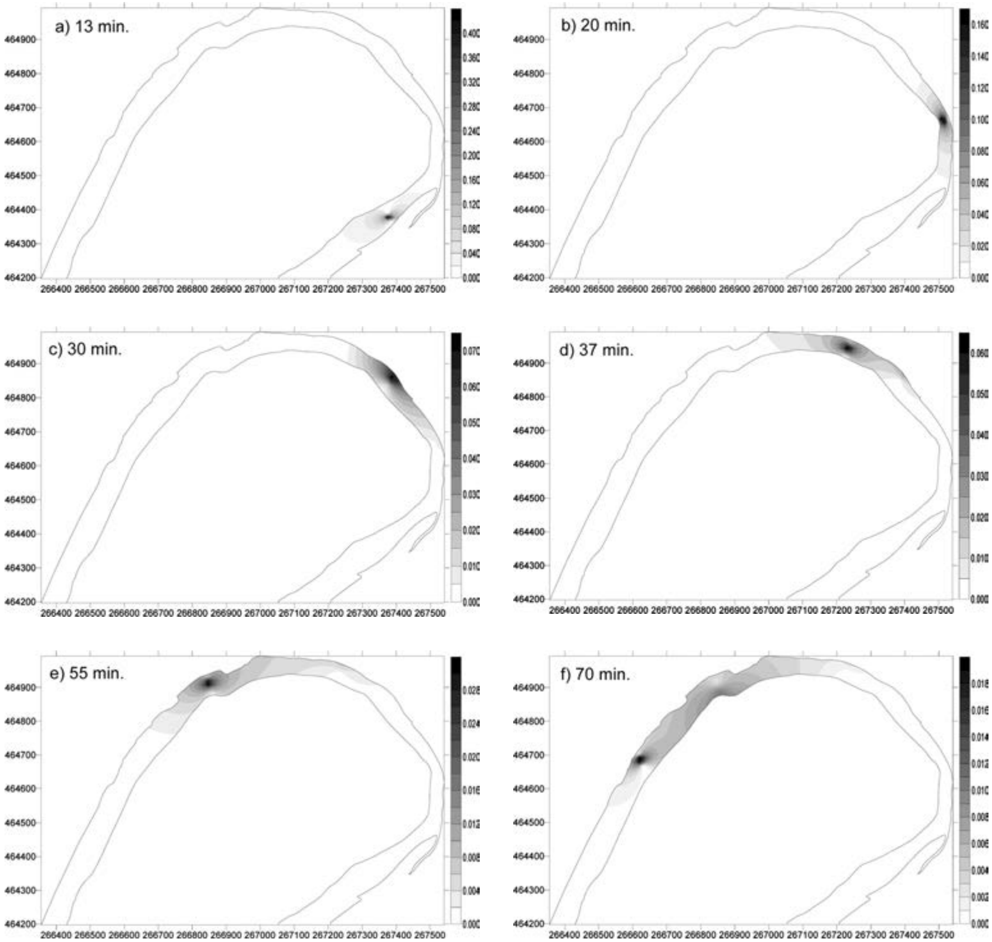

Figure 6. Behavior of tracer cloud for H-Expt 1.

effect of meander. It is observed that the tracer cloud is transporting downstream following the maximum velocity line.

5 EVALUATION OF TRANSVERSE DISPERSION COEFFICIENTS

The simple moment method and the stream-tube moment method were used to evaluate the transverse dispersion coefficient. When the simple moment method and the stream-tube moment method are applied to test sites, the dispersion coefficients can be obtained through the gradient of the variances according to longitudinal distance. The results of applying the stream-tube routing procedure are tabulated in Table 1. As shown in Table 1, the results of the stream-tube routing procedure agree well with those of other methods. The observed transverse dispersion coefficients in the cases of the S-curved reach and the sharp curved reach were higher than those in other cases. This means that the additional transverse mixing occurs due to the effect of the sharp or alternative meander. On the other hand, the transverse dispersion coefficients in the mild curved reaches were not higher than those in the straight reach. This implies that a mild curvature may little affect the increase of the transverse mixing.

Table 1. Comparison of observed transverse dispersion coefficients.

Case	D_T/HU_* Simple MM Eq. (1)	Stream-tube MM Eq. (6)	Stream-tube RP Eq. (12)	
S-Expt 1	0.45	0.43	0.46	Sec. 3 – 6
S-Expt 2	0.76	0.85	1.21	Sec. 2 – 4
S-Expt 3	0.27	0.32	0.30	Sec. 1 – 5
C-Expt 1	0.24	0.34	0.27	Sec. 2 – 5
H-Expt 1	0.47	0.85	0.64	Sec. 2 – 6
H-Expt 2	0.24	0.24	0.23	Sec. 2 – 6

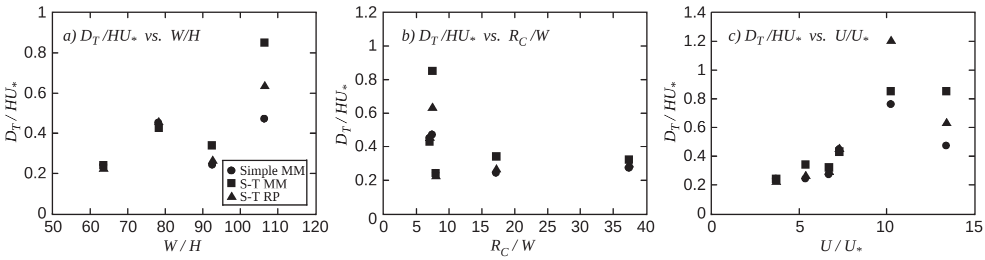

Figure 7. Transverse dispersion coefficients according to hydraulic ratios.

In order to investigate the effect of the geometric and hydraulic properties on the transverse dispersion coefficients more quantatively, plots of the dimensionless dispersion coefficients versus the hydraulic ratios are depicted in Figure 7. As the ratio of width to depth becomes larger, the transverse dispersion coefficients tend to increase irrespective of evaluation methods (Figure 7a). On the other side, the transverse dispersion coefficients are in inverse proportion to the ratio of curvature to width (Figure 7b). This result is reasonable because large radius of curvature decreases the meandering effect on the transverse mixing. And the transverse dispersion coefficients have a tendency to increase, as the ratio of mean velocity to shear velocity becomes larger (Figure 7c).

6 CONCLUSIONS

The transverse mixing characteristics in meandering streams were analyzed two-dimensionally, and calculation methods of the transverse dispersion coefficient were developed. As the result of field experiments, it was observed that the transverse distributions of the velocity and depth were biased by the effects of the meander. Through the tracer tests, it was observed that the tracer cloud spread following the peak velocity line. Using the stream-tube routing procedure proposed in this study, the transverse dispersion coefficients were determined in each field site. The evaluated transverse dispersion coefficients by the routing procedure were in good agreement with those by the moment method and the stream-tube moment method. Those results calculated by three methods are in good agreement with each other. It is also found that the transverse dispersion coefficient is inversely proportional to the dimensionless radius of curvature of the meander (R_c/W), whereas TDC is increasing as the aspect ratio (W/H) increases. TDC also tends to increase with increasing ratio of average velocity to the shear velocity (U/U_*).

ACKNOWLEDGEMENTS

This research work was supported by the 21C Frontier project of the Ministry of Science and Technology. This research conducted in the Research Institute of Engineering Science of Seoul National University, Seoul, Korea. The authors thank KICT, KAERI, and GeoGlobus for acquisition of field data.

REFERENCES

Beak, K. O. 2004. Transverse mixing in meandering channels with unsteady pollutant source. PhD thesis, Seoul, Korea.

Beltaos, S. 1975. Evaluation of transverse mixing coefficients from slug tests. *J. of Hydr. Res.*, IAHR, 13(4), 351–360.

Beltaos, S. 1980. Transverse mixing tests in natural streams. *J. of Hydr. Div.*, ASCE, 106(HY10), 1607–1625.

Carslaw, H. S., and Jaeger, J. C. 1959. *Conduction of heat in solids*, Oxford University Press, New York.

Fischer, H. B. 1968. Dispersion predictions in natural streams. *J. Sanit. Engrg. Div.*, ASCE, 94(SA5), 927–943.

Holley, E. R. 1971. Transverse mixing in rivers. *Laboratory Report No. S-132*, Delft Hydraulics Lab., Delft, Netherlands.

Holley, E. R., Siemons, J., and Abraham, G. 1972. Some aspects of analyzing transverse diffusion in rivers. *J. of Hydr. Res.*, IAHR, 10(1), 27–57.

Sayre, W. W. 1979. Shore-attached thermal plumes in rivers. *Modelling in Rivers*, Wiley-interscience, London.

Sayre, W. W., and Chang, F. M. 1968. A laboratory investigation of open channel dispersion processes for dissolved, suspended, and floating dispersants. *Professional Paper No. 433-E*, U.S. Geological Survey.

Environmental Hydraulics and Sustainable Water Management – Lee & Lam (eds)
© 2005 Taylor & Francis Group, London, ISBN 04 1536 546 5

Effects of variable river geometry on longitudinal dispersion

Mirmosadegh Jamali
Department of Civil Engineering, Sharif University of Technology, Teheran, Iran

Gregory A. Lawrence
Department of Civil Engineering, University of British Columbia, Vancouver, Canada

ABSTRACT: Most analyses of turbulent mixing in rivers assume constant hydraulic geometry (width, depth, and velocity), despite the fact that in natural rivers these variables typically increase downstream. A comprehensive set of data for the rivers and streams in the United States is used to derive generalized equations for variations in hydraulic geometry. As a preliminary investigation of the importance of these variations, an approximate analytical solution to the one-dimensional advective-dispersion equation is derived for rivers with variable velocity, cross-sectional area, and dispersion coefficient. The solution compares well with previous analyses of field data, and is used to show that the downstream concentrations of a tracer are considerably lower than those calculated assuming constant hydraulic geometry.

1 INTRODUCTION

Prediction of the impacts of contaminant discharges into rivers on downstream water quality is one of the classic problems in Environmental Engineering, see Fischer et al. (1979) and Rutherford (1994). In these books, and most other references on the subject, the hydraulic geometry (average width, depth and velocity) of the river and the dispersion coefficients are generally assumed to remain constant. However, the impact of a release may extend to a point where both the cross-sectional area of the river and the discharge have increased considerably. The effects of variable river properties are most likely to be important in the far-field where cross-sectional mixing is complete and one-dimensional longitudinal dispersion dominates.

In its most general form the one-dimensional (longitudinal) advective-diffusion equation (conservation of solute mass) can be written as:

$$\frac{\partial AC}{\partial t} + \frac{\partial}{\partial x}(uAC) = \frac{\partial}{\partial x}\left[KA\frac{\partial C}{\partial x}\right] \tag{1}$$

where C is concentration, t is time, x is downstream distance, A is the cross-sectional area of the river, u is the cross-sectionally averaged velocity, and K is the longitudinal dispersion coefficient. The adequacy of the constant river model has been called into question for some time. Nordin and Sabol (1974) reported that the constant Fickian type equation can not adequately describe longitudinal dispersion in rivers. Day (1977a,b) found significant disagreement between his experimental results and the solution of the constant longitudinal dispersion equation for an instantaneous point source. His data showed that that the longitudinal dispersion coefficient increased indefinitely with distance downstream.

Hunt (1999) used a similarity technique to find an analytical solution to the one-dimensional equation in which the dispersion coefficient was linearly proportional to the distance downstream of an instantaneous point source. He compared his solution and the results obtained with the constant coefficient model with the field data of Day and Wood (1976) and Day (1977a,b) and concluded that in all cases the variable dispersion coefficient model provided a much more accurate description of experimental results.

Jobson (1996, 1997) reported tracer data collected by the U.S. Geological Survey in over 60 different rivers representing a wide range of sizes, slopes, and geomorphic types. He incorporated variations in hydraulic geometry in an empirical method to predict the rate of attenuation of the peak concentration of a conservative contaminant, and to predict the time required for a contaminant plume to pass a particular point.

The present paper presents an analytical solution to the one-dimensional dispersion equation for an instantaneous point release into a river with slowly varying velocity, cross-sectional area, and dispersion coefficient. The solution is then compared with the "standard" constant geometry solution, the solution of Hunt (1999), and with the results of Jobson (1996, 1997). Calculations are presented that demonstrate the potential importance of variations in hydraulic geometry on longitudinal dispersion.

2 THEORETICAL DEVELOPMENT

The hydraulic characteristics of a river or stream are the main factors in determining the rate of mixing and dispersion of a solute. As a river flows downstream, tributaries add to the discharge and as a result, river width, depth, and velocity increase. Our primary objective is to solve the advective-diffusion equation (1) for the case where A, u and K are slowly varying functions of downstream position. Before attempting to solve (1) it is useful to examine how these properties vary in a general sense.

2.1 *Variations of river properties*

Even though all rivers are different, downstream variations of river properties tend to follow certain hydraulic equations, see Leopold (1994). To provide a framework for the assessment of the effects of downstream variations on dispersion we use a summary of data for the rivers and streams of the United States first presented by Leopold (1962) and later extended by Keup (1985). Linearly regressing the width w (m), depth d (m), and velocity u (m/s) against the discharge Q (m^3/s) in the data set yields:

$$w = 8.04Q^{0.456}, \qquad d = 0.244Q^{0.417}, \qquad u = 0.510Q^{0.127} \tag{2}$$

The purpose of (2) is not to accurately describe any particular river system, but to provide a framework for our analysis of the effects of variations in hydraulic geometry on dispersion. Jamali et al. (2004) extended Keup's data set and found the following equation for variation of Q (m^3/s) with $\hat{x}$(m), where $\hat{x}$ denote the distance from the river source.

$$Q = 8.36 \times 10^{-8}\,\hat{x}^{1.73} \tag{3}$$

Combining (2) and (3), and noting that $\hat{x} = x + L$, where x is the distance downstream of the spill, and L is the distance between the spill location and the river source, gives

$$w = w_o(1 + x/L)^{0.79}, \qquad d = d_o(1 + x/L)^{0.72}, \qquad u = u_o(1 + x/L)^{0.22} \tag{4}$$

where the subscript o refers to conditions at the spill location. The distance L can be also interpreted as a representative length-scale for variation of the properties of the river. From (4), the equation for the downstream variation in cross-sectional area is

$$A = A_o(1 + x/L)^{1.51} \tag{5}$$

Therefore, the variation of cross-sectional area with downstream distance cannot be ignored unless $x \ll L$. Note that if the river discharge at the spill location $Q_o = 10\,\text{m}^3/\text{s}$, then (3) yields $L = 46$ km, so there are likely to be many circumstances where variation of the cross-sectional area is important.

Another important factor in the analysis of downstream mixing is the longitudinal dispersion coefficient, which specifies the rate of dispersion along the river once cross-sectional mixing is complete. An approximate expression for the longitudinal dispersion coefficient is given by:

$$K = \frac{0.011u^2w^2}{du_*} \tag{6}$$

(Fischer et al., 1979), where u_* is shear velocity. Taking the shear velocity to be proportional to u, from (4) we can write:

$$K = K_0(1 + x/L)^{1.08} \tag{7}$$

The above equations will be used in the application of our solution of longitudinal dispersion in rivers with varying characteristics.

2.2 *Solution to the variable coefficient advective-diffusion equation*

Jamali et al. (2004) found the following approximate solution to the variable coefficient advective-diffusion equation (1) for an instantaneous release of a point mass M into an infinitely long river at $x = 0$ and $t = 0$, when u, K, and A all vary downstream.

$$C(x,t) = \frac{M}{A(x)} \frac{1}{\sqrt{4\pi \int_0^t K(\bar{x})dt}} \exp\left[\frac{-(x-\bar{x})^2}{4\int_0^t K(\bar{x})dt}\right] \tag{8}$$

where $\bar{x}(t)$ is the distance traveled by the center of the tracer cloud in time t and is calculated from

$$\int_0^{\bar{x}} u(x)^{-1} dx = t. \tag{9}$$

The key assumption in derivation of (8) is that in natural rivers the length-scale L is much greater than the diffusion length-scale $L_d \approx \sqrt{2Kt}$, which is generally valid (Jamali et al., 2004). When u, A and K are constant, (8) reduces to the solution for a uniform river. Note that Equation (8) is also the fundamental solution to the variable-geometry river problem when $L \gg L_d$ regardless of the form of variation of A, u, and K with x. With (8) the solution to a wide range of problems including continuous releases, or problems with different initial and boundary conditions can be constructed using the techniques discussed in Fisher et al. (1979).

3 COMPARISON WITH PREVIOUS SOLUTIONS AND FIELD DATA

Hunt (1999) considered the problem of one-dimensional dispersion in a uniform river (constant u and A) in which the longitudinal dispersion coefficient increases linearly with the downstream distance from the release location of an instantaneous point source, i.e. $K = \varepsilon ux$, where ε is a constant and $x = 0$ is the release point. A comparison of (8) and Hunt' solution for $\varepsilon = 0.01$ is given in Figure 1, which indicates a good agreement between the solutions.

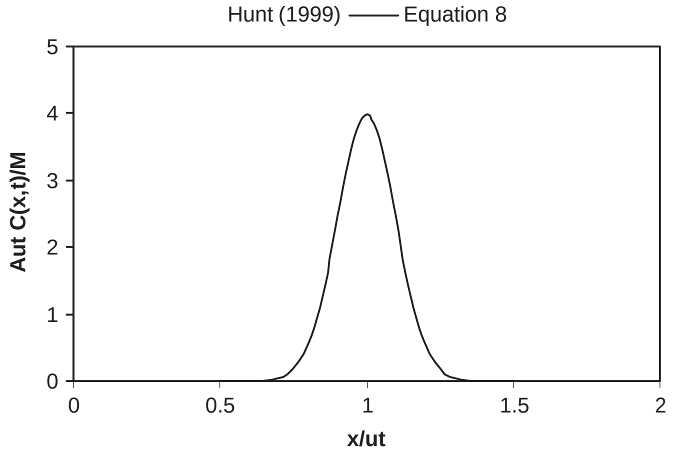

Figure 1. Comparison of our solution with that of Hunt (1999) for $\varepsilon = 0.01$. A and u are assumed constant for the purpose of comparison.

Jobson (1997) showed that the quantity:

$$C_{up} = 10^6 \frac{C_{peak}}{M} Q\Big|_{x=ut} \tag{10}$$

known as unit-peak concentration, has strong correlation with travel time t of tracer according to the field measurements for 422 cross sections obtained from more than 60 different rivers in the U.S. These data represent mixing conditions in rivers with a wide range of size, slope, and geomorphic type. All the measured rivers had varying hydraulic geometry in the downstream direction. From a regression analysis of the field data, Jobson (1996, 1997) found that:

$$C_{up} \propto t^{-\beta} \tag{11}$$

with $\beta = 0.89$. This value of β is close to the value of 0.7 reported by Nordin and Sabol (1974). Fickian dispersion in a uniform river yields $\beta = 0.5$ (Fischer et al., 1979). Using (10), we obtain $\beta = 0.91$ at large times (Jamali et al., 2004). Therefore, an explanation for the deviation of β from the Fickian value of 0.5 is that the river geometry variations facilitate attenuation of the peak concentration.

4 APPLICATION OF SOLUTION

The analytical solution provides a tool for calculating downstream concentrations in a river with varying hydraulic geometry. The solution is used here to assess the impact of an accidental release of 90 tonnes of a miscible liquid, corresponding to the approximate size of a rail car, into a small river with $w_0 = 23$ m, $d_0 = 0.64$ m, $u_0 = 0.68$ m/s, and $k_0 = 62$ m^2/s.

In Figure 2, the peak concentration curves from the uniform- and variable-river models are compared. It is seen that the uniform river model greatly overestimates the downstream concentrations. It takes more than 1200 km for the concentration to drop below 100 mg/L in the uniform river model, but less than 100 km in the variable river model. In reality a river vary considerably over a few hundreds kilometer, so the uniform river model is not appropriate for an accurate prediction of dispersion in a small river.

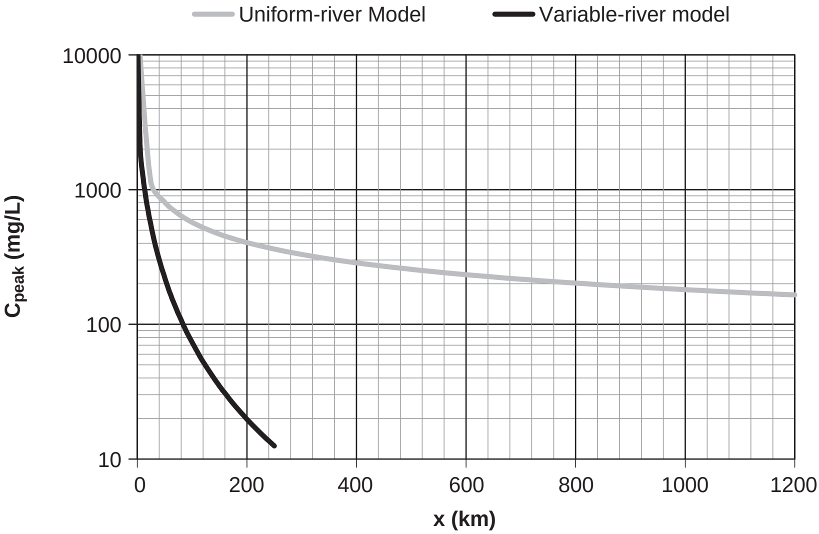

Figure 2. Comparison of the peak concentration curves obtained from the variable-coefficient and uniform-river model for the release scenario of 90 tonnes of miscible liquid into a small river ($Q_0 = 10\,\mathrm{m}^3/\mathrm{s}$).

5 SUMMARY AND CONCLUSIONS

We have presented the fundamental solution to the one-dimensional advective-diffusion equation for a river with variable velocity, cross-sectional area, and longitudinal dispersion coefficient. The results are consistent with the field data of Jobson (1996, 1997) and the theoretical results of Hunt (1999), and provide support for the contention that downstream variations in river properties are important. When the variable coefficients are allowed to vary in accordance with the results of Keup (1985), the rate of attenuation of peak concentration is much higher than predicted using the standard constant coefficient solution and is consistent with Jobson's (1996, 1997) analysis of data from 60 different rivers. The solution was used to provide an assessment of the possible behavior of an accidental instantaneous release of a miscible liquid into a typical small river. The resulting concentrations were very much less than those predicted using the standard solution.

The primary limitation to the discussed model is that the exact one-dimensional dispersion equation (1) is not always appropriate. It should not be applied immediately downstream of the discharge before cross-sectional mixing is complete. This limitation can be very important in the case of a non-buoyant discharge, although it is of less concern in the case of a highly buoyant substance, like methanol, where transverse mixing is accelerated.

REFERENCES

Day, T. J., and Wood, I. R. 1976. "Similarity of the mean motion of fluid particles dispersing in a natural channel." *Water Resour. Res.*, 12(4), 655–666.

Day, T. J. 1977a. "Longitudinal dispersion of fluid particles in mountain streams: 1.Theory and field evidence." *J. Hydro. New Zealand*, 16(1), 7–25.

Day, T. J. 1977b. "Longitudinal dispersion of fluid particles in mountain streams: 2. Similarity of the mean motion and its application." *J. Hydro. New Zealand*, 16(1), 26–52.

Fischer, H. B., List, E. J., Koh, R. Y. C., Imberger, J., and Brooks, N. H. 1979. *Mixing in inland and coastal waters*. Academic Press, San Diego, Calif.

Hunt, B. 1999. "Dispersion model for mountain streams." *J. Hydr. Engrg.*, ASCE, 125(2), 99–105.

Jamali, M., Lawrence, G., and Maloney, K. 2004. "Dispersion in varying-geometry rivers with application to methanol releases." To appear in *J. Hydr. Engrg.*, ASCE.

Jobson, H. E. 1996. "Prediction of travel time and longitudinal dispersion in rivers and streams." *Water-Resources Investigations Rep. 89-4133*, U.S. Geological Survey.

Jobson, H. E. 1997. "Predicting travel time and dispersion in rivers and streams." *J. Hydr. Engrg.*, ASCE, 123(11), 971–978.

Keup, L. E. 1985. "Flowing water resources." *Water Resour. Bull*., 21(2), 291–296.

Leopold, L. B. 1962. "Rivers." *American Scientist*, 50, 511–537.

Leopold, L. B. 1994. *A View of the River*. Harvard University Press.

Nordin, C. F. Jr., and Sabol, G. V. 1974. "Empirical data on longitudinal dispersion in rivers." *Water-Resour. Investigations*, 20–74, U. S. Geological Survey.

Rutherford, J. C. 1994. *River Mixing*. John Wiley and Sons, Ltd., England.

Environmental Hydraulics and Sustainable Water Management – Lee & Lam (eds)
© 2005 Taylor & Francis Group, London, ISBN 04 1536 546 5

Vertical turbulent mixing in tidal estuary

Yanliang Du
Hydrosoft Technology Institute, Japan

Junda Chu
Environmental Science & Engineering College, Hohai University, China

ABSTRACT: The vertical turbulent mixing of the isodensity oscillation current in tide estuary has been studied in this paper. On the basis of the governing equation and character analysis of the tidal flow, the expression of time-space distribution of shear stress, which is influenced by gravity and inertia, has been derived. Considering the terms of gravity and inertia, the theoretical equation of turbulent exchange coefficient of the tide estuary flow has been developed. Then the vertical average and the time average equations have also been obtained. To verify those equations, the time-space distribution of vertical turbulent exchange coefficient in Yangtze Estuary has been calculated according to measure data. Its variation character with the flood and ebb tide has been analyzed.

1 INTRODUCTION

Usually the turbulent exchange coefficient E_z of channel is calculated by the equation of $E_z = 0.067HU_*$ (Lane E.W. & Kalinske A.A), which only considers the influence of gravity. In tidal estuary, E_z becomes more complex when the current moves to and fro, and E_z should vary with the tide flow. It is difficult to obtain the value of bottom shear stress, which causes vertical mixing, neither on theory nor on really measure. Therefore usually the experienced equation has been applied into practical case, such as the one developed by Bowdernis used to calculated the time-averaged E_z, $\bar{E}_z = 0.0025\,\bar{u}_a H$. Evidently, the variation of E_z in the whole tide period can't be obtained by that one. Tamai Nobuyuki used electromagnetism velocity meter and hotwire velocity meter to measure the tideway of Tama River in Japan and got much data of turbulence, used the Taylor's equation, E_z has been calculated, and the equation has been obtained as $E_z = 0.0005(1 + \sin 2\omega t)$ by analysis. It can be seen easily that E_z varies periodically with time, and the period is half of the tidal. E_z equals 0 when slack tide. In that equation, E_z has no relationship with the hydrodynamic characteristic, and that sounds unreasonable. In this paper further research and analysis on the vertical turbulent exchange coefficient of the tidal estuary have been carried out on the former achievements of scholars.

2 HYDRODYNAMIC ANALYSIS OF TIDAL ESTUARY

2.1 *Basic equation*

Considering of density gradient, the basic equation of tidal flow is:

$$\frac{\partial u}{\partial t} + u\frac{\partial u}{\partial x} + v\frac{\partial u}{\partial z} + 2gD\left(1 - \frac{z}{H} + \frac{u^2}{gH}\right) - \frac{1}{\rho}\frac{\partial \tau}{\partial z} = gI \tag{1}$$

where $u =$ longitudinal velocity component; $v =$ lateral velocity component; $x =$ longitudinal direction; $t =$ time; $z =$ vertical direction; $H =$ averaged depth of flow; $g =$ gravitational acceleration; $I =$ surface slope; $\tau =$ shear stress; $D =$ density gradient, $D = H/2\rho \cdot \partial\rho/\partial x$.

2.2 *Determination of hydraulic factors*

H.B. Fisher mentioned that longitudinal velocity of tidal flow could be calculated by $u = u_a \sin \omega t$ in estuary. Yuliang Li and Zhengju Bian ect. Used $u(z,t) = [U_s + u_*/\kappa ln(1-\eta)]\sin(\omega t - \phi)$ when study on longitudinal dispersion of tide flow. In which $u(z,t)$ is logarithm profile in vertical. It was also supposed that both velocity direction of the surface flow and bottom flow change simultaneously. Miu Jin used $u = U_s \eta^m \sin(\omega t - \phi)$ for Huangpu River in China. On the research of to and fro oscillation current, Anthony Kay used equation as $u(t) = U_1 + U_2 \sin \omega t$, where $\eta =$ relatively depth; $\eta = z/H$; $m =$ velocity exponent; $\kappa =$ Karman constant; $\omega =$ angular frequency; $\varphi =$ phase difference, and subscript $a =$ average value; $s =$ values at water surface.

In this paper, considered the difference period of the tide flow and synthesizing Jin and Kay's equations, the velocity, slope and depth of tide flow are divided into two parts: the U_{1s}, I_{1s}, H_1 are of time-averaged flow and the U_{2s}, I_{2s}, H_2 are caused by tidal flow, respectively, and the u has the exponent distribution in vertical, it is expressed as:

$$u(x, z, t) = U_{1s}(x)\eta^m + U_{2s}\eta^m \sin(\omega t - \phi) \tag{2}$$

It is supposed that there is no phase difference of velocity in whole depth. The process of the surface slope and flow depth are $I = I_{1s} + I_{2s} \sin \omega t$ and $H = H_1 + H_2 \sin(\omega t - \phi_h)$.

2.3 *Hydrodynamic analysis*

Some data of the Yangtze River in Nantong section was used to analyze the quantity grade of each term in equation (1). The quantity grade of D is 10^{-7}, and the others are all 10^{-5}. Hence the density slope can be neglected, and equation (1) can be simplified as:

$$\frac{\partial u}{\partial t} + u\frac{\partial u}{\partial x} + v\frac{\partial u}{\partial z} = gI + \frac{1}{\rho}\frac{\partial \tau}{\partial z} \tag{3}$$

Used equation (2) to calculate u, each term in equation (3) may be written as

$$\frac{\partial u}{\partial t} = U_{2s} \cdot \eta^m \cdot \omega \cdot \cos(\omega t - \phi) \quad ; \quad \frac{\partial u}{\partial x} = \frac{\partial U_{1s}}{\partial x}\eta^m + \frac{\partial U_{2s}}{\partial x}\eta^m \sin(\omega t - \phi) \tag{4}$$

Used the continual equation, other terms can be obtained, then integrated it over η and input the boundary condition as $\eta = 0$, $v = 0$, the following equation can be get.

$$v = -H\frac{\partial U_{1s}}{\partial x}\frac{\eta^{1+m}}{1+m} - H\frac{\partial U_{2s}}{\partial x}\frac{\eta^{1+m}}{1+m}\sin(\omega t - \phi); \quad v\frac{\partial u}{\partial z} = -\frac{m\eta^m}{1+m}U\left[\frac{\partial U_{1s}}{\partial x} + \frac{\partial U_{1s}}{\partial x}\sin(\omega t - \phi)\right] \tag{5}$$

Equation (3) can be transformed to

$$\tau = \int_0^H \rho\left[\frac{\partial u}{\partial t} + \left(u\frac{\partial u}{\partial x} + v\frac{\partial u}{\partial x}\right) - gI\right]dz \tag{6}$$

Substituting the equations (4) and (5) into (6), integrate over η, then $\tau = \tau(I, H, g, \rho, U, \eta, \ldots) + C$. Input the boundary condition $\eta = 1$, $\tau = 0$, and obtain C, then the shear stress distribution of tide flow in equation (6) can be rewritten as:

$$\tau = \rho gHI(1-\eta) - \rho H[U_{1s} + U_{2s}\sin(\omega t - \phi)]\left[\frac{\partial U_{1s}}{\partial x} + \frac{\partial U_{2s}}{\partial x}\sin(\omega t - \phi)\right]\frac{1-\eta^{1+2m}}{(1+m)(1+2m)} - \rho HU_{2s}\omega\cos(\omega t - \phi)\frac{1-\eta^{1+m}}{1+m} \tag{7}$$

It may be seen from equation (7) that the shear stress is divided into three parts: (1) part one is caused by the gravity force; (2) the second term is caused by the spatial inertia; (3) the third one is cause by the time inertia.

3 VERTICAL TURBULENT EXCHANGE COEFFICIENT

3.1 *Theoretic equations*

On the basis of the theory of Prandtl mixing length, the turbulent exchange coefficient or momentum exchange coefficient ν_t can be written as

$$\nu_t = \frac{\tau}{\rho\, \partial u / \partial z} \tag{8}$$

From equation (4), that is

$$\frac{\partial u}{\partial z} = \frac{m}{H}\eta^{m-1}\left[U_{1s} + U_{2s}\sin(\omega t - \phi)\right] = \frac{mu}{\eta H} \tag{9}$$

Substituting equation (7) into (8), the turbulent exchange coefficient ν_t can also be written as three parts. According to the Prandtl's assume, the momentum of liquid particle hold the constant after move the distance L, so that assume is based on steady uniform flow. It is unreasonable when that assume is used into the time inertia term. For the gravity term and the spatial inertia term, it can be supposed that the flow is approximate steady uniform flow in the minute Δt. Compared with the gravity term, the time inertia term is less, and can be ignored. So ν_t can be written as two parts: $\nu_t = \nu_{t1} + \nu_{t2}$. Calculate each term of the equation respectively, both u_s and $\bar{u}$ vary with the time. According to 3.2, the phase difference between velocity and surface slope can be ignored. Since $\bar{u} = C_c\sqrt{HI}$, ν_{t1} can be rewritten as:

$$\nu_{t1} = \frac{H(t)^{3/2}\eta(1-\eta)g\sqrt{\left|I_{1s} + I_{2s}\sin\omega t\right|}}{m(1+m)\eta^m C_c} \tag{10}$$

where C_c = Chezy coefficient. Then, the second part ν_{t2} can be written as:

$$\nu_{t2} = \frac{-H(t)^2\eta\left(1-\eta^{1+2m}\right)\left[\dfrac{\partial U_{1s}}{\partial x} + \dfrac{\partial U_{2s}}{\partial x}\sin(\omega t - \phi)\right]}{m(1+m)(1+2m)\eta^m} \tag{11}$$

The sum of ν_{t1} and ν_{t2} is the theoretical vertical exchange coefficient, and the dimension is [L^2/T]. It varies with the varieties of depth and time. For the tideway, the processes of flood tide and ebb tide can be regarded as two independent half period tidal processes, then ω, U_s, I_s have different value in flood and ebb time respectively. Therefore it can be regarded as $U_{1s} = 0$, $I_{1s} = 0$ approximately, hence ν_t can be derived as:

$$\nu_t = \frac{H(t)^{3/2}g\eta(1-\eta)\sqrt{\left|\theta_1 I_{2se}\sin\omega_e t - \theta_2 I_{2sf}\sin\omega_f t\right|}}{m(1+m)\eta^m C_c} + \frac{-H(t)^2\eta\left(1-\eta^{1+2m}\right)\left[\theta_1\left(\dfrac{\partial U_{2s}}{\partial x}\right)_e\sin(\omega_e t - \phi) + \theta_2\left(\dfrac{\partial U_{2s}}{\partial x}\right)_f\sin(\omega_f t - \phi)\right]}{m(1+m)(1+2m)\eta^m} \tag{12}$$

where m and H are also different in different time. $\theta_1 = 1$ and $\theta_2 = 0$, when it is ebb tide; and $\theta_1 = 0$ and $\theta_2 = 1$, when it is flood tide.

3.2 *Calculation of vertical turbulent exchange coefficient in tideway*

The observation data in Yangtze River are used to analyze and calculate the correlated terms for the verification of equation (12).

3.2.1 *Definitions of hydraulic factors*

The observation data in this paper are from the spring and neap tides of Nantong section of Yangtze estuary in Jan. 1999.

(1) Phase difference between velocity and surface slope

The process of velocity is lag than the surface slope, and the lagged phase is φ. Compared with the whole tide period, φ is minute. According to the observations data of process of velocity and surface slope in Fig. 1, φ can be ignored.

Therefore, the surface slope can be also written as $I \approx I_{0s} \sin(\omega t - \phi)$.

(2) Velocity exponent m

Lots of research works on velocity exponent m of nature river has been done, usually $m = 1/6 \sim 1/7$. m also be influenced by the flood tide and ebb tide, and become more complex. The values of m are determined by observation data during relative stable flow of race ebb and flood tide. It may be deduced that $m = 1/6$ for ebb tidal flow, $m = 1/5$ for ebb tidal flow. The comparison of velocity calculated with observed in ebb and flood tide is shown in Fig. 2.

It can be seen from Fig. 2 that the velocity calculated and observed are in good agreement. It shows that vertical velocity distribution during flow relative stable of race ebb tidal and race flood tidal is coincident with that of channel flow.

(3) Variety of velocity amplitude with the distance

According to the spring tide data of Yangtze River in Jan. 1999, using the depth averaged 2D numerical model, the vertical averaged velocity processes of two points located at upstream and down stream respectively is obtained and showed in Fig. 3.

The distance of those calculated two points in Fig. 3 is 3119.4 m. It can be seen that the ebb tidal period of upstream is longer than that of downstream, and it is reversed in flood tide. The difference of velocity amplitude is about 0.09 m/s in ebb tide, while it is 0.05 m/s in flood tide. Let $m = 1/6$ in ebb tide and $m = 1/5$ in flood tide when those are transformed into the surface velocity, then the

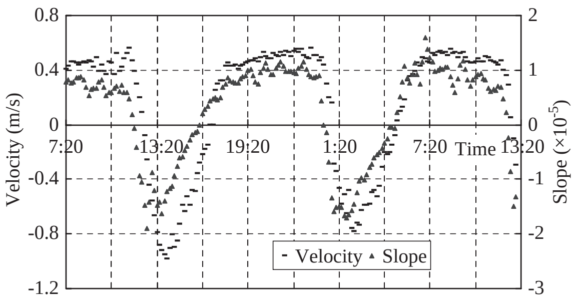

Figure 1. Process of velocity with surface slope.

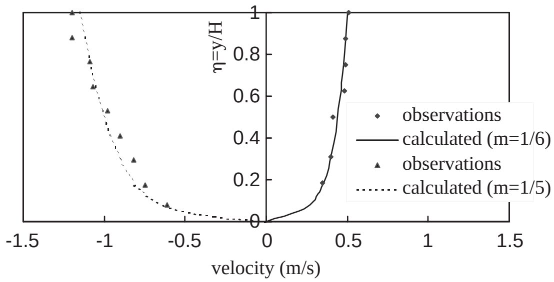

Figure 2. Comparison of velocity calculated with observed data.

following can be obtained:

$$\left(\frac{\partial U_{0s}}{\partial x}\right)_e = -3.1\times10^{-5}s^{-1}\ ;\ \left(\frac{\partial U_{0s}}{\partial x}\right)_f = 2.2\times10^{-5}s^{-1} \tag{13}$$

(4) Value of angular frequency ω

The current is influenced by river flow and the tide flow, the averaged period is about 12 hours and 25 minutes, the period of ebb tide is 8.25 hours, and that of flood tide is about 4.15 hours, so we obtain ω as

$$\omega_e = 1.06\times10^{-4}s^{-1};\quad \omega_f = 2.1\times10^{-4}s^{-1} \tag{14}$$

(5) Phase difference φ_h between level and surface slope

According to the observation, we may obtain the phase difference $\varphi_h = 1.115$ between level and surface slope, the water level amplitude $H_{2e} = 1.94$ m of ebb tide and $H_{2f} = 0.77$ m of flood tide. The process of level and surface slope in Yangtze estuary is shown in Fig. 4.

So the process of the water depth is written as $H = H_1 + H_2 \sin(\omega t + 0.355\pi)$.

3.2.2 *Vertical distribution of turbulent exchange coefficient*

Substituting equations above, we have carried out analysis and calculation on turbulent exchange coefficient ν_t as follows.

The time of slack tide, $\omega t - \varphi = k\pi$, $k = 0, \pm1, \pm2, \ldots$, and $\sin(\omega t - \varphi) = 0$, so $\nu_t = 0$.

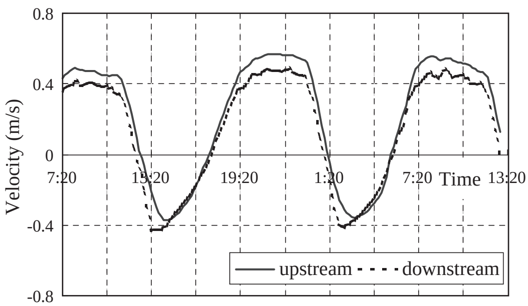

Figure 3. Velocity process of upstream and downstream in Yangtze River estuary.

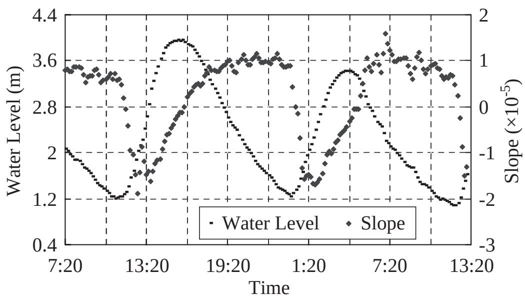

Figure 4. Process of level and surface slope in Yangtze estuary.

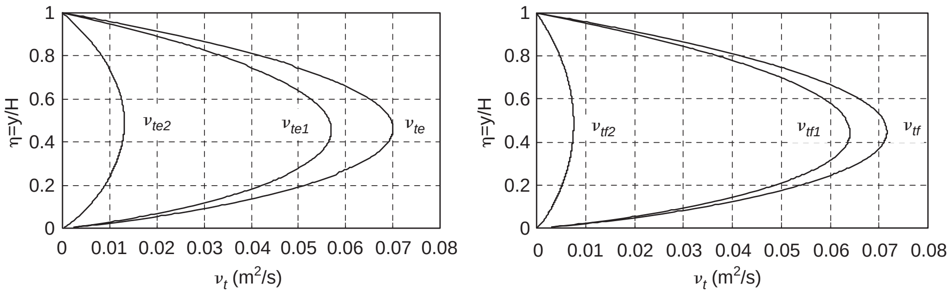

Figure 5. Vertical distribution of ν_t in race ebb tide and flood tide.

The time of race ebb tide, $\omega t - \varphi = 2k\pi + \pi/2$, $k = 0, \pm 1, \pm 2, \ldots$, and $\sin(\omega t - \varphi) = 1$, so

$$\nu_{te} = \frac{H^{3/2} g\eta(1-\eta)\sqrt{I_{2se}}}{m(1+m)\eta^m C_c} + \frac{-H^2\eta\left(1-\eta^{1+2m}\right)\left(\frac{\partial U_{0s}}{\partial x}\right)_e}{m(1+m)(1+2m)\eta^m} \tag{15}$$

The time of race flood tide, $\omega t - \phi = 2k\pi + 3\pi/2$, $k = 0, \pm 1, \pm 2, \ldots$, then $\sin(\omega t + \phi) = -1$, so

$$\nu_{tf} = \frac{H^{3/2} g\eta(1-\eta)\sqrt{I_{2sf}}}{m(1+m)\eta^m C_c} + \frac{H^2\eta\left(1-\eta^{1+2m}\right)\left(\frac{\partial U_{0s}}{\partial x}\right)_f}{m(1+m)(1+2m)\eta^m} \tag{16}$$

where the subscript e = values in ebb tide; f = values in flood tide. According to the observation of Yangtze estuary, the vertical distribution of turbulent exchange coefficient in race ebb tide and flood tide can be calculated, and be showed in Fig. 5.

3.2.3 *Variation of vertical maximum and averaged ν_t with the time*

The maximum exchange coefficient ν_{tmax} in vertical locals at $\eta = 0.45$ from Fig. 5, so it can also be calculated by (12).

Integrate equation (12) of η, the averaged coefficient in vertical can be get.

$$\nu_t(t) = \frac{H(t)^{3/2} g\sqrt{\theta_1 I_{2se}\sin\omega_e t - \theta_2 I_{2sf}\sin\omega_f t}}{m(1+m)(2-m)(3-m)C_c} + \frac{-H(t)^2\left[\theta_1\frac{\partial U_{2se}}{\partial x}\sin(\omega_e t-\phi)+\theta_2\frac{\partial U_{2sf}}{\partial x}\sin(\omega_f t-\phi)\right]}{m(1+m)(2-m)(3+m)} \tag{17}$$

Assumed $\varphi = 0$, inputted the ebb tide and flood tide value respectively, ν_t in the whole period can be obtained and be showed in Fig. 6. From Fig. 6, ν_{tmax} varies with time, and reaches the maximum in the ebb tide or flood tide.

3.3 *Analysis of the result*

A.A. Kalinske had ever observed the displacement of dyed sediment grain, its specific gravity is larger than water, and deduced the turbulent intension and turbulent diffusivity, then obtained the vertical distribution of diffusion coefficient and momentum exchange coefficient in channel flow. Those values are about 0 at both bottom and surface. The maximum turbulent diffusion in vertical is at $y = 0.4H$, while for momentum exchange coefficient, it is at $y = 0.45H$. In several decades after A.A. Kalinske, many scholars researched this problem through experiments, such as Jobson, Ueda, and get the same conclusion of uniformed flow, and only gravity term has been considered. In this

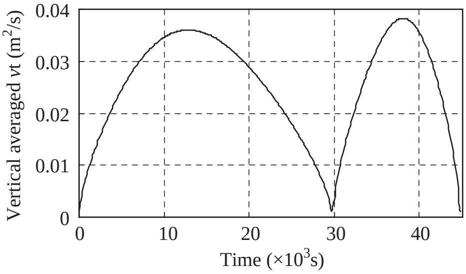

Figure 6. Variation of vertical averaged ν_t with time.

paper, the studied material is dissolvable solute and has the same specific gravity as water, and moves of solute with water particle are synchronous, so the values of turbulent diffusion coefficient are same as turbulent momentum exchange coefficient.

Some conclusion can be followed from Fig. 5 and Fig. 6. (1) The vertical turbulent exchange coefficient of estuary flow is composed with two parts: gravity term and inertial term. Usually gravity term is larger than the later. (2) The vertical distribution of the coefficient closes to parabola. The value is 0 at bottom and surface, and the maximum local at $0.45H$. That is similar to the result of A.A. Kalinske. (3) The exchange coefficient varies with tide, it is zero in slack tide, and reach maximum at race ebb tide and flood tide. The maximum of flood tide is a little bigger than that of ebb tide. (4) At the time of race ebb tide, the flow is similar to the channel flow, used Equation (17) to calculate $E_z = 0.037\, m^2/s$ of the same section, and while $E_z = 0.0389\,\mathrm{m}^2/\mathrm{s}$ calculated by $E_z = 0.067HU_*$. Those two values are approached.

4 CONCLUSIONS

In this paper, on the basis of the governing equation in estuary, the character of the tide flow has been analyzed. The expression of time-space distribution of shear stress, which is influenced by gravity and inertia, has been derived. Considering the terms of gravity and inertia, the theoretical equation of turbulent exchange coefficient of the estuary flow has been developed. To verify those equations, the time-space distribution of vertical turbulent exchange coefficient of Yangtze River's estuary has been calculated according to measure data. Its variation character following the flood and ebb tide has been analyzed.

REFERENCES

Fischer, H.B, et al. 1979. *Mixing in land and coastal waters*. Academic Press, Inc. San Dalif.

Yongliang Zhang, Peizhe Liu, 1991. *Handbook of water environmental capacity*, Tsinghus University Press 522–528 (in Chinese).

Yuliang Li, Zhengju Bian, 1995. "Longitudinal dispersion of Guangzhou Zhujiang River", *J. Water Resource Science*. 6 (1): 10–15 (in Chinese).

Miu Jin, 1965. *Sediment transportation in Huangpu River*, Master paper of Hohai University: 21.

Anthony Kay, 1997. "Advection-diffusion in reversing and oscillating flow: 2 flow with multiple reversals", *J. Applied Mathematics*. l58: 185–210.

Ning Chien, Zhaohui Wan, 1983. *Dynamics of sediment*, Science Press (in Chinese).

Environmental Hydraulics and Sustainable Water Management – Lee & Lam (eds)
© 2005 Taylor & Francis Group, London, ISBN 04 1536 546 5

Experimental scale effect of pollutant diffusion/dispersion in rivers

L. Luo, M.J. Wang & Y.L. Jiang
State Key Laboratory of Hydraulics, Sichuan University, Chengdu, Sichuan, China

ABSTRACT: Scale effect of pollutant diffusion/dispersion in laboratory experiment was investigated. Based on the flow governing equations, the diffusion/dispersion equations, and the fundamental similarity law in hydraulic experiment, the similarity laws about diffusion/dispersion between the laboratory experiment and the prototype flow were introduced. The derived formulas were validated by the published data. It shows that the diffusion/dispersion coefficient ratio of the prototype over the laboratory experiment is the 2/3 power of the scale. The pollutant release amount ratios of river over laboratory experiment are the 3rd power for the instant point source, the 5/2 power for the continuous point-source and the 3/2 power for the continuous line source, of the scale, respectively.

1 INTRODUCTION

Pollutant diffusion/dispersion in rivers is a very important issue in the environmental hydraulics field. Even the numerical simulation approach advances to a very effective way to investigate the pollutant movement phenomenon in a river, it is still necessary to deploy laboratory experiment to get the first-hand data and to validate the numerical models. Before a field monitoring implementation, the laboratory experiment can be carefully processed to propose the convenient approach for a better result. Only be understood good enough the scale effect of diffusion/dispersion, the experimental results in the laboratory can be truly used to explain the pollutant behavior in the real world. In this paper, authors addressed the similarity law for the laboratory experiment of pollutant movement in rivers from the fundamental theory of hydraulic similarity law, the flow governing Equations, and the pollutant diffusion/dispersion equations. The derived formulas are validated by published experimental and field monitoring data.

2 BASIC SIMILARITY CONDITION FROM FLOW FEATURES (XIE, 1990)

According to the pollutant diffusion manner in rivers, the fixed bed model of the river can be adopted. Considering two systems, one is laboratory physical model, and another is prototype river. From the similarity law, the scale ratios for different variables in the same mathematical equation to describe the above two systems must be the same. But for a typical physical model system, it is almost impossible to maintain all of the scale ratios be equal simultaneously. For the diffusion/dispersion problems, the most important factors are the inertial force and the turbulent shear stress.

In the continuity Equation:

$$\frac{\partial \rho}{\partial t} + \frac{\partial(\rho \overline{u_j})}{\partial x_j} = 0 \tag{1}$$

and the 3D incompressible Reynolds Averaged N-S (RANS) Equations:

$$\frac{\partial(\rho\overline{u_i})}{\partial t}+\frac{\partial(\rho\overline{u_i u_j})}{\partial x_j}=-\frac{\partial p}{\partial x_i}+\frac{\partial}{\partial x_j}\left(\mu\frac{\partial\overline{u_i}}{\partial x_j}-\rho\overline{u_i'u_j'}\right) \tag{2}$$

the inertial force and the turbulent shear stress should be similar. The undistorted model is chosen, or $\lambda_x = \lambda_y = \lambda_z = \lambda_l$, in which λ_x is the length scale in the x direction, λ_y in the y direction, λ_z in the z direction, and λ_l is the universal length scale. The experimental fluid, water, is considered as incompressible; its density will be a constant. Hence the scale ratio relationship which meets the basic geometric similarity:

continuity similarity

$$\lambda_t\lambda_u/\lambda_l = 1 \tag{3}$$

or

$$\lambda_Q/\lambda_l^2\lambda_u = 1 \tag{4}$$

the inertia force/gravity similarity

$$\lambda_u^2/\lambda_l = 1 \tag{5}$$

and the inertia/friction force similarity

$$\lambda_f = 1 \tag{6}$$

or

$$\lambda_n = \lambda_l^{1/6} \tag{7}$$

in which λ_u is the velocity scale, λ_t the time scale, λ_Q the flow rate scale, λ_f the friction force coefficient scale, and λ_n the roughness scale of the prototype over the model values. Due to the Reynolds similarity condition is difficult to meet in a model experiment, it is necessary to maintain the turbulence condition in the model, or the Reynolds number R_e must be greater than 1000–2000. Another requirement for the model is that its depth should be greater than 1.5 cm to avoid the surface tension interference.

3 SIMILARITY CONDITION FROM THE POLLUTANT DIFFUSION EQUATION

It is an efficient way to obtain the similarity condition by means of the physical equations. The similarity conditions based on different pollutant diffusion/dispersion equations are analyzed as follows:

3.1 *Turbulent diffusion*

In the environmental hydraulic engineering field, the turbulent diffusion is usually much greater than the molecular one, so only the turbulent diffusion case is analyzed here. By following the turbulent diffusion equation (Fisher, 1979)

$$\frac{\partial C}{\partial t}=\frac{\partial}{\partial x}\left(E_x\frac{\partial C}{\partial x}\right)+\frac{\partial}{\partial y}\left(E_y\frac{\partial C}{\partial y}\right)+\frac{\partial}{\partial z}\left(E_z\frac{\partial C}{\partial z}\right) \tag{8}$$

in which x, y, z are the coordinates in three directions, C is the averaged pollutant concentration, E_x, E_y, E_z are the turbulent diffusion coefficients in corresponding directions. In the prototype and the model, there are

$$\frac{\partial C_p}{\partial t_p}=\frac{\partial}{\partial x_p}\left(E_{xp}\frac{\partial}{\partial x_p}\right)+\frac{\partial}{\partial y_p}\left(E_{yp}\frac{\partial}{\partial y_p}\right)+\frac{\partial}{\partial z_p}\left(E_{zp}\frac{\partial}{\partial z_p}\right) \tag{9}$$

$$\frac{\partial C_m}{\partial t_m}=\frac{\partial}{\partial x_m}\left(E_{xm}\frac{\partial}{\partial x_m}\right)+\frac{\partial}{\partial y_m}\left(E_{ym}\frac{\partial}{\partial y_m}\right)+\frac{\partial}{\partial z_m}\left(E_{zm}\frac{\partial}{\partial z_m}\right) \tag{10}$$

in which the subscript p indicates the prototype, and the subscript m the model. Substituting the following relationship

$$\begin{cases} C_p=\lambda_C C_m \\ t_p=\lambda_t t_m \\ E_{ip}=\lambda_E E_{im} \quad (i=x,y,z) \\ x_p=\lambda_x x_m, \quad y_p=\lambda_y y_m, \quad z_p=\lambda_z z_m \end{cases} \tag{11}$$

into Equation 9, and both sides are divided by the λ_C/λ_t, one obtained

$$\frac{\partial C_m}{\partial t_m}=\frac{\lambda_t\lambda_E}{\lambda_l^2}(\frac{\partial}{\partial x_m}E_{xm}\left(\frac{\partial C}{\partial x_m}\right)+\frac{\partial}{\partial y_m}E_{ym}\left(\frac{\partial C}{\partial y_m}\right)+\frac{\partial}{\partial z_m}E_{zm}\left(\frac{\partial C}{\partial z_m}\right)) \tag{12}$$

In order to make Equation 12 match Equation 10, which describes the same model activity, the similarity index can be derived

$$\lambda_E\lambda_t/\lambda_l^2=1 \tag{13}$$

in which λ_C is the concentration scale, λ_E the turbulent diffusion coefficient scale, of the prototype over the model values. Equation 13 can be rewritten as

$$\lambda_E=\lambda_l^2/\lambda_t=\lambda_l^{3/2} \tag{14}$$

The above equation can be described as that the scale relationship of the turbulent diffusion coefficient between the prototype and the model should be decided by Equation 14 when the flow similarity condition is provided by Equations 3 and 5.

If the isotropic diffusion condition is assumed, $E_x=E_y=E_y=E$, the solution of Equation 8 under instant release point source is

$$C=\frac{m}{8(\pi Et)^{3/2}}\exp(-\frac{x^2+y^2+z^2}{4Et}) \tag{15}$$

If the same concentration values are expected at the corresponding scale points, or $\lambda_C=1$, it requires that

$$\lambda_m/(\lambda_E\lambda_t)^{3/2}=1 \quad \text{or} \quad \lambda_m=\lambda_l^3 \tag{16}$$

in which λ_m is the pollutant release amount ratio of the prototype over the model.

3.2 *Turbulent convection and diffusion*

From the turbulent convection and diffusion equation (assuming that $E_x = E_y = E_y = E$)

$$\frac{\partial C}{\partial t} + u_x \frac{\partial C}{\partial x} + u_y \frac{\partial C}{\partial y} + u_z \frac{\partial C}{\partial z} = E(\frac{\partial^2 C}{\partial x^2} + \frac{\partial^2 C}{\partial y^2} + \frac{\partial^2 C}{\partial z^2}) \tag{17}$$

The similarity index, which is similar with the derivation of Equation 13, can be written as

$$\lambda_E \lambda_t / \lambda_l^2 = 1 \tag{18}$$

The solution of Equation 17, in which the main stream flow direction, x, is assumed, and the u_y and u_z are negligible, is as follows

$$C = \frac{m}{8(\pi E t)^{3/2}} \exp[-\frac{(x-ut)^2 + y^2 + z^2}{4Et}] \tag{19}$$

Substituting with the scales into the above equation, and expecting $\lambda_C = 1$ at the corresponding scale points, Equation 16 is required to be met. Again, the release amount ratio of the prototype over the model should equal λ_l^3.

3.3 *Convection and diffusion under continuous point source*

For the continuous point source, there is no time scale. The solution under the 3D continuous point source is (Zhang, 1987)

$$C = \frac{m}{4\pi E x} \exp[-\frac{u_x (y^2 + z^2)}{4Ex}] \tag{20}$$

The 2D solution under the continuous line source is

$$C = \frac{m}{u\sqrt{4\pi E x / u}} \exp(-\frac{u_x y^2}{4Ex}) \tag{21}$$

In Equation 20, there are $\lambda_E = \lambda_l^{3/2}$ and $\lambda_m = \lambda_l^{5/2}$, when $\lambda_C = 1$ is expected at the corresponding scale points.

In Equation 21, there are $\lambda_E = \lambda_l^{3/2}$ and $\lambda_m = \lambda_l^{3/2}$, when $\lambda_C = 1$ is expected at the corresponding scale points.

3.4 *Dispersion in turbulent flows*

The dispersion in turbulent flows is the supplement diffusion effect resulted from the non-uniform velocity distribution in a cross-section. It is obvious that the friction is the main reason of non-uniform distribution of the velocities. Then Equation 6 or 7, which means the inertia/friction force similarity, must be satisfied in laboratory model experiment. The 2D turbulent dispersion equation is as follows

$$\frac{\partial C}{\partial t} + u_x \frac{\partial C}{\partial x} + u_y \frac{\partial C}{\partial y} = \frac{\partial}{\partial x}(E_L \frac{\partial C}{\partial x}) + \frac{\partial}{\partial y}(E_y \frac{\partial C}{\partial y}) \tag{22}$$

Adopting the Taylor methodology to the 2D open channel flow dispersion problem (Zhao, 1986), ignoring the longitudinal turbulent diffusion items, and letting $u_y = 0$, the similarity index can be obtained

$$\lambda_{E_L} / \lambda_l \lambda_u = 1 \tag{23}$$

The similarity index can be derived from Elder's result on Taylor's method for 2D open channel dispersion problem, too

$$E_L = -\int_A \hat{u}\hat{C}dA \Big/ A\frac{\partial \overline{C}}{\partial \xi} \quad \text{or} \quad E_L \propto u_* h \tag{24}$$

Considering the above relationship, Equation 23 is obtained, then.

For the continuous source, like Equation 20 and 21, the λ_m can be chosen from $\lambda_{E_L} = \lambda_u \lambda_l = \lambda_l^{3/2}$, so as to make $\lambda_C = 1$.

4 VALIDATION OF THE SIMILARITY LAW OF POLLUTANT DIFFUSION/DISPERSION

4.1 *Validation with experimental data of different scale models in laboratory*

The experimental data (Zhao, 1986) was collected by Okoye in a laboratory open channel experiment (see Table 1). The E_z denotes the lateral diffusion coefficient in the channel. The data in Table 1 shows that the two models maintain roughly geometrical similarity, and the velocities in two cases meet the requirement of Equation 5. From the above analysis about the similarity law, we have

$$\lambda_{E_z} = \lambda_l^{3/2} \tag{25}$$

in addition

$$(hu_*)_{\text{mod}\,el1} / (hu_*)_{\text{mod}\,el2} = h_{\text{mod}\,el1} / h_{\text{mod}\,el2} \cdot u_{*\text{mod}\,el1} / u_{*\text{mod}\,el2} \tag{26}$$

In a river or an open channel flow, $u_* = \sqrt{ghi}$, so the above equation can be written as

$$(hu_*)_{\text{mod}\,el1} / (hu_*)_{\text{mod}\,el2} = h_{\text{mod}\,el1} / h_{\text{mod}\,el2} \cdot u_{*\text{mod}\,el1} / u_{*\text{mod}\,el2} = \lambda_l^{3/2} \tag{27}$$

Then it can be drawn from Equation 25

$$\begin{aligned}(E_z / hu_*)_{\text{mod}\,el1} / (E_z / hu_*)_{\text{mod}\,el2} &= E_{z\,\text{mod}\,el1} / E_{z\,\text{mod}\,el2} \cdot (hu_*)_{\text{mod}\,el2} / (hu_*)_{\text{mod}\,el1} \\ &= \lambda_{E_z} / \lambda_l^{3/2} = 1\end{aligned} \tag{28}$$

Equation 28 claims that the dimensionless value of E_z/hu_* should be equal in the prototype (model 1) and the model (model 2). For the actual distorted models listed here, the result shown in Table 1 could be considered as meeting the claim.

Table 1. Experiment data by Okoye and the scale calculation result.

Data time	Rough-ness	River width $B\,(cm)$	Averaged depth $h\,(cm)$	Averaged velocity $u\,(cm/s)$	Friction velocity $u_*\,(cm/s)$	Lateral diffusion coefficient $E_z\,(cm^2/s)$	E_z/hu_*
1968	Smooth	85	1.5–17.3	27.1–42.8	1.6–2.2	0.64–2.9	0.09–0.20
1970	Smooth	110	1.7–22.0	30.0–50.4	1.4–2.6	0.79–3.3	0.11–0.24
Calculated scale		1.29	1.13–1.27	1.10–1.18	0.88–1.18	1.14–1.23	1.20–1.22

Table 2. Data collected by Holley Abraham on I Jssel river and its model (Zhao, 1986).

Data type	river width $B\,(m)$	Depth $h\,(m)$	Averaged velocity $u\,(m/s)$	Friction velocity $u_*\,(m/s)$	E_z/hu_*
I Jssel river	69.5	4.0	0.96	0.075	0.51
I Jssel model	1.22	0.9	0.13	0.0078	0.45–0.77
Calculated scale	56.97	4.44	7.38	9.62	0.66–1.13

4.2 *Validation with I. Jssel river model and its prototype data*

The data was collected by Holley Abraham in 1973, including the I Jssel River and its laboratory model (see Table 2). It is shown that the E_z/hu_* values in the River and the model are almost the same. According to the analysis in chapter 4.1, the data collected in the prototype and the model are satisfied with the similarity law in this paper.

5 CONCLUSIONS

In the laboratory model experiment of pollutant diffusion/dispersion in water, the similarity law between the different scales should be counted to obtain the correct data that will be applied into the prototype water body later. In this paper, the similarity law for pollutant diffusion/dispersion is derived from the hydrodynamic features and the diffusion/dispersion formulas:

1. Either turbulent diffusion or dispersion, and instant or continuous source, the following similarity law should be followed for the diffusion/dispersion coefficient between the prototype and the model:

$$\lambda_E = \lambda_u \lambda_l = \lambda_l^{3/2}$$

2. In order to make the expected concentration at the corresponding scale points between the prototype and the model equal, the release amount of pollutant, or tracer, should be counted as follows, according to the different cases:

   Instant point source

$$\lambda_m = \lambda_l^3$$

   Continuous point source

$$\lambda_m = \lambda_l^{5/2}$$

   Continuous line source

$$\lambda_m = \lambda_l^{3/2}$$

The results in this paper can provide design guidelines for laboratory experiment about diffusion/dispersion in water. Further detailed study should be conducted to get the more solid evidence of the similarity of diffusion/dispersion in a laboratory experiment. And the similarity law under the bio-degradation effect will be studied in the future.

ACKNOWLEDGEMENT

The project is supported by the Trans-Century Training Programme Foundation for the Talents by the Ministry of Education, China.

REFERENCES

Fisher, H.B. et al. 1979. *Mixing in Inland and Coastal Waters*. New York: Academic Press.
Xie, Jiaheng. 1990. *River Simulation (in Chinese)*. Beijing: Water Resource and Hydropower Press.
Zhang, Shunong. 1987. *Environmental Hydraulics (in Chinese)*. Nanjing: Hohai University Press.
Zhao, Wenqian. 1986. *Environmental Hydraulics (in Chinese)*. Chengdu: Chengdu University of Science and Technology Press.

This page intentionally left blank

Environmental Hydraulics and Sustainable Water Management – Lee & Lam (eds)

Trace experimental study on diffusion coefficients at heavy sediment-carrying reach of Yellow River

Hu Guo-Hua
School of River & Ocean Engineering, Changsha University of Science & Technology, Changsha Hunan, China

Xiao Xiang-Qun
Institute of Water Resource Protection of the Yellow River, Zhengzhou Henan, China

ABSTRACT: To determine the diffusion coefficients, a field trace experiment was made at Mengjin reach of the Yellow River. The sodium dichromate was selected as the tracer. The tracer was continuously thrown in a constant rate during the finite time along the bank. The mixing and transporting law of the tracer in mixing area is quantitatively described by using a steady-state two-dimensional Taylor's equation. The diffusion coefficients in the equation are calculated using a finite difference method. Based on the observed data, the calculated values of transverse mixing and longitudinal dispersion coefficients are $0.32\,m^2/s$ and $40\,m^2/s$, respectively. The equation $E = \alpha H u_*$ was selected as the empirical formula that can be used to deduce directly diffusion coefficients from hydraulic parameters. By using the empirical formula and the experimental data, the calculated values of dimensionless transverse mixing and longitudinal dispersion coefficients in the experimental reach is 3.61 and 451.25, respectively.

1 INTRODUCTION

The Yellow River is a famous heavy sediment-carrying river in the world. The heavy sediment-carrying reach of the Yellow River channel is much wide than deep. Pollutants travel in an inhomogeneous concentration for a long distance at this reach. The transverse mixing and longitudinal dispersion coefficients (hereafter called diffusion coefficient) are two important parameters that describe the mixing and transporting process of the pollutants in mixing region. The determination of diffusion coefficient is an important content of simulation and predication for the river water quality. Though many empirical and half-empirical formulas have been used to calculate the diffusion coefficients in natural rivers (Elder, 1959; Fischer, 1967; Yotsukura and Sayre, 1976; Zhou et al., 1986; Zhou, 1988), the determination of the empirical constants in the formulas is dependent on the hydrological and hydraulic characteristics of the given river. The empirical constants are difficult to be revise by relate theory. If the constants yielded from other rivers or laboratory were used to calculate the diffusion coefficients in the Yellow River, a significant difference between the calculated values and the real values might be caused. Therefore, the integrated method of empirical formulas with field diffusion trace experiment is still the most reliable method to gain the diffusion coefficients of pollutants in the river. In order to determine the transverse mixing and longitudinal dispersion coefficients at heavy sediment-carrying reach of the Yellow River, a field diffusion trace experiment was made at Mengjin reach of the Yellow River.

2 RATIONALE OF DISPERSION TRACE EXPERIMENT

2.1 *Diffusion and transport equation of pollutant*

When a pollutants material is discharged from bank to river in a form of continuous point source, its transport processes can be divided into vertical mixing, transverse mixing and longitudinal transport process. Based on the principle of continuity of incompressible fluid and law of conservation of mass, the three-dimensional diffusion equation under turbulent condition in rectangular coordinates system can be elicited using the method on the analogy of molecular one under the considering that turbulent diffusion effect is much bigger than molecular one.

$$\frac{\partial c}{\partial t}+u_x\frac{\partial c}{\partial x}+u_y\frac{\partial c}{\partial y}+u_z\frac{\partial c}{\partial z}=E_x\frac{\partial^2 c}{\partial x^2}+E_y\frac{\partial^2 c}{\partial y^2}+E_z\frac{\partial^2 c}{\partial z^2}-kc \tag{1}$$

where $c=$ the concentration of pollutant, mg/L; u_x, u_y and $u_z=$ longitudinal, vertical, and transverse velocities of water body in river, m/s, respectively; x, y and $z=$ longitudinal, vertical, and transverse coordinates of water body in river, m, respectively; E_x, E_y and $E_z=$ longitudinal dispersion, vertical mixing, and transverse mixing coefficients, m^2/s, respectively; $t=$ time, s; $k=$ attenuation coefficient of pollutant, s^{-1}.

For the wide and shallow river channel, transverse mixing process, in comparison with vertical mixing process, lasts more time, so the vertical mixing processes can be neglected, that is, the distribution of a pollutant in vertical direction can be considered as uniform. As transverse mixing and longitudinal transporting process go on, pollutant and river water mix homogeneously gradually, pollutant concentration in some transverse section is uniform. The reach during this section is called mixing area. If the pollutant quantity discharged into river were steady and continuous, the mean river water velocity did not vary with time, that is called steady-state condition, the dilution and dispersion rule of pollutant in mixing area can be quantitatively described using the steady-state two-dimensional Taylor's equation (Taylor, 1921):

$$u_x\frac{\partial c}{\partial x}+u_z\frac{\partial c}{\partial z}=E_x\frac{\partial^2 c}{\partial x^2}+E_z\frac{\partial^2 c}{\partial z^2}-kc \tag{2}$$

For the relatively straight river channel, the declination of river flow is small, and the transverse velocity is bound to be very small, so the second term of equation (2) may be neglected. Moreover, the tracer is usually relatively steady and scarcely decays in the reach; consequently the item kc may be neglected too. Therefore, equation (2) can be simplified as:

$$u_x\frac{\partial c}{\partial x}=E_x\frac{\partial^2 c}{\partial x^2}+E_z\frac{\partial^2 c}{\partial z^2} \tag{3}$$

The partial differential equation (3) can be quickly solved by a finite difference method.

2.2 *Identification of diffusion coefficient*

In the view of mathematics, the identification of diffusion coefficients in partial differential equation, which describes the diffusion and transportation of pollutant, falls into a inverse problem of partial differential equation, that is inversely to find coefficients of partial differential equation after the solution of partial differential equation is given. As regards identifying the uniqueness and existence of dispersion coefficients in diffusion equation, theoretic proofs have been given in mathematics.

Field trace experiment method is to inject the tracer into the river and trail the variation of its concentration, and then calculate diffusion coefficients by mathematical approaches. A group of observed concentration values of tracer in river are obtained via throwing tracer into river, simulating pollutant discharged into river from receiving outlet, and determining tracer concentration value injected into river. If the deviation between the observed concentration values of tracer (c) and the simulated concentration values (c^*) of tracer computed using diffusion equation is minimum, the diffusion coefficients in the diffusion equation are the optimal identified parameters (E_x, E_z). To identify the parameters, given:

$$f(E_x, E_z) = \sum\sum(c^* - c)^2 \tag{4}$$

Based on experience we learn that: within the ranges of $20 \le E_x \le 300$ and $0.01 \le E_z \le 1.0$, $f(E_x, E_z)$ has a minimum point, that is $\min f(E_x, E_z)$. The E_x and E_z is optimal identified values.

3 DIFFUSION TRACE EXPERIMENT METHODOLOGY

3.1 *Selection of tracer*

When selecting the tracer for diffusion trace experiment in river, following characteristics are usually required: ① dissolvable in water, and flowing with water, not divorced from the study system for sedimentation, absorption et al. and not affected by biological and chemical changes; ② low natural existent value in river and distinct differences with natural background; ③ easy to determine and possible to measure its low concentration value; ④ cheap and easy to buy, low injection quantity and simple injection method; ⑤ healthy to human being and creature in river, no harm to the use of water and no danger to the beauty of water or leave unhealthy influence.

Now, tracer in common use including: ① inorganic salt, such as NaCl, $CaCl_2$, NH_4Cl, LiCl, NaI, NaF and $NaCr_2O_7$; ② dyes, for instance luciferin, rhodanmine B, eosline, malachite green, methylene blue; ③ radioactive isotope, such as Br82, Na24, I131, T; ④ pollutant of outlet, that is selecting pollutant discharged from the outlet of traced river as tracer.

For the heavy sediment-carrying reach of the Yellow River, if radioactive isotope is chosen as tracer, special analytical equipments will be required, moreover, the use of radioactive isotope tracer will be strictly controlled, ordinary dyes are easily to be absorbed by sediment in water, for example, sediment has a strong absorption to rhodanmine B (Shao and Zhang, 1994), so inorganic salt was selected as tracer in this study. As the background concentration of sodium dichromate in Yellow River is nearly zero, and its analysis and measurement method are mature, moreover it is easily bought and has a low price, sodium dichromate was selected as the tracer in this experiment. Besides, indoor absorption test shows (Table 1): $NaCr_2O_7$ is hardly absorbed by the suspended sediment in Yellow River.

3.2 *Summary of trace experiment*

The reach for tracer experiment is in the Mengjin reach of the Yellow River. Being restrained by a control and training project, the river channel of the reach is relatively straight, the surface water is wide, and main current is steady. It belongs to typical wide-shallow and heavy sediment-carrying channel.

Table 1. Absorption test of $Cr_2O_7^{2-}$ in the Yellow River water.

Sediment concentration (g/L)	Amount of added $Cr_2O_7^{2-}$ (μg)	Amount of recovery $Cr_2O_7^{2-}$ from clean water (μg)	Amount of $Cr_2O_7^{2-}$ adsorbed on suspended sediment (μg)
5	100.0	100.0	0.0
5	50.0	49.9	0.1
5	25.0	25.0	0.0
10	100.0	100.0	0.0
10	50.0	49.9	0.1
10	25.0	24.9	0.1

Table 2. Distances of sampling sections from injection point.

Section I	Section II	Section III	Section IV	Section V	Section VI
−20 m	300 m	600 m	1000 m	1500 m	2000 m

Table 3. Measured values of water depth and flow velocity at each sampling point.

Section	Hydrological parameter	Sampling point 1	2	3	4	5	6	7	8	9	10	11	12
III	Water depth, m	1.50	1.36	1.28	1.30	1.32	1.30						
	Velocity, m/s	1.31	1.30	1.28	1.20	1.17	1.18						
IV	Water depth, m	1.42	1.43	1.38	1.36	1.28	1.29	1.34	1.30				
	Velocity, m/s	1.38	1.47	1.35	1.24	1.13	1.15	1.20	1.23				
V	Water depth, m	1.40	1.55	1.43	1.28	1.32	1.28	1.30	1.34	1.34			
	Velocity, m/s	1.30	1.42	1.31	1.22	1.10	1.14	1.17	1.20	1.30	1.27		
VI	Water depth, m	1.44	1.50	1.38	1.35	1.35	1.37	1.35	1.33	1.26	1.28	1.26	1.30
	Velocity, m/s	1.28	1.36	1.27	1.24	1.14	1.15	1.18	1.25	1.26	1.25	1.30	1.29

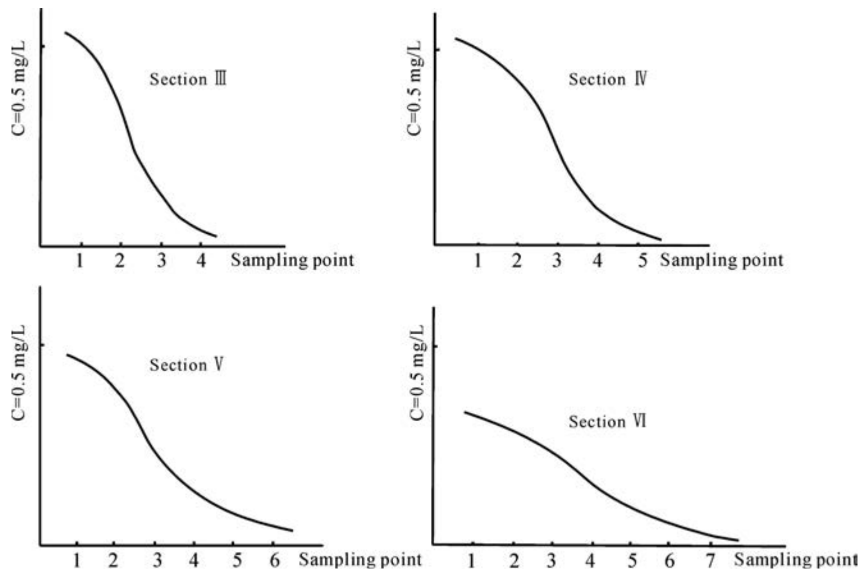

Figure 1. The distribution of measured tracer concentration at each section.

The tracer injection point was 7 m from the left bank. In the reach, 5 tracer-sampling sections and one control section were selected (Table 2). According to the dispersion capacity estimated from float method, 4–12 sampling points which interval is 10 m were selected on each section.

At the injection point, the given concentration sodium dichromate was continuously injected at a constant rate until the sampling was finished. When the tracer concentrations at each section were steady, samples were simultaneously collected at each section every 20 minutes. Four batches of samples were collected altogether and the flow velocity and water depth at each sampling point were measured at the same period (Table 3). Within the valid time of the preservation, the water samples were sent to the laboratory for determination. The distribution of measured tracer concentration at each section is showed in Figure 1.

4 DETERMINATION AND VERIFICATION OF DIFFUSION COEFFICIENT

4.1 *Determination of diffusion coefficient*

The reach for the tracer experiment, which is 300×2000 m, were divided into 30×100 subareas with the two groups of parallels (whose unit distances are $h_x = 20$ m, $h_z = 10$ m, respectively). At each grid point, a difference equation can be formed which has an unknown number $c_{i,j}$, so there is a equation set which consists of 30×100 equations. Using the initial and boundary conditions, the equation set can be solved using a line over-relaxation method.

In a given interval for finding the optimal diffusion coefficients, a “computer scanning and calculation – gradient search method” may be used to determine the parameters (diffusion coefficients) of the steady-state two dimensional Taylor’s model. The computer scans the given interval and calculates all the target values ($c_{i,j}$), which is corresponding to the given diffusion coefficients, according to a given step and an order. Comparing the calculated value and the measured value of a tracer, the minimum target and its corresponding diffusion coefficients in the given interval may be found by the computer. The range of one step around the diffusion coefficients corresponding to the minimum target value is regarded as a new given interval for finding the optimal diffusion coefficients. Correspondingly, the step is reduced. The computer scans the new given interval in the reduced step and calculates. Repeat like that until the minimum target value and the corresponding diffusion coefficients trend to steady and reach an established precision and yield a global approximate optimal solution.

According to the longitudinal and transverse diffusion coefficients at the Tuoketuo and Hejin reach of the Yellow River (Shao and Zhang, 1994), we suppose the interval for finding the optimal longitudinal diffusion coefficient is $20 \leq E_x \leq 300$, the interval for finding the optimal transverse mixing coefficient is $0.01 \leq E_z \leq 1.00$. To avoid a sudden error in the calculation process, the search step at the first time must be in the range of an allowable error of diffusion coefficient variables. To ensure the calculation precision, the global optimal solution is regarded as initial diffusion coefficients. An optimal search of the gradient method is made again to the global optimal solution. Calculating by a computer, the yielded optimal solution is $E_x = 40\,\mathrm{m^2/s}$, $E_z = 0.32\,\mathrm{m^2/s}$, respectively.

4.2 *Verification of diffusion coefficient*

To verify the two diffusion coefficients, substituting the coefficients into equation (3), using the initial and boundary conditions to simulate the tracer experiment transport and to yield the calculated value of the tracer concentration at each sampling point, comparing the calculated value with the measured value of tracer concentration from another batch of the tracer experiment, the results are listed in Table 4.

From table 4, the relative error is less than 27.2%, the precision is relatively high, which shows the diffusion coefficients yielded from this tracer experiment are reliable, and can be used to modify the empirical constants of the empirical equation for calculating diffusion coefficients, thereby to determine the diffusion coefficients of a traced river channel under different hydrological conditions and to quantitatively describe the diffusion transport of a pollutant.

5 MODIFICATION OF DIMENSIONLESS DIFFUSION COEFFICIENT

Although the diffusion coefficients gained from field trace experiment were relatively reliable, they can only stand for the diffusion capacity of the reach under the hydrological and hydraulic

Table 4. Comparison of calculated value and measured value of tracer diffusion transport.

Sampling point		1	2	3	4	5	6
Section I	Calculated value, mg/L	0.57	0.31	0.12			
	Measured value, mg/L	0.52	0.36	0.13			
	Relative error, %	9.6	−13.9	−7.7			
Section II	Calculated value, mg/L	0.51	0.35	0.20	0.10		
	Measured value, mg/L	0.50	0.47	0.25	0.10		
	Relative error, %	2.0	−25.5	−20.0	0		
Section III	Calculated value, mg/L	0.44	0.34	0.24	0.14	0.08	
	Measured value, mg/L	0.48	0.40	0.22	0.11	0.07	
	Relative error, %	8.3	−15.0	9.1	27.2	14.3	
Section IV	Calculated value, mg/L	0.39	0.32	0.24	0.17	0.11	0.06
	Measured value, mg/L	0.33	0.28	0.20	0.16	0.10	0.05
	Relative error, %	18.2	14.3	20.0	6.3	10.0	20.0

condition when the trace experiment was carrying out. In actual application, the diffusion situation of a reach in different hydrological and hydraulic conditions still must be learned. Therefore, the empirical formula in which the diffusion coefficients can be deduced from hydrological and hydraulic parameters usually should be formed.

According to Taylor's theory, the diffusion coefficient of pollutant in river is product of Lagrange linear measure and turbulence intensity. Based on this conception, the general expression formula of diffusion coefficient can be given:

$$E = \alpha H u_* \tag{5}$$

$$u_* = \sqrt{gHI} \tag{6}$$

where $E =$ diffusion coefficient, m^2/s; $\alpha =$ dimensionless diffusion coefficient; $H =$ water depth, m; $u_* =$ friction velocity, m/s; $g =$ acceleration of gravity, m/s^2; $I =$ hydraulic gradient.

Formula (5) is a universal one, which can be applied to vertical, transverse and longitudinal dispersions. The only difference among them is the value of dimensionless diffusion coefficient assumed. From formula (5) we know that: water depth, friction velocity and dimensionless diffusion coefficient will influence diffusion coefficients. For a certain reach, both of water depth and friction velocity can be obtained from observing or riverbed data. Thus the problem of evaluating diffusion coefficient is converted to estimate the value of α.

If we define transverse coordinate as Z and longitudinal coordinate as X, the corresponding transverse mixing coefficient E_z and longitudinal dispersion coefficient Z_x can be denoted as:

$$E_z = \alpha_z H u_* \tag{7}$$

$$E_x = \alpha_x H u_* \tag{8}$$

where $\alpha_z, \alpha_x =$ dimensionless transverse mixing coefficient and longitudinal dispersion coefficient, respectively, which are usually a constant.

As to the calculation of α_z and α_x, a lot of experiment have been studied. Based on analysis and calculation of results observed from diffusion trace experiments, the values of α_z and α_x in the experimental river are yielded in this paper, which are 3.61 and 451.25, respectively. Analysis shows that the dimensionless diffusion coefficients determined are matched with the fact of trace experiment reach. From formula (7) and (8), the longitudinal dispersion coefficients and transverse mixing coefficients of the reach under different hydrological and hydraulic conditions can be calculated.

6 CONCLUSIONS

It is important to select the tracer in the diffusion experiment for the heavy sediment-carrying reach of Yellow River. We selected sodium dichromate as the tracer for the trace experiment at Mengjin reach of the Yellow River.

The mixing and transporting law of the tracer in mixing region of the river, which surface water is relative wide and water depth is relative shallow, can be described by a steady-state two-dimensional Taylor's diffusion equation. The diffusion coefficients in the equation can be calculated using the finite difference and optimization method.

The integrated method of empirical formulas with the field diffusion trace experiment is the most reliable method to determine the empirical formula used to deduce directly diffusion coefficients from hydraulic parameters and the dimensionless diffusion coefficients of the empirical formula.

REFERENCES

Elder, J.W. 1959. The dispersion of marked fluid in turbulent shear flow. *Journal of fluid mechanics* 5(4): 544–560.

Fischer, H.B. 1967. The mechanics of dispersion in natural streams. *J. Hydraul. Div, ASCE*, 93(HY6): 187–216.

Shao, Q.S. & Zhang, H.J. 1994. The study on dispersion of pollutants in muddy River. *Advances in environmental science* 2(3): 65–70.

Taylor, G.I. 1921. Diffusion by continuous movements. In: Proceedings London Mathematical Society, Series 2, 20: 196–212.

Yotsukura, N. & Sayre, W.W. 1976. Transverse mixing in natural channels. *Water resources research* 12(4): 695–704.

Zhou, K.Z., Yu, C.Z. & Zhang, Y.L. 1986. Study on the method calculating longitudinal dispersion coefficient of trace experiment in natural rivers. *Journal of environmental science* 6(3): 314–326.

Zhou, Y. 1988. Study on transverse mixing coefficient of natural rivers. *Journal of hydraulic engineering* (6): 56–60.

This page intentionally left blank

Environmental Hydraulics and Sustainable Water Management – Lee & Lam (eds)
© 2005 Taylor & Francis Group, London, ISBN 04 1536 546 5

Advection and dispersion of substance discharged by intermittent point source in rivers

Wu Zhouhu & Qiao Haitao
Qingdao Polytechnic University

ABSTRACT: Suppose that an intermittent point source discharge cycle T, a discharge duration time $t_0(t_0 < T)$, and the discharge strength in the discharge duration W are kept constant. According to the one-dimensional advection and dispersion equation, the spatially varied concentration of contaminants is obtained which discharged by the intermittent point source at the downstream dispersal period. Reasonableness of the solution is deserved. The consistency of the analytical solution and the simplified equation at given condition are discussed.

1 INTRODUCTION

As a stream of effluent is discharged into a river, what happens can be divided into three stages: the initial dilution, the mixture across the cross section and the longitudinal dispersion after the cross-sectional mixing. If the effluent discharge is not instantaneous, and not at a constant rate, but a continuous discharge during one period and a non-discharge during the next period, and so on, this pollution source is termed an intermittent discharge source. In most practical cases, the intermittent discharge point source can be seen frequently. The plants periodically produce polluted water. If the polluted water discharges directly, water quality downstream will vibrate cyclically. In this case, the instantaneous discharge concentration of the contaminants far exceeds the average concentration of the same amount at the constant discharge rate. In order to heighten the level of analyzing the monitoring datum of the water quality and the level of water management, we must analogy the advection and dispersion of contaminants discharged by the intermittent point source precisely. In this paper, suppose that an intermittent point source discharge cycle T, a discharge duration time $t_0(t_0 < T)$, and discharge strength in the discharge duration W are kept constant. According to the one-dimensional advection and dispersion equation, the spatially varied concentration distribution law of contaminants is obtained which discharged by the intermittent point source at the downstream dispersal period.

2 BASIC EQUATION AND ITS CONDITIONS OF DEFINITE SOLUTION

Suppose that a point discharge source at the origin of x-coordinate system in a one-dimensional flow, let the downstream be the positive direction at initial time $t = 0$ the concentration is zero everywhere along the axis. During the period $nT < t \le nT + t_0(n = 0, 1, 2, 3, \ldots\ldots)$, the effluent discharge concentration at the rate C_0 at the point $x = 0$ and is held at that value. During the period $nT + t_0 < t \le (n + 1)T$, the concentration is zero at the point $x = 0$. Then the one-dimensional advection and dispersion equation will be:

$$\frac{\partial C}{\partial t} + U\frac{\partial C}{\partial x} = D\frac{\partial^2 C}{\partial x^2} - KC \tag{1}$$

in which, U is the flow velocity in the x direction, the D is the longitudinal dispersion, and K is the mass degradation coefficient.

The conditions for solution are: $C|_{t=0,all\,x}=0$, $C|_{nT<t\leq nT+t_0,x=0}=C_0$, $C|_{nT+t_0<t\leq(n+1)T,x=0}=0$, $C|_{t>0,x=L}=0$, L is large.

3 ANALYTIC SOLUTION

For variable replacement, let $C(t,x)=\mathrm{e}^{\frac{Ux}{2D}}Q(t,x)$, eq. (1) becomes:

$$\frac{\partial Q}{\partial t}=D\frac{\partial^2 Q}{\partial x^2}-\left(K+\frac{U^2}{4D}\right)Q=D\frac{\partial^2 Q}{\partial x^2}-K'Q \tag{2}$$

in which $K'=K+(U^2/4D)$. Corresponding conditions of solution become: $Q_{|t=0,}=0$, $Q|_{nT<t\leq nT+t_0,x=0}=C_0$, $Q|_{nT+t_0<t\leq(n+1)T,x=0}=0$, $Q|_{t>0,x=L}=0$. Taking second variable transformation, let $Q(t,x)=\mathrm{e}^{-K't}V(t,x)$, eq. (2) becomes:

$$\frac{\partial V}{\partial t}=D\frac{\partial^2 V}{\partial x^2} \tag{3}$$

Corresponding conditions of solution become: $V|_{t=0,all\,x}=0$, $V|_{nT<t\leq nT+t_0,x=0}=C_0\mathrm{e}^{K't}$, $V|_{nT+t_0<t\leq(n+1)T,x=0}=0$, $V|_{t>0,x=L}=0$.

For eq. (3), taking Laplace transform about t ($t=nT$ and $nT+t_0$ are first kind discontinuous point, meet the condition of Laplace).

$U(p,x)=\int_0^\infty V(t,x)\mathrm{e}^{-\mathrm{pt}}\mathrm{d}t$, eq.(3) becomes:

$$\frac{\mathrm{d}^2U(p,x)}{\mathrm{d}x^2}-\frac{1}{D}[pU(p,x)-V(0^+,x)]=0$$

Substituting $V|_{t=0,all\,x}=0$ into above equation, we have:

$$\frac{\mathrm{d}^2U(p,x)}{\mathrm{d}x^2}-\frac{p}{D}U(p,x)=0 \tag{4}$$

Corresponding conditions of solution become: when $nT<t\leq nT+t_0$, $U(p,0)=L[C_0\mathrm{e}^{K''}]=C_0/p-K'$; when $nT+t_0<t\leq(n+1)T$, $U(p,0)=0$; $U(p,L)=0$.

The general solution of eq. (4) is:

$$U(p,x)=C_1\mathrm{e}^{-\sqrt{\frac{p}{D}}x}+C_2\mathrm{e}^{\sqrt{\frac{p}{D}}x} \tag{5}$$

According to the conditions of solution, when L is big enough and $U(p,L)=0$ it can be obtained $C_2=0$.Therefore when $nT<t\leq nT+t_0$, $C_1=C_0/p-K'$; when $nT+t_0<t\leq(n+1)T$ $C_1=0$,

we have:

$$\begin{cases} U(p,x) = \dfrac{C_0}{p-K'} e^{-\sqrt{\frac{p}{D}}x} & (nT < t \le nT + t_0) \\ U(p,x) = 0 & (nT + t_0 < t \le (n+1)T) \end{cases} \tag{6}$$

For eq. (6), taking Laplace transform, it can be obtained:

$$V(t,x) = L^{-1}\left[\frac{C_0}{p-K'} e^{-\sqrt{\frac{p}{D}}x}\right] = C_0 L^{-1}\left[\frac{1}{p-K'} e^{-\sqrt{\frac{p}{D}}x}\right] = C_0 g_1(t) * g_2(t) \tag{7}$$

In which $g_1(t) * g_2(t)$ is called convolution of $g_1(t)$ and $g_2(t)$.

$$g_1(t) = L^{-1}\left[\frac{1}{p-K'}\right] = e^{K't}, g_2(t) = L^{-1}\left[e^{-\sqrt{\frac{p}{D}}x}\right] = \frac{x}{2\sqrt{\pi D t}^{3/2}} e^{-\frac{x^2}{4Dt}}$$

Substituting $g_1(t) * g_2(t)$ into eq. (7) and using the convolution there in, When $nT < t \le nT + t_0$:

$$V(t,x) = \frac{2C_0}{\sqrt{\pi}}\left[\sum_{j=0}^{n-1} \int_{jT}^{jT+t_0} e^{K'\tau} e^{-\left(\frac{x}{2\sqrt{D(t-\tau)}}\right)^2} d\left(\frac{x}{2\sqrt{D(t-\tau)}}\right) + \int_{nT}^{t} e^{K'\tau} e^{-\left(\frac{x}{2\sqrt{D(t-\tau)}}\right)^2} d\left(\frac{x}{2\sqrt{D(t-\tau)}}\right)\right] \tag{8}$$

when $nT + t_0 < t \le (n+1)T$:

$$V(t,x) = \frac{2C_0}{\sqrt{\pi}} \sum_{j=0}^{n} \int_{jT}^{jT+t_0} e^{K'\tau} e^{-\left(\frac{x}{2\sqrt{D(t-\tau)}}\right)^2} d\left(\frac{x}{2\sqrt{D(t-\tau)}}\right) \tag{9}$$

let $v = x/(2\sqrt{D(t-\tau)})$, we have $\tau = t - x^2/4Dv^2$, τ and v's corresponding relationship is illustrated in Table 1, then the second integration becomes:

$$\int_{nT}^{t} e^{K'\tau} e^{-\left(\frac{x}{2\sqrt{D(t-\tau)}}\right)^2} d\left(\frac{x}{2\sqrt{D(t-\tau)}}\right) = e^{K't} \int_{\frac{x}{2\sqrt{D(t-nT)}}}^{\infty} e^{-\left(\frac{K'x^2}{4Dv^2}+v^2\right)} dv$$

$$= \frac{\sqrt{\pi}}{4} e^{K't}\left[e^{-\sqrt{\frac{K'}{D}}x} \operatorname{erfc}\left(\frac{x}{2\sqrt{D(t-nT)}} - \sqrt{K'(t-nT)}\right) + e^{\sqrt{\frac{K'}{D}}x} \operatorname{erfc}\left(\frac{x}{2\sqrt{D(t-nT)}} + \sqrt{K'(t-nT)}\right)\right] \tag{10}$$

$$= \frac{\sqrt{\pi}}{4} e^{K't} e^{-\frac{Ux}{2D}} f(t-nT, x)$$

in which, $f(t,x) = e^{Ux/2D}[e^{-(\sqrt{K'/D})x} \operatorname{erfc}(x/(2\sqrt{Dt}) - \sqrt{K't}) + e(\sqrt{K'/D})x \operatorname{erfc}(x/(2\sqrt{Dt}) + \sqrt{K't})]$. It's last item is neglected except that the value of x is low.

Table 1. The corresponding relationship of τ and v.

τ	$jT+t_0$	jT	t	nT
v	$\frac{x}{2\sqrt{D(t-jT-t_0)}}$	$\frac{x}{2\sqrt{D(t-jT)}}$	∞	$\frac{x}{2\sqrt{D(t-nT)}}$

In the same reason, for eq. (8), taking integral transform and simplifying, we have:

$$V(t,x) = \frac{C_0}{2} e^{K't} e^{-\frac{Ux}{2D}} [\sum_{j=0}^{n} f(t-jT,x) - \sum_{j=0}^{n-1} f(t-jT-t_0,x)] \qquad (nT < t \leq nT + t_0) \quad (11)$$

Eq. (9) becomes:

$$V(t,x) = \frac{C_0}{2} e^{K't} e^{-\frac{Ux}{2D}} \sum_{j=0}^{n} [f(t-jT,x) - f(t-jT-t_0,x)] \qquad (nT + t_0 < t \leq (n+1)T) \quad (12)$$

so:

$$C(t,x) = e^{\frac{Ux}{2D}} Q = e^{\frac{Ux}{2D}} e^{-K't} V(t,x) = \frac{C_0}{2} [\sum_{j=0}^{n} f(t-jT,x) - \sum_{j=0}^{n-1} f(t-jT-t_0,x)] (nT < t \leq nT + t_0) \quad (13)$$

$$C(t,x) = \frac{C_0}{2} \sum_{j=0}^{n} [f(t-jT,x) - f(t-jT-t_0,x)] \qquad (nT + t_0 < t \leq (n+1)T) \quad (14)$$

Equation (13) and eq. (14) are the analytic solution for one dimensional advection and dispersion model of intermittent discharge point source.

4 DISCUSSION

To illustrate the method, suppose that the velocity of river flow $U = 1.0$ m/s, dispersion coefficient $D = 30\,\text{m}^2/\text{s}$, discharge cycle of intermittent point source $T = 2$ h, discharge duration time $t_0 = 1$ h are taken. The solution of concentration distribution according to eq. (13) and eq. (14) is depicted graphically in Fig. 1 and Fig. 2. In Fig. 1 and Fig. 2, the full line represents the conservative substance when the degradation coefficient $K = 0$. The broken line represents the non-conversation substance when $K = 0.26\,\text{d}^{-1}$. It can be seen from the Fig. 1, the concentration is zero at the origin of the one-dimensional system at the middle of discharge duration of the intermittent point source $t = nT + t_0/2$. Because of the advection the contaminants discharged previously diffuses to downstream gradually according to discharge cycle ($X = UT$), which becomes the cyclical concentration vibration law along the flow. Because of dispersion the peak spreads out in a decaying distribution. The concentration of the flow zone at the discharge duration decreases along the flow. The concentration of the flow zone at the non-discharge duration increases along the flow. The difference between the maximum concentration and the minimum concentration decreases gradually. When x is quiet big the maximum and the minimum concentration tend to accord with the concentration distribution of the one-dimensional advection and dispersion model of the constant continuous point source in the direction of flow. That is, when $K = 0$, the maximum and the minimum concentration will both take the horizontal line $C/C_0 = t_0/T$ as asymptotic line .When $K \neq 0$ the maximum and the minimum concentration will take the decline curve $C/C_0 = t_0/T \exp[Ux/2D(1 - \sqrt{1 + 4DK/U^2})]$ as the asymptotic line. Certainly, if the discharge cycle of an intermittent point source T is quiet long, and the non-discharge duration $(T - t_0)$ is also long, the cyclical vibration law of the concentration

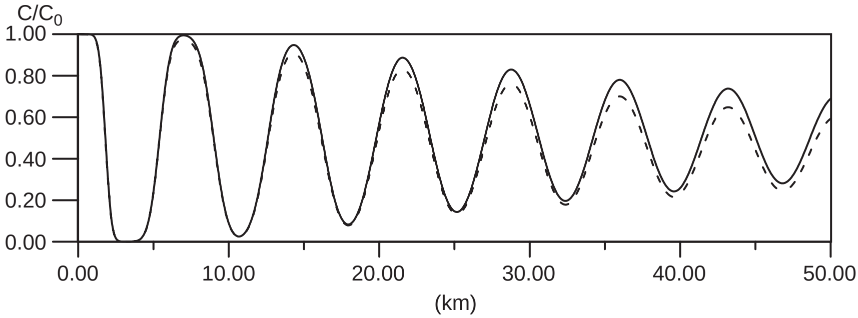

Figure 1. The concentration distribution of the intermittent discharge point source at $t = nT + t_0/2$ ($T = 2$ h, $t_0 = 1$ h, $n \geq 7$).

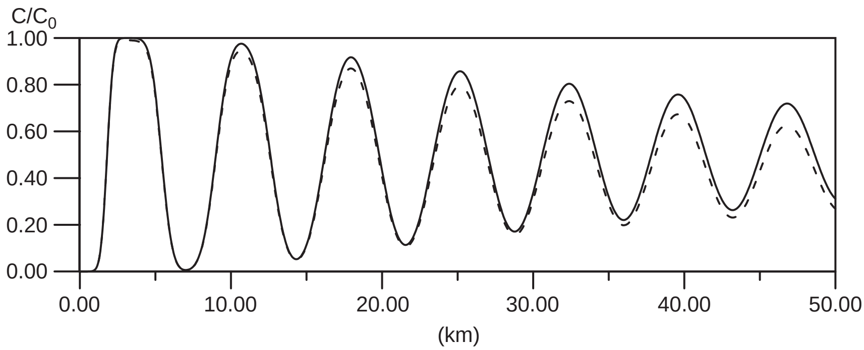

Figure 2. The concentration distribution of the intermittent discharge point source at $t = nT + (T + t_0)/2$ ($T = 2$ h, $t_0 = 1$ h, $n \geq 7$).

distribution along the flow will remain very long distance or overall length. It can be seen from Fig. 2, at the middle of non-discharge duration of the intermittent point source $t = nT + (T + t_0)/2$, the concentration of point source is zero. The cyclically vibrated concentration distribution curve disperses to downstream with half cycle in the direction of flow compared to Fig. 1. The concentration distribution law along the flow is the same with the analysis of Fig. 1.

Suppose that the discharge period of intermittent point source $T = 3$ h. discharge duration $t_0 = 1$ h. In the middle of the discharge duration $t = nT + t_0/2$ the concentration distribution along the flow is shown in Fig. 3. Suppose that the discharge period of intermittent point source $T = 3$ h, discharge duration $t_0 = 2$ h. In the middle of the discharge duration $t = nT + t_0/2$, the concentration distribution along the flow is shown in Fig. 4. It can be seen from Fig. 3 and Fig. 4, that there is a concentration distribution law along the flow which is the same with the law of the Fig. 1, memrly it has a longer cycle. In Fig. 3, the non-discharge duration is longer than the discharge duration. The low concentration zone is longer. In Fig. 4, the non-discharge duration is shorter than the discharge duration. High concentration zone is longer. When x is comparatively large, the maximum and the minimum concentrations in Fig. 3 and Fig. 4 both take:

$C/C_0 = t_0/T \exp\left[Ux/2D(1 - \sqrt{1 + 4DK/U^2})\right]$ as the asymptotic line accordingly.

When $x = 0$, the concentration C_0 is derived from the assumption, the contaminants consumption in the whole river reach is equal to the discharge strength W. That is:

$$W\frac{t_0}{T} = A\int_{-\infty}^{\infty} KC\mathrm{d}x = AK\int_{-\infty}^{\infty} C\mathrm{d}x \tag{15}$$

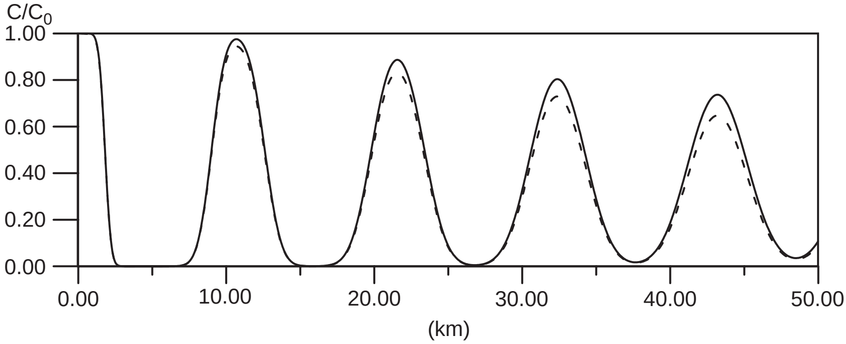

Figure 3. The concentration distribution of the intermittent discharge point source at $t = nT + t_0/2 (T = 3\,\text{h}, t_0 = 1\,\text{h}, n \geq 5)$.

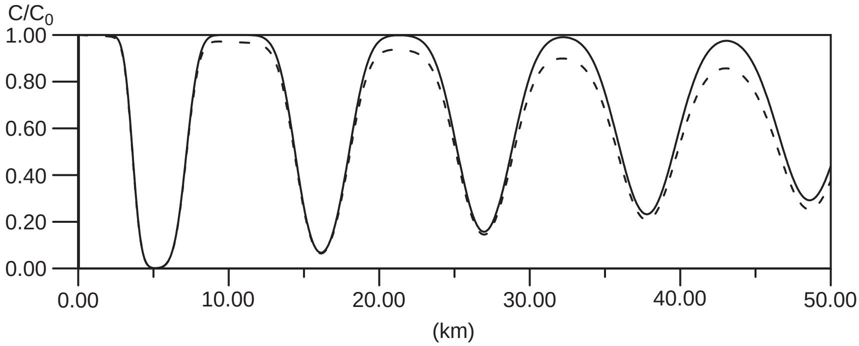

Figure 4. The concentration distribution of the intermittent discharge point source at $t = nT + t_0/2 (T = 3\,\text{h}, t_0 = 2\,\text{h}, n \geq 5)$.

in which, when $x \geq 0$ substituting $C = C_0(t_0/T) \exp [Ux/2D(1 - \sqrt{1 + 4DK/U^2})]$ into eq. (15) and taking integral transform. When the contaminants disperse toward upstream its influence span is very short. In this paper we don't analyze it in detail. But it has an influence on the computing result of C_0. Therefore when $x < 0$ substituting $C = C_0(t_0/T) \exp [Ux/2D(1 + \sqrt{1 + 4DK/U^2})]$ into eq. (15) and taking integral transform. This is the same with the integral result of substituting periodical concentration distribution along the flow. That is:

$$W\frac{t_0}{T} = AKC_0\frac{t_0}{T}\{\int_{-\infty}^{0} \exp[\frac{Ux}{2D}(1+\sqrt{1+\frac{4DK}{U^2}})]dx + \int_{0}^{\infty} \exp[\frac{Ux}{2D}(1-\sqrt{1+\frac{4DK}{U^2}})]dx\} = AUC_0\frac{t_0}{T}\sqrt{1+\frac{4DK}{U^2}}$$

Therefore, $C_0 = \frac{W}{Q}/\sqrt{1 + 4DK/U^2}]$, in which $Q = AU$ is the river flow quantity, A is the cross section area.

There is a discussion between the simplified equation at corresponding conditions of eq. (13) and eq. (14) and comparably analytic solution, as follows:

(1) when $t_0 = T$, the eq. (13) and eq. (14) become:

$$C(t,x) = \frac{C_0}{2} e^{\frac{Ux}{2D}} [e^{-\sqrt{\frac{K'}{D}}x} \operatorname{erfc}(\frac{x}{2\sqrt{Dt}} - \sqrt{K't}) + e^{\sqrt{\frac{K'}{D}}x} \operatorname{erfc}(\frac{x}{2\sqrt{Dt}} + \sqrt{K't})]$$

It is the same with the analytic solution of one-dimensional advection and dispersion model of continuous discharge point source in the reference 1.

(2) when $U = 0$, $K = 0$, $n = 0$, eq. (13) and eq. (14) become:

$$\begin{cases} C = C_0 \operatorname{erfc}\left(\dfrac{x}{2\sqrt{Dt}}\right) & (0 < t \le t_0) \\ C = C_0\left[\operatorname{erfc}\left(\dfrac{x}{2\sqrt{Dt}}\right) - \operatorname{erfc}\left(\dfrac{x}{2\sqrt{D(t-t_0)}}\right)\right] & (t > t_0) \end{cases}$$

It is the same with analytic solution of parallel problem in reference 2.

Through the above derivation and demonstration, analyzing and discussing the solution shows that the simplified equation at corresponding conditions is consistent with the comparably analytic solution. The distribution law of concentration is reasonable. It is sure that eq. (13) and eq. (14) are the analytic solution of one-dimensional advection and dispersion model for intermittent discharge point source.

REFERENCES

Li Wei. 1999, Environmental Hydraulics Progress. Wuhan: Wuhan Hydraulics and Electric power University Press.

Li Wenxun (American), 1982, Translated by Han Zuheng, Zheng Kaiqi. The differential equation and its application in hydraulics. Shanghai: Scientific and Technical Press of Shanghai.

Yu Changzhao, M. Microfsche, Li Yuliang. 1989,Contaminants diffusion and advective theory and water quality model in water environment. Beijing: Environmental Scientific Press of China.

This page intentionally left blank

1.3 Gas transfer

This page intentionally left blank

Environmental Hydraulics and Sustainable Water Management – Lee & Lam (eds)

Modeling wind-driven gas-transfer in a lake

Carlo Gualtieri
University of Napoli Federico II, Napoli, Italy

ABSTRACT: Several predictive equations have been proposed to estimate wind-driven gas-transfer rate in a lake. They have different structure and numerical constants and were mostly obtained from correlations with experimental data. The present paper proposes a turbulence-based model developed to estimate wind-driven gas transfer rate through the air–water interface of a lake. The model compares the laminar boundary layer at the air–water interface with the bottom classic laminar sublayer. Comparison with field data demonstrates that the proposed model can capture field data at low wind speed, whereas for higher values of W_{10}, the model tends to under-estimate gas-transfer process. This result should be expected because the model do not consider the contribution of waves to the gas-transfer process. Also, the model exhibits an exponent $-2/3$ for the Schmidt number Sc ($Sc = \nu/D_m$) which is consistent with gas-transfer theory and literature experimental data for smooth surfaces.

1 FOREWORD

Gas transfer of chemicals, such as oxygen, nitrogen and toxins, across the air–water interface of lakes and streams is an effective process for the environmental quality of the aquatic ecosystem (Chapra, 1997). In standing waters, such as lakes, impoundments and wide estuaries, wind is the predominant factor in causing gas-transfer. Also, gas exchange between the atmosphere and the ocean is believed to be affected by turbulence associated with wind waves at the air–water interface (Jähne & Haußecker, 1998). Several predictive equations have been proposed to estimate wind-driven gas-transfer rate in a lake. They have different structure and numerical constants and were mostly obtained from correlations with experimental data. Moreover, some equations directly compute gas-transfer rate for a chemical, whereas other ones follow the so-called approach of *reference substance*, which relates the gas-transfer rate for a chemical to that of a reference substance (Rathbun, 1998). However, research efforts are needed to better describe and quantify wind-driven gas-transfer. The present paper proposes a turbulence-based model developed to estimate wind-driven gas-transfer rate through the air–water interface of a lake at low wind speed. The model provides a linear relationship between gas-transfer rate and wind speed. Finally, the model was compared with literature data.

2 WIND-INDUCED GAS-TRANSFER: THEORY

The *gas-transfer* is an *interphase mass-transfer process* that occurs at the air–water interface if a non-equilibrium condition between the air phase and the water phase exists for a chemical. This condition is related to the gradient in concentration across the interface, which is the *driving force* of the process. The flux of chemical Φ across the air–water interface [$ML^{-1}T^{-2}$] is:

$$\Phi = K_L \cdot (C_{sat} - C_w) \tag{1}$$

where K_L is the gas-transfer rate [LT^{-1}] and C_{sat} and C_w are the equilibrium, or saturation, and bulk water concentration of the chemical [ML^{-3}], respectively. For gas of low solubility, K_L depends on the molecular and turbulent transport processes in the waterside of the air–water interface. Molecular transport depends mainly on the molecular diffusion coefficient of the dissolved gas into water D_m [L^2/T], which is a gas characteristic. On the other hand, the turbulent transport is governed by the forcing that is active in the natural environment. As turbulent eddies approach the air–water interface, this interface tends to damp them as they approach closer than their length scale (Moog & Jirka, 1999). Thus, away from the interface turbulent transport is predominant, whereas it gradually decreases toward the interface, where molecular transport takes control. This process gives rise to a *diffusive* or *concentration* boundary layer (CBL) on both sides of the interface. Its thickness δ_c depends on D_m and turbulence intensity near the surface. Outside these layers, turbulent motions provide full vertical mixing and the gas profile is uniform at the bulk concentration. Within the CBLs, the fluid is intermittently mixed by surface renewal process, which periodically occurs with a frequency that is a function of the turbulent characteristics of the flow. Thus, the relation between the turbulence structure near the free-surface and the gas-transfer process should be investigated (Jähne & Haußecker, 1998; Nakayama, 2000). Generally, three conditions hold. In open-channel flow, the surface turbulence is mainly due to the interaction of the water flow with the bottom shear (bottom-shear generated turbulence). Also, free surface fluctuations affect the turbulent redistributions near the air–water interface, which are greatly dependent on Froude number Fr and the bed slope J_b. At the contrary, the surface of lakes and reservoirs is not affected by bottom features, and the shear stress exerted at the air–water interface by the wind blowing above the water surface is the main physical factor of turbulence (wind-shear generated turbulence). Finally, in estuaries, bottom shear and interfacial shear are both present (combined wind/stream turbulent conditions). Thus, gas-transfer modeling approaches are different according to the nature of the forcing mechanism. For wind-shear condition, the gas-transfer mechanism is someway complicated by the presence of waves. Three distinct wave formation regions have been identified depending on wind speed W_{10}, which is usually used to quantify the turbulence intensity at the air–water interface (Jean-Baptiste & Poisson, 2000). In the first region, for $W_{10} < 2$–4 m/s, K_L increases only slightly with the wind speed. As the wind speed is low, the wind stress is supported by viscous drag and the height of the roughness elements of the surface is completely encompassed by the viscous boundary layer (VBL) on the water side of the air–water interface. Thus, this interface could be characterized as a smooth surface. The second region, for 2–$4 < W_{10} < 10$–13 m/s, corresponds to the presence of capillary waves, with an increasing dependence of K_L on W_{10}. The turbulent wind field transfers energy not only into the mean shear current but also into the waves and the air–water interface could be considered as a rough surface. Notably, for laboratory measurements a W_{10} of about 4 m/s is the breakpoint from smooth to rough surfaces (Thibodeaux, 1996), while for field studies smooth surface holds up to 6–7 m/s (O'Connor, 1983). Finally, the third region, for $W_{10} > 10$–13 m/s, where K_L increases greatly with W_{10}, is characterized by the occurrence of breaking waves. However, wind is just an indirect factor affecting near-surface turbulence and it can describe only approximately the real physical and dynamic conditions at the interface. This fact could explain the large scatter among the different literature data. Nevertheless it is traditionally used due its global availability. Sometimes, gas-transfer rate K_L was related with the shear velocity on the air side of the interface $u_a^*[L \cdot T^{-1}]$ (Nakayama, 2000; Chu & Jirka, 2003). Finally, as laboratory and field studies have demonstrated that gas-transfer is enhanced by the formation of bubbles due to wave breaking, K_L was recently associated both with wind speed and development degree of wind waves using a breaking-wave parameter $R_B = u_a^{*2}/(\omega_p \cdot \nu)$, which can be regarded as a kind of Reynolds number formed by u_a^* and by the spectral peak angular frequency of wind waves ω_p. Thus R_B describes the intensity of turbulence induced in water when wind waves are produced (Zhao et al., 2004). However, K_L is classically:

$$K_L = a \cdot Sc^b \cdot W_{10}^c \tag{2}$$

where a, b and c are numerical constant, W_{10} is the wind speed measured at 10 m above the water surface [$L \cdot T^{-1}$], and $Sc = \nu / D_m$ is the Schmidt number, ratio of water kinematic viscosity ν to molecular diffusivity $D_m \cdot Sc$ is in the order of 10^3 and it could be seen as the ratio between diffusion of momentum and diffusion of mass through molecular transport. Notably, ν decreases with temperature, while D_m increase with temperature. The value of the exponent b has been the focus of both theoretical and experimental studies. The differences in that value correspond to various assumption regarding the boundary layer processes and boundary conditions, corresponding to different dynamic states of the air–water interface, going from purely diffusive to turbulent (Jean-Baptiste & Poisson, 2000). Literature agrees that b value tends to increase when the transfer regime becomes more energetic. Both theoretical models and experimental values show that b is rising from $-2/3$ at low regime, where the water surface is smooth, to $-1/2$ at higher regimes, for water surface with waves (Crusius & Wanninkhof, 2003). Finally, the exponent c is ranging from 1 to 2 (Crusius & Wanninkhof, 2003).

3 THE PROPOSED MODEL

The proposed model provides the estimation of the thickness δ_c of the CBL on the water side. The model compares the VBL at the air–water interface with the bottom VBL. The bottom layer lies on a solid boundary, which has an infinite surface tension, whereas the VBL below the air–water interface, due to its surface tension, could be considered as a semi-solid boundary.

To follow this analogy, first of all, the velocity distribution in the VBL near the water surface can be defined starting from the velocity distribution in the VBL near the bottom, which is known. Notably a similar analysis was applied to characterize reaeration rate in a river (Gualtieri & Gualtieri, 2004). The shear stress distribution in the water column is:

$$\tau = \tau_b \cdot \frac{y}{h} - \tau_w \cdot \left(1 - \frac{y}{h}\right) \tag{3}$$

where τ_b and τ_w are the shear stress on the bottom and on the water-side of the free surface due to the wind, respectively, $[N \cdot L^{-2}]$, y is the vertical distance downward from the air–water interface [L] and h is water depth [L] (Fig. 1). Eq. (3) could be equated to the Newton's expression for the shear stress $\tau = -\rho \cdot \nu \cdot (du/dy)$, where u is water velocity $[L \cdot T^{-1}]$ and ρ is water density $[M \cdot L^{-3}]$. Integrating eq. (3) near the water surface, a velocity distribution is defined as:

$$\rho \cdot \nu \cdot (u_0 - u) = \frac{\tau_b + \tau_w}{h} \cdot \frac{y^2}{h} - \tau_w \cdot y \tag{4}$$

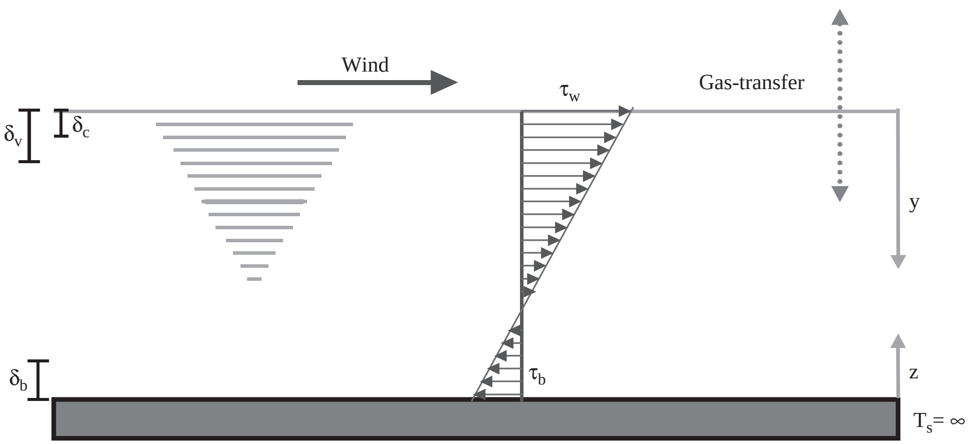

Figure 1. The proposed model.

where u_0 is the water velocity for $y = 0$. Notably, the shear stress on the bed τ_b is related to the shear stress τ_w. In fact, a wind acting on the water surface causes a drift current near the free surface in the direction it blows and a bottom return flow in the opposite direction (Wu & Tsanis, 1995). The value of the bed shear stress τ_b is usually presented in literature as $\tau_b = \eta\tau_w$ where η is a coefficient that depends on $Re_w = u_w h/\nu$, which is the Reynolds number related to the wind-induced flow velocity at the interface u_w. The ratio $\eta = \tau_b/\tau_w$ has in laminar flow the constant value of -0.50 (Tsanis & Leutheusser, 1988) and it decreases with increasing Re_w (Gualtieri, in press). Introducing this relation between τ_b and τ_w, eq. (4) yields:

$$\rho \cdot \nu \cdot (u_0 - u) = \left[\left(\frac{1+\eta}{2 \cdot h}\right) \cdot y - 1\right] \cdot \tau_w \cdot y \tag{5}$$

Assuming the continuity of the stress at the air–water interface, the shear stress τ_w is equal to τ_a, which is the shear stress on the air-side of the interface (O'Connor, 1983; Thibodeaux, 1997):

$$\tau_a = C_D\, \rho_a\, W_{10}^2 \tag{6}$$

where C_D is the drag coefficient and ρ_a is air density $[\mathrm{M} \cdot \mathrm{L}^{-3}]$. Introducing eq. (6) into eq. (5):

$$u_0 - u = \left[\left(\frac{1+\eta}{2 \cdot h}\right) \cdot y - 1\right] \cdot y \cdot \frac{C_D}{\nu} \cdot \frac{\rho_a}{\rho} \cdot W_{10}^2 \tag{7}$$

Also, in the VBL near the bottom, equating the Newtonian expression for bottom shear stress and from the friction velocity expression $\tau_b = \rho \cdot u^{*2}$, a linear velocity distribution holds:

$$\frac{u}{u^*} = \frac{z \cdot u^*}{\nu} \tag{8}$$

where u^* is the friction velocity $[\mathrm{L} \cdot \mathrm{T}^{-1}]$ and z is the distance upward from the bottom (Fig. 1). Also, from the expression of the Reynolds number Re, it yields:

$$Re = \frac{z \cdot u}{\nu} = \frac{z \cdot u}{\nu} \cdot \frac{u^*}{u^*} = \frac{z \cdot u^*}{\nu} \cdot \frac{u}{u^*} \tag{9}$$

From eqs. (8) and (9), it yields:

$$Re = \left(\frac{z \cdot u^*}{\nu}\right)^2 \tag{10}$$

The thickness of the viscous boundary layer near the bottom δ_b (Fig. 1) is:

$$\delta_b = \frac{5 \cdot \nu}{u^*} \tag{11}$$

From eqs. (10) and (11), if u_b is the velocity at $z = \delta_b$, its Reynolds number is given by:

$$Re = \frac{\delta_b \cdot u_b}{\nu} = \left(\frac{\delta_b \cdot u^*}{\nu}\right)^2 = 5^2 = 25 \qquad \text{at the bottom} \tag{12}$$

Now, the outlined analogy between the laminar layers at the air–water interface and at the bottom could be used to estimate the thickness of the VBL δ_v at the air–water interface (Fig. 1). In fact, if $u_{\delta v}$ is the velocity at the lower bound of the VBL near the interface, it is possible to write an expression analogous to eq. (12), where $(u_0 - u_{\delta v})$ has the same meaning as u_b:

$$\frac{\delta_v \cdot (u_0 - u_{\delta v})}{\nu} << 5^2 \qquad \text{at the air-water interface} \tag{13}$$

Notably, $\delta_v \cdot (u_o - u_{\delta v})/\nu$ must be lower than 5^2 because the air–water interface has a finite surface tension. In fact, the value of 5^2 holds for a boundary with infinite surface tension. Eq. (13) allows to define a particular Reynolds number for gas-transfer, namely Re_{g-t}:

$$Re_{g\text{-}t} = \frac{\delta_v \cdot (u_0 - u_{\delta v})}{\nu} \tag{14}$$

and, thus, the gas-transfer Reynolds number $Re_{g-t} < 25$. Equating $(u_0 - u_{\delta v})$ in eqs. (7) and (14):

$$Re_{g\text{-}t} \cdot \frac{\nu}{\delta_v} = \left[\left(\frac{1+\eta}{2 \cdot h}\right) \cdot y - 1\right] \cdot y \cdot \frac{C_D}{\nu} \cdot \frac{\rho_a}{\rho} \cdot W_{10}^2 \tag{15}$$

The term in the square bracket could be approximated to the unity. In fact, η ranges from -0.26 to -0.07 (Gualtieri, in press), δ_ν is in the order of 1×10^{-4} m and h typically ranges from 1×10^1 to 1×10^2 m. Thus, for $y = \delta_\nu$, we have:

$$\delta_v = \frac{\nu}{W_{10}} \cdot {Re_{g\text{-}t}}^{1/2} \cdot \left(\frac{1}{C_D} \cdot \frac{\rho}{\rho_a}\right)^{1/2} \tag{16}$$

Since the CBL thickness δ_c is related with the VBL thickness δ_ν as $\delta_c = \delta_\nu / Sc^{1/3}$, eq. (16) yields:

$$\delta_c = \frac{{Re_{g\text{-}t}}^{1/2}}{W_{10}} \cdot (\nu \cdot D_m)^{1/3} \cdot \left(\frac{1}{C_D} \cdot \frac{\rho}{\rho_a}\right)^{1/2} \tag{17}$$

The gas-transfer rate K_L could be related with CBL thickness δ_ν as:

$$K_L = \frac{D_m}{\delta_c} \tag{18}$$

and, finally, the gas-transfer rate K_L is:

$$K_L = \frac{1}{{Re_{g\text{-}t}}^{1/2}} \left(\frac{D_m}{\nu}\right)^{2/3} \left(C_D \frac{\rho_a}{\rho}\right)^{1/2} W_{10} \tag{19}$$

Equation (19) provides a linear relationship between K_L and W_{10}. This is consistent with other equation derived for low wind speed ($W_{10} < 4$ m/s), when air–water interface is a smooth surface (O' Connor, 1983). Also, the model exhibits an exponent $-2/3$ for the Schmidt number Sc which is consistent with gas-transfer theory and literature experimental data for smooth surfaces.

4 ANALYSIS OF DATA MODEL RESULTS

The proposed model has been verified using literature experimental data, that are taken from studies carried out in lakes and rivers using as tracer SF_6 (Wanninkhof et al., 1991; Tucker et al., 1996;

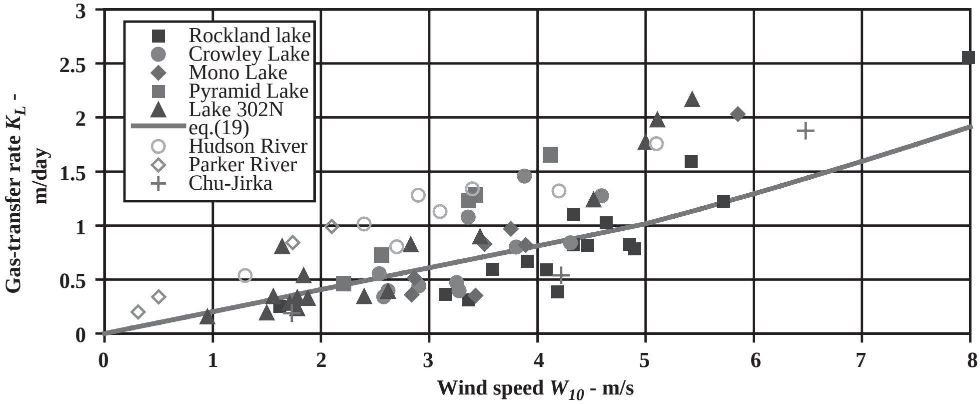

Figure 2. K_L predictions from eq. (19) against field data.

Crusius & Wanninkhof, 2003) or ^{3}He (Clark et al., 1996). Some data collected in laboratory flume using oxygen as exchanged gas were also considered (Chu-Jirka, 2003).

Wanninkhof and Crusius-Wanninkhof data sets were collected in lakes, whereas Clark and Tucker data sets refer to rivers and estuaries measurements. The temperature of the considered data is in the range from 5.0 to 23.0°C and *Sc* values of SF_6 are accordingly from 2257 to 812. The available data shows generally a significant scatter as expected (Fig. 2). Notably, the data collected in rivers, i.e. Hudson River and Parker River data sets, exhibit generally at the same W_{10} value gas-transfer rate higher than the data collected in lakes (Fig. 2). This is due to the fact that in rivers and estuaries bottom shear and interfacial shear are both present. In these conditions, K_L measured data include also the contribution of stream turbulence.

In eq. (19) the drag coefficient C_D was calculated using the equation proposed by Wu. (Thibodeaux, 1996), which assumes that C_D is constant for $W_{10} < 5$ m/s and increases linearly with W_{10} for $W_{10} > 5$ m/s. Water temperature was assumed to be $T = 20°C$ where the Schmidt number of SF_6 is 946 and the ratio between air and water density is $\rho_a/\rho = 0.001206$. Finally, Re_{g-t} was $Re_{g-t} = 20$. The comparison between results from eq. (20) and field data is presented in Fig. 2, where the proposed model can capture field data at low wind speed ($W_{10} < 5$ m/s), whereas for higher values of W_{10} ($W_{10} > 5$ m/s) the model tends to underestimate gas-transfer process. However this result should be expected because the model do not consider the contribution of waves to the gas-transfer process that it is significant at the higher wind speeds.

5 CONCLUDING REMARKS

The paper proposed a model to predict gas-transfer rate K_L due to the wind blowing above the air–water interface of a lake, where the shear stress produced by the wind is the main physical factor of turbulence. The model was developed comparing the viscous boundary layer (VBL) at the air–water interface with the bottom VBL and assuming that the interface could be characterized as a smooth surface with no-waves condition. The model provides a linear relationship between gas-transfer rate K_L and wind speed W_{10} that is consistent with previous literature empirical equations for low wind speed conditions. Comparison with field data demonstrated that the proposed model can capture field data at low wind speed ($W_{10} < 5$ m/s), whereas for higher values of W_{10}($W_{10} > 5$ m/s) the model tends to underestimate gas-transfer process because it cannot consider the contribution of wind waves to the gas-transfer process.

REFERENCES

Chapra S.C. (1997). *Surface water quality modeling.* McGraw-Hill, New York, USA

Chu C.R. & Jirka G.H. (2003). Wind and stream flow induced reaeration. *Journal of Environmental Engineering, ASCE,* vol. 129, n. 12, December 2003, pp. 1129–1136

Crusius J. & Wanninkhof R. (2003). Gas transfer velocities measured at low wind speed over a lake. *Limnology & Oceanograph*y, vol. 48, n. 3, March 2003, pp. 1010–1017

Gualtieri C. & Gualtieri P. (2004). Turbulence-based models for gas transfer analysis with channel shape factor. *Environmental Fluid Mechanic*s, vol. 4, n. 3, September 2004, pp. 249–271

Gualtieri C. (in press). Discussion on *M.Higashino, H.G. Stefan and C.J. Gantzer: Periodic diffusional mass transfer near sediment/water interface: Theory. J. Env. Eng., ASCE, vol. 129, n. 5, May 2003*. *Journal of Environmental Engineering, ASCE*, pp. 447–455, in press

Jähne B. & Haußecker H. (1998). Air–water gas exchange. *Annual Review Fluid Mechanics*, vol. 30, 1998, pp. 443–468

Jean-Baptiste P. & Poisson A. (2000). Gas transfer experiment on a lake (Kerguelen Islands) using ^{3}He and SF_6. *Journal of Geophysical Research*, vol. 105, n. C1, pp. 1177–1186

Moog D.B. & Jirka G.H. (1999). Air–water gas transfer in uniform channel flow. *J. Hydraulic Engineering, ASCE*, 125, 1, January 1999, pp. 3–10

Nakayama T. (2000). Turbulence and coherent structures across the air–water interface and relationship with gas-transfer. *PhD Dissertation*, Kyoto University, Kyoto, Japan

O'Connor D.J. (1983). Wind effects on gas-liquid transfer coefficients. *Journal of Environmental Engineering Division, ASCE*, vol. 109, 3, June 1983, pp. 731–752

Rathbun R.E. (1998). Transport, behavior and fate of volatile organic compounds in streams. U.S. Geological Survey Professional Paper n. 1589, Washington, DC

Thibodeaux L.J. (1996). *Environmental chemodynamics*. John Wiley & Sons, Chichester, U.K.

Tucker J., Carini S., Weston N., Vallino J., Hopkinson C., Giblin A. and Garritt R. (1996). Direct measurement of gas exchange rates in the Parker River Estuary. *http://ecosystems.mbl.edu/PIE/data/PHY/PHYSF6Description.htm*

Wanninkhof R., Ledwell J.R. and Crusius J. (1991). Gas transfer velocities on lakes measured with sulfur hexafluoride. in Proceedings of the *2nd International Conference on gas transfer at water surfaces*, Minneapolis, MN

Wu J. & Tsanis I.K. (1995). Numerical study of wind-induced water currents. *J. Hyd. Eng., ASCE*, vol. 121, n. 5, May 1995, pp. 388–395

Zhao D., Toba Y., Suzuki Y. and Komori S. (2003). Effect of wind waves on air-sea exchange: proposal of an overall CO_2 transfer velocity formula as a function of breaking-wave parameter. *Tellu*s, vol. 55B, pp. 478–487

This page intentionally left blank

Environmental Hydraulics and Sustainable Water Management – Lee & Lam (eds)
© 2005 Taylor & Francis Group, London, ISBN 04 1536 546 5

Experimental study on air-water interfacial turbulent hydrodynamics and gas transfer in wind-induced open channel flows

K. Yoshida
Ph.D. Student, Dept. of Civil & Earth Resources Engg., Kyoto University, Kyoto, Japan

I. Nezu
Professor, Dept. of Civil & Earth Resources Engg., Kyoto University, Kyoto, Japan

ABSTRACT: This study focuses on the fundamental relationship between air-water turbulent motions and the associated gas transfer phenomena in wind-induced open channel flows by some unique measurements. The purpose of the present study is mainly to clarify the gas transfer phenomena across the wavy deformed air-water interface on the basis of the wall-sheared bursting phenomena of turbulence, and also to evaluate the effects of the coherent vortex motions on gas exchanges across the interface. In the experiments, the turbulent motions caused by both the bottom wall-shear and the air-shear force were intensively measured with the conditional sampling methods using laser Doppler anemometers (LDA), and the basic characteristics of coherent dynamics were investigated by a wavelet analysis and 4th quadrant threshold method. Furthermore, the dissolved oxygen in the bulk water layer was measured in order to investigate the gas transfer coefficients. As the results, it was found that the coherent motions have a great influence on gas transfer phenomena. Especially, it can be pointed out that the gas transfer phenomena between air-water interfaces are governed by the specific coherent motions in each flow pattern.

1 INTRODUCTION

Recently, gas transfer phenomena across the largely deformed air-water interfaces, such as CO_2, O_2, NO_x and SO_x have greatly attracted the vigorous researchers all over the world, because of the serious global environmental problems. In addition, it is so important to clarify the reaeration mechanism, by which the stream usually recovers the biochemical oxygen from air. In previous studies, it has been pointed out that the gas transfer phenomena are greatly affected by the turbulent motions near the interface, e.g., see Rashidi *et al*. (1991) and Komori *et al*. (1993). However, few studies to make clear the gas exchange mechanism across air-water interface have been carried out because of lack of measurement accuracy and experimental difficulties. Thus, it is necessary to investigate the air-water interfacial turbulent hydrodynamics and the associated gas transfer in wind-induced open channel flows, which are often observed in natural rivers, lakes and oceans.

It has been previously recognized that the transfer of low-solubility gases between air and water like CO_2, and O_2 is governed in the very thin water layer beneath the interface in which the turbulent motions control and have influence on the gas transfer. This is because the transfer of the low-solubility gases undertakes the high degree of resistance in the water side of the interface in spite of the great turbulent mixing. Therefore, the gas transfer coefficient is then called K_L. In the gas transfer theory in the early time, the effects of the turbulent eddies was not taken account of, for example, Danckwerts (1951) proposed the renewal theory which described the random replacement of fluid particles near the air-water interface. Later, the renewal theory has been successfully developed with the effects of the turbulent eddies and suggested as the 'large eddy model (LEM)' by Fortescue and Pearson (1967) and 'small eddy model (SEM)' by Lamont and

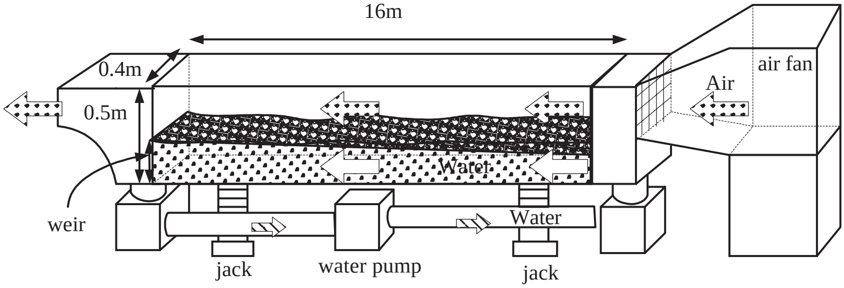

Figure 1. An air-water tunnel.

Scott (1970). In the models, the gas transfer coefficient is formulated as follows,

$$K_L^+ \sqrt{Sc} = \frac{K_L}{u'} \sqrt{Sc} \propto \mathrm{Re}^{-1/2} \text{ (LEM)} \tag{1}$$

$$K_L^+ \sqrt{Sc} \propto \mathrm{Re}^{-1/4} \quad \text{(SEM)} \tag{2}$$

where $Sc \equiv \nu/D_l$ is Schmidt number, ν and D_l are the kinetic viscosity and the molecular diffusion of water, respectively. u' is the turbulence intensity. Many researchers have intensively investigated the relationship between the gas transfer and the Reynolds number, however the gas transfer mechanism remains unknown. Especially, there are few findings by Eloubaidly & Plate (1972) and Chu & Jirka (1995) on the gas transfer across the air-water interface in wind-induced open channel flows.

In this study, the relationship between gas transfer phenomena and the associated turbulent motions in wind-induced open channel flows was intensively investigated by the experimental method. In the experiments, the turbulent motions in the water side were measured by LDA and the basic characteristics of coherent dynamics were investigated by a wavelet analysis and 4th quadrant threshold method.

2 EXPERIMENTAL PROCEDURE

In this study, the experiments were conducted in a 16 m long, 40 cm wide and 50 cm deep wind-water tunnel, in which the channel slope was possible to be accurately adjusted (see Fig. 1, a schematic description of the present air-water tunnel). Fig. 2 shows a LDA system with an ultrasonic wave gauge and coordinate system. The coordinate system is as follows:x is the horizontal coordinate and z is the upward vertical one from the bottom wall. In addition, the corresponding velocity fluctuations are u and v. Air blew over open channel surfaces in a wide range, and water went through the channel and passed the pipe under the channel for recirculation. Table 1 shows the hydraulic conditions of these experiments. The water depth is fixed at 7.0 cm. $U_{a,\max}$ is the maximum air velocity, U_{*a} is the friction velocity on the airside by evaluating mean velocity profiles near the interface using log-law and U_{*w} is the friction velocity on the bottom wall. U_m is the mean velocity of water stream and $\mathrm{Fr} \equiv U_m h/\nu_w$ means the Froude number of water flow. A laser Doppler anemometer (LDA, Dantec) was used to measure the instantaneous velocity and an ultrasonic wave gauge was simultaneously used with LDA in order to investigate a correlation between the velocity fluctuation and an air-water interface fluctuation η from mean water depth. Moreover, the dissolved oxygen instrument (called as the DO meter, hereafter) was used to measure the bulk concentration of oxygen in the water flume, see Moog *et al.* (1999).

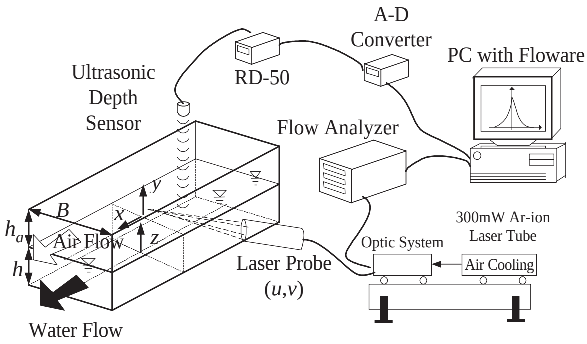

Figure 2. LDA system with an ultrasonic wave gauge and coordinate system.

Table 1. Hydraulic condition.

RUN	$u_{a,\max}$ (m/s)	u_{*a} (cm/s)	u_m (cm/s)	Fr	u_{*w} (cm/s)
OPEN1	0.0	0.0	8.3	0.10	0.39
OPEN2	0.0	0.0	16.6	0.20	1.15
OPEN3	0.0	0.0	24.8	0.30	1.30
OPEN4	0.0	0.0	33.1	0.40	1.58
OPEN5	0.0	0.0	41.4	0.50	1.97
OPEN6	0.0	0.0	49.7	0.60	2.37
OPEN8	0.0	0.0	66.3	0.80	2.78
COM21	1.58	5.80	16.6	0.20	1.12
COM22	2.23	6.91	16.6	0.20	1.10
COM23	3.58	12.5	16.6	0.20	1.09
COM24	4.31	17.0	16.6	0.20	1.15
COM25	5.06	17.6	16.6	0.20	1.31
COM26	5.83	23.8	17.4	1.21	1.46
COM27	6.56	26.9	17.4	0.21	1.41
COM28	7.24	29.1	18.2	0.22	1.48
COM51	1.11	4.3	41.4	0.50	1.35
COM52	1.11	9.1	42.2	0.51	1.31
COM53	1.11	15.6	43.1	0.52	1.29
COM81	3.93	3.94	66.3	0.80	2.78
COM82	3.93	9.23	66.3	0.80	2.76
COM83	3.93	13.6	67.1	0.81	2.70

3 RESULTS AND DISCUSSIONS

3.1 *Fundamental turbulent properties*

The fundamental statistics of coherent motions in the water layer were investigated by the one-point measurements by LDA using a linear filtering technique (LFT) by Benilov *et al.* (1974) and a wavelet analysis of Daubechies (1988). A LFT has been frequently used to clarify the semi-periodic flows like wind-induced waves flows (see, Cheung and Street, 1988). Fig. 3 shows the vertical profiles of the flatness value $F_v \equiv \overline{v^4}/\overline{v^2}^2$ calculated by the data of the vertical velocity fluctuation v (open circle) and decomposed velocity fluctuation v^* (open triangle) in the case of OPEN, COM22 and COM26. Here, v^* means the data in which the wind-induced semi-periodic component is removed with a LFT. It is clearly observed that there's the large value of F_v not only near the bed due to the wall turbulence, but also near the interface due to the air-sheared flow.

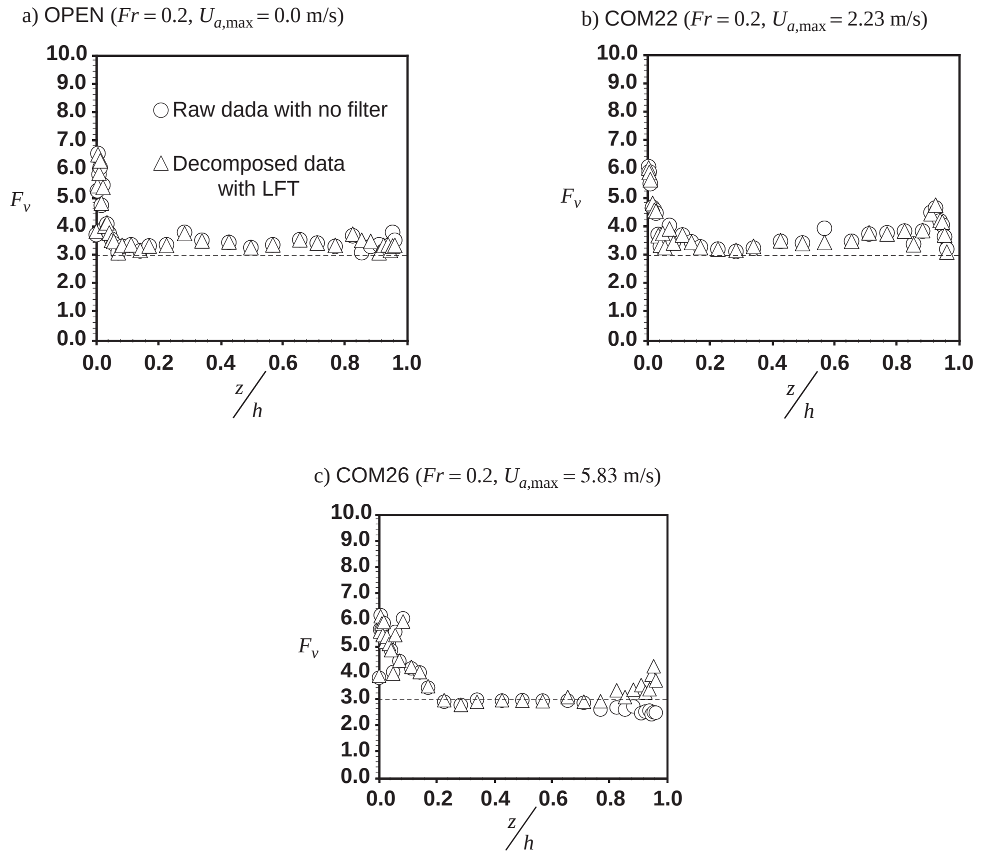

Figure 3. Flatness value $F_v \equiv \overline{v^4}/v'^4$ (Case: OPEN, COM22 and COM26).

This is because that the coherent motions are generated by the air-sheared flows and these motions correspond to the result which was observed in the visualization of the flow with the hydrogen bubbles method, mentioned before. In addition, it is interestingly notified that the turbulence, which is not associated with the interface fluctuation, is generated, when the high-speed wind blows over the water surface.

Fig. 4 (a) shows the relationship between the non-dimensional bursting period $T_B^+ \equiv T_B U_{*w}^2/\nu_w$ and the friction Reynolds number $R_* \equiv U_{*w}h/\nu_w$ in no air-sheared open channel flows. The current data was analyzed by the 4th quadrant half-threshold value method by Nakagawa & Nezu (1978). In the figure, the data of Nakagawa & Nezu (1978) was added. Fig. 4 (b) shows the relationship between the non-dimensional bursting period $T_B^+ \equiv T_B U_{*s}^2/\nu_w$ and the friction Reynolds number $R_{*\eta} \equiv U_{*s}\eta'/\nu_w$in wind-induced open channel flows. Here, $\eta' \equiv \sqrt{\overline{\eta^2}}$ is the root mean square (rms) value of η. It is recognized that for the relatively high Reynolds number, T_B^+ is likely to be proportional to $R_*^{1/2}$ or $R_{*\eta}^{1/2}$ in both open channel flows and wind-induced open channel flows.

$$T_B^+ \propto R_*^{1/2} \quad \text{or} \quad T_B^+ \propto R_{*\eta}^{1/2} \tag{3}$$

In addition, from the renewal theory, when these bursting motions contribute the renewal motions beneath the air-water interface and the representative velocity of renewal motions can be replaced

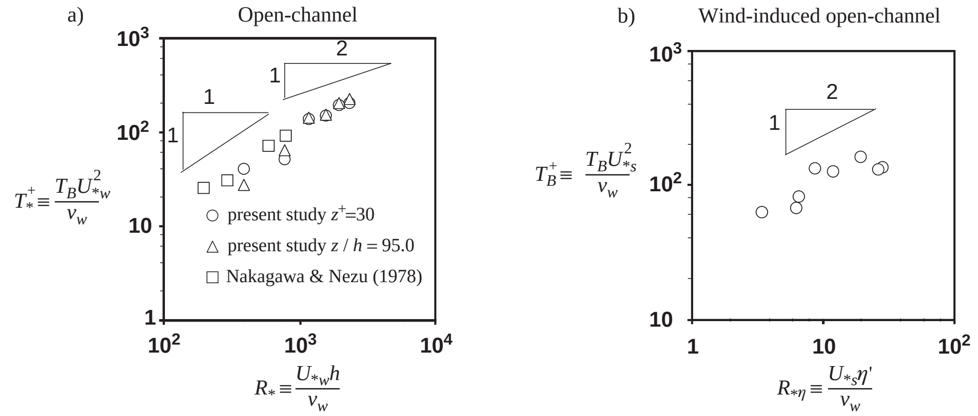

Figure 4. Relationship between the bursting period and the Reynolds number (a) open channel flows, (b) wind-induced open channel flows).

by the friction velocity U_{*w} or U_{*s}, then the following equation can be obtained,

$$K_L^+\sqrt{Sc} = \frac{K_L}{U_{*w}}\sqrt{Sc} = \left(T_B^+\right)^{-1/2} \propto R_*^{-1/4} \text{ or } K_L^+\sqrt{Sc} = \frac{K_L}{U_{*s}}\sqrt{Sc} = \left(T_B^+\right)^{-1/2} \propto R_{*\eta}^{-1/4} \tag{4}$$

3.2 *Gas transfer and turbulent motion*

The reaeration coefficient K_2 has been effectively used to monitor the environmental quality of water in rivers and lakes. K_2 is defined as follows,

$$\frac{\partial C_b}{\partial t} \equiv K_2(C_s - C_b) \tag{5}$$

where C_s is the equilibrium concentration of the gas in water in contact with air, and C_b is the bulk concentration of the gas. t denotes time. Also, K_L is defined as follows,

$$J \equiv K_L(C_s - C_b) \tag{6}$$

J means the gas flux across the air-water interface. From Eqs.(5) and (6), the following equation to evaluate K_L is derived,

$$K_L = K_2 \cdot (V/A) \cong K_2 \cdot h \tag{7}$$

where V denotes the water volume and A shows the air-water interface area where the gas flux occurs. Eq.(7) is roughly derived by the assumption that the fluctuation of air-water interface is approximately neglected in comparison with the water depth. In this study, K_2 was calculated by the two-station method suggested by Rathbun (1988) . Fig. 5 shows a sketch of typical length scales and the concentration profile of oxygen gas beneath the air-water surface, accompanied with the DO meter in this experiment. In this study, it is assumed that the bulk concentration of oxygen gas is nearly constant along the water depth. In the two-station method, K_2 is calculated as follows (see Fig. 6),

$$K_2 = K_{2,acc} + K_{2,conv} = -\frac{\Delta(\ln D)}{\Delta t} - U_m \frac{\Delta(\ln D)}{\Delta x} \tag{8}$$

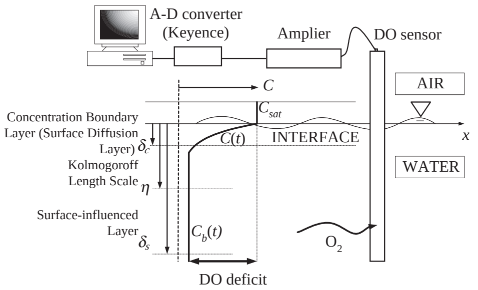

Figure 5. Sketch of typical length scales and concentration profile of oxygen gas beneath the air-water interface.

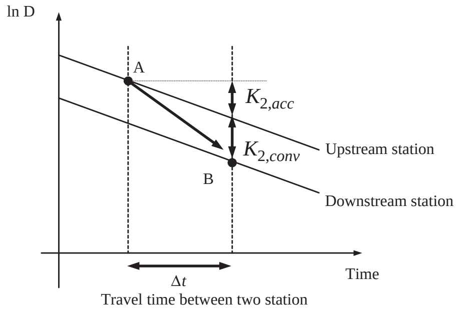

Figure 6. Sketch of two station method in order to analyze the gas transfer coefficient [9].

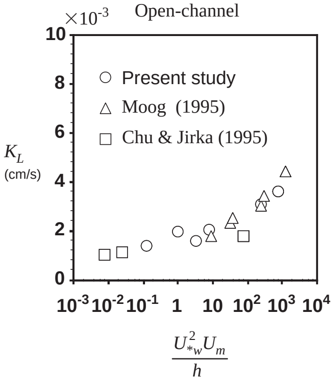

Figure 7. Gas transfer coefficient and power of mean water stream in open channel flows.

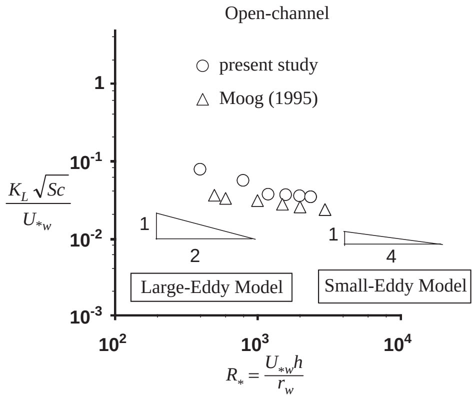

Figure 8. Gas transfer coefficient and the fricition Reynolds number in open channel flows.

where $D \equiv C_s - C_b$ denotes the deficit of the dissolved oxygen in water flow, Δt means the travel time of fluid between two station (A and B), Δx is the distance between them. In this method, K_L can be obtained by the Eq.(7) and (8). In addition, it is well known that K_L varies dependently on the temperature, therefore, K_L in the following figures means the gas transfer coefficient at 20 degree C (Elmore & West, 1961).

Fig. 7 shows the relationship between the non-dimensional gas transfer coefficient $K_L^+\sqrt{Sc}$ and the friction Reynolds number R_* in no air-sheared open channel flows. In the figure, the dataset of Moog (1995) is added. It is recognized that the dependency of $K_L^+\sqrt{Sc}$ to R_* is from $-1/4$ to $-1/2$. This tendency corresponds to the small eddy model and the large eddy model. It can be suggested that as R_* becomes larger, the gas transfer is governed by the small eddy model, as suggested by Theofanous *et al.* (1976). Fig. 9 shows K_L against the friction velocity U_{*a} in wind-induced open channel flows. In the figure, the data of Chu (1993) is included. It is observed that the data of $\mathrm{Fr} = 0.2$ (open circle) is greatly affected by the air shear. This may be because the coherent motions beneath the air-water interface are generated by the air-sheared flows. Fig. 10 shows the non-dimensional gas transfer coefficient $K_L^+\sqrt{Sc}$ and the friction Reynolds number $R_{*\eta}$ in wind-induced open channel flows at $\mathrm{Fr} = 0.2$. It is observed that the dependency of $K_L^+\sqrt{Sc}$ to $R_{*\eta}$ is about $-1/4$, which corresponds to the small eddy model.

After all, the above experimental results of the dependency of $K_L^+\sqrt{Sc}$ to R_* are explained by the Eq.(4) which means that bursting motions contribute the surface renewal motions beneath the air-water interface.

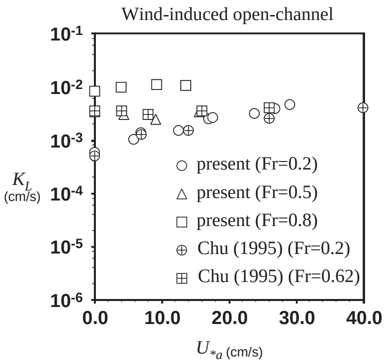

Figure 9. Gas transfer coefficient and the friction velocity in wind-induced open channel flows.

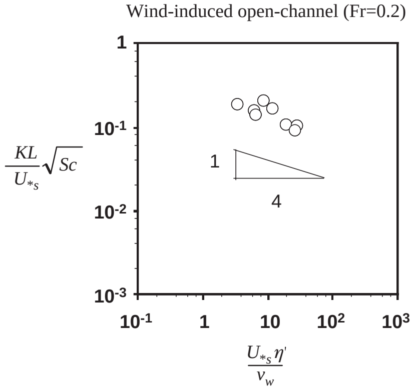

Figure 10. Gas transfer coefficient and the friction Reynolds number in wind-induced open channel flows.

4 CONCLUDING REMARKS

This study focuses on fundamental relationship between air-water turbulent motions and gas transfer phenomena in wind-induced open channel flows by unique measurements. As the results, it was shown that the coherent motions have a great influence on gas transfer phenomena and it was clarified that the dependency of non-dimensional gas transfer coefficient to the Reynolds number is about $-1/4$ by the experimental method.

REFERENCES

Benilov, A.Y. et al. (1974): *Boundary Layer Meteo*., Vol.6, pp.269–285.

Cheung, T.K. and Street, R.L. (1988): *J. Fluid Mech.*, Vol.194, pp.133–151, 1988.

Chu, C.R. (1993): *Ph.D Thesis presented to Cornell University*.

Chu, C.R and Jirka, G.H. (1995): *Air-Water Gas Transfer*, B. Jahne and E.S.Monahan eds., AEON Verlag, pp.553–569.

Daubechies, I. (1988): *Comm. Pure and Appl. Math*., Vol.41, pp.909–996.

Danckwerts, P.V. (1951): *Indust. & Eng. Chem.*, Vol.43 (6), pp.1460–1467.

Elmore, H.L. and West, W.F. (1961): *J. Sanitary Eng*., ASCE, Vol.87, No.SA6, pp.59–71, 1961.

Eloubaidly, A.F. and Plate, E.J. (1972): *J. Hydraulics Div*., ASCE, Vol.98, pp.153–170, 1972.

Fortescue, G.E. and Pearson, J.R.A. (1967): *Chemical Engrg. Sci*., Vol.22, pp.1163–1176.

Higbie, R. (1935): *AIChE Trans*, Vol.31, pp.365–390.

Komori, S *et al*. (1993): *J. Fluid Mech*., Vol.249, pp.161–183.

Lamont, J.C. and Scott, D.S. (1970): *AIChE J.*, Vol.16 (4), pp.513–519.

Moog, D.B. (1995): *Ph.D Thesis presented to Cornell University*.

Moog *et al.* (1999): *J. Hydr. Eng.*, ASCE, Vol.125, pp.3–10.

Nezu, I. and Nakagawa, H. (1993): Turbulence in Open Channel Flows, IAHR-monograph, Balkema, Netherlands.

Rashidi *et al.* (1991): *Int. J. Heat and Mass Transfer*, Vol.34, No.7, pp.1799–1810.

Rathbun, R.E. (1988): *J. Enrironr. Eng.*, ASCE, Vol.114, No.2, pp.473–475.

Theofanous, T.G. *et al.* (1976): *Int. Heat Mass Transfer*, Vol.19, pp.613–624.

This page intentionally left blank

Environmental Hydraulics and Sustainable Water Management – Lee & Lam (eds)
© 2005 Taylor & Francis Group, London, ISBN 04 1536 546 5

Estimation of the transfer velocity of carbon dioxide at the surface of wind waves

H. Tsumori & Y. Sugihara
Department of Earth System Science and Technology, Kyushu University, Kasuga, Fukuoka, Japan

A. Masuda
Research Institute for Applied Mechanics, Kyushu University, Kasuga, Fukuoka, Japan

ABSTRACT: An experimental study for estimating accurately the transfer velocity of CO_2 at the surface of wind waves is presented. Vertical profiles of the mean wind speed and the concentration of CO_2 in the air were measured in a wind-wave tank. The local flux of CO_2 was estimated at several fetches by using the profile method. The concentration of CO_2 dissolved in the water was measured by using a gas-liquid equilibrator made of hydrophobic porous tube. The local CO_2 transfer velocity on the water side was obtained from the local flux and the concentration difference across the air-water interface. The transfer velocity increases monotonously with the friction velocity, and also increases remarkably with the fetch under the condition of the same friction velocity.

1 INTRODUCTION

The gas transfer velocity of CO_2 at the air-sea interface has frequently been investigated through laboratory wind-wave experiments and field observations. Various empirical expressions for the transfer velocity have been proposed and most of them have been represented in terms of functions of the mean wind speed referred to the 10 m height. The developments of wind waves and turbulent boundary layer depend strongly on the fetch of the sea surface, so that the transfer velocity under the condition of the same wind speed seems to vary owing to the degree of their developments. Thus, it is very important to reveal quantitatively the fetch dependence of the gas transfer velocity. However, in most previous experiments, the overall transfer velocity averaged over the whole interface in a wind-wave tank has been measured. There are few laboratory studies concerning the fetch dependence of the transfer velocity.

Komori et al. (1993) measured the local CO_2 transfer velocity in a laboratory wind-wave tank. They set a control volume on the air side over the region of fetch = 3 to 5 m, and obtained the local flux across the air-water interface from the budget of CO_2 within the volume. As an alternative method to quantify the local gas transfer rates, we may think of the eddy correlation method and the profile method. Especially, the latter allows us to estimate the local flux from laboratory measurements of vertical profiles of the wind speed and the concentration of CO_2 in the air.

The purpose of this study is to estimate experimentally the transfer velocity of CO_2 at the surface of wind waves. Vertical profiles of the mean wind speed and the mean concentration of CO_2 in the air were measured in a wind-wave tank. In order to estimate the local CO_2 flux at a certain fetch, we employed the profile method in laboratory experiments. The concentration of CO_2 in the water was measured by using a gas-liquid equilibrator made of hydrophobic porous tube. The local CO_2 transfer velocity was obtained from the local flux and the concentration difference of CO_2 across the air-water interface. The dependence of the transfer velocity on the fetch was also examined.

2 ESTIMATION OF CO_2 TRANSFER VELOCITY

In order to estimate the local CO_2 flux at a certain fetch F (mol/m^{2}s), the profile method was used. For the turbulent transfer of passive scalar, the turbulent Schmidt number ν_t/K_t, where ν_t (m^2/s) is the eddy viscosity and K_t (m^2/s) the eddy diffusivity of CO_2, is close to the unity. By using the mixing-length model, we obtain

$$F = -K_t \frac{\partial C_a}{\partial z} \approx -\nu_t \frac{\partial C_a}{\partial z} = -\kappa u_{*a} z \frac{\partial C_a}{\partial z}, \tag{1}$$

where C_a (mol/m^3) is the mean concentration of CO_2 in the air, z the vertical coordinate axis taken upward from the still water surface, u_{*a} (m/s) the friction velocity on the air side and κ the von Kármán constant (=0.4). After the integration for both sides of (1), we obtain a logarithmic law for the mean concentration of CO_2 in the air:

$$\frac{C_a(z_0) - C_a(z)}{C_*} = \frac{1}{\kappa} \ln\left(\frac{z}{z_0}\right), \tag{2}$$

where C_* (mol/m^3) is a representative concentration defined as F/u_{*a} and $C_a(z_0)$ the concentration at the height of the roughness length z_0. We can estimate the local fluxes at several fetches from the product of C_* and u_{*a}, which are obtained according to logarithmic laws. Consequently, the local gas transfer velocity on the water side k_L (m/s) can be obtained from the following relation:

$$F = C_* u_{*a} = k_L (C_w - C_s), \tag{3}$$

where C_w (mol/m^3) is the concentration of CO_2 in the bulk of water and C_s (mol/m^3) is the equilibrium concentration on the water side balanced with the concentration of CO_2 on the air side at the air-water interface.

3 EXPERIMENTAL PROCEDURES

Experiments were made by using a wind-wave tank as illustrated schematically in Figure 1. The tank was 17 m long, 0.60 m wide and 0.80 m deep, and the water depth was kept at 0.39 m. The horizontal coordinate axis x was taken leeward from the upwind edge in the tank, and x indicates the fetch. In order to estimate the CO_2 flux from the water side to the air side, the concentration of CO_2 in the water was increased in advance to about 40,000 ppm by injecting the 100% CO_2 gas

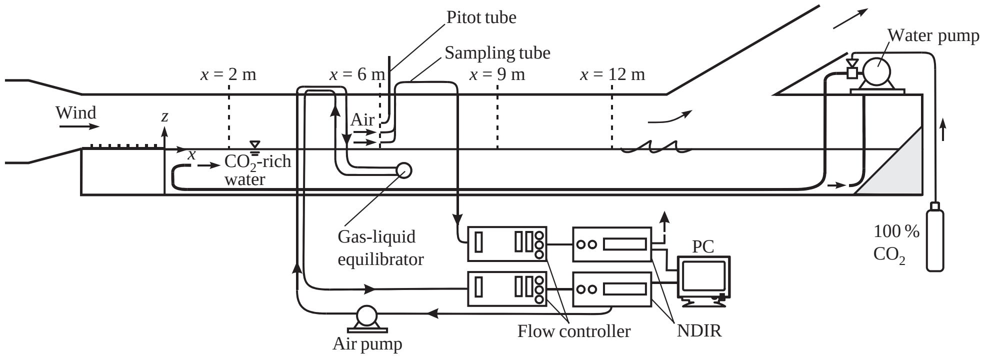

Figure 1. Schematic diagram of experimental apparatus.

into the circulating water. After the aeration, wind waves were generated by blowing the air above the water surface. The reference wind speed at the entrance of the wind tunnel *Ur* was varied from 4.0 to 12.0 m/s. Vertical profiles of the wind speed and the concentration of CO_2 in the air were measured at the fetch $x = 2.0$, 6.0, 9.0 and 12.0 m along the centerline of the tank. The vertical profile of the wind speed was measured by using a Pitot tube in the range of 0.30 m above the still water surface. u_{*a} was calculated by fitting the logarithmic law to the vertical profile. The 10 m-wind speed U_{10} was calculated by extrapolating the wind speed to 10 m height according to the logarithmic law.

Figure 2a shows a schematic diagram of the measuring system for the concentration of CO_2 in the air. The air in the wind tunnel was sampled by two inlet tubes, which were traversed vertically in the range of $z \leq 20$ cm. The sampling flow rate was about 1 l/min. The control of the sampling flow rate and the dehumidification of the air were made by a flow controller instrument. The concentration in the air was measured by using a non-dispersive infrared gas analyzer (NDIR, LI-COR LI-6252). The NDIR was calibrated with 198 and 498 ppm standard CO_2 gases. The data were recorded on a personal computer at 1 Hz. Though the air was sampled for 90 s at each level, only the data for the latter 60 s were used to evaluate the mean concentration.

Figure 2b shows a schematic diagram of the measuring system for the concentration of CO_2 dissolved in the water. The partial pressure of CO_2 in the water was quantified by using a gas–liquid equilibrator made of hydrophobic porous tube. There were a large number of small holes on the surface of the tube, and the diameter of the holes was about 1 μm. The CO_2 gas can be exchanged between the equilibrator and the water through such holes. An air-circulating circuit through the gas–liquid equilibrator and NDIR was set as shown in the figure. The position of the gas-liquid equilibrator was changed depending on experimental conditions. The equilibrator was located at 0.20 m below the still water surface and 0.50 m backward from the measuring position on the air side. The air CO_2 flowing in the hydrophobic porous tube was rapidly equilibrated with the dissolved CO_2 in the water. The equilibrated gas was dehumidified by both the peltier dryer and the magnesium perchlorate ($Mg(ClO_4)_2$). The partial pressure of CO_2 in the equilibrated gas pCO_2 was measured by a NDIR (RMT DX-6100) which can measure up to 50,000 ppm. The concentration of CO_2 in the water C_w was evaluated on the basis of Henry's law. The solubility of CO_2 in the water was calculated by using a function of Weiss (1974).

The mean concentration of CO_2 in the water during the flux measurement was used as C_w in (3) because the concentration decreases temporally. According to Henry's law, C_s was calculated from the partial pressure on the air side at the interface obtained by extrapolating the concentration profile to $z = 0$. The gas transfer velocity of CO_2 was normalized to k_{L600} for the fresh water at the standard reference temperature of 20°C by means of the Schmidt number dependence proposed by Jähne et al. (1987). The Schmidt number *Sc* is defined as ν_w/D, where ν_w is the kinematic viscosity of the water and D the molecular diffusivity of CO_2 in the water. We computed *Sc* by using a function of Wanninkhof (1992).

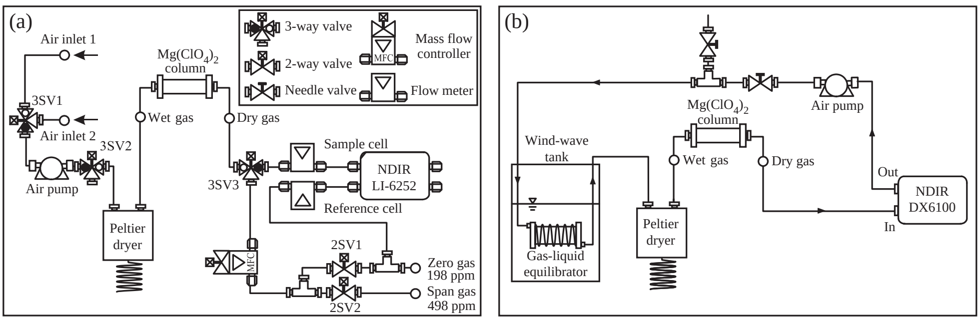

Figure 2. Schematic diagram of measuring system for CO_2: (a) on the air side and (b) on the water side.

4 RESULTS AND DISCUSSION

Figure 3 shows the vertical profiles of the mean concentration of CO_2 in the air in the case of $Ur = 6.0$ m/s. The solid lines indicate the fitting curves for the logarithmic law obtained by the least square method. Though the concentration on the water side is unequal for each case in the strict sense, it is clear that the vertical gradient of the concentration increases with the fetch. It is also apparent that logarithmic layers are formed near the water surface. The values of C_* were evaluated by fitting (2) to these logarithmic layers.

The corresponding profiles normalized by using u_{*a} and z_0 are shown in Figure 4, where the solid line indicates (2) and all the data in the present study are plotted. A large scattering of the data are seen around the solid line in the region of $z/z_0 > 3.0 \times 10^2$ because the logarithmic law is applicable only to the profile at small z. It is observed that the data agree accurately with (2) in the vicinity of the water surface. This implies that C_* estimated from the experimental results has a good accuracy.

Figure 5 shows the time variation of the partial pressure in the water pCO_2, from the start of the aeration to the end of the measurement in the case of $x = 9.0$ m and $Ur = 8.0$ m/s. pCO_2 increases gradually from the start of the aeration, and reaches about 40,000 μ atm after about 4,000 s. A rapid change of pCO_2 is found as soon as the wind begins to blow, and the partial pressure decreases monotonously due to the transfer of CO_2 from the water side to the air side.

In Figure 6, the time variations of pCO_2 during the flux measurement are shown for the cases of $x = 9.0$ m and $Ur = 4.0$, 8.0 and 12.0 m/s. We should note that the partial pressures are

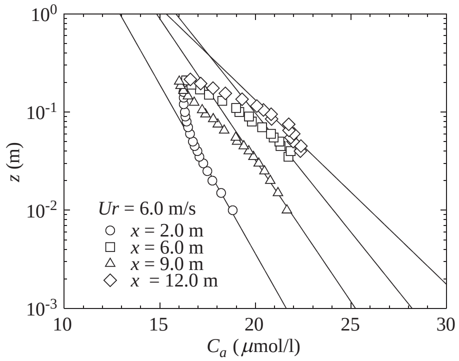

Figure 3. Vertical profiles of mean concentration of CO_2 in the air.

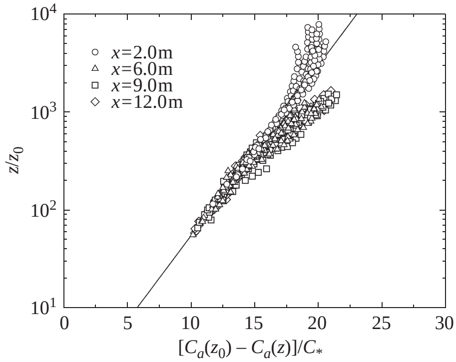

Figure 4. Normalized vertical profiles of mean concentration of CO_2 in the air.

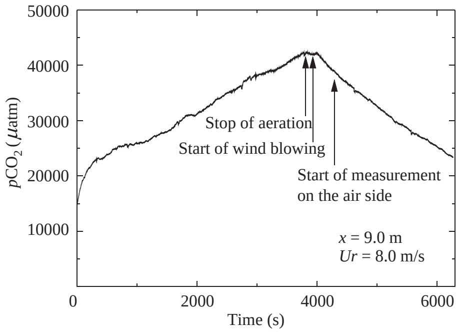

Figure 5. Time variation of pCO_2.

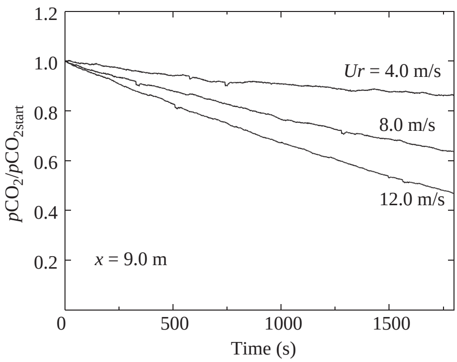

Figure 6. Dependence of the reduction rate of pCO_2 on the wind speed.

non-dimensionalized by the value at the start of the measurement $pCO_{2\mathrm{start}}$. The figure shows that the reduction rate of pCO_2 increases with the wind speed and the transfer velocity should increase with the wind speed. By averaging the partial pressure during the flux measurement, we calculated the values of C_w, which are necessary when estimating the transfer velocity.

Figure 7 shows the relations between the CO_2 transfer velocity on the water side k_L and the friction velocity on the air side u_{*a}. The results of experiments and field observations obtained by other researchers are also plotted in the figure. All the data in the figure have been normalized to k_{L600}. The experimental data of Komori et al. (1993) and Komori & Shimada (1995), and the field data of McGillis et al. (2001) correspond to the results of local flux measurements. On the other hand, the data of Broecker et al. (1978) (quoted from Jähne et al., 1979) and Ocampo-Torres et al. (1994) correspond to the transfer velocities averaged over the whole interface in a wind-wave tank. The results in this study show that the transfer velocity increases monotonously with the friction velocity, and also increases remarkably with the fetch under the condition of the same friction velocity. Komori et al. (1993) pointed out that the airflow separated at the wave crest reattaches in front of the leeward wave, where a high-shear region is formed and surface renewal eddies are generated. For a longer fetch, the airflow is separated more frequently, so that surface renewals may be more active. Therefore, the transfer velocity increases with the fetch if the mechanism of Komori et al. (1993) controls the mass transfer across the air-water interface. Though the dependence of wind waves and water-side turbulence on the fetch cannot be shown in the present study, the growth of them may be closely connected with the fetch dependence of the transfer velocity. It is also observed that the present results are relatively larger than the fetch-averaged transfer velocity obtained by other researchers. The difference between the present results and McGillis et al. (2001) becomes large in the region of low wind speed, whereas in the region of $u_{*a} > 0.5$ m/s, their data are close to the present results in the case of long fetch.

In the case of $x = 2.0$ m, the increasing rate of the transfer velocity begins to decrease around $u_{*a} = 0.3$ m/s, and it tends to increase again in the range of high friction velocity. This behavior has been already reported by Komori et al. (1993) and Komori & Shimada (1995). In their experiments, the measurements were carried out in the region of $x = 3$ to 5 m. Therefore, their results correspond to the transfer velocity in the case of short fetch. On the basis of the comparison of the present results with their ones, it is deduced that the transfer velocity in the case of short fetch indicates such a behavior against the friction velocity. As a reason why the transfer velocity tends to saturate in the region of intermediate friction velocity, Komori et al. (1993) concluded that the energy transferred from the airflow to water-side turbulence tends to saturate because of the energy consumption by wave growth.

In order to compare the experimental data in the present study with previous empirical expressions, the relations between the gas transfer velocity k_L and the 10 m-wind speed U_{10} are shown in Figure 8, where all the data have been normalized to k_{L600}. The results in the present study become larger than those of Liss & Merlivat (1986) and Nightingale et al. (2000) within the wind range

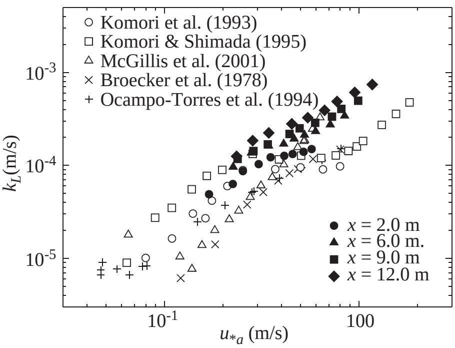

Figure 7. Relation between k_L and u_{*a}.

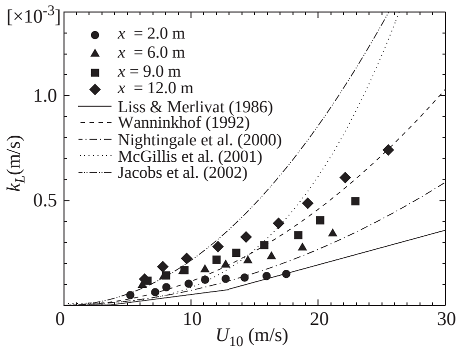

Figure 8. Relation between k_L and U_{10}.

shown in the figure. In the region of $U_{10} < 10$ m/s, the present results except the case of $x = 2.0$ m agree approximately with the expression of Jacobs et al. (2002), while in the region of $U_{10} > 15$ m/s, the results for $x = 9.0$ and 12.0 m are comparatively close to the expression of Wanninkhof (1992). The difference between the present results and the expressions of Jacobs et al. (2002) and McGillis et al. (2001), which provide the local transfer velocities based on the eddy correlation method, is found to be large in the region of high wind speed. However, their field observations were made in the region of $U_{10} < 15$ m/s, in which the present data almost exist between their expressions.

5 CONCLUSIONS

This paper presents laboratory wind-wave experiments to estimate the CO_2 transfer velocity at the surface of wind waves. In the experiments, the vertical profiles of the wind speed and the concentration of CO_2 in the air were measured at several fetches, and the local CO_2 flux was estimated by using the profile method. The concentration of CO_2 dissolved in the water was quantified by using the gas-liquid equilibrator. The local transfer velocity on the water side was obtained from these experimental results. The transfer velocity increases monotonously with the friction velocity and also increases remarkably with the fetch under the condition of the same friction velocity. In addition, the transfer velocity in the present study becomes relatively large compared with that averaged over the whole interface obtained by other researchers. With regard to the dependence on U_{10}, in the region of $U_{10} < 10$ m/s, the present results agree approximately with the empirical expression of Jacobs et al. (2002) except the case of $x = 2.0$ m, while in the region of $U_{10} > 15$ m/s, the results in the cases of $x = 9.0$ and 12.0 m are comparatively close to the expression of Wanninkhof (1992). The fetch dependence of the transfer velocity seems to be closely connected with the growth of wind waves and turbulent boundary layer, so that it is reasonable to suppose that an empirical expression for the transfer velocity should be described in terms of local characteristics of wind waves and turbulence.

REFERENCES

Broecker, H.C., J. Petermann & W. Siems 1978. The influence of wind on CO_2-exchange in a wind-wave tunnel, including the effect of monolayers. *J. Mar. Res.* 36: 595–610.

Jacobs, C., J.F. Kjeld, P. Nightingale, R. Upstill-Goddard, S. Larsen & W. Oost 2002. Possible errors in CO_2 air-sea transfer velocity from deliberate tracer releases and eddy covariance measurements due to near-surface concentration gradients. *J. Geophys. Res.* 107: doi:10.1029/2001JC000983.

Jähne, B., K.O. Münnich & U. Siegenthaler 1979. Measurements of gas exchange and momentum transfer in a circular wind-water tunnel. *Tellus* 31: 321–329.

Jähne, B., K.O. Münnich, R. Bösinger, A. Dutzi, W. Huber & P. Libner 1987. On the parameters influencing air-water gas exchange. *J. Geophys. Res.* 92: 1937–1949.

Komori, S., R. Nagaosa & Y. Murakami 1993. Turbulence structure and mass transfer across a sheared air-water interface in wind-driven turbulence. *J. Fluid Mech.* 249: 161–183.

Komori, S. & T. Shimada 1995. Gas transfer across a wind-driven air-water interface and the effects of sea water on CO_2 transfer. In B. Jähne & E.C. Monahan (eds), *Air-Water Gas Transfer*: 553–569. Hanau: AEON.

Liss, P.S. & L. Merlivat 1986. Air-sea gas exchange rates: Introduction and synthesis. In P. Baut-Ménard (ed.) *The Role of Air-Sea Exchange in Geochemical Cycling*: 113–127. Dordrecht: D. Reidel.

McGillis, W.R., J.B. Edson, J.E. Hare & C.W. Fairall 2001. Direct covariance air-water CO_2 fluxes. *J. Geophys. Res.* 106: 16729–16745.

Nightingale, P.D., G. Malin, C.S. Law, A.J. Watson, P.S. Liss, M.I. Liddicoat, J. Boutin & R.C. Upstill-Goddard 2000. In situ evaluation of air-sea gas exchange parameterizations using novel conservative and volatile tracers. *Global Biogeochem. Cycles.* 14: 373–387.

Ocampo-Torres, F.J., M.A. Donelan, N. Merzi & F. Jia 1994. Laboratory measurements of mass transfer of carbon dioxide and water vapour for smooth and rough flow conditions. *Tellus* 46B: 16–32.

Wanninkhof, R. 1992. Relationship between wind speed and gas exchange over the ocean. *J. Geophys. Res.* 97: 7373–7382.

Weiss, R.F. 1974. Carbon dioxide in water and seawater: The solubility of a non-ideal gas. *Mar. Chem.* 2: 203–215.

Environmental Hydraulics and Sustainable Water Management – Lee & Lam (eds)
© 2005 Taylor & Francis Group, London, ISBN 04 1536 546 5

Surface-renewal eddies at the air-water interface in oscillating-grid turbulence

Y. Sugihara & H. Tsumori
Department of Earth System Science and Technology, Kyushu University, Kasuga, Fukuoka, Japan

ABSTRACT: Characteristics of surface-renewal eddies are investigated experimentally to examine the mechanism of gas transfer at the air-water interface. The experiments are performed in oscillating-grid turbulent flows with various water depth. The horizontal velocity fields on the interface are measured using a particle image velocimetry. The gas transfer velocities on the water side are also obtained through aeration experiments of O_2. Statistical quantities such as the dissipation rate and the free-surface divergence are obtained from the results of velocity measurements. The experimental data support that the root-mean-square of the free-surface divergence increases in proportion to $(\varepsilon_s/\nu)^{1/2}$, where ε_s is the dissipation rate and ν the kinematic viscosity of the water. The gas transfer velocity is found to depend on $-1/4$ power of a turbulent Reynolds number. This implies that the interfacial gas transfer due to oscillating-grid turbulence should be described by a certain kind of small-eddy model.

1 INTRODUCTION

For sparingly soluble gases such as O_2 and CO_2, the gas transport across the air-water interface is usually controlled by the resistance in the water phase, so that interfacial gas transport rates are determined by the gas transfer velocity on the water side. The formulation of the transfer velocity has frequently been made in terms of turbulent characteristic quantities concerning surface-renewal eddies. Thus, detailed observations of such eddies are an important subject from viewpoints of environmental hydraulics and chemical engineering.

One of the simple laboratory flow systems is turbulence in the absence of mean flow, which is often generated using an oscillating grid. Chu & Jirka (1992) examined the concentration boundary layer of O_2 on the water side close to the air-water interface in grid-generated turbulent flows. They pointed out on the basis of cospectra from velocity and concentration fluctuations that large eddies in a lower frequency range dominate the interfacial gas transfer, so concluded that a dimensionless gas transfer velocity is in proportion to $-1/2$ power of a turbulent Reynolds number. On the other hand, using a similar experimental apparatus, Asher & Pankow (1986) and Dickey et al. (1984) found out the relation $k_L \propto D^{1/2}(\varepsilon_s/\nu)^{1/4}$ with D being the molecular diffusivity of O_2 in the water. This finding supports that the gas transfer should be represented in terms of a small-eddy model (e.g. Jähne & Monahan, 1995). These earlier experiments thus become inconsistent though turbulent fields are simple enough.

The purpose of this study is to present some laboratory results of relevance to surface-renewal eddies at the air-water interface in oscillating-grid turbulent flows. The horizontal velocity fields on the air-water interface are measured using a particle image velocimetry (PIV), and turbulent characteristic quantities of such eddies are obtained from the results of the measurements. The relations between the quantities and the gas transfer velocity on the water side are also examined.

2 EXPERIMENTAL PROCEDURE

Figure 1 shows a schematic diagram of experimental apparatus. The size of a rectangular water tank was 25 cm long, 25 cm wide and 60 cm deep. A horizontal square grid was oscillated in the vertical direction to generate turbulence. The mesh size of the grid M was 5.0 cm, and the width of crossing square bars was 1.0 cm. Tap water across a filter system for purification was used as the working fluid. Experimental parameters are summarized in Table 1, where f_g and S_g denote the frequency and the stroke of the grid oscillation, respectively and z_s is the distance from the center of the grid oscillation to the water surface. *Re* indicates a grid Reynolds number defined as $f_g S_g^2/\nu$.

A particle image velocimetry (PIV) was used for velocity measurements on the air-water interface; the setup is shown in Figure 1a. A horizontal plane very close to the interface was illuminated with a 1 kW slide projector, and flow pattern images in this plane were taken with a digital video camera. The PIV analyses with two digital images taken at an interval of 30 s were conducted for the region of $20 \times 20\,\mathrm{cm}^2$ far from walls of the water tank. The number of pixels in the image is listed in the table. The spatial resolution in the present analyses Δl becomes 0.58 mm or 0.63 mm. Statistical quantities, i.e. the turbulent kinetic energy k_s, the dissipation rate of the energy ε_s, the vertical vorticity ω, Taylor's micro length scale λ and the integral length scale l defined as $k_s^{3/2}/\varepsilon_s$, were obtained from the results of velocity measurements. The free-surface divergence β, i.e.

$$\beta = \frac{\partial u}{\partial x} + \frac{\partial v}{\partial y}, \tag{1}$$

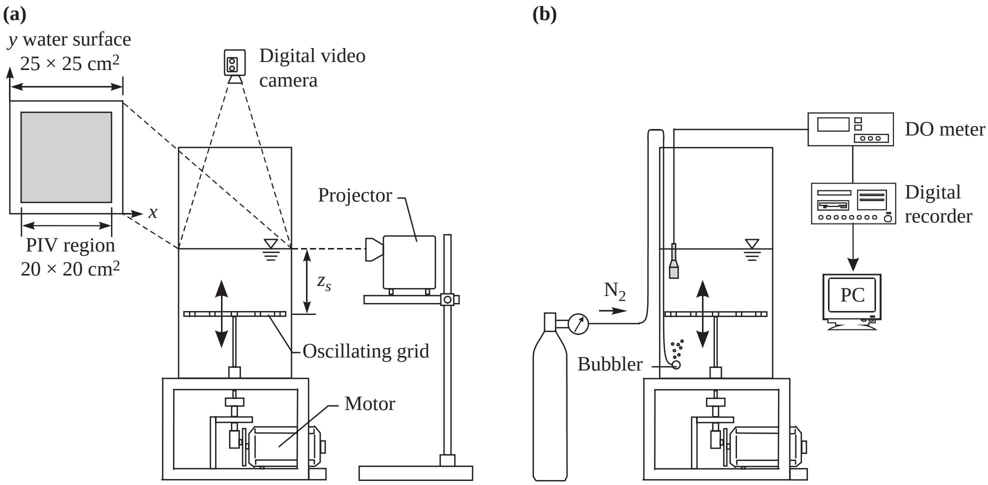

Figure 1. Schematic diagram of experimental apparatus: (a) for PIV and (b) for aeration experiments.

Table 1. Experimental parameters.

Run No.	f_g (Hz)	S_g (cm)	M (cm)	z_s (cm)	*Re*	Pixels	Δl (mm)	k_L (cm/s)
1	2.0	4.0	5.0	15	3.73×10^3	344 × 344	0.58	8.18×10^{-4}
2	2.0	4.0	5.0	10	3.73×10^3	316 × 316	0.63	9.74×10^{-4}
3	2.0	4.0	5.0	7.5	3.73×10^3	316 × 316	0.63	1.20×10^{-3}
4	4.0	4.0	5.0	15	7.47×10^3	344 × 344	0.58	9.69×10^{-4}
5	4.0	4.0	5.0	10	7.47×10^3	316 × 316	0.63	1.31×10^{-3}
6	4.0	4.0	5.0	7.5	7.47×10^3	316 × 316	0.63	1.76×10^{-3}
7	2.0	6.0	5.0	15	8.40×10^3	344 × 344	0.58	1.46×10^{-3}
8	4.0	6.0	5.0	15	1.68×10^4	344 × 344	0.58	2.61×10^{-3}

with u and v being fluctuating velocities in x and y directions, respectively, was also deduced because it has been thought to be directly associated with surface renewal eddies. McKenna & McGillis (2004) conducted laboratory experiments concerning the gas transfer due to oscillating-grid turbulence, and they concluded that bulk turbulence estimates are unable to provide a strong relationship for the gas transfer velocity, whereas the free-surface divergence becomes important in the interfacial gas transport. Under assumptions that horizontal velocity fluctuations are isotropic in a horizontal plane and both the vertical velocity and the vertical gradient of horizontal velocity are set to zero at the air-water interface, these statistical quantities were calculated by averaging arithmetically the mean values for five instantaneous velocity fields. Longitudinal wavenumber spectra for velocity fluctuations along pixel lines in x and y directions were also calculated, and the statistical mean values $F(k)$ with k being the wavenumber were obtained from the ensemble averages over all the spectra for five velocity fields.

The gas transfer velocities on the water side k_L were obtained through aeration experiments of O_2; the setup is shown in Figure 1b. The concentration of O_2 in the water was decreased in advance by injecting N_2 into the water in the tank. After the injection, turbulence was generated by oscillating the grid. The transfer velocities were determined from the increasing rate of O_2 transferred from the air side to the water side. The values of k_L are given in Table 1.

3 RESULTS AND DISCUSSION

Figure 2 shows a snapshot of the instantaneous horizontal velocity field on the air-water interface, which has been obtained from PIV measurements in the case of Run1. It is observed from the figure that the turbulent structure is almost isotropic and homogeneous in the horizontal plane. Also, relatively large horizontal eddies are found to form in the turbulence.

Contour maps of the vertical vorticity and the free-surface divergence calculated from the velocity field shown in Figure 2 are drawn in Figures 3 and 4, respectively. Here, the solid and dotted lines indicate the positive values and negative ones, respectively. The values of the integral length scale and the Taylor micro length scale are given in these figures, and they are 2.73 cm and 0.61 cm, respectively. In the regions for large vorticity exist the horizontal eddies appearing in Figure 2, and the spatial scale of these regions corresponds approximately to the integral length scale. On the other hand, the spatial scale of the free-surface divergence is significantly smaller than that of the vorticity, and it seems to be characterized by the micro length scale rather than the integral length scale.

Figure 5 shows longitudinal wavenumber spectra for velocity fluctuations under the conditions of Runs 1 to 3, for which the grid conditions were remained fixed and the water depth was varied

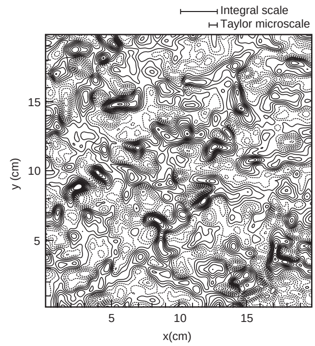

Figure 2. Instantaneous horizontal velocity field on the air-water interface.

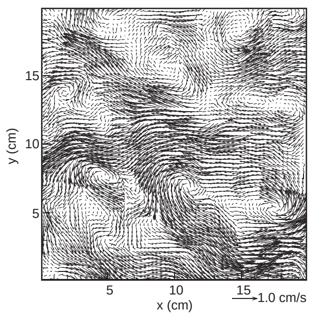

Figure 3. Contour map of instantaneous vertical vorticity.

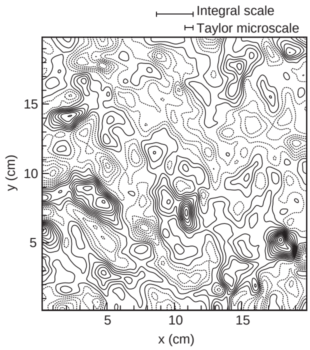

Figure 4. Contour map of instantaneous free-surface divergence.

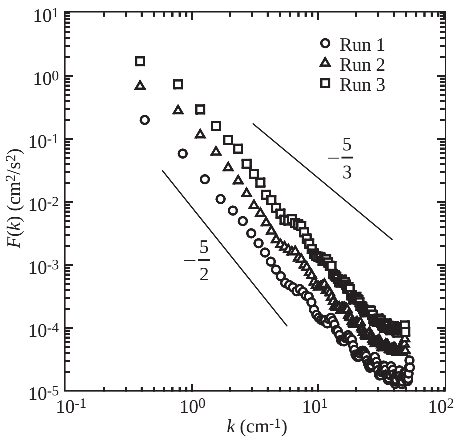

Figure 5. Longitudinal wavenumber spectra for velocity fluctuations.

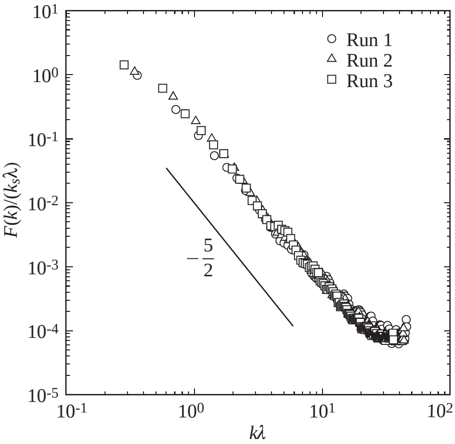

Figure 6. Dimensionless longitudinal wavenumber spectra.

from 7.5 to 15 cm. The slope of the spectra is found to be independent of the water depth, though the magnitude is decreased with increasing the water depth. The spectra decay approximately in proportion to $-5/2$ power of k, and the spectral slope becomes steep compared with $-5/3$ power for isotropic turbulence. The power exponent is comparatively close to that for oscillating-grid turbulence obtained experimentally by Brumley & Jirka (1987). These spectra have been nondimensionalized by using the turbulent kinetic energy and the Taylor micro length scale, and the dimensionless profiles are shown in Figure 6. The figure shows that the dependence of the spectra on the water depth has vanished, and they have been normalized to a universal relation. It should be noted that in the case where the water depth or the integral length scale is used for the normalization, the dimensionless profiles cannot be expressed universally. These facts suggest that the micro length scale is significant to quantify statistical properties of surface-renewal eddies very close to the air-water interface.

Considering the units of the free-surface divergence, we examine the dependence of the root-mean-square (*RMS*) of the surface divergence β_{rms} on the ratio of the turbulent velocity $k_s^{1/2}$ to the integral length scale l or the micro length scale λ. Figure 7 shows the relationship between β_{rms} and $k_s^{1/2}/l$. It is difficult to find a certain relation between both, so that l is not suitable for characterizing the free-surface divergence. Figure 8 also demonstrates the dependence of β_{rms} on $k_s^{1/2}/\lambda$. The *RMS* of the surface divergence β_{rms} increases linearly with $k_s^{1/2}/\lambda$, and the proportionality constant is independent of the water surface. Thus, the free-surface divergence is closely connected with the micro length scale. Here, let us check the relationship between the dissipation rate ε_s and $\nu k_s/\lambda^2$, which is represented in Figure 9. A strong proportional correlation is observed between both, the proportionality constant appears to be somewhat smaller than 15 for isotropic turbulence. According to Figures 8 and 9, β_{rms} should be proportional to the inverse of Kolmogorov's time scale $(\varepsilon_s/\nu)^{1/2}$. Figure 10 shows the dependence of β_{rms} on $(\varepsilon_s/\nu)^{1/2}$, and the experimental data support the following relation:

$$\beta_{rms} = 0.35\sqrt{\varepsilon_s/\nu}\ . \tag{2}$$

The relation between the gas transfer velocity k_L and the *RMS* of the free-surface divergence β_{rms} is shown in Figure 11. It is seen from the figure that k_L is proportional to 1/2 power of β_{rms}. From the experimental results, we obtain

$$k_L = 0.30\sqrt{D\beta_{rms}}\ . \tag{3}$$